THE UNIVERSITY *of* EDINBURGH

This thesis has been submitted in fulfilment of the requirements for a postgraduate degree (e.g. PhD, MPhil, DClinPsychol) at the University of Edinburgh. Please note the following terms and conditions of use:

This work is protected by copyright and other intellectual property rights, which are retained by the thesis author, unless otherwise stated.
A copy can be downloaded for personal non-commercial research or study, without prior permission or charge.
This thesis cannot be reproduced or quoted extensively from without first obtaining permission in writing from the author.
The content must not be changed in any way or sold commercially in any format or medium without the formal permission of the author.
When referring to this work, full bibliographic details including the author, title, awarding institution and date of the thesis must be given.

Investigating CDK9 inhibitor treatment during the innate inflammatory and regenerative response in a zebrafish model of cardiac injury

Aryan Kaveh

Doctor of Philosophy

The University of Edinburgh

2021

Declaration

I hereby declare that the work presented in this thesis has been performed by myself at the University of Edinburgh, unless stated otherwise. This thesis has not been submitted for any other degree or professional qualification.

Aryan Kaveh

May 2021

Publications

Data I acquired during this project has been published or is under review for publication at the time of thesis submission, as indicated below.

Taylor JM, Nelson CJ, Bruton FA, **Kaveh A**, Buckley C, Tucker CS, Rossi AG, Mullins JJ, Denvir MA. **Adaptive prospective optical gating enables day-long 3D time-lapse imaging of the beating embryonic zebrafish heart**. Nat Commun. 2019 Nov 15;10(1):5173. doi: 10.1038/s41467-019-13112-6.

Kaveh A, Bruton FA, Buckley C, Oremek MEM, Tucker CS, Mullins JJ, Taylor JM, Rossi AG, Denvir MA. **Live Imaging of Heart Injury in Larval Zebrafish Reveals a Multi-Stage Model of Neutrophil and Macrophage Migration**. Front Cell Dev Biol. 2020 Oct 19;8:579943. doi: 10.3389/fcell.2020.579943.

Kaveh A, Bruton FA, Oremek MEM, Tucker CS, Taylor JM, Mullins JJ, Rossi AG, Denvir MA. **Selective CDK9 inhibition resolves neutrophilic inflammation and enhances cardiac regeneration in larval zebrafish**. Development (*in review 2021 May*).

Abstract

Neutrophils and macrophages are crucial effectors and modulators of cardiac repair following myocardial infarction (MI). Sustained neutrophilic inflammation is detrimental for cardiac repair and associated with adverse MI outcomes. An attractive therapeutic strategy to treat acute inflammatory disorders, such as MI, is to resolve infiltrating neutrophils to positively influence downstream reparative mechanisms. CDK9 inhibitor compounds enhance the resolution of neutrophilic inflammation, however, their effects on cardiac repair/regeneration are unknown. Unlike adult mammalian hearts, zebrafish hearts regenerate following injury via cardiomyocyte proliferation. Prolonged neutrophil retention has been shown to impair cardiomyocyte proliferation and myocardial wound regression following cardiac injury in zebrafish. I therefore hypothesised that CDK9 inhibitor treatment enhances the resolution of neutrophilic inflammation following injury and promotes cardiac regeneration in zebrafish.

I first refined a larval zebrafish cardiac laser injury model and developed bespoke epifluorescence and 4D heartbeat-synchronised light sheet fluorescence microscopy techniques. I characterised the innate inflammatory response to cardiac injury, specifically examining neutrophil and macrophage migration to the injured heart using high resolution imaging of transgenic reporter fish. Additionally, neutrophil and macrophage migratory responses were compared to the archetypal tail fin injury model. Live *in vivo* imaging permitted mapping of neutrophil and macrophage migration throughout the zebrafish larvae, from primary hematopoietic sites to the myocardial lesion. I found a conserved sequence of events marked by an early and acute phase of neutrophil recruitment followed by sustained macrophage recruitment. In each injury model I found the innate inflammatory response resolves by reverse migration.

I used the characterised zebrafish cardiac injury model to test whether CDK9 inhibitors, AT7519 and Flavopiridol (FVP), resolve neutrophil infiltration and whether this regulates downstream macrophage involvement and cardiac repair/regeneration. AT7519 and FVP were found to enhance the resolution of neutrophilic inflammation by inducing neutrophil reverse migration from the injured heart. While continuous exposure to AT7519 or FVP caused adverse cardiac phenotypes, transient (pulsed) treatment accelerated neutrophil resolution and avoided these effects. Transient treatment with AT7519, but not FVP, augmented *TNF* polarisation of wound-associated macrophages, in turn enhancing cardiomyocyte number expansion and the rate of myocardial wound closure. Furthermore, I developed a selectivity assay using *cdk9*$^{-/-}$ knockout mutants that demonstrated AT7519 is a more selective CDK9 inhibitor than FVP. These findings highlight the potential of AT7519 as a promising treatment that resolves neutrophilic inflammation following cardiac injury and promotes cardiomyocyte regeneration.

In collaboration with BioAscent Discovery Ltd, I performed an *in silico* ligand-based screen of a 125k compound library. The chemical structure of AT7519 and five other potent and selective CDK9 inhibitor compounds (AZD4573, LDC000067, iCDK9, NVP-2 and MC180295) were used to perform a 3D similarity search against BioAscent's 125k diversity library, with the aim of identifying novel and efficacious CDK9 inhibitors. For each of the six query compounds, the top 1000 BioAscent compounds were ranked based on 3D similarity score. Common (duplicated) compounds between the six ranked query lists were shortlisted and any compounds that displayed pan-assay interference properties were removed. This yielded a final focussed library of 598 BioAscent compounds. Further work is needed to develop a high throughput *in vitro* CDK9 inhibition assay to screen the custom library and identify promising candidate compounds for downstream validation and optimisation.

Lay Summary

A heart attack occurs when a blood vessel in the heart becomes blocked, causing billions of heart muscle cells to die. Neutrophils are inflammatory white blood cells that circulate within the bloodstream, acting as the first line of defence against injury or infection. Shortly after a heart attack, circulating neutrophils sense damage and are recruited to the heart. Once at the heart, neutrophils recruit other white blood cells called monocytes, which eventually turn into macrophages. Both neutrophils and macrophages play important roles during heart repair after injury. However, if neutrophils persist at the injured heart, they can cause additional damage, leading to worse outcomes after a heart attack. One approach to improve repair of the injured heart is to administer drugs that resolve neutrophil infiltration. A specific class of drugs, known as CDK9 inhibitors, have been shown to help remove neutrophils following injury or infection in mice. However, it is not known if these drugs can promote repair of the heart following injury. Unlike mammals, zebrafish have a remarkable capacity to completely regenerate their hearts after injury. In the zebrafish heart, existing heart muscle cells can divide to replace dead heart muscle cells. Studies in zebrafish have shown that neutrophils have negative effects on heart regeneration. In this project I tested whether CDK9 inhibitor drugs can resolve neutrophils and promote heart regeneration after injury in zebrafish.

I used 3-day old zebrafish larvae as they are transparent, small and genetically modifiable, allowing live imaging of fluorescently tagged neutrophils, macrophages and heart muscle using advanced microscopy. I measured neutrophil and macrophage responses following heart laser injury and compared this to a well-characterised tail fin injury method. This allowed me to better understand neutrophil and macrophage recruitment to the injured heart. I found a similar sequence of events in both injury settings, where neutrophils are recruited first, and macrophages later.

Having better understood the neutrophil and macrophage response following heart injury, I next tested if CDK9 inhibitor drugs, AT7519 and Flavopiridol (FVP), can help resolve neutrophil infiltration. I also tested if these drugs affect macrophage involvement and heart regeneration. I found that both AT7519 and FVP resolve neutrophils at the injured heart by causing them to migrate away. I found that pulsed treatment with AT7519 converted more macrophages to a reparative state, which boosted heart regeneration. I showed that AT7519 is a more effective drug as it displays greater specific activity against CDK9 compared to FVP. My findings highlight the potential of AT7519 as a promising drug therapy that resolves infiltrating neutrophils and promotes heart regeneration after injury.

Acknowledgements

First and foremost, I would like to offer my sincere gratitude to my supervisors, Dr Martin Denvir and Prof Adriano Rossi, for their continuous guidance, support and advice throughout the PhD. The COVID-19 pandemic presented unforeseen hurdles during my final year; I especially thank you for your mentorship during this time.

Special thanks to Dr Carl Tucker for acting as a third supervisor and providing zebrafish-related assistance during these four years, all the while maintaining a world-class aquatics facility.

Many thanks to my funders, Medical Research Scotland, for this opportunity.

Thank you to Dr Jonny Taylor for developing the exceptional heart synchronisation software and assisting with all thing's electronics and optics.

A big thank you to my PhD lab partner, Finn Bruton, for your invaluable encouragement and support whether that be during our runs around Edinburgh or in the lab. It's been a pleasure to share this experience with you from start to finish.

Thanks to my PhD committee, Prof Scott Webster and Prof Catherina Becker, for their constructive advice.

Thanks to the Rossi lab, especially Magdalena Oremek, Giulia Rinaldi and Dr Calum Robb for lending a helping hand with the human neutrophil work.

Thanks to Dr Charlotte Buckley for initially helping me get accustomed to the light sheet fluorescence microscope and assisting with image analysis.

Thanks to Prof John Mullins for critically reviewing my manuscripts.

Thanks to the staff at BioAscent, especially Dr Sylviane Boucharens, Dr Mike Piper and Dr Stuart McElroy for their support, despite our drug screening plans being disrupted by the pandemic.

Thanks to Dr Steven Shave for kindly assisting with the ligand-based virtual screen.

Thanks to Prof Steve Renshaw and Prof Graham Lieschke for providing useful zebrafish lines.

To all my friends, thank you for showing genuine interest in my research.

A special thank you to Giovana for always being there, especially around the time of thesis submission.

Finally, to my mum, dad and sister for their unconditional support, I dedicate this thesis to you.

Table of Contents

List of Figures

List of Tables

List of Abbreviations

A – Atrium

Aa – Aortic arches

AnnV – Annexin V

ANOVA – Analysis of variance

ATAC – Assay for transposase-accessible chromatin

ATP – Adenosine triphosphate

Ba – Bulbus arteriosus

Bcl-2 – B cell lymphoma-2

C5a – Complement component 5a

CCL – C-C motif chemokine ligand

Cdc – Cell division cycle

CDK – Cyclin-dependent kinase

CDK9i – CDK9 inhibitor

CFP – Cyan fluorescent protein

CHT – Caudal hematopoietic tissue

CRISPR/Cas9 – Clustered regularly interspaced short palindromic repeats/caspase 9

CTD – Carboxyl terminal domain

CV – Cardinal vein

CXCL – Chemokine C-X-C motif ligand

CXCR – C-X-C chemokine receptor

DA – Dorsal aorta

DAMP – Damage-associated molecular pattern

DAPI – 4', 6-diamidino-2-phenylindole

DLAV – Dorsal lateral anastomotic vessel

DMSO – Dimethyl sulfoxide

DNA – Deoxyribonucleic acid

Dpf – Day post fertilisation

Dpi – Day post injury

FACS – Fluorescent-activated cell sorting

FEP – Fluorinated Ethylene Propylene

FPR – Formyl peptide receptor

FVP – Flavopiridol

gDNA – Genomic DNA

GFP – Green fluorescent protein

GM-CSF – Granulocyte-macrophage-colony stimulating factor

Hpf – Hours post fertilisation

Hpi – Hours post injury

Hpt – Hours post treatment

I/R – Ischaemia/reperfusion

IL-1β – Interleukin 1 beta

IMDM – Iscove's modified dulbecco's medium

ISV – Intersegmental vessel

kDA – Kilodaltons

LPS – Lipopolysaccharide

LSFM – Light sheet fluorescence microscopy

LTB_4 – Leukotriene B_4

Mcl-1 – Myeloid cell leukaemia 1

MerTK – Myeloid-epithelial-reproductive tyrosine kinase

MI – Myocardial infarction

Mpx – Myeloperoxidase

mRNA – Messenger RNA

n – Number of individual subjects

NADPH – Nicotinamide adenine dinucleotide phosphate

NF-κB – Nuclear factor kappa-light-chain-enhancer of activated B cells

Ns – Non-significant

NTR – Nitroreductase enzyme

p – Calculated probability value

P-TEFb – Positive transcription elongation factor b

PAINS – Pan-assay interference compounds

PALM – Photo activated laser microdissection

PBS – Phosphate-buffered saline

PCI – Percutaneous coronary intervention

PCL – Parachordal lymphatic

PCR – Polymerase chain reaction

PFA – Paraformaldehyde solution

PRR – Pattern recognition receptor

PTU – Phenylthiourea

Q-VD-OPh – Quinoline-Val-Asp-Difluorophenoxymethylketone

RFP – Red fluorescent protein

RNA – Ribonucleic acid

RNAPII – RNA Polymerase II

ROS – Reactive oxygen species

SD – Standard deviation

SEM – Standard error of the mean

Tg – Transgenic

TGFβ – Transforming growth factor β

TLR – Toll-like receptor

TNF – Tumour necrosis factor

TUNEL – Terminal deoxynucleotidyl transferase dUTP nick end labelling

V – Ventricle

Vc – Venous cavernous

VEGF – Vascular endothelial growth factor

Chapter 1. Introduction

1.1. Myocardial infarction

Myocardial infarction (MI) is a leading cause of morbidity and mortality worldwide. A MI arises when a thrombus occludes a coronary artery, which primarily occurs following atherosclerotic plaque rupture (Bentzon et al., 2014). Consequently, this causes a sudden and dramatic reduction in blood flow to the myocardium, leading to coronary ischaemia and extensive cardiomyocyte necrosis. In the majority of MI cases, an emergency clinical procedure known as percutaneous coronary intervention (PCI) is performed to mechanically restore blood flow to the injured heart muscle and limit further damage (Silber et al., 2005). Although coronary reperfusion mitigates further ischaemia and infarct expansion, sudden restoration of blood flow to the infarcted myocardium may also exert additional tissue damage (Heusch, 2020). This phenomenon is referred to as myocardial ischemia/reperfusion (I/R) injury. Strikingly, a MI can cause up to a billion of ventricular cardiomyocytes to undergo necrosis, leading to a reduction in cardiac function (Laflamme and Murry, 2005). As the heart can no longer sustain the metabolic demands of the body following MI, secondary complications such as heart failure often arise (Lewis et al., 2003). In the weeks and months following a MI, cardiac dysfunction can be exacerbated by adverse ventricular remodelling and scarring, the extent of which varies depending on the infarct size (Frangogiannis, 2012). As the injured heart attempts to repair and compensate, surviving cardiomyocytes undergo hypertrophy and the infarcted region is eventually replaced by non-contractile, poorly conductive fibrotic scar tissue (Talman and Ruskoaho, 2016). Despite a lack of myocardial regeneration, MI can be successfully treated and managed with analgesic and antithrombotic agents, such as aspirin (Anderson and Morrow, 2017). Additionally, other commonly used clinical therapies such as beta-adrenoreceptor antagonists and angiotensin converting enzyme inhibitors can substantially

improve cardiac function by targeting maladaptive and counter-regulatory mechanisms, thereby reducing the risk of heart failure (Fang, 2005). However, there are currently no approved treatments that directly promote repair/regeneration of the damaged myocardium. The inflammatory response following MI is being increasingly recognised as a crucial effector and regulator of myocardial repair. As such, immunomodulatory therapies have recently garnered notable interest as a strategy for treating MI (Panahi et al., 2018 and Huang and Frangogiannis, 2018).

1.2. The innate inflammatory response post MI

1.2.1. Initiation of inflammation

Inflammation is essential for host defence following injury or infection. In the context of tissue injury, a tightly regulated and multifaceted innate inflammatory response is required to restore tissue homeostasis. However, in many disease scenarios, chronic inflammation aggravates the original pathology. Immediately following a MI, necrotic cardiomyocytes release their extracellular and intracellular contents which act as endogenous “danger signals” to initiate the innate immune response. These signals include an extensive family of mediators referred to as damage-associated molecular patterns (DAMPs), which alarm the body of injury (Bianchi, 2007). More specifically, DAMPs are formed of extracellular matrix proteins (e.g., biglycan), cytosolic mediators (e.g., ATP), nuclear components (e.g., DNA and RNA), mitochondrial components (e.g., mitochondrial DNA and formylated peptides), amongst other factors (Roh and Sohn et al., 2018). Upon their release, DAMPs bind pattern recognition receptors (PRRs), such as toll-like receptors (TLRs) and inflammasomes to activate the innate immune system (Mann, 2011). In murine models of MI, genetically knocking out TLR2 or TLR4 was shown to be protective following ischaemic cardiac injury by preserving cardiac function and reducing myocardial fibrosis (Arslan et al., 2010; Oyama et al., 2004 and Timmers et al., 2008).

The activation of PRRs by DAMPs promotes downstream pro-inflammatory signaling, such as the activation of nuclear factor (NF)-κB, a transcription factor involved in producing inflammatory cytokines and chemokines. The expression of pro-inflammatory cytokines, such as tumour necrosis factor (TNF) and interleukin 1 beta (IL-1β) are upregulated in the injured heart within an hour of MI (Herskowitz et al., 1995). The role of TNF following cardiac injury is pleiotropic as it can enhance inflammation-induced injury but also protect against cardiomyocyte apoptosis (Frangogiannis et al., 1998; Maekawa et al., 2002 and Kurrelmeyer et al., 2000). IL-1β has been shown to enhance leukocyte recruitment to the infarcted heart and its inhibition ameliorates cardiac dysfunction following MI (Bujak et al., 2008; Sager et al., 2015 and Abbate et al., 2011). Other signaling pathways, such as the complement cascade are also activated and involved in engaging the immune response early following MI. Depletion or inhibition of complement factors was also found to be cardioprotective by reducing myocardial tissue damage and preserving viable myocardium (Vogel, 2020). Furthermore, reactive oxygen species (ROS), are synthesised early following MI and play equally vital roles in regulating inflammation-induced injury. During coronary reperfusion, the sudden reintroduction of oxygen-rich blood to hypoxic tissue can enhance ROS-mediated signaling, leading to further cardiomyocyte death (Peoples et al., 2019). This is a particularly prominent feature of myocardial I/R injury. Overall, TLR activation, cytokines, the complement cascade and ROS are required for inflammatory signal transduction, however, when overstimulated following MI, their activity promotes inflammation-induced injury and exacerbates myocardial dysfunction. Importantly, the aforementioned inflammatory signals are responsible for upregulating chemokine expression in the infarcted heart. Chemokines are a family of chemotactic cytokines; therefore, their primary function is to orchestrate leukocyte migration. It is well established that chemokines are responsible for leukocyte extravasation to the infarcted myocardium following MI (Chen and Frangogiannis, 2021). Two leukocytes, the neutrophil and monocyte, have especially important roles during myocardial injury and repair.

1.2.2. Role of neutrophils

In humans, neutrophils account for approximately 70% of circulating leukocytes and they have crucial roles during host defence (Duffin et al., 2010). Neutrophils protect against invading pathogens by releasing cytotoxic granules and displaying phagocytic capabilities (Rosales, 2018). In order for a large number of neutrophils to be trafficked to a site of infection/injury, they require to be mobilised from the bone marrow, the largest neutrophil reservoir in mammals (Furze and Rankin, 2008). Following tissue wounding, circulating neutrophils are recruited to the injury site within minutes where they are required for downstream wound repair (Su and Richmond, 2015). However, if not removed in a timely fashion, neutrophils can be detrimental to tissue repair. For example, during I/R injury, neutrophils release cytotoxic granules and exacerbate the inflammatory response (Bratton and Henson, 2011). In the context of MI, neutrophils are rapidly recruited to the infarcted myocardium in large numbers. The neutrophil response peaks at 1-day post MI, decreasing to low levels by 6-days post MI (Nahrendorf et al., 2007 and McSweeney et al., 2010). Neutrophils are initially recruited to the infarct in response to DAMPs released by necrotic cardiomyocytes (McDonald et al., 2010; Oka et al., 2012 and Zhang et al., 2010). Mitochondrial DAMPs, such as formylated peptides and mitochondrial DNA, bind formyl peptide receptor-1 (FPR1) and TLR9 on the surface of neutrophils respectively, thereby activating them. Furthermore, the chemokine (C-X-C motif) ligand 8 (CXCL8) is rapidly upregulated by the infarcted myocardium to further potentiate neutrophil chemotaxis via binding of C-X-C chemokine receptor type 2 (CXCR2) (Chen and Frangogiannis, 2021 and Ma et al., 2013). Inhibition of CXCL8 or its receptors CXCR1/2 reduces neutrophil recruitment to the myocardial infarct (Mahler, 2004 and Montecucco et al., 2010). Additionally, lipid-derived mediators such as leukotriene B_4 (LTB_4), have been shown to have potent chemotactic effects on neutrophils in murine models of sterile injury (Lammermann et al., 2013). The authors of this study found that LTB_4, alongside other chemoattractants, contribute to the coordinated infiltration and clustering of neutrophils around damaged tissue, a phenomenon termed neutrophil swarming (Lammermann et al., 2013).

In the context of MI, activated neutrophils home in on the injured heart by adhering to and subsequently transmigrating across the endothelium. Neutrophil transendothelial migration is mediated under the guidance of local chemoattractants and adhesion molecules expressed on activated endothelial cells (Filippi, 2019). This allows infiltrating neutrophils to undergo conformational changes and pass between cellular junctions to reach the infarcted myocardium. Upon arrival at the wounded myocardium, neutrophils adhere to infarct-bordering cardiomyocytes where they phagocytose any cellular debris (Swirski and Nahrendorf, 2013). Neutrophils can exert potent cytotoxic effects by undergoing degranulation and secreting proteases that collectively promote the breakdown of necrotic cardiomyocytes and in collateral, viable extracellular matrix, thus promoting maladaptive ventricular remodelling (Ma et al., 2013; Dewald et al., 2005 and Briaud et al., 2001). Concomitant with degranulation, recruited neutrophils also produce and release ROS, specifically free radicals mediated by NADPH oxidase, which can exacerbate the apoptosis of healthy cardiomyocytes (Swirski and Nahrendorf, 2013 and Morris et al., 2017). Therefore, the magnitude of myocardial neutrophil recruitment is directly proportional to infarct size (Vinten-Johansen, 2004). The first studies to investigate the role of neutrophils in MI used antiserum to deplete neutrophils prior to I/R injury (Romson et al., 1983 and Jolly et al., 1986). Similar studies found neutrophil-depleted animals displayed smaller infarct sizes, suggesting that reperfusion-induced myocardial injury is neutrophil-dependent (Litt et al., 1989 and Hatori et al., 1991). Interestingly, neutrophils can also play protective roles following MI. Neutrophil depletion prior to MI impedes the removal of necrotic cells or worsens cardiac function, indicating the importance of neutrophils in debridement and encouraging cardiac repair (Heymans et al., 1999 and Horckmans et al., 2017). In support of this, recent studies have found that neutrophils transition from a classical inflammatory state, apparent at 1-day post MI, to a more anti-inflammatory phenotype at 7-days post MI (Ma et al., 2016 and Daseke et al., 2019). Together, these studies suggest that

neutrophils have a biphasic role post MI, which is likely influenced by the MI model being studied. Nevertheless, in several models of I/R injury, neutrophils have been implicated as primary and secondary mediators of myocardial damage and their persistence at the wound is associated with diminished repair (Romson et al., 1983; Jolly et al., 1986; Litt et al., 1989; Hatori et al., 1991; Jordan et al., 1999; Montecucco et al., 2010 and Garcia-Prieto et al., 2017). As such, elevated neutrophil accumulation and persistence following MI augments inflammation, promotes cardiomyocyte death, contributes to infarct expansion and leads to adverse structural remodelling (Frangogiannis et al., 2002; Vinten-Johansen, 2004; Garlichs et al., 2004; van Hout et al., 2015 and Schloss et al., 2016). Indeed, blood neutrophilia is recognised as an indicator of adverse clinical outcomes following MI (Arruda-Olson et al., 2009 and Chia et al., 2009). During the post MI inflammatory response, infarct-recruited neutrophils secrete chemoattractants to amplify their mobilisation, and also recruit another important leukocyte, the monocyte (Dewald et al., 2005 and Nahrendorf et al., 2007).

1.2.3. Role of monocytes and macrophages

Similar to neutrophils, monocytes are haematopoietic-derived leukocytes that are recruited to the infarcted myocardium during the early stages of MI. Circulating monocytes are categorised into two subpopulations in mice, Ly6C^{hi} and Ly6C^{low} (Geissmann et al., 2003). Following MI, Ly6C^{hi} monocytes are mobilised from the spleen into circulatory blood. Pro-inflammatory Ly6C^{hi} monocytes are trafficked to the injured heart in a C-C Motif Chemokine Ligand 2 (CCL2)/CCR2-dependent manner, and their recruitment peaks between 3- and 5-days post MI (Dewald et al., 2005 and Nahrendorf et al., 2007). Upon extravasation to the infarcted border zone, Ly6C^{hi} monocytes directly contribute to the inflammatory response by secreting mediators such as TNF, cathepsins and matrix metalloproteinases (van der Laan et al., 2014 and Frantz and Nahrendorf, 2014). In contrast, Ly6C^{low} monocytes, which are regarded as anti-inflammatory/pro-repair, are recruited via CX3C chemokine receptor 1 (CX3CR1) and peak

between 4- and 7- days post MI (Nahrendorf et al., 2007). Genetic ablation of circulating monocytes using a CCL2 antibody led to delayed macrophage recruitment, increased cardiomyocyte death, defective macrophage differentiation, prolonged inflammation and reduced left ventricular remodelling (Dewald et al., 2005). This study suggests that, similar to neutrophils, monocytes also have dual roles following MI. After infiltrating the infarcted heart, recruited Ly6C^{hi} monocytes begin to differentiate into either pro-inflammatory macrophages or Ly6C^{low} pro-repair macrophages (Hilgendorf, 2014). The expansion of Ly6C^{low} macrophages peaks at 7 days post MI, which later persist in the remodelling myocardium. Macrophages also have diverging roles during cardiac injury and repair, which is largely attributed to their ontogeny and heterogeneous phenotypes (Gordon and Taylor, 2005). Classical inflammatory, or M1, macrophages phagocytose invading pathogens or dead cells to digest them enzymatically (Frantz and Nahrendorf, 2014). Conversely, anti-inflammatory, or M2, macrophages promote wound repair and limit fibrosis by expressing a variety of immunoregulatory proteins, such as IL-10, RELMα, chitinase-like proteins, CD206 and arginase 1 (London et al., 2011; Pesce et al., 2009; Stein et al., 1992; Savage, 2008 and Gordon and Martinez, 2010). As pro-inflammatory signaling in the infarcted heart abates, M2 macrophages produce growth factors such as TGF-β and platelet-derived growth factor. These secreted factors promote the differentiation of fibroblasts to myofibroblasts, and stimulate myofibroblasts to produce extracellular matrix proteins, thus promoting advantageous wound healing (Roberts et al., 1986; Shimokado, 1985; Murray et al., 2011 and Frangogiannis, 2014). The balance of M1 and M2 macrophage activation is considered to be a determining factor for the outcome of myocardial repair following MI (Walter et al., 2018).

1.2.4. Resolution of inflammation

Once an inflammatory stimulus has been appropriately neutralised during the peak innate immune response, the resolution of acute inflammation is initiated. The resolution of

inflammation was originally considered to be a passive process; however, this dogma has now changed. Numerous studies have demonstrated that the resolution of inflammation requires the coordinated inhibition of pro-inflammatory molecules and stimulation of pro-resolving molecules (Sugimoto et al., 2016 and Buckley et al., 2013). Collectively, these cellular and molecular signals promote tissue repair, integrity and homeostasis (Ortega-Gomez et al., 2013). As mentioned, dysregulated or sustained myocardial inflammation can cause excessive cardiomyocyte death and fibrosis, which impairs cardiac function (Frangogiannis, 2014). The timely resolution of inflammation following MI is therefore considered crucial for efficient cardiac repair. Once the acute inflammatory response starts to resolve (3-7 days post MI), myocardium-infiltrating neutrophils undergo apoptosis (Daseke et al., 2019). Apoptotic neutrophils are subsequently efferocytosed by inflammatory macrophages, triggering a series of anti-inflammatory/pro-resolving pathways that promote cardiac repair (Savill et al., 2002; Schwab et al., 2007; Frangogiannis, 2012 and Ma et al., 2013). Apoptotic neutrophils can initiate this process via different mechanisms. For example, they can release mediators such as annexin A1 and lactoferrin to suppress secondary neutrophil recruitment and act as chemoattractants for phagocytic cells (Bournazou et al., 2009 and Ortega-Gomez et al., 2013) (**Figure 1.1**). The efferocytosis of apoptotic neutrophils by pro-inflammatory macrophages reprograms them to an M2 phenotype (Savill et al., 2002). Thus, converted macrophages secrete anti-inflammatory/pro-resolving mediators such as TGF-β, IL-10, lipoxin A4, resolvins and protectins (Soehnlein and Lindbom, 2010 and Ortega-Gomez et al., 2013) (**Figure 1.1**). These secreted factors enhance the resolution of inflammation in the injured heart, limiting/preventing further injury and infarct expansion (Huynh et al., 2002; Nathan and Ding, 2010; Frangogiannis, 2012 and Frangogiannis, 2014).

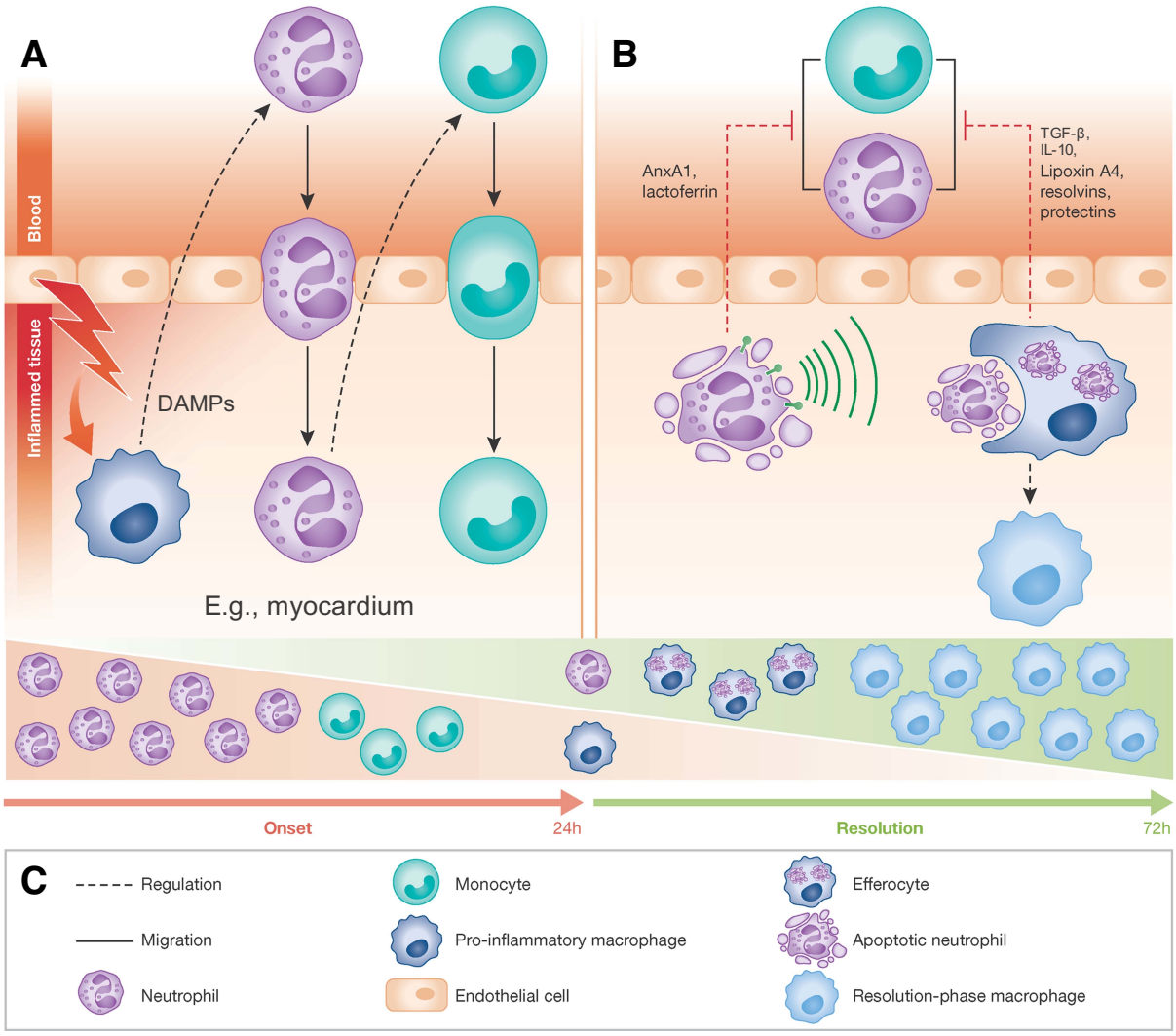

Figure 1.1: Overview of neutrophil, monocyte and macrophage involvement during the onset (left) and resolution (right) of inflammation. (A) The inflammatory response is initiated within 24 hours post injury following the release of DAMPs from damaged tissue (e.g., myocardium). Secreted inflammatory mediators rapidly recruit circulatory neutrophils, which in turn recruit circulatory monocytes to the inflamed tissue. **(B)** The resolution of inflammation commences when tissue-infiltrating neutrophils undergo apoptosis and simultaneously release factors such as annexin A1 (AnxA1) and lactoferrin that inhibit further neutrophil recruitment and act as chemoattractants for phagocytic pro-inflammatory macrophages. Pro-inflammatory macrophages efferocytose apoptotic neutrophils which promotes their conversion to a reparative/resolution-phase macrophage. Resolution-phase macrophages release mediators such as TGF-β, IL-10, lipoxin A4, resolvins and protectins to dampen the inflammatory response and promote downstream tissue-reparative mechanisms. **(C)** Key indicating cell types, interactions and migration paths. Adapted from Ortega-Gomez et al., 2013.

In an important study, Horckmans et al. (2017) found that neutrophils directly interact with macrophages to promote M2 macrophage polarisation during the reparative phase of murine cardiac repair. Specifically, neutrophil-derived lipocalin was found to be responsible for M2 macrophage polarisation, with M2 macrophages expressing higher levels of myeloid-epithelial-reproductive tyrosine kinase (MerTK), a marker of macrophage-induced neutrophil phagocytosis. Similarly, in a separate study, neutrophil depletion was found to inhibit macrophage M2 polarisation, which was necessary for the clearance apoptotic neutrophils (Daseke et al., 2020 and Daseke et al., 2021). Thus, the timely resolution of acute neutrophilic inflammation positively contributes to cardiac repair by augmenting M2 macrophage polarisation. Numerous downstream repair processes are enhanced by M2 macrophages in the infarcted mammalian heart including angiogenesis, myofibroblast differentiation, scar formation via collagen deposition and beneficial ventricular remodelling (Frangogiannis, 2015 and Ma et al., 2018). Experimental approaches targeting the resolution of inflammation as a therapeutic strategy have shown promising results for promoting cardiac repair in preclinical models of MI (Kain et al., 2015; Lichtenauer et al., 2011a; Lichtenauer et al., 2011b; Harel-Adar et al., 2011 and Schumacher et al., 2021). Furthermore, recent clinical trials have investigated immunomodulatory therapies that inhibit pleiotropic inflammatory pathways following MI (Ridker et al., 2017 and Tardif et al., 2019). These therapies lower the incidence of cardiovascular events post-MI but increase the risk of infection, indicating the clinical potential of such treatment strategies. CDK9 inhibitor compounds, which are currently in clinical trials as anti-cancer therapies, promote the resolution of neutrophilic inflammation in murine models of injury and infection (Rossi et al., 2006 and Cartwright et al., 2019). However, whether CDK9 inhibitors influence myocardial inflammation or repair following injury has yet to be examined.

1.3. CDK9 inhibitors and the resolution of inflammation

1.3.1. CDK9 structure and function

Cyclin-dependent kinases (CDKs) are a family of evolutionarily conserved serine/threonine protein kinases. In eukaryotes, CDKs form heterodimers with cyclin partner proteins at different stages of the cell cycle (G1, S, G2 and M). The function of CDKs is to phosphorylate target proteins, thereby regulating cell cycle progression or gene transcription (Malumbres, 2014). Mammals have up to 20 CDKs, 11 of which encode CDKs, and 9 others encoding CDK-like proteins which are structurally similar (Malumbres and Barbacid, 2005). CDKs are generally classified into two groups based on whether they control cell cycle progression or gene transcription. In humans, CDKs 1, 2, 3, 4 and 6 are responsible for regulating the cell cycle, whereas CDKs 7, 8, 9, 12 and 13 are responsible for regulating gene transcription. Similar to other protein kinases, CDKs have a conserved N- and C-terminal domain, with both contributing to its ATP-binding site (Wood and Endicott, 2018). Due to their diverse roles in regulating cellular function, CDKs have proven to be attractive therapeutic targets for treating human disease. Of all the CDKs, CDK9 and its inhibition has been widely studied in the context of treating cancer and inflammatory-driven diseases (Krystof et al., 2012). CDK9 is expressed in all mammalian tissues but more prominently in post-mitotic/terminally differentiated cells. Humans express two isoforms of CDK9, with weights of 42kDa and 55kDa (Shore et al., 2003). Both isoforms dimerise with cyclin T, however, they are localised to different parts of the cell and differentially expressed in tissues (Shore et al., 2005 and Romano, 2013). The role of CDK9 is to specifically promote transcription. CDK9 binds cyclin T to form the positive transcription elongation factor b (P-TEFb), which is required to activate transcription elongation of protein coding genes (Peng et al., 1998 and Price, 2000). The P-TEFb complex specifically phosphorylates serine 2 residues on the C-terminal domain of RNA Polymerase II (RNAPII), facilitating the elongation of RNA transcripts (Price et al., 2000). Importantly, P-TEFb regulates the transcription of core transcription factors such as NF-κB (**Figure 1.2**), which is responsible

for the production of inflammatory cytokines such as IL-1β, IL-8 and IL-6 (Sundar et al., 2020; Ni et al., 2020; Xue et al., 2019; Li et al., 2010; Schmerwitz et al., 2011; Falco et al., 2002 and Hu et al., 2016). Furthermore, genetic knockout of cyclin T2 (binding partner of CDK9) in mice is embryonic lethal, indicating the functional importance of CDK9 during development (Kohoutek et al., 2009). Thus, CDK9 activation is required for the transcription of key developmental and primary inflammatory response genes.

1.3.2. CDK9 and neutrophil apoptosis

In addition to transcribing inflammatory mediators, CDK9 is required for the transcription of neutrophil-specific genes. Of particular importance is myeloid cell leukaemia 1 (Mcl-1), a conserved and short-lived neutrophil anti-apoptotic protein (Tibes and Bogenberger, 2019). Mcl-1 has been proposed to be the most important protein required for neutrophil survival (Edwards et al., 2004). Mcl-1 knock-out in murine myeloid precursors results in neutropenia caused by a 3-fold increase in the apoptosis of circulating and hematopoietic neutrophils, without affecting macrophage survival (Dzhagalov, 2007). Similarly, overexpression of Mcl-1 in myeloid progenitor cells inhibits cell death (Fu et al., 2005). Mcl-1 is a member of the B cell lymphoma-2 (Bcl-2) family responsible for regulating apoptosis via the release of cytochrome C from mitochondria into the cytosol which activates caspases. The specific role of Mcl-1 is to sequester pro-apoptotic Bcl-2 members, preventing permeabilisation of the mitochondrial membrane and subsequent efflux of cytochrome C. Relative to other Bcl-2 family members, neutrophils express particularly high levels of Mcl-1 (Milot and Filep, 2011). Isolated and cultured human neutrophils display a gradual decline in CDK9 and Mcl-1 expression, which is associated with increased levels of neutrophil apoptosis (Wang et al., 2012). Conversely, cytokines including IL-1β, IL-6 and TNF, in addition to granulocyte-macrophage-colony stimulating factor (GM-CSF) upregulate Mcl-1 expression and promote neutrophil survival (Chao et al., 1998; Jourdan et al., 2000; Le Gouill et al., 2004 and Cartwright et al., 2019). Pro-

apoptotic factors, for example ROS, can induce neutrophil apoptosis by overriding neutrophil survival factors such as GM-CSF (Kobayashi et al., 2005). A therapeutic strategy of great interest to our laboratory is enhancing neutrophil apoptosis via pharmacological inhibition of CDK9.

1.3.3. Pharmacological CDK9 inhibitors

CDK9 inhibitor drugs act by competitively binding the ATP binding site. Due to the conserved proteomic structure of CDKs, CDK9 inhibitor compounds can also target other CDKs with varying degrees of potency (Krystof et al., 2012). In some cases, CDK9 inhibitor drugs display off-target effects, which has limited their success clinically (Morales and Giordano, 2016). Despite the caveats with specificity, pharmacological CDK9 inhibitors have been extensively studied as treatments in cancer studies due to their pro-apoptotic mechanism of action (Cassandri et al., 2020 and Tibes and Bogenberger, 2019). CDK9 inhibitors are particularly effective for treating cancers that aberrantly express c-MYC, a proto-oncogene which drives cell growth and cell cycle progression (Lu et al., 2015). Thus, overstimulation of CDK9 is a mechanism that promotes cell survival and cancer development via the overexpression of Mcl-1 (Xiang et al., 2018). This effect is particularly apparent in hematopoietic cancers, specifically acute myeloid leukaemia (Tibes and Bogenberger, 2019). As mentioned, CDK9 is also required for the transcription of inflammatory cytokines and neutrophil survival genes (Sundar et al., 2020; Krystof et al., 2012 and Eyvazi et al., 2019). Pharmacological inhibition of CDK9 therefore provides a therapeutic opportunity to preferentially suppress the transcription of short-lived inflammatory disease drivers. Four FDA approved CDK9 inhibitors are currently in clinical trials as anti-cancer therapies (Eyvazi et al., 2019 and Morales and Giordano, 2016) (**Table 1.1**). These compounds could be repurposed to resolve acute or chronic neutrophilic inflammation in different clinical settings such as myocardial infarction, acute respiratory distress syndrome or rheumatoid arthritis (Rossi et al., 2007).

Table 1.1: CDK9 inhibitors currently in active clinical trials for the treatment of cancer. Table modified from Eyvazi et al., 2019. Status of compounds was confirmed on ClinicalTrials.gov.

CDK9 inhibitor	Formula	Molecular Weight	IC50
Dinaciclib (SCH727965)	$C_{21}H_{28}N_6O_2$	396.49 g/mol	4nM
Alvocidib (Flavopiridol)	$C_{21}H_{20}ClNO_5$	401.843 g/mol	6nM
AT7519	$C_{16}H_{17}Cl_2N_5O_2$	382.245 g/mol	<10nM
Seliciclib (Roscovitine)	$C_{19}H_{26}N_6O$	354.458 g/mol	0.8μM

Flavopiridol (FVP) was the first CDK9 inhibitor to enter clinical trials and remains one of the most potent and well-studied CDK9 inhibitors to date. Although it has displayed off-target effects clinically, likely due to inhibition of other CDKs (Lanasa et al., 2015 and Morales and Giordano, 2016), its primary anti-cancer mechanism is through transcriptional inhibition of CDK9, P-TEFb and RNAPII (Chao et al., 2000 and Baumli et al., 2008). AT7519 was later developed in a high-throughput drug discovery study and has been well tolerated in patients with solid refractory tumours (Mahadevan et al., 2011). Importantly, AT7519 displays many efficacious properties for therapeutic use in different cancer settings, primarily via the inhibition of CDK9 (Santo et al., 2010; Wyatt et al., 2008; Mahadevan et al., 2011). Recently developed CDK9 inhibitors, such as iCDK9 and NVP-2, display higher CDK9 selectivity *in vitro* (Lu et al., 2015 and Olson et al., 2018), however they require further validation *in vivo* to determine potential human translatability. Both FVP and AT7519 have been shown to enhance the resolution of acute or non-resolving inflammation following injury or infection in various *in vitro* and *in vivo* model systems (Cartwright et al., 2019) (**Figure 1.2**).

1.3.4. CDK9 inhibitor drugs and inflammation resolution

Extensive research from our group and others has shown that CDK9 inhibitor compounds induce neutrophil apoptosis, reduce neutrophil infiltration and promote the resolution of

inflammation in a variety of *in vitro* and *in vivo* model systems (Rossi et al., 2006; Loynes et al., 2010; Leitch et al., 2012; Wang et al., 2012; Lucas et al., 2013; Lucas et al., 2014 and Hoodless et al., 2016). Roscovitine was the first CDK9 inhibitor shown to induce neutrophil apoptosis and it was found to do so in a time- and dose-dependent manner via downregulation of Mcl-1 (Rossi et al., 2006). In this seminal study, Roscovitine-treated cells displayed enhanced Annexin V binding and cleaved caspase 3 expression, concomitant with reduced Mcl-1 expression. Additionally, Roscovitine dampened inflammatory cell recruitment and cytokine expression, which aided lung repair in a murine model of carrageenan-induced pleurisy (Rossi et al., 2006). These effects were reversed using a pan caspase inhibitor, demonstrating that the pro-apoptotic mechanism of action induced was indeed caspase dependent. Roscovitine was also utilised in two other disease models in this study, bleomycin-induced lung injury and serum-induced arthritis, both of which exhibited reduced inflammatory responses following drug treatment. Later studies confirmed that Roscovitine can override granulocyte pro-survival mediators to drive neutrophil and eosinophil apoptosis via inhibition of CDK9 and CDK7, which reduces phosphorylation of RNAPII (Leitch et al., 2010; Leitch et al., 2012 and Duffin et al., 2009). Naturally derived flavone compounds such as wogonin, apigenin and luteolin are structurally similar to CDK9 inhibitors. Comparable to Roscovitine, these flavones were shown to drive time-, dose- and caspase-dependent neutrophil apoptosis via downregulation of Mcl-1 (Lucas et al., 2013). Furthermore, FVP has also been shown to accelerate human neutrophil apoptosis by reducing Mcl-1 protein levels without affecting Bcl-2A expression (Wang et al., 2012). In a model of concanavalin A–induced hepatitis, FVP was shown to suppress neutrophil accumulation in injured liver tissue (Schmerwitz et al., 2011). In the same study, using intravital imaging, FVP was shown to inhibit neutrophil transendothelial migration in the mouse cremaster muscle via inhibition of endothelial cell adhesion molecules. Additionally, endothelial knockdown of CDK9 inhibited adhesion molecule expression, suggesting that the anti-inflammatory effects observed with FVP were CDK9 dependent (Schmerwitz et al., 2011). The more recently developed and clinically studied CDK9 inhibitor,

AT7519, was also found to effectively induce neutrophil apoptosis in a concentration-dependent manner following LPS-induced lung inflammation by reducing Mcl-1 expression *in vivo* (Lucas et al., 2014). Although AT7519 does not induce monocyte-derived macrophage apoptosis (Lucas et al., 2014), it does promote eosinophil apoptosis and inflammation resolution in a murine model of allergic pleurisy (Alessandri et al., 2011). Moreover, isolated human neutrophils from acute respiratory distress syndrome patients exhibit a pro-survival phenotype with reduced levels of apoptosis. AT7519 overrides this phenotype by reducing Mcl-1 and enhancing caspase-dependent neutrophil apoptosis (Dorward et al., 2017). Isolated neutrophils from patients with cystic fibrosis similarly display delayed apoptosis, as such AT7519 treatment also reversed this by promoting neutrophil apoptosis, which incidentally reduced extracellular trap formation (Gray et al., 2018). Taken together, these studies demonstrate that pharmacological CDK9 inhibitors resolve neutrophilic inflammation via the induction of apoptosis (**Figure 1.2**), which enhances the resolution of inflammation and promotes a more tissue reparative milieu. In addition to murine models, the larval zebrafish has been utilised by several groups to investigate inflammatory responses following injury *in vivo* (Henry et al., 2013; Xie et al., 2021 and Miskolci et al., 2019).

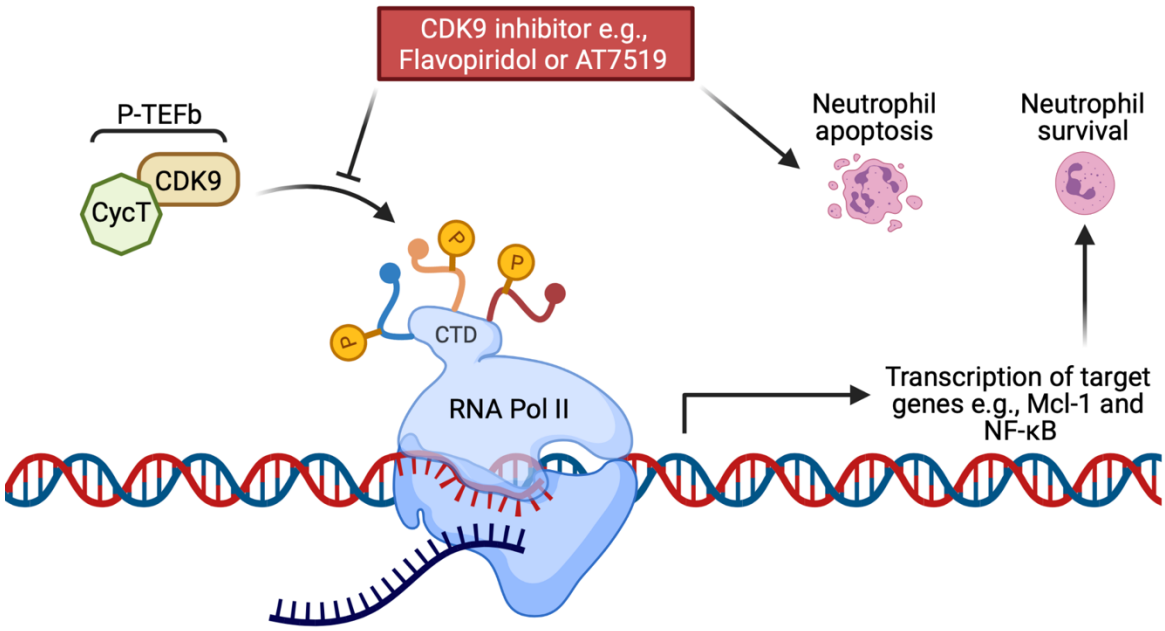

Figure 1.2: Role of CDK9 and pharmacological CDK9 inhibitors in regulating the transcription of pro-survival/inflammatory target genes. CDK9 binds cyclin T (CycT) to form the positive transcription elongation factor b (P-TEFb). The P-TEFb complex phosphorylates the C-terminal domain (CTD) of RNA Polymerase II (RNA Pol II), facilitating the elongation of RNA transcripts and thus the transcription of target genes. Transcribed targets include the neutrophil pro-survival gene Mcl-1 and the core inflammatory transcription factor NF-κB. CDK9 inhibitor compounds, such as Flavopiridol and AT7519, prevent the phosphorylation of RNA Pol II, thereby inhibiting the transcription of target genes. Following CDK9 inhibitor treatment, Mcl-1 expression is suppressed which causes neutrophil apoptosis (Cartwright et al., 2019). Created with BioRender.com.

1.4. Zebrafish as a model of wounding inflammation

1.4.1. Zebrafish as an animal model

The zebrafish (*Danio rerio*) is a freshwater teleost that has become increasingly popular as an animal model in biomedical research. Zebrafish originally emerged as a model in the 1970's for the study of early vertebrate developmental biology (Streisinger et al., 1981). In recent times, the zebrafish is recognised as a powerful model across all biomedical disciplines, with many laboratories across the world using zebrafish as their primary model, or, in adjunct with more traditional mammalian systems. The zebrafish possesses many advantageous properties for scientific study. They are amenable to genetic and pharmacological

manipulation, develop rapidly, are small in size and, importantly, during early stages of development, are optically transparent. A single zebrafish pair mating can produce over 200 eggs which are fertilised externally, allowing non-invasive *in vivo* imaging experiments to be performed. These unique features make the zebrafish an ideal model to study developmental/disease-related processes (Lieschke and Currie, 2007 and Patton and Tobin, 2019). Furthermore, the zebrafish genome is largely conserved, with approximately 70% of all human genes having functional zebrafish orthologues (Howe et al., 2013). Another key advantage of using zebrafish for biomedical research is the plethora of transgenic reporter lines that are available. For example, there are numerous immune-related transgenic lines that report expression of inflammatory cytokines (e.g., TNF, IL-1β and NF-κB) and innate immune cell types (e.g., neutrophils and macrophages) (Nguyen-Chi et al., 2015; Ogryzko et al., 2018; Feng et al., 2012; Renshaw et al., 2006 and Ellet et al., 2013). Hence, different fluorescent cells/tissues can be simultaneously visualised using fluorescence microscopy, allowing live cell-cell interactions to be studied with relative ease *in vivo*. However, there are some limitations with using zebrafish compared to mammalian models. Although there has been one case of a therapy identified in zebrafish being directly translated to a patient suffering from a rare disease (Li et al., 2019), zebrafish studies often need to be replicated in mammalian models which can be time consuming. Secondly, the zebrafish genome underwent a duplication event following the divergence of teleosts and mammals. Therefore, some zebrafish genes have multiple orthologues which can complexify their study (Taylor et al., 2003). Thirdly, zebrafish are ectothermic, thus their physiology can be easily influenced by their local environment (Lahiri et al., 2005). As such, laboratory parameters such as water quality, temperature and light exposure must be closely regulated to mitigate any confounding experimental variables.

1.4.2. Modelling inflammatory responses in larval zebrafish

The cellular and molecular inflammatory responses that occur following injury are highly conserved across vertebrate species (Traver et al., 2003). Due to their amenability for live *in vivo* imaging, larval zebrafish have been widely used to study the migration of innate immune cells during development and tissue inflammation (Rosowski, 2020). The zebrafish innate immune system is functional during the early stages of development and displays a high degree of homology to mammals (Renshaw and Trede, 2012). Similar to other vertebrate species, zebrafish display a primitive and definitive wave of haematopoiesis that produce myeloid cells and haematopoietic stem cells respectively (de Jong and Zon, 2005 and Lieschke et al., 2002). Throughout development, myeloid cells continually proliferate and gradually colonise the zebrafish kidney marrow, the equivalent of human bone marrow (Chen and Zon, 2009). Importantly, during the first four weeks of zebrafish development, adaptive immunity is not yet fully established, thus the immune response is largely dependent on innate immunity (Trede et al., 2004). The zebrafish innate immune response displays many functional similarities to mammals, including the presence of neutrophils and macrophages, inflammatory cytokines such as TNF, IL-1β and NF-κB, in addition to TLRs and complement factors (Lieschke and Currie, 2007 and Zanandrea et al., 2020). Furthermore, zebrafish neutrophils exhibit several similar traits to mammalian neutrophils. These include their morphology (polymorphic nuclei and cytoplasmic granules), containing microbicidal enzymes such as myeloperoxidase (mpx) and NADPH oxidases, their ability to phagocytose bacteria and produce extracellular traps (Lieschke et al., 2001 and Harvie and Huttenlocher, 2015). Zebrafish *mpx* is expressed in all neutrophils and from 1 day post fertilisation (dpf) these neutrophils can be visualised within the vasculature (Bennett et al., 2001 and Renshaw et al., 2006). From around 3 dpf, *mpx*$^{+}$ neutrophils are present throughout the larva, but mostly reside within the caudal hematopoietic tissue and head (Lam and Huttenlocher, 2013). At 3 dpf neutrophil recruitment to zebrafish wounds can be clearly observed *in vivo* (Bennett et al.,

2001; Renshaw et al., 2006 and Hoodless et al., 2016) (**Figure 1.3**). The dynamics of the neutrophil response has been extensively studied following tail fin injury, which is widely considered the archetypal wounding model in larval zebrafish (**Figure 1.3**).

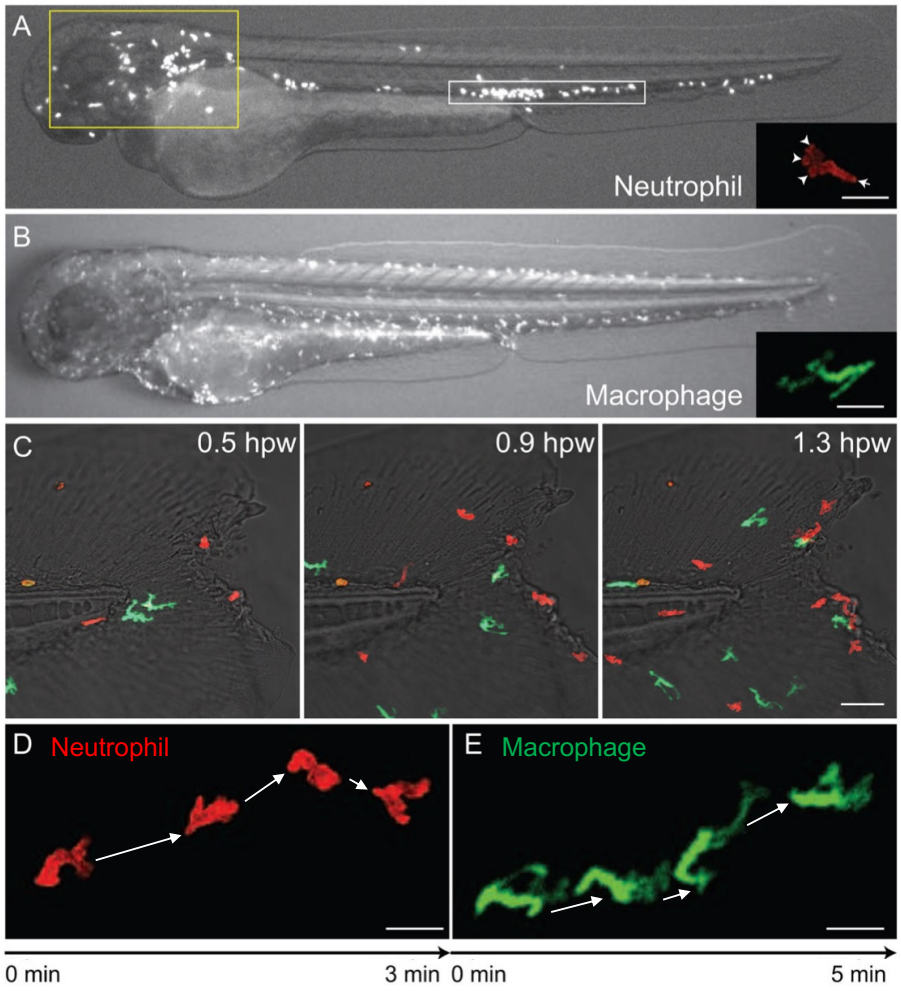

Figure 1.3: Transgenic 3 dpf larval zebrafish allow visualisation of tissue-resident neutrophil and macrophage locations, morphology and behaviour following tail fin wounding *in vivo*. (A) Neutrophil distributions throughout a zebrafish larva. The majority of neutrophils reside within the caudal hematopoietic tissue (white box) and head (yellow box). Magnified view displays a migrating neutrophil, arrowheads indicate protruding pseudopods and arrow indicates a uropod, scale bar = 20 µm. **(B)** Macrophage distributions throughout a zebrafish larva. Macrophages are more evenly distributed throughout the body of larval zebrafish. Magnified view displays a migrating macrophage with fine dendritic protrusions, scale bar = 20 µm. **(C)** Timestamp series of neutrophils (red) and macrophages (green) migrating towards the wounded tail fin. Hpw = hours post wounding, scale bar = 50 µm. Overlaid timestamp images of an individual neutrophil **(D)** and macrophage **(E)** migrating towards the wounded

tail fin. Arrows indicate migration paths, scale bar = 20 μm. Neutrophils and macrophages are labelled using specific transgenic reporter lines and imaged using fluorescence microscopy. Adapted from Lam and Huttenlocher, 2013.

In brief, larval zebrafish tail fin injury initiates a rapid and acute neutrophil recruitment response that later resolves via reverse migration (Henry et al., 2013 and Ellett et al., 2015). Although less common, neutrophil apoptosis can also contribute to neutrophil resolution following tail fin wounding (Li et al., 2012; Robertson et al., 2014 and Hoodless et al., 2016). Neutrophils are the first cells to respond following tissue injury in zebrafish. The first neutrophils are recruited within minutes and the neutrophil response peaks between 4 and 6 hours post injury (hpi) in larval zebrafish (Loynes et al., 2018). Similar to mammalian injury, DAMPs such as ATP are released to initiate the innate immune response (de Oliveira et al., 2015 and de Oliveira et al., 2014). Within a matter of seconds, intracellular calcium is upregulated at the wound margin, which can act to recruit neutrophils via the eicosanoid pathway (Enyedi et al., 2016 and Yoo et al., 2012). Minutes later, ROS (specifically hydrogen peroxide) is produced by dual oxidase (Niethammer et al., 2009 and Rieger and Sagasti, 2011). ROS also acts as a neutrophil chemoattractant via the activation of Lyn, a Src family kinase member (Niethammer et al., 2009 and Yoo et al., 2011). Wound-infiltrating neutrophils secrete *mpx* to dampen hydrogen peroxide levels and curtail the ROS-enhanced inflammatory milieu (Pase et al., 2012). This sequence of events is thought to be conducted in a linear pathway (Cordeiro and Jacinto, 2013; de Oliveira et al., 2015; de Oliveira et al., 2014 and Niethammer, 2016), however it may also occur simultaneously with feedback at each stage of the response. The molecular chemokine requirements of larval zebrafish neutrophils are also conserved, with the CXCL8-CXCR2 axis implicated in neutrophil recruitment to sites of injury/infection and subsequent reverse migration during inflammation resolution (Deng et al., 2013; Zuniga-Traslavina et al., 2017 and Powell et al., 2017). Moreover, macrophages develop across the same time scale as neutrophils in zebrafish (Rosowski, 2020). In larval zebrafish, macrophages typically

accumulate at sites of injury after neutrophils are recruited (Li et al., 2012 and Miskolci et al., 2019) (**Figure 1.3**). However, the chemoattractant signals governing macrophage recruitment following zebrafish wounding is less clearly defined.

Unlike mammals, zebrafish have a remarkable capacity to regenerate most of their tissues and organs. The role of neutrophils and macrophages during tail fin regeneration has been widely studied in zebrafish. Genetic ablation of neutrophils prior to tail fin wounding improves regeneration, whereas macrophage ablation delays tail fin regeneration (Li et al., 2012 and Petrie et al., 2014). More recent studies have unravelled a molecular mechanism for these observations during larval zebrafish regeneration (Hasegawa et al., 2017; Hasegawa et al., 2015 and Tsarouchas et al., 2019). A reduction in tail-recruited macrophages was shown to enhance cell death and decrease cell proliferation between 12 hpi and 24 hpi. These regenerative defects were associated with elevated *il-1β* expression, a marker of epithelial damage. Hasegawa et al. (2017) revealed that ectopic *il-1β* expression increased tail fin cell death and *il-1β* knockdown in macrophage-ablated zebrafish rescued the tail fin regeneration defects. In a larval zebrafish model of spinal cord injury, macrophage ablation similarly augmented *il-1β* expression, but this was mostly derived from infiltrating-neutrophils. Inhibition of *il-1β*$^{+}$ neutrophils rescued functional spinal cord regeneration in macrophage ablated larvae. However, inhibiting *il-1β* during early wounding impaired regeneration (Tsarouchas et al., 2019), indicating that *il-1β* is required to activate regeneration. Together, these findings suggest that unlike neutrophils, macrophages play a protective role following wounding by dynamically resolving pro-inflammatory cytokines, primarily neutrophil-derived *il-1β,* to ensure subsequent regeneration is appropriately conducted. An appealing feature of using larval zebrafish to study innate inflammation is that molecular targets of interest can be inhibited in a high-throughput manner using chemical compounds dissolved in incubation medium (Zanandrea et al., 2020). Previous studies from our group and others have demonstrated that

neutrophil reverse migration or apoptosis can be pharmacologically modulated following wounding in larval zebrafish (Loynes et al., 2010; Lucas et al., 2013; Robertson et al., 2014; Robertson et al., 2016 and Hoodless et al., 2016) (**Figure 1.4**).

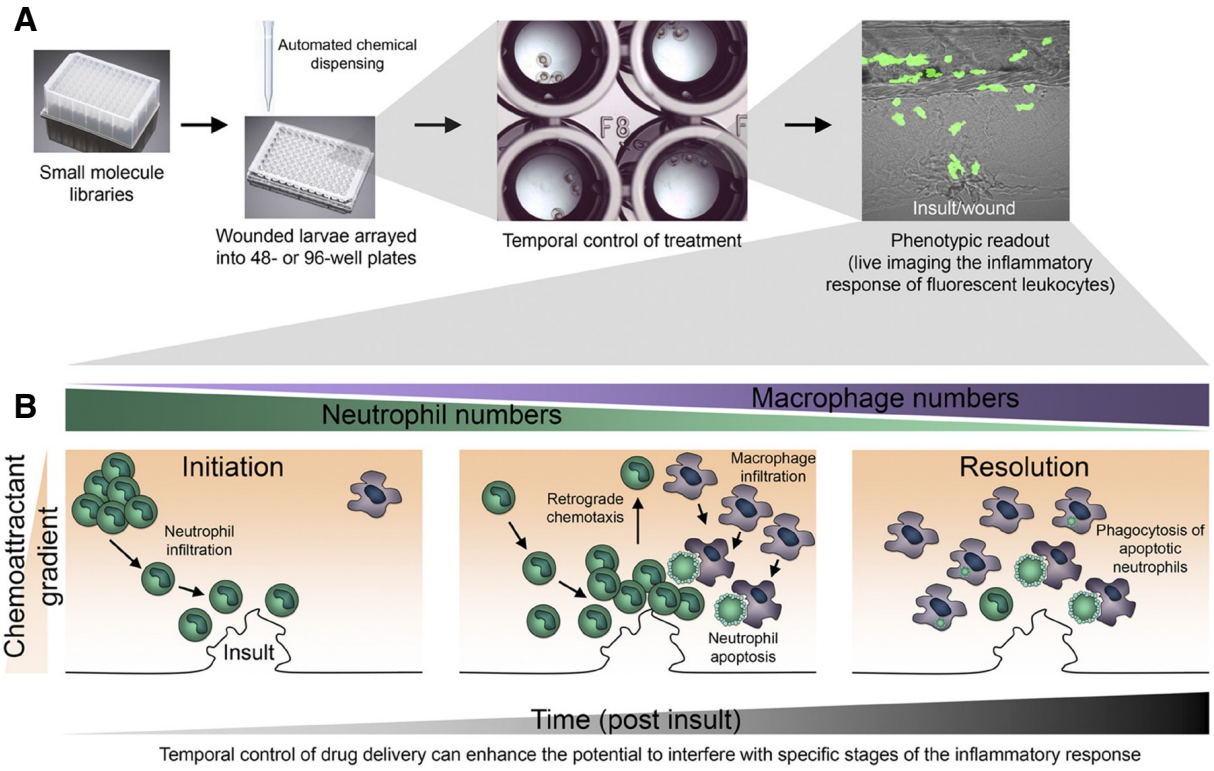

Figure 1.4: High throughput *in vivo* drug screening using larval zebrafish to interrogate the onset or resolution of inflammation following tissue wounding. (A) General drug screening pipeline to assess neutrophil or macrophage responses following wounding in larval zebrafish *in vivo*. Wounded larvae can be arrayed into 48- or 96-well plates containing small molecule compounds dissolved in zebrafish incubation medium. **(B)** This assay can be used to identify compounds that modulate the initiation or resolution of inflammation in a high throughput manner *in vivo*. Pharmacological effects can be determined during the inflammatory response by quantifying neutrophil or macrophage accumulation at the wound site. The initiation or resolution of inflammation can be targeted following tissue wounding by temporally controlling drug incubation. Pre-incubating larvae prior to wounding allows compound effects to be assessed during the initial infiltration of neutrophils or macrophages. Alternatively, incubating wounded larvae during the peak inflammatory response allows compound effects to be assessed during the resolution of inflammation, such as the regulation of neutrophil apoptosis, neutrophil reverse migration or macrophage polarisation. Adapted from Hall and Crosier, 2010.

1.4.3. CDK9 and inflammation resolution in larval zebrafish

Zebrafish possess all CDK genes with a high degree of human homology. Zebrafish CDK9 is very well conserved with 94.4% protein homology. Mcl-1 has two orthologues (Mcl-1a and Mcl-1b) that are less well conserved, nevertheless both CDK9 and Mcl-1 were originally implicated in zebrafish cell survival (Chen et al., 2000 and Kratz et al., 2006). The Renshaw laboratory were the first to show that the CDK9 inhibitor Roscovitine reduces neutrophil persistence following the peak inflammatory response in tail resected larval zebrafish (Loynes et al., 2010). In the same study, the authors found that wound-recruited macrophages engulf apoptotic neutrophils, whereas pan caspase inhibition or pro-inflammatory stimuli (such as LPS) delays the resolution of inflammation by reducing neutrophil apoptosis (Loynes et al., 2010). Similarly, the flavone compound wogonin, which displays CDK9 inhibitory activity, reduces neutrophil accumulation at the wounded tail fin (Lucas et al., 2013). This pro-resolving effect was reversed using a pan caspase inhibitor, thus suggesting wogonin promotes neutrophil resolution via the induction of apoptosis (Lucas et al., 2013). Most recently, the Rossi laboratory investigated the role of CDK9 during the resolution of inflammation in larval zebrafish using the established tail fin resection model (Hoodless et al., 2016). Importantly, this study demonstrated that CDK9 was required for the resolution of neutrophil-driven inflammation *in vivo*. Specifically, CDK9 inhibitor compounds, FVP and AT7519, suppressed neutrophil presence at the tail wound by enhancing neutrophil apoptosis without affecting macrophage accumulation. This was supported by CDK9 morphant and stable mutant experiments, where genetic knockdown or knockout of CDK9 resulted in reduced wound neutrophil presence at the tail fin (Hoodless et al., 2016). The effect of CDK9 inhibitor treatment during the later repair and regeneration phases following tissue wounding has, however, yet to be explored. Due to their potent pro-resolving effects, CDK9 inhibitor compounds offer an interesting and potentially viable therapeutic strategy to promote repair/regeneration following injury (**Figure 1.4**).

1.5. Zebrafish as a model of cardiac regeneration

1.5.1. Cardiac injury models and stages of regeneration

Following injury, the adult mammalian heart is incapable of regenerating and instead repairs by compensatory cardiomyocyte hypertrophy and scar formation (Talman and Ruskoaho, 2016). Conversely, zebrafish are capable of complete cardiac regeneration following injury during larval and adult stages (Matrone et al., 2013; Poss et al., 2002 and Gonzalez-Rosa et al., 2011). Cardiac regeneration post MI has long remained a holy grail in cardiology. In the last two decades the zebrafish has provided invaluable insights into the cellular/molecular mechanisms that govern successful cardiac regeneration (Gonzalez-Rosa et al., 2017 and Sanz-Morejon and Mercader, 2020). Zebrafish emerged as a model for heart regeneration in 2002 when it was discovered that following ventricular resection adult hearts functionally regenerate within 60 days via cardiomyocyte proliferation (Poss et al., 2002). Alternative heart injury methods have since been developed, most notably ventricular cryoprobe injury. In contrast to ventricular resection, the cardiac cryoinjury model causes a severe apoptotic response across all cardiac cell types (epicardium, myocardium and endocardium), with a necrotic myocardial core initially retained at the injury site (Chablais et al., 2011 and Gonzalez-Rosa et al., 2011). Hence, cardiac cryoinjury more closely replicates mammalian myocardial infarction. Cardiac regeneration following cryoinjury usually occurs within three months in adult zebrafish. This dynamic process can be summarised in three sequential and overlapping stages (Gonzalez-Rosa et al., 2017) (**Figure 1.5**):

1. Inflammatory stage: chemotaxis of neutrophils and macrophages to the injury site for the removal of dead cells and matrix debris.

2. Reparative stage: endocardial and epicardial cells are activated and proliferate. Myofibroblasts synthesise extracellular matrix proteins (e.g., collagen) to form a scar and stabilise the infarct.

3. Regenerative stage: border zone cardiomyocytes dedifferentiate, proliferate and redifferentiate to replace the fibrotic scar tissue with new viable myocardium.

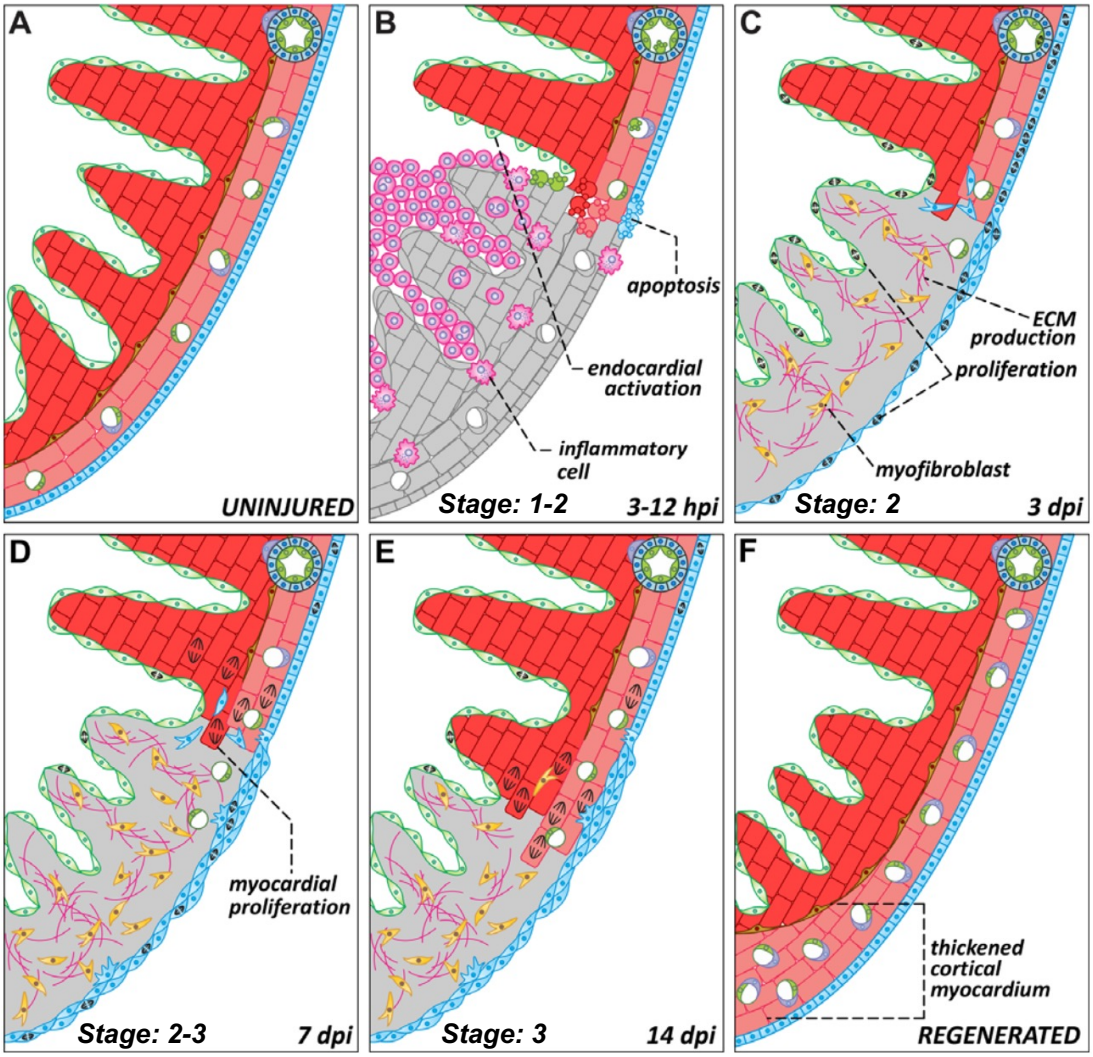

Figure 1.5: The cellular stages of adult zebrafish heart regeneration. (A) Absence of injury. **(B-E)** Three sequential and overlapping stages of regeneration following ventricular cryoinjury in adult zebrafish, as described above. **(F)** Complete regeneration of the damaged ventricular tissue with cortical myocardial expansion. Dpi = days post injury. Tissue necrosis is depicted in grey. Blue cells = epicardium, red cells = myocardium, green cells = endocardium, yellow cells = myofibroblasts, purple strands = extracellular matrix. Adapted from Gonzalez-Rosa et al., 2017.

In 2013, the Denvir laboratory described a new model of cardiac injury in larval zebrafish using highly targeted laser pulsing (Matrone et al., 2013). This cardiac laser injury model is comparable to adult zebrafish cardiac cryoinjury and mammalian models of MI as it causes the localised death of ventricular cardiomyocytes (Matrone et al., 2013 and Kaveh et al., 2020). This model provides many unique advantages compared to other cardiac injury systems. Three primary advantages of this model are:

1. Live *in vivo* imaging of events that occur during the inflammatory, reparative and regenerative stages following cardiac injury (**Figure 1.5**).
2. Cardiac regeneration is completed within two-days post injury.
3. Amenable to high throughput pharmacological/genetic screening *in vivo*.

Light sheet fluorescence microscopy (LSFM) is a powerful imaging method that has rapidly progressed in zebrafish research due to its advantages over other 3D scanning microscopes, such as confocal microscopy (Power and Huisken, 2017). In collaboration with Dr Jonathan Taylor (University of Glasgow), our laboratory has developed a bespoke LSFM imaging system that is coupled to heart synchronisation software (Taylor et al., 2019). This unique imaging approach allows real-time, high resolution and non-invasive imaging of the beating larval zebrafish heart, a feat not possible using other approaches/models (Taylor et al., 2011; Taylor et al., 2012 and Taylor et al., 2019). Prior to this study, real-time 3D LSFM imaging of the larval zebrafish heart was only limited to a few hours (Taylor et al., 2011 and Taylor et al., 2012). We have since optimised this approach which is now capable of unsupervised timelapse imaging for up to 24 hours (Taylor et al., 2019). In a proof-of-concept study, we used this optical gating technique to illustrate detailed developmental processes in the beating heart, specifically chamber morphogenesis and myocardial trabeculation (Taylor et al., 2019). Moreover, we examined neutrophil and macrophage migration on the injured heart, demonstrating that the

bespoke system is capable of tracking and quantifying the behaviour of wound-infiltrating immune cells on the beating heart (Taylor et al., 2019).

1.5.1.1. Role of the innate inflammatory response

Cardiac injury studies in adult zebrafish have indicated that the early inflammatory response is required for heart regeneration to effectively occur. The expression of pro-inflammatory mediators (*il-1β*, *tnf*, *il-8*, *ptgs-2b* and *mpx*) are elevated in the heart from 3 hours post injury (Huang et al., 2013). Consistent with other regeneration studies, pre-treatment with the anti-inflammatory glucocorticoid, beclomethasone, suppresses inflammatory cytokine expression and immune cell recruitment, which impairs heart regeneration by inhibiting coronary angiogenesis and cardiomyocyte proliferation (Huang et al., 2013). Similarly, pre-depletion of phagocytes with clodronate liposomes or pre-treatment with another glucocorticoid, flumethasone, decreases cardiomyocyte proliferation and inhibits matrix metalloproteinase remodelling, leading to scar accumulation and lack of complete regeneration after cryoinjury (de Preux Charles et al., 2016). The role of neutrophils and macrophages during zebrafish cardiac regeneration has only begun to be unravelled in recent years. The Stainier laboratory provided compelling evidence for innate immune cells regulating heart regeneration by comparing cardiac cryoinjury responses between adult zebrafish and medaka, a closely related and less regenerative teleost (Lai et al., 2017). Following cardiac cryoinjury, medaka display delayed and reduced macrophage recruitment, but prolonged neutrophil retention. Pre-treatment with clodronate liposomes in zebrafish delayed macrophage recruitment, which reduced neutrophil clearance and subsequently suppressed cardiomyocyte proliferation, neovascularisation and scar resolution (Lai et al., 2017). Furthermore, two recent studies by the Cheng laboratory reported that excessive inflammation following adult zebrafish cryoinjury is associated with aberrant cardiac regeneration (Xu et al., 2019 and Xu et al., 2019). In the first study, the authors explored the responses to heart injury in *breakdance* mutant zebrafish,

a model of cardiac arrythmia that is linked to dysregulated inflammation (Peal et al., 2011 and Medenwald et al., 2014). Comparative analysis revealed that *breakdance* mutants display an upregulation of innate inflammatory genes following cardiac injury. This was correlated with increased apoptosis in the heart and impaired scar degradation, which was partially rescued using the anti-inflammatory glucocorticoid, dexamethasone (Xu et al., 2019). The second study investigated a mechanism for neutrophil mediated inflammation in the cryoinjured zebrafish heart. The authors showed that inhibition of the CXCL8/CXCR2 axis prolonged neutrophil retention at the injured heart, which consequently enhanced apoptosis and delayed cardiomyocyte regeneration (Xu et al., 2019). Together, these studies suggest that the resolution of neutrophilic inflammation is crucial for timely heart regeneration. Harnessing the inflammatory response by enhancing the resolution of neutrophilic inflammation following cardiac injury therefore has potential as a therapeutic strategy to improve myocardial repair/regeneration. Our group has shown that AT7519 and FVP drive neutrophil resolution in a CDK9-dependent manner following tail fin injury in larval zebrafish (Hoodless et al., 2016). However, it is not known whether these CDK9 inhibitor compounds influence myocardial inflammation and repair/regeneration follow cardiac injury in larval zebrafish.

1.6. Study hypothesis and aims

In this study, I used a larval zebrafish model of cardiac laser injury to examine the migration of neutrophils and macrophages following myocardial wounding. By developing a combination of imaging modalities and transgenic tools, I characterised each stage of the immune response, starting with egress from hematopoietic tissue, to arrival at the injured myocardium and subsequent resolution of inflammation (Kaveh et al., 2020).

I also used this cardiac injury model to investigate whether CDK9 inhibitor treatment with AT7519 or Flavopiridol resolves neutrophil infiltration and whether this regulates downstream macrophage involvement and cardiac regeneration (Kaveh et al., 2021, *in review*).

1.6.1. Hypothesis

Enhancing the resolution of neutrophilic inflammation improves cardiac regeneration following injury in larval zebrafish.

1.6.2. Aims

1. Characterise cardiac injury, immune cell migration and repair/regeneration responses in a larval zebrafish model.
2. Investigate the effect of CDK9 inhibitor treatment during the innate inflammatory and regenerative response following cardiac injury in larval zebrafish.
3. Identify novel and efficacious CDK9 inhibitors in collaboration with BioAscent Discovery Ltd.

Chapter 2. Methods

2.1. General zebrafish techniques

2.1.1. Application and ethical review

All zebrafish experiments were conducted in accordance with the Animals (Scientific Procedures) Act, 1986 and approved by The University of Edinburgh Animal Welfare and Ethical Review Board in a United Kingdom Home Office-approved establishment. Experiments were performed on staged animals aged between 3- and 5-days post fertilisation (dpf), as according to Kimmel et al. (1995).

2.1.2. Lines used

Throughout the studies reported in this thesis various genetically modified zebrafish lines were used. These include: *Tg(myl7:eGFP)*^{twu26} (Huang et al., 2003), *Tg(myl7:h2b-GFP)*^{zf52} (Mickoleit et al., 2014), *Tg(nfkb:eGFP)*^{i235} (Feng et al., 2012), *Tg(mpx:mCherry)*^{uwm7} (Yoo et al., 2010), *Tg(mpeg1:mCherry)*^{gl23} (Ellett et al., 2011), *Tg(BACmpx:GFP)*^{i114}, abbreviated to *Tg(mpx:GFP)* (Renshaw et al., 2006), *Tg(mpx:gal4;UAS:Kaede)*^{i222} (Ellett et al., 2015), *Tg(fms:Gal4.VP16)*^{i186}, referred to as *csf1r:gal4* (Gray et al., 2011), *Tg(UAS-E1b:NfsB-mCherry)*^{c264}, abbreviated to *UAS:mCherry-NTR* (Davison et al., 2007), *Tg(fli1:eGFP)*^{y1tg} (Lawson and Weinstein, 2002), *Tg(kdrl:mCherry)*^{ci5} (Proulx et al., 2010), *Tg(kdrl:GFP)*^{la116} (Choi et al., 2007), and *Tg(h2az2a:h2az2a-GFP)*^{kca6}, abbreviated to *Tg(h2a:GFP)* (Pauls et al., 2001), *Tg(myl7:DsRed2-NLS)*^{f2} (Rottbauer et al., 2002), *Tg(TNFa:eGFP)*^{sa43296} (Nguyen-Chi et al., 2015) and *cdk9*^{ed9} mutant (Hoodless et al., 2016). Adult zebrafish were bred to yield desired combinations of transgenes in embryos.

2.1.3. Husbandry and breeding

Adult zebrafish were housed according to standard operating procedures (Westerfield, 2007), at 28.5°C with a 14 hour light and 10 hour dark cycle. To obtain zebrafish embryos, adult

zebrafish were bred by pair mating one female and one male overnight and collecting eggs the following morning. The eggs were maintained at 28.5°C in conditioned aquarium water containing methylene blue (0.5mg/l of methylene blue in conditioned water) until further use. Embryos were staged at 7 hours post fertilisation (hpf) and sorted into petri dishes, with approximately 40 embryos per petri dish containing 50mls methylene blue conditioned water. All experimental procedures were conducted at room temperature (23°C), and embryos/larvae were housed at 28.5°C between experimental timepoints.

2.1.4. Phenylthiourea treatment

To reduce pigment formation and thus enhance the optical clarity of larval zebrafish for imaging studies, staged embryos at 7 hpf were treated with 0.003% phenylthiourea (PTU) (Fisher Scientific) dissolved in conditioned water until the end of the experiment (Karlsson et al., 2001).

2.1.5. Anaesthesia

Prior to experimental procedures, larvae were anesthetised by immersing in 40 µg/ml tricaine methanesulfonate (Sigma Aldrich) in conditioned water. When required, larvae were transferred to conditioned water only for recovery.

2.1.6. Cardiac laser injury

The hearts of 72 hpf larval zebrafish were precisely injured using a Zeiss Photo Activated Laser Microdissection (PALM) system, as described in Taylor et al. (2019) and Kaveh et al. (2020). In summary, individual anaesthetised larvae were pipetted onto a glass slide in 20µl anesthetised conditioned water and laterally oriented so that the head is pointing leftward. This was to ensure that the ventricle was the uppermost chamber and thus easily targetable. Individual larvae were positioned adjacent to each other and navigated on the slide using the automated PALM controls. The laser was focussed specifically on the ventricular apex and subsequently fired through a 20X objective. Targeting this region increased reproducibility as it is anatomically unambiguous and avoids the risk of cardiac rupture, which typically releases erythrocytes into the pericardial space and interferes with cardiac imaging. Larval hearts were

laser pulsed until ventricular contractility had noticeably diminished, the apex had visibly shrunk, and the myocardial wall had swollen (**Figure 2.1**). This typically occurred after three laser pulses, however some hearts required additional pulsing. Cardiac ruptured larvae that displayed pericardial bleeding following laser injury were appropriately disregarded. Successful cardiac injury typically resulted in the ventricular apex losing fluorescent myocardial signal and/or displaying an elevated immune cell recruitment response, which was visualised using transgenic reporter zebrafish and fluorescence microscopy (**section 2.3.1**). Uninjured (control) larvae were treated in the same manner up to the point of laser injury, when they were separated and maintained in the same environmental conditions as injured fish.

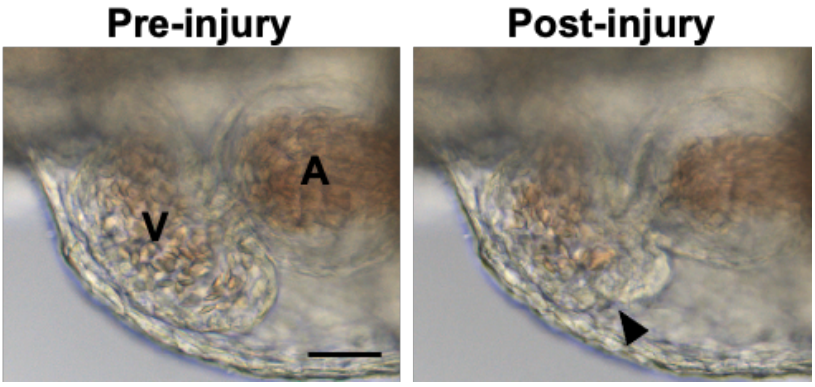

Figure 2.1: Localised cardiac laser injury. Brightfield image of a 3 dpf zebrafish heart pre-injury and immediately post-injury, viewed laterally. Black arrowhead indicates the ventricular apex laser injury site which appears shrunk and swollen. V = ventricle; A = atrium. Scale bar = 50 µm.

2.1.7. Tail fin resection

The tail fins of 72 hpf larval zebrafish were resected using a sterile scalpel, avoiding damage to the end of the notochord and vascular loop, as described by Lucas et al. (2013) and performed by Kaveh et al. (2020). Individual anaesthetised larvae were positioned adjacent to each other on a glass slide which was placed inside a petri dish containing 30ml anesthetised conditioned water. The tail fins of laterally oriented larvae were resected one at a time on the immersed glass slide using a 6X objective on a brightfield stereomicroscope. This approach

allowed tail fins to be carefully resected in a high throughput manner while avoiding dehydrating the larvae. Uninjured (control) fish were treated in the same manner up to the point of resection, when they were separated and maintained in the same environmental conditions as resected fish.

2.2. Treating zebrafish with pharmacological compounds

Individual larval zebrafish were treated with small molecule compounds dissolved in DMSO by incubation in conditioned water using 24 or 48 well plates. Drugs were dissolved in 100% DMSO maintained at stock concentrations of 1mM (Flavopiridol), 5mM (SB225002) or 50mM (AT7519). Working drug concentrations were prepared by diluting stock solutions in PTU-treated conditioned water.

2.2.1. Cxcr1/2 inhibition

Larvae were pre-incubated in 5µM SB225002 (Sigma Aldrich) or 0.1% DMSO vehicle (Sigma Aldrich) in conditioned water at 70 hpf for two hours prior to heart or tail injury, as performed in Kaveh et al. (2020) and previously characterised (Deng et al., 2013; Powell et al., 2017 and Zuniga-Traslavina et al., 2017). Following injury, individual larvae were continuously bathed in a 24-well plate containing 1ml of 5µM SB225002 or vehicle throughout the duration of the experiment. During the experiment larvae were only removed for serial timepoint imaging (**section 2.3.1**) at 2 hours post injury (hpi), 6 hpi, 24 hpi and 48 hpi.

2.2.2. Cdk9 inhibition

Larvae were incubated in AT7519 (Astex Pharmaceuticals) or Flavopiridol (Sigma Aldrich) in conditioned water at the following working concentrations: 1µM or 50µM AT7519, 1µM or 3µM Flavopiridol in ≤0.3% DMSO from 72 hpf or 4 hpi, depending on the experiment. For continuous treatments, larvae were incubated in drug or vehicle from 4 hpi until 24 hpi or 48 hpi. For transient treatments, larvae were incubated in drug or vehicle from 4 hpi until 6 hpi, at which

point they were transferred to fresh conditioned water. For serial timepoint experiments (**section 2.3.1**), individual larvae were incubated per well of a 48-well plate containing 500µl of CDK9 inhibitor or DMSO. During these experiments larvae were briefly removed for imaging at 6 hpi, 24 hpi or 48 hpi. For light sheet fluorescence microscopy (LSFM) timelapse experiments (**section 2.3.2**), individual anesthetised larvae were embedded in 1% low melting point agarose (ThermoFisher) in conditioned water containing 50µM AT7519, 3µM Flavopiridol (FVP) or DMSO. During LSFM timelapse imaging, larvae were continually anaesthetised using tricaine methanesulfonate conditioned water containing 50µM AT7519, 3µM Flavopiridol or DMSO, as appropriate, for up to 24 hours.

2.3. Microscopy

2.3.1. Epifluorescence microscopy

A Leica M205 FA stereomicroscope with standard GFP and mCherry filters were used for all serial timepoint fluorescence imaging experiments (**Figure 2.2**). An EVOS FL Auto2 imaging system (Thermofisher) with standard GFP, RFP and DAPI filters were used for automated whole larvae timelapse fluorescence imaging, as performed in Kaveh et al. (2020).

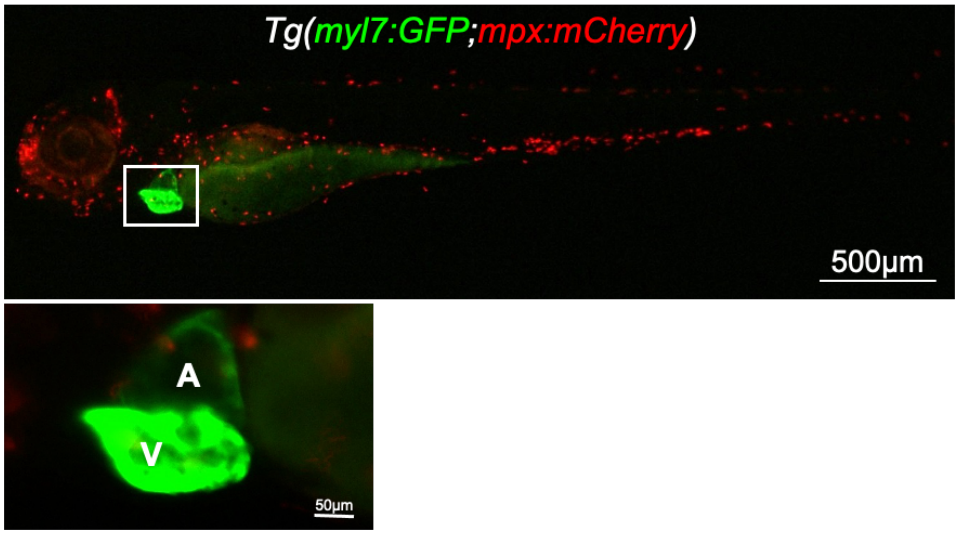

Figure 2.2: Cardiomyocyte (*myl7*) and neutrophil (*mpx*) transgenic reporting zebrafish larva. Image of a 3 dpf *Tg(myl7:GFP;mpx:mCherry)* zebrafish whole larva (top) and pericardium (bottom).

Larva was laterally imaged using a Leica M205 epifluorescence microscope. V = ventricle; A = atrium. Scale bar lengths indicated.

2.3.1.1. Mounting and preparation for serial timepoint imaging

Prior to serial timepoint imaging, larvae were anesthetised and individually pipetted onto a glass slide in 50µl anaesthetic conditioned water and oriented laterally so that the head is pointing leftward. This was to improve cardiac and immune cell imaging clarity (**Figure 2.2**).

2.3.1.2. Immune cell recruitment to heart wound

The number of immune cells on the ventricle were quantified by counting neutrophils or macrophages moving synchronously with the beating heart, as performed in Kaveh et al. (2020). Cardiac images were acquired using a 16X objective on the Leica M205 FA stereomicroscope.

2.3.1.3. Immune cell recruitment to tail wound

The number of immune cells at the tail fin were quantified by counting from the caudal end of the vascular loop to the wound edge as performed in Kaveh et al. (2020) and by others (Miskolci et al., 2019). Tail fin images were acquired using an 8X objective on the Leica M205 FA stereomicroscope.

2.3.1.4. Hematopoietic tissue immune cells

Images of the caudal hematopoietic tissue (CHT) were acquired to analyse immune cell CHT quantity (**section 2.4.3**), as performed in Kaveh et al. (2020). CHT images were acquired using a 6X objective on the Leica M205 FA stereomicroscope.

2.3.1.5. Immune cell mobilisation into the vasculature

The number of circulating immune cells were quantified by observing whole larvae for liberated neutrophils or macrophages, which can be detected in real time migrating through the

vasculature, as performed in Kaveh et al. (2020). Trunk timelapse images were acquired using an 8X objective on the Leica M205 FA stereomicroscope.

2.3.1.6. Photoconversion of regional immune cells

Neutrophils and macrophages were regionally photoconverted using *Tg(mpx:gal4;UAS:kaede)* and *Tg(csf1r:gal4;UAS:kaede)* larvae respectively and a Leica M205 epifluorescence stereomicroscope. A digital reticule was designed to inform of fluorescent beam location using a 16X objective. The reticule was specifically positioned to target one of two specific regions: the head and/or the pericardium. Prior to photoconversion, larvae were positioned laterally (head leftward) in 50µl conditioned water on a glass slide. A Mercury Vapor Lamp at 50W power was used in conjunction with a BFP filter and 16X objective to regionally photoconvert kaede-labelled immune cells. Larvae were either differentially photoconverted 1 hour prior to heart injury and imaged at 2 hpi and 6 hpi (immune cell tissue origin assay), or the pericardium was fully photoconverted at 6 hpi and imaged at 24 hpi (immune cell reverse migration assay). To assess immune cell tissue origins, the head was first fully photoconverted from green to red by exposing larvae for 60 seconds (until no green kaede signal was detectable above background). Next, the pericardium was semi-converted from green to brown (red and green) by exposing larvae for 30 seconds (immune cells retain 1:1 ratio of unconverted green vs converted red kaede fluorophore). Non-converted regions of the larvae (termed trunk) maintained endogenous green kaede fluorophore, hence producing three differentially labelled immune cell populations in the same larvae. Larvae were imaged up to, but not beyond, 24 hpi as shortly after this time converted kaede fluorophore became difficult to detect in semi-converted cells. To assess immune cell reverse migration, the pericardium was fully photoconverted from green to red by locally exposing larvae for 60 seconds (until no green kaede signal was detectable above background). Following photoconversion, larvae were imaged using both GFP and mCherry filters to detect immune cell kaede fluorophore levels, therefore allowing neutrophil and macrophage migration to be mapped (Kaveh et al., 2020).

2.3.1.7. Whole-body immune cells

Images of whole-body immune cells were acquired to analyse global neutrophil and macrophage numbers (**section 2.4.11**). Whole-body larvae images were acquired using a 2.5X objective on the Leica M205 FA stereomicroscope.

2.3.1.8. Sample preparation for timelapse imaging

Anesthetised larvae were embedded laterally (head leftward) in 1% low melting point agarose within a 6-well plate. Three larvae were positioned adjacent to each other per well. To ensure larvae remain anesthetised, once the agar had set, 500µl of anaesthetic conditioned water was added to each well prior to timelapse imaging, as performed in Kaveh et al. (2020).

2.3.1.9. Whole-body immune cell timelapse imaging

An EVOS Auto2 epifluorescence microscope was used to acquire images per well of a 6-well plate in an automated manner using a 2X objective at 1-minute intervals up to 24 hpi, as performed in Kaveh et al. (2020).

2.3.2. Light sheet fluorescence microscopy (LSFM)

To image the heart and/or immune cells at greater spatial and temporal resolution light sheet fluorescence microscopy (LSFM) was used (Reynaud et al., 2008; Power and Huisken, 2017 and Taylor et al., 2019). A bespoke light sheet fluorescence microscope was constructed by Dr Laura Young and is continually optimised by Dr Jonathan Taylor for larval zebrafish cardiac imaging (Taylor et al., 2019). In brief, a light sheet is projected into the sample chamber by the illumination arm and a fluorescence z-plane is imaged perpendicular to the light sheet via the imaging arm (**Figure 2.3**). The sample is scanned through the light sheet to reconstruct a 3D image stack. Specifically, GFP, mCherry and CFP channels are excited along the imaging arm using 488nm, 561nm and 405nm Vortran Versalase laser light respectively. Fluorescent signals are separated using a dichroic beam splitter, passed through 525/39nm, 630/69nm and 470/40nm emission filters and images acquired using CCD cameras. Shadow effects are minimised using a 4kHz resonant scanning mirror. Laser power is maintained at 4mW for all

experiments. Brightfield images are simultaneously recorded at 80 frames/second using a Prosillica CCD camera. Laser and camera activation are controlled using custom-built user interface software developed by Dr Jonathan Taylor. A whole zebrafish larva is manually mounted, positioned and scanned using micrometre and motor-driven stages. The setup of this custom-built LSFM system (**Figure 2.3**) has been previously reported in detail by our laboratory (Taylor et al., 2019).

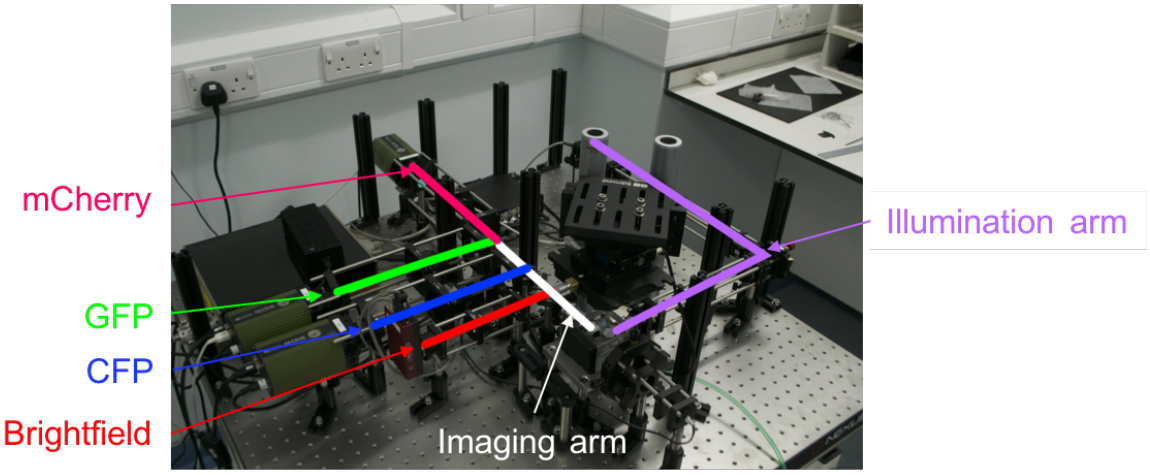

Figure 2.3: Custom-built LSFM setup. The LSFM is divided into two 'arms': the illumination arm, where the laser is activated and the light sheet is formed, and the imaging arm, where the sample is imaged by up to four cameras (brightfield**,** mCherry, GFP and CFP).

2.3.2.1. Sample preparation

Anesthetised larvae were placed in 1% low melting-point agarose and individually embedded inside 1.3mm diameter FEP tubing (Adtech) using a bespoke syringe-plunger construct (**Figure 2.4**). One larva was embedded per FEP tube. Once the agar had set, the tubing was plugged with blu-tak, and the construct was mounted onto the LSFM using a bespoke 3D printed metal collar (**Figure 2.4**).

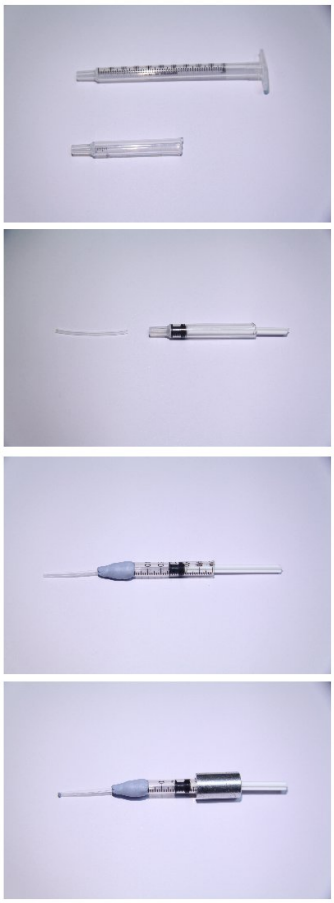

Figure 2.4: Protocol for preparing a zebrafish sample inside FEB tubing using a bespoke syringe-plunger construct and metal collar.

2.3.2.2. Heartbeat-synchronised (optically gated) cardiac imaging

Heartbeat-synchronisation (optical gating) software has been developed by Dr Jonathan Taylor and is directly coupled to the bespoke LSFM system. Both prospective and more recent adaptive prospective gating methods have been previously described in detail (Taylor et al., 2011; Taylor et al., 2012 and Taylor et al., 2019). The software allows real time 3D fluorescence imaging of the beating zebrafish heart by ensuring fluorescence images are consistently acquired at the same phase of the cardiac cycle (e.g., peak systole or peak diastole, or anywhere in between). This approach permits individual 3D z-stacks and timelapse (4D) datasets to be acquired as if the heart was computationally “frozen”, even though it is

beating normally. The synchronisation software continually monitors the brightfield camera and generates electronic triggers to acquire individual fluorescence z-planes only when the heart is at a fixed, predetermined phase of its heartbeat cycle. The user activates the synchronisation system, which automatically selects a phase of the heartbeat cycle to synchronise to. Alternatively, the user can select a different target phase of the heartbeat cycle if preferred (e.g., if heart synchronisation is not optimal). When synchronisation is activated, the system establishes one full heartbeat cycle of reference frames and will then generate an electrical trigger to cause fluorescence cameras to subsequently acquire a z-stack once on every heartbeat. When synchronisation is reset (either manually by the user, or automatically during a long-term timelapse experiment), the synchronisation module ensures the reference frame is updated so that triggers are sent at the same target phase in the heartbeat. The entire heart is scanned in 3D with a z-plane spacing of 1µm, and each image stack is stored as a .tif file. 3D image stacks can be viewed as maximum intensity projection images during acquisition, and if necessary, the settings can be altered between acquisitions to optimise the quality of subsequently acquired images. For timelapse imaging, the heart was z-scanned every 3 minutes for up to 24 hours. By limiting laser activation to a designated phase of the heartbeat cycle, the lightsheet only illuminates each z-plane for a few milliseconds, minimising the impact of phototoxicity and photobleaching (Taylor et al., 2019).

2.3.2.3. Non-synchronised timelapse imaging

The LSFM was also used for immune cell migration imaging within the tail fin. As the tail fin has no movement, heart-synchronisation was not required. 3D z-scans of the tail fin were acquired every 1 minute with a z-plane spacing of 1µm for up to 24 hours.

2.4. Image analysis

Unless stated otherwise, all image analysis was performed using open access ImageJ (Fiji) software (National Institute of Health).

2.4.1. Ventricular ejection fraction

The hearts of *Tg(myl7:GFP)* larvae were imaged in real time using epifluorescence microscopy (**section 2.3.1**) to capture points in the cardiac cycle when the ventricle is in diastole and systole. Ventricular area in diastole and systole was measured and ventricular ejection fraction (by area) was calculated using the formula: 100 X [(Diastolic Area – Systolic Area)/Diastolic Area], as performed in Kaveh et al. (2020).

2.4.2. Photoconverted immune cells

Epifluorescence images of photoconverted larvae (**section 2.3.1.6**) were analysed to quantify the number of immune cells that were fully converted (red), semi-converted (red and green) or unconverted (green) on the heart, or to identify immune cell locations in whole larvae following heart injury. For the reverse migration (immune cell location) assay, each larva was divided into 48 equally sized square zones (3 rows of 16 with an individual zone size of 31000 μm^2). The number of photoconverted immune cells within each square zone at 24 hpi was quantified per larva, averaged and normalized per zone. Using this data, a whole larva heat map summarising the dispersal of photoconversion-tracked immune cells was generated, as performed in Kaveh et al. (2020).

2.4.3. Immune cell CHT quantity

Epifluorescences images of immune cells within the CHT (**section 2.3.1.4**) were quantified across timepoints and normalised to preinjury (0 hpi) for each larva. Quantification was performed in a semi-automated manner using a Fiji macro. In brief, a rectangular region of interest (766µm × 151µm) was positioned over the CHT. This region was cropped, and brightness/contrast enhanced to identify all neutrophils and macrophages. The background signal was subtracted then an unsharp mask and watershed threshold were applied. The 'Analyze Particles' Fiji plugin was run to measure the thresholded area of neutrophils and macrophages in the CHT, as performed in Kaveh et al. (2020).

2.4.4. Whole-body immune cell tracking

Whole-body immune cell epifluorescence timelapse images were analysed using the Fiji plugin 'Trackmate' (Tinevez et al., 2017), which automated the tracking of neutrophil and macrophage migration. The following Trackmate parameters were used: LOG detector, diameter 14µm and threshold 5µm. Linear Assignment Problem (LAP) algorithms was used with the following parameters: linking distance 27µm, max closing distance 15µm and gap-closing max frame gap 2. The following analyses were then performed. 1) Vessel use incidence: the use incidence of each vessel for heart injury datasets was obtained manually by plotting a line along the dorsoventral axis one somite anterior to the cloaca and counting how many cells pass the line during 1–12 hpi for each vessel. The same method was used for tail resection datasets except the dorsoventral line was drawn four somites anterior to the tail fin. The reason for this being that the majority of distally migrating cells will be coming from the CHT, which is located between the heart and tail fin wound sites, hence immune cells are expected to move in opposite directions depending on the injury model. 2) Cell behaviour: cells were tracked during 1.5–8 hpi specifically within the trunk region. Non-migrating cells were excluded from the analysis based on displacement. Remaining immune cell migration tracks were used to plot speed and meandering index. Meandering index was calculated using the Trackmate output data 'Displacement', 'Duration' and 'Speed', where Meandering index = Displacement/(Duration/Speed). Whole-body immune cell tracking analysis was performed as described in Kaveh et al. (2020).

2.4.5. Surface rendering and immune cell tracking

LSFM z-stacks of the myocardium, endocardium, immune cells and nuclei were surface rendered using Imaris software (Bitplane). Rendered immune cells were tracked using an autoregressive motion algorithm where default and suggested parameters were used. Individual tracks were surface rendered for display.

2.4.6. Immune cell behaviour on the heart

LSFM timelapses of the heart (myocardium and neutrophils or macrophages) were processed as maximum intensity projections. The Fiji plugin 'MTrackJ' (Meijering et al., 2012) was used to manually track immune cells from when they migrate onto the ventricular myocardium until they reverse migrate from the ventricular myocardium or, as is commonly the case for persistent macrophages, until the end of the timelapse, as performed in Kaveh et al. (2020).

2.4.7. Immune cell behaviour at the resected tail fin

LSFM timelapses of the resected tail fin (**section 2.3.2.3**) were analysed using Imaris. Default and suggested parameters were used for tracking using the autoregressive motion algorithm. Co-positive cells were designated with a *mpx*:*mpeg1* ratio less than 3:1 and greater than 1.33:1. This method overcomes variability in absolute intensity as immune cells migrate through the tail fin and change shape. Plotted values are calculated from the average of all cells in one larva 2–3 hpi following tail fin resection, as performed in Kaveh et al. (2020).

2.4.8. Fluorescence intensity plots of immune cell z-planes

LSFM z-stacks of resected tail fins (**section 2.3.2.3**) were analysed using the Fiji 'plot profile' function to measure the intensity of a desired fluorophore across a manually drawn line and assess the distribution of fluorophore intensity within an immune cell, as performed in Kaveh et al. (2020).

2.4.9. Temporal colour coding immune cell migration

LSFM-acquired z-stacks of neutrophil and macrophage migration on the injured heart (**section 2.3.2.2**) were processed as maximum intensity projections and overlaid across the indicated timepoints. The 'Temporal-Color Code' Fiji tool was applied to the hyperstack such that each overlaid timepoint is a different hue, producing a single image which summarises immune cell migration on the injured heart.

2.4.10. Ventricular cardiomyocyte number

Individual LSFM-acquired z-stacks of *Tg(myl7:DsRed2-NLS)* hearts (**section 2.3.2.2**) were processed as maximum intensity projections to visualise cardiomyocyte nuclei throughout the heart. The 'TrackMate' Fiji plugin was applied to each image and the following settings were used: LoG detector, Median filter and Sub-pixel localisation, Estimated blob diameter = 6µm and 'Threshold' = 6. Atrial cardiomyocytes were subtracted from the total to give a final ventricular cardiomyocyte count.

2.4.11. Whole-body immune cell number

Whole-body epifluorescence images of larvae (**section 2.3.1.7**) were used to estimate global immune cell numbers in a semi-automated manner using a Fiji macro. Individual images were thresholded using the 'Yen' technique, converted to binary and whole-body immune cell threshold area was quantified (**Figure 2.5**). The area of three thresholded immune cells were measured at random. Whole-body immune cell threshold area was divided by average immune cell area to estimate global immune cell numbers per larva.

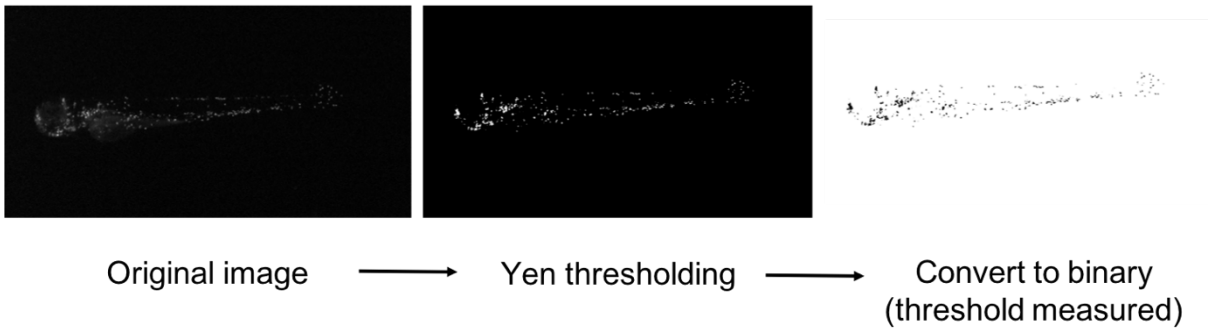

Figure 2.5: Fiji macro used to estimate global immune cell numbers. Original whole larvae images obtained using epifluorescence microscopy were thresholded using the Yen technique, converted to binary and the threshold area was measured.

2.4.12. Ventricular *TNF*$^{+}$ macrophage number

Individual LSFM-acquired z-stacks of *Tg(mpeg1:mcherry;TNFa:GFP)* hearts (**section 2.3.2.2**) were processed as maximum intensity projections to visualise macrophages and *TNF*

expression throughout the heart. The number of ventricular macrophages expressing *TNF* (above that of background levels) were counted. *Tg(mpeg1:mcherry)* larvae were used as a measure of background fluorescence and a negative control in this context.

2.4.13. Myocardial wound area

Individual LSFM-acquired z-stacks of *Tg(myl7:GFP)* injured hearts (**section 2.3.2.2**) were 3D rendered using Imaris software based on absolute intensity and suggested segmentation and rendering parameters. Rendered hearts were saved as separate images and imported into Fiji. The *myl7:GFP* negative area at the ventricular apex (visualised as a render-free hole in the myocardium) was manually traced around and quantified to give myocardial wound area (μm^2).

2.5. Zebrafish cell death staining

2.5.1. TUNEL staining

To assess cellular apoptosis at the injured heart whole-mount TUNEL staining was performed, as optimised by Buckley et al. (2017), and adapted by Kaveh et al. (2020). Larvae were fixed in 4% PFA for 30 minutes and transferred to a 1:10 dilution of PBS. Larvae were subsequently digested in 1µg/ml Proteinase K for 1 hour. Larvae were re-fixed in 4% PFA for 20 minutes and then washed in PBT three times. TUNEL staining was performed using the ApopTag Red *In situ* kit (Millipore) to label apoptotic cells. Larvae were incubated in pre-chilled acetone:ethanol at -20°C for 7 minutes and subsequently washed in PBT three times. Larvae were then incubated in equilibration buffer for 45 minutes at room temperature and subsequently removed. 16µl of TdT enzyme and 30µl reaction buffer was administered for 90 minutes at 37 °C and then removed. The reaction was stopped by adding 200µl stop buffer and incubating for 180 minutes at 37 °C. Larvae were subsequently washed in PBT three times and maintained in the dark. At this point, larvae were incubated in 62µl of Anti-Digoxigenin antibody and 68µl of blocking solution overnight at 4°C. Larvae were washed four times in PBT and then imaged using LSFM.

2.5.2. Acridine orange live staining

To determine the level of cell death following injury, acridine orange live staining was used (Tucker and Lardelli, 2007), as described in Kaveh et al. (2020). Larvae were incubated in 10 ng/µl of Acridine orange solution (ThermoFisher) in the dark for 20 minutes. Larvae were subsequently washed three times in conditioned water for 10 minutes and immediately imaged using heartbeat-synchronised LSFM (**section 2.3.2.2**).

2.6. Genotyping *cdk9* mutant zebrafish

Knockout *cdk9* mutant zebrafish were previously generated by our laboratory (Hoodless et al., 2016). Genotyping was performed on adult zebrafish tail fin clips and whole larvae to identify wild-type or mutant *cdk9* alleles. This protocol was adapted from Hoodless et al. (2016).

2.6.1. Genomic DNA extraction

Genomic DNA (gDNA) was extracted from both adult zebrafish tail fin clips and euthanised whole larvae using the same protocol. To obtain adult zebrafish tail fin clips, zebrafish were anesthetised and momentarily laid on wet tissue paper. A small section of one tail fin lobe was resected using a sterile scalpel. Zebrafish were subsequently recovered and individually housed in labelled tanks and tail clips were individually transferred to respectively labelled polymerase chain reaction (PCR) tubes on ice containing lysis buffer (20µL dH_2O, 2.5µL 10x Taq buffer and 1.25µL Proteinase K). The PCR tubes were incubated at 67°C for 60 minutes and the digest was ended with a 95°C incubation for 15 minutes to denature the Proteinase K. The PCR tubes were then vortexed thoroughly and centrifuged. All gDNA samples were stored at 4°C until required.

2.6.2. PCR amplification

2.6.2.1. Primers used for *cdk9* mutant amplification

Forward and reverse primers were designed to specifically amplify the mutated *cdk9* allele. Primers were ordered from IDT and diluted to a working stock solution of 10µM.

Table 2.1: Primer sequences used for *cdk9* genotyping.

Primer	**Sequence**
CDK9 Forward	GCCGAAAGAAAACGCGAAGT
CDK9 Reverse	ACGGGCCATATGGGGATTTC

2.6.2.2. PCR master mix for *cdk9* amplification

Each sample was incubated in the following 25µL PCR reaction mix:

Table 2.2: PCR master mix components.

Component	**Volume**
gDNA	2µL
OneTaq Quick-load 2x master mix	12.5µL
Forward primer	0.5µL
Reverse primer	0.5µL
dH_2O	9.5µL
Total	**25µL**

The following PCR parameters were used for amplification of *cdk9* alleles:

Table 2.3: PCR amplification parameters.

Step	**Temperature (°C)**	**Time**
Initial denaturing	94	2 minutes
Denaturing	94	30 seconds
Annealing	58	30 seconds
Extension	68	1 minute
Cycle back to denaturing step 37 times		
Final extension	68	1 minute
Hold	4	∞

2.6.3. Restriction enzyme digest

The *cdk9* mutation results in the loss of a restriction site for the *Hpy188I* enzyme. Amplified *cdk9* PCR product was incubated with *Hpy188I* restriction enzyme to identify wild-type, heterozygous and homozygous mutant alleles. In wild-type fish, the *Hpy188I* restriction enzyme cut site in intact, thus the PCR product which is 415 bp is digested into 270 bp and 145 bp bands (**Figure 2.6**). In heterozygous mutant fish, the *Hpy188I* restriction enzyme partially digests the PCR product. In homozygous mutant fish, the *Hpy188I* restriction enzyme cut site is not present, thus the PCR product (415 bp) is not digested (**Figure 2.6**). Each sample was incubated in the following 17µL restriction enzyme digest mix:

Table 2.4: Restriction enzyme digest mix components.

Component	**Volume**
PCR product	12.5µL
Hpy188I restriction enzyme (NEB)	1µL
Cutsmart buffer (NEB)	2µL
dH_2O	1.5µL
Total	**17µL**

The samples were incubated at 37°C for 60 minutes and subsequently heat inactivated by incubating at 65°C for 20 minutes. Restriction enzyme digested samples were stored at 4°C until required.

2.6.4. DNA gel electrophoresis

Agarose DNA gels were run to confirm restriction enzyme digest band sizes and thus *cdk9* genotype for each sample. A 2% agarose gel was prepared by heating and mixing 2g of agarose powder with 100ml 1x TAE and 2 µL of Sybr Safe Gel Stain. The gel was then poured into a mould. Once the gel had set, 5uL of 100 bp Hyperladder (NEB) was loaded into the first and last well of each row to aid assessment of band size. 6µL of restriction enzyme digested samples were loaded into the other wells. The gel was run at 125V for 30 minutes, until the dye was approaching the end of the gel. Gels were imaged using a UVdoc imager to determine the band size of each sample and confirm individual zebrafish genotypes (**Figure 2.6**).

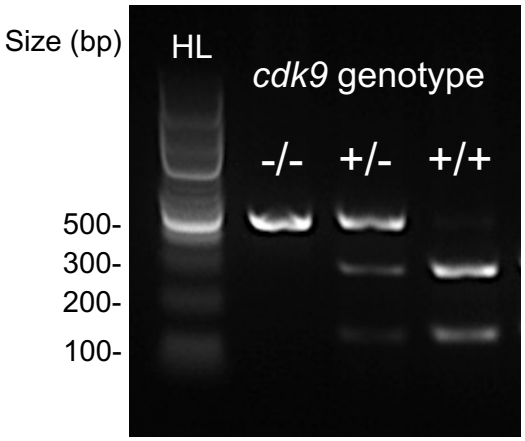

Figure 2.6: Restriction enzyme digest of the *cdk9* allele in wild-type, heterozygous and homozygous mutant zebrafish. Base pair (bp) size of hyperladder (HL) bands and individual genotype bands (in order: *cdk9*$^{-/-}$, *cdk9*$^{+/-}$ and *cdk9*$^{+/+}$) are indicated. The *Hpy188I* restriction enzyme cut site is present in wild-type fish, thus it is digested to produce a 270 bp and a 145 bp band. Homozygous mutant fish do not have a *Hpy188I* restriction enzyme cut site, thus remain undigested producing a single 415 bp band. Heterozygous mutant fish display partial DNA digestion.

2.7. CDK9 inhibitor selectivity zebrafish assay

As homozygous knockout *cdk9* mutants are not viable at adulthood, adult heterozygous *cdk9* mutants were identified by genotyping (**section 2.6.1**) and subsequently incrossed yielding a mendelian mix of wild-type (25%), heterozygous (50%) and homozygous (25%) mutant zebrafish embryos. Homozygous knockout *cdk9* mutants are phenotypically distinguishable during larval stages (Hoodless et al., 2016), which was confirmed by genotyping (**section 2.6.1**). At 72 hpf, *cdk9* homozygous mutant larvae were phenotypically selected and treated with AT7519, FVP or DMSO vehicle (**section 2.2.2**). Following this, heart rate (beats/minute) was measured per larva by manually counting heartbeats per twelve seconds using a brightfield stereomicroscope and multiplying by five. This was performed between groups at 2 hours post treatment (hpt), 6 hpt, 12 hpt, 24 hpt and 48 hpt as a proxy for overall health, allowing individual larvae to be assessed in real time. Larvae with no heartbeat were regarded as dead.

2.8. Ligand-based virtual screening of BioAscent's compound library

Ligand-based virtual screening of BioAscent's 125k diversity library and subsequent compound selection was performed with kind assistance from Professor Scott Webster and Dr Steven Shave.

2.8.1. Identifying known efficacious CDK9 inhibitor compounds

A literature search was performed to identify efficacious CDK9 inhibitors that have been developed. In addition to AT7519, the following compounds were identified as potent and selective CDK9 inhibitors based on published IC50 values for CDK9 and other kinases. The chemical structure of these compounds was used for subsequent *in silico* modelling.

Table 2.5: Highly potent and selective CDK9 inhibitors identified following a literature search.

Compound	Structure	CDK9 IC50	DOI
AT7519	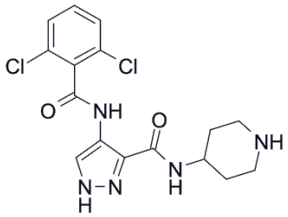	<10nM	10.1158/1535-7163.MCT-08-0890
AZD4573	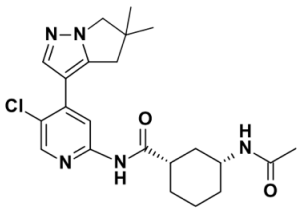	3nM	10.1158/1078-0432.CCR-19-1853
iCDK9	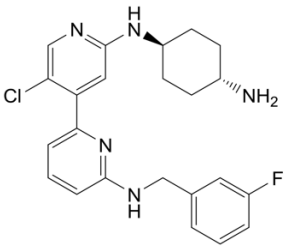	<0.4nM	10.7554/eLife.06535.001
LDC000067	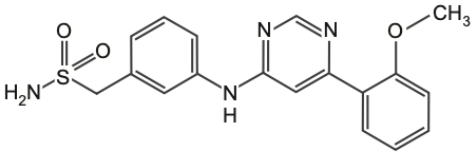	44nM	10.1111/bph.12408
MC180295	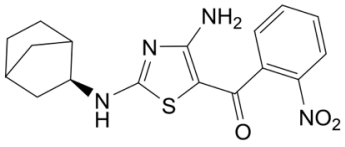	5nM	10.1016/j.cell.2018.09.051
NVP-2	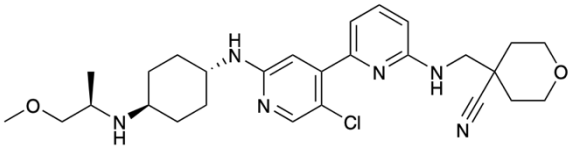	0.5nM	10.1038/nCHeMBIO.2538

2.8.2. Structural 3D similarity screen of BioAscent's compound library

Each of the six chemical structures (**Table 2.5**) were used to perform a computational similarity screen against BioAscent's 125k diversity compound library (Cereto-Massague et al., 2015). The USRCAT 3D similarity method (RDKit implementation) was used with query (**Table 2.5**) and candidate (BioAscent) conformers generated using the Ebejer protocol (Ebejer et al., 2012). USRCAT is a 3D similarity method which selects molecules that share similar 3D shapes in terms of their atom, hydrophobic, acceptor, donor and aromatic atom distributions (Schreyer and Blundell, 2012). The top 1000 BioAscent compounds ranked by USRCAT molecular similarity against each of the six query compounds were taken forward. Duplicated compounds (molecules that appeared in two or more query lists) were subsequently identified between the six ranked query lists and shortlisted.

2.8.3. Inspecting shortlisted compounds for pan-assay interference properties

Shortlisted compounds were manually inspected for structural pan-assay interference (PAINS) properties using open-source DataWarrior software. Common PAINS molecules/properties include: toxoflavin (redox cycler – produces hydrogen peroxide which disrupts protein activity), isothiazolones (covalent modifier – binds to proteins non-specifically), curcumin (covalent modifier – disrupt membrane receptors), hydroxyphenyl hydrazones (covalent modifier – sequesters metal ions which inactivates proteins), rhodanines (covalent modifier and metal complexer), phenol-sulphonamides (redox cycler and covalent modifier, unstable compound which gives false negatives), enones (covalent modifier), quinones and catechols (redox cycler, metal complexer and covalent modifier), as described by Baell and Holloway. (2010). Molecules that clearly displayed these PAINS features were removed from the shortlisted library to generate a final focussed library.

2.9. Human neutrophil apoptosis assay with Flavopiridol

This assay was performed with kind assistance from Dr Calum Robb, Giulia Rinaldi and Magdalena Oremek.

2.9.1. Neutrophil isolation, culture and Flavopiridol treatment

Approximately 60mL of blood was collected from healthy human donors in 50mL microcentrifuge tubes with 3.8% sodium citrate (Sigma Aldrich) by a trained phlebotomist. Collected blood was centrifuged at 300g for 20 minutes and platelet-rich plasma was removed. Leukocytes were subsequently separated from erythrocytes by dextran sedimentation for 25 minutes using 6% dextran. The upper leukocyte-rich layer was aspirated, and the volume adjusted to 50ml using pre-warmed (37°C) 0.9% saline. Leukocytes were pelleted by centrifugation at 350g for 6 minutes. Polymorphonuclear leukocytes were separated from mononuclear leukocytes using discontinuous Percoll (9:1 ratio of percoll:10xPBS) gradients (81%, 70% and 55% Percoll in 1x PBS without calcium and magnesium cations). Each leukocyte-rich layer was removed and transferred to a fresh 50ml tube, and the volume was adjusted to 50ml with saline. The tubes were then centrifuged at 350g for 6 minutes. The pellets from the two tubes of cells were resuspended in 3ml of 55% Percoll and the gradients were centrifuged at 720g for 20 minutes. Polymorphonuclear leukocytes at the 70/81 interface were extracted and cell yield was estimated using a haemocytometer. Leukocytes were washed twice more in PBS (without cations) and then centrifuged at 300g for 5 minutes. The supernatant was discarded, and cell viability was assessed using trypan blue staining. This confirmed that at least 98% of isolated polymorphonuclear leukocytes were neutrophils based on cell morphology. Cells were re-suspended at $5x10^6$ cells/mL in Iscove's modified dulbecco's medium (IMDM) with 50 U/mL penicillin and 50 U/mL penicillin/streptomycin plus 10% autologous serum. Isolated and resuspended neutrophils were cultured in flat-bottomed 96 well plates at $5x10^6$ cells/mL in IMDM (with autologous serum and penicillin/streptomycin). 75µl

of the $5x10^6$ cells/mL suspension was pipetted into individual wells of a flat-bottomed 96 well plate. To treat with CDK9 inhibitor, pan caspase inhibitor or vehicle, 15µl of 10µM Flavopiridol, 10µM Q-VD-OPh or DMSO were respectively added to 60µl of IMDM/serum and 75µl of neutrophil suspension. The plate was incubated at 37°C in an incubator at 5% CO_2 for 22 hours.

2.9.2. Assessment of neutrophil apoptosis by flow cytometry

After 22 hours of incubation, flow cytometry was used to assess neutrophil apoptosis and necrosis using annexin-V binding and propidium iodide (PI) staining respectively. Annexin-V solution was diluted 1:500 in Annexin-V binding buffer (HBSS + Ca^{2+}). 200µl of Annexin-V binding buffer was added to FACS tubes and kept on ice. Neutrophil cultures ($5x10^6$cells/ml) were vigorously aspirated and 30µl was subsequently added to each FACS tube. Samples were incubated on ice in the dark for 10 minutes. Immediately before processing the samples on a flow cytometer, 1µl of PI (1mg/mL) was added to each FACS tube. FlowJo software was used to analyse the flow cytometry data.

2.9.3. Assessment of neutrophil apoptosis by microscopy

Neutrophil apoptosis was also assessed morphologically by preparing cytospins from the cultured cells. 100µl of neutrophil cultures ($5x10^6$cells/ml) were cytocentrifuged at 300g for 3 minutes. The cells were air-dried and subsequently fixed in methanol for 2 minutes. The slides were then stained with Diff-Quik solution, rinsed with dH_2O and air-dried. A drop of DPX mountant was applied to each slide and a coverslip was placed on top. Slides were then imaged using a light microscope with 40x and 100x objectives and neutrophil morphology was assessed.

2.10. Graphing and statistical analysis

Graphs were curated and statistical analysis was performed using GraphPad Prism 9 software. The normal distribution of quantitative data was confirmed using the Shapiro-Wilk test and then analysed using parametric or non-parametric tests, as appropriate. If normally distributed, data were analysed by One-way ANOVA or Two-way ANOVA followed by a multiple comparison *post hoc* test. If not normally distributed, data were analysed using the Mann–Whitney *U*-test. Error bars indicate standard error of the mean (SEM) or standard deviation (SD). All statistical tests, *p*-values and *n* numbers used are provided in figure legends. * $p < 0.05$, ** $p < 0.01$, *** $p < 0.001$, **** $p < 0.0001$ and ns indicates non-significant.

Chapter 3. Live imaging of heart injury in larval zebrafish reveals a multi-stage model of neutrophil and macrophage migration

3.1. Introduction

Neutrophils and macrophages are crucial regulators of cardiac repair/regeneration following injury (Trajano and Smart, 2021). However, immune cells are difficult to observe in mammals at high resolution *in vivo*. The optically transparent larval zebrafish is becoming an invaluable tool for studying inflammation due to its amenability to *in vivo* imaging. These qualities make it ideal for the rapidly evolving area of immune cell modulation of tissue regeneration, with many groups now adopting larval zebrafish wounding models of their own (Gurevich et al., 2018, Herzog et al., 2018; Tsarouchas et al., 2018; Stoddard et al., 2019 and Miskolci et al., 2019). However, there is a need to better understand each stage of the immune cell response following tissue wounding in larval zebrafish, from recruitment to resolution. It is not known if the general patterns of immune cell migration are consistent across injury models. Our laboratory has established a larval zebrafish model of localised cardiac laser injury (Matrone et al., 2013; Taylor et al., 2019 and **Appendix Figure 1**). This model allows for close examination of local and systemic neutrophil and macrophage responses following cardiac injury *in vivo*, a feat which is currently not possible in other models. In this chapter, I develop and apply a range of bespoke live imaging techniques to interrogate the migratory response of neutrophils and macrophages following cardiac injury *in vivo*. I compare our findings to the well-characterised tail resection model (Hoodless et al., 2016), and propose a unifying multi-stage model of immune cell migration following injury in larval zebrafish.

3.2. Publication

The results of this chapter are published:

Kaveh A, Bruton FA, Buckley C, Oremek MEM, Tucker CS, Mullins JJ, Taylor JM, Rossi AG, Denvir MA. **Live imaging of heart injury in larval zebrafish reveals a multi-stage model of neutrophil and macrophage migration**. Frontiers Cell and Developmental Biology. 2020 Sep 8:579943. https://doi.org/10.3389/fcell.2020.579943.

The associated supplementary material for this article can be found online at the following link: https://www.frontiersin.org/articles/10.3389/fcell.2020.579943/full#supplementary-material.

This is an open-access article distributed under the terms of the Creative Commons Attribution License (CC BY).

In line with the University of Edinburgh guidelines for including publications in postgraduate research theses, for this chapter I wrote a separate introduction and discussion. The paper referenced above was published in Frontiers Cell and Developmental Biology on October 19th 2020 and has been enclosed in full within this chapter.

3.3. Contributions

This study was performed in collaboration with two other PhD students, Finnius Bruton and Magdalena Oremek. I was responsible for performing the heart injury characterisation (Figure 1) and all neutrophil sections (Figures 2-7) in the manuscript. FAB was responsible for the macrophage sections (Figures 2-7), MEMO was responsible for the flow cytometry sections (Supplementary Figure 7), and CB helped acquire and analyse data for Figure 4. Overall, AK, FAB, and MAD conceived and designed the study. AK, FAB, MEMO, and CB carried out all experiments. AK, FAB, and CB performed the image analysis. JMT provided LSFM-related technical assistance. AK and FAB wrote the manuscript. CB, JMT, CST, JJM, AGR, and MAD edited the manuscript. MAD, AGR, and CST supervised the study.

frontiers in Cell and Developmental Biology

ORIGINAL RESEARCH
published: 19 October 2020
doi: 10.3389/fcell.2020.579943

Live Imaging of Heart Injury in Larval Zebrafish Reveals a Multi-Stage Model of Neutrophil and Macrophage Migration

Aryan Kaveh[1†], Finnius A. Bruton[1*†], Charlotte Buckley[1,2], Magdalena E. M. Oremek[3], Carl S. Tucker[1], John J. Mullins[1], Jonathan M. Taylor[4], Adriano G. Rossi[3] and Martin A. Denvir[1]*

[1] Centre for Cardiovascular Science, Queen's Medical Research Institute, University of Edinburgh, Edinburgh, United Kingdom, [2] Strathclyde Institute of Pharmacy and Biomedical Sciences, University of Strathclyde, Glasgow, United Kingdom, [3] Centre for Inflammation Research, Queen's Medical Research Institute, University of Edinburgh, Edinburgh, United Kingdom, [4] Department of Physics, University of Glasgow, Glasgow, United Kingdom

OPEN ACCESS

Edited by:
Vincenzo Torraca,
University of London, United Kingdom

Reviewed by:
Sofia de Oliveira,
Albert Einstein College of Medicine, United States
Tomasz Prajsnar,
Jagiellonian University, Poland

***Correspondence:**
Aryan Kaveh
Aryan.Kaveh@ed.ac.uk
Finnius A. Bruton
s1102712@sms.ed.ac.uk

† These authors have contributed equally to this work

Specialty section:
This article was submitted to Molecular Medicine, a section of the journal Frontiers in Cell and Developmental Biology

Received: 03 July 2020
Accepted: 11 September 2020
Published: 19 October 2020

Citation:
Kaveh A, Bruton FA, Buckley C, Oremek MEM, Tucker CS, Mullins JJ, Taylor JM, Rossi AG and Denvir MA (2020) Live Imaging of Heart Injury in Larval Zebrafish Reveals a Multi-Stage Model of Neutrophil and Macrophage Migration. Front. Cell Dev. Biol. 8:579943. doi: 10.3389/fcell.2020.579943

Neutrophils and macrophages are crucial effectors and modulators of repair and regeneration following myocardial infarction, but they cannot be easily observed *in vivo* in mammalian models. Hence many studies have utilized larval zebrafish injury models to examine neutrophils and macrophages in their tissue of interest. However, to date the migratory patterns and ontogeny of these recruited cells is unknown. In this study, we address this need by comparing our larval zebrafish model of cardiac injury to the archetypal tail fin injury model. Our *in vivo* imaging allowed comprehensive mapping of neutrophil and macrophage migration from primary hematopoietic sites, to the wound. Early following injury there is an acute phase of neutrophil recruitment that is followed by sustained macrophage recruitment. Both cell types are initially recruited locally and subsequently from distal sites, primarily the caudal hematopoietic tissue (CHT). Once liberated from the CHT, some neutrophils and macrophages enter circulation, but most use abluminal vascular endothelium to crawl through the larva. In both injury models the innate immune response resolves by reverse migration, with very little apoptosis or efferocytosis of neutrophils. Furthermore, our *in vivo* imaging led to the finding of a novel wound responsive *mpeg1*+ neutrophil subset, highlighting previously unrecognized heterogeneity in neutrophils. Our study provides a detailed analysis of the modes of immune cell migration in larval zebrafish, paving the way for future studies examining tissue injury and inflammation.

Keywords: zebrafish, heart, tail, injury, neutrophil, macrophage, migration, imaging

INTRODUCTION

Myocardial infarction occurs when an atherosclerotic plaque ruptures and occludes a coronary artery, resulting in myocardial cell necrosis and loss of contractile function. Immune cells are subsequently recruited to the infarct where they play important roles during the repair process (Dewald et al., 2005; Nahrendorf et al., 2007; Horckmans et al., 2016). However, if not resolved in a timely fashion, this immune response can be detrimental to repair (Dewald et al., 2005; Ma et al., 2013). Therapeutic modulation of

the immune response may ameliorate adverse heart inflammation whilst retaining its benefits (Adamo et al., 2020). Such treatments have been shown to improve clinical outcomes following myocardial infarction, but at the expense of a higher risk of infection (Ridker et al., 2017; Tardif et al., 2019). This indicates a clear need to better understand the local and systemic mobilization of immune cells to cardiac injury.

The zebrafish is an invaluable animal model for the study of cardiac injury, repair and immune cell function (Lai et al., 2018). Unlike mammals, zebrafish hearts are highly regenerative, with adults able to fully regenerate up to a quarter of the myocardium in 60 days (Gonzalez-Rosa et al., 2011). Similarly, larval zebrafish are capable of complete heart regeneration within 2 days (Matrone et al., 2013, 2015). Larval zebrafish offer many unique advantages for live imaging as they are small, transparent and genetically tractable, permitting generation of transgenic lines with cell-specific fluorophores. Transgenic lines for two innate immune cells, the neutrophil and macrophage, allow the migration of both cell types to be examined following wounding (Barros-Becker et al., 2017; Rosowski, 2020). Our laboratory established a larval zebrafish model of cardiac injury that produces an accurate and reproducible laser injury at 3 days post fertilization (Matrone et al., 2013; Taylor et al., 2019). This model allows us to closely interrogate local and systemic neutrophil and macrophage responses *in vivo* following cardiac injury, a feat which is currently not possible in other models. Furthermore, it is not known if the immune cell migration sequence in larval zebrafish is consistent across injury models. By directly comparing the heart laser injury to that in the archetypal tail transection model, we seek to determine a conserved sequence of steps involved in immune cell migration to injury.

In this study we use our refined larval zebrafish laser injury model to examine the mobilization of neutrophils and macrophages to cardiac injury. Using a combination of imaging modalities and transgenic tools, we studied each stage of the immune response, starting with egress from hematopoietic tissue, to arrival at the injured myocardium and subsequent resolution of inflammation. We found the majority of both neutrophils and macrophages are recruited to the heart lesion locally and their numbers later resolved by reverse migration. Neutrophils and macrophages are recruited from distal sites and also mobilize into peripheral blood, using abluminal endothelial surfaces of lymphatic and blood vessels as migration highways. Finally, light sheet fluorescence microscopy (LSFM) timelapse imaging identified a novel wound-responsive neutrophil subset defined as *mpx*:GFP+ *mpeg1*:mCherry+, whose role will require further study. In addition to shedding light on previously unappreciated neutrophil heterogeneity, our work provides a multi-stage model of larval zebrafish immune cell migration following injury.

RESULTS

Heart Laser Injury Is Characterized by Localized Cardiomyocyte Cell Death

Our laboratory has previously used targeted laser ablation to injure specific regions of the 3 dpf larval zebrafish heart (**Figure 1A**; Matrone et al., 2013, 2014). We further optimized this approach to induce a localized injury at the ventricular apex of 3 dpf larvae (**Supplementary Figure 1-supplement 1**). Targeting this region increases reproducibility as it is anatomically unambiguous and minimizes the risk of heart rupture, thus avoiding the release of erythrocytes into the pericardium, which interferes with imaging. These refinements therefore provide a cardiac injury model that more closely mimics a human MI.

Immediately following laser injury, the myocardium at the apex swells and contraction diminishes (**Figure 1B**). Injured ventricles display a lack of contractility leading to a reduced ventricular ejection fraction compared to uninjured larvae at 2 h post injury (hpi) (**Figure 1C** and **Supplementary Video 1**). The injured region is marked by a loss of GFP signal in the cardiomyocyte reporter line *Tg(myl7:GFP)* (**Figure 1D** and **Supplementary Video 1**). Staining with propidium iodide (PI) shows this GFP negative region is necrosed myocardium (**Supplementary Figure 1-supplement 2A**). TUNEL staining of injured hearts at 2 hpi shows the GFP-negative border zone containing apoptotic cardiomyocytes (**Figure 1E**), which was corroborated using acridine orange staining (**Supplementary Figure 1-supplement 2B**). To further validate the injury response, we utilized the *Tg(myl7:mCherry;nfkb:GFP)* line to determine if NFkB, an important regulator of programmed cell death, is upregulated following heart injury, as reported in other animal models of MI (Tillmanns et al., 2006; Karra et al., 2015). We observed increased *nfkb* expression in cardiomyocytes bordering the ventricular lesion at 24 hpi (**Figure 1F**). This ring-like expression pattern (**Figure 1G**) mimicked TUNEL staining (**Figure 1E**), again supporting that laser-targeted cardiomyocytes undergo programmed cell death.

Neutrophils and Macrophages Are Recruited to the Cardiac Injury Site and Display Distinct Recruitment Dynamics

To characterize the recruitment of neutrophils and macrophages to the heart following laser injury we serially imaged *Tg(myl7:GFP;mpx:mCherry)* and *Tg(myl7:GFP;mpeg1:mCherry)* larvae respectively over a two-day period at 2, 6, 24, and 48 hpi using epifluorescence microscopy (**Figures 2A,B**). Following heart injury, neutrophil numbers on the ventricle increased from 2 hpi, peaked at 6 hpi (3.2 ± 0.4), and gradually resolved to uninjured levels at 48 hpi (0.6 ± 0.2) (**Figures 2A,C**). While macrophage numbers increased significantly from 6 hpi, cardiac macrophages aggregated at the lesion from 2 hpi (**Figure 2B**). Macrophage numbers remain elevated at 24 hpi (7.6 ± 0.7), decreasing but not returning to uninjured levels by 48 hpi (5.1 ± 0.4 vs 1.8 ± 0.3) (**Figures 2B,C**). Both neutrophils and macrophages localized primarily at the ventricular apex injury site (**Figures 2A,B** and **Supplementary Video 2**). We also observed neutrophils cyclically migrating around the injured heart, being propelled forwards with each cardiac contraction in real time (**Supplementary Video 3**).

We contextualized the findings of our heart injury model by comparing it to the well-characterized larval tail fin transection

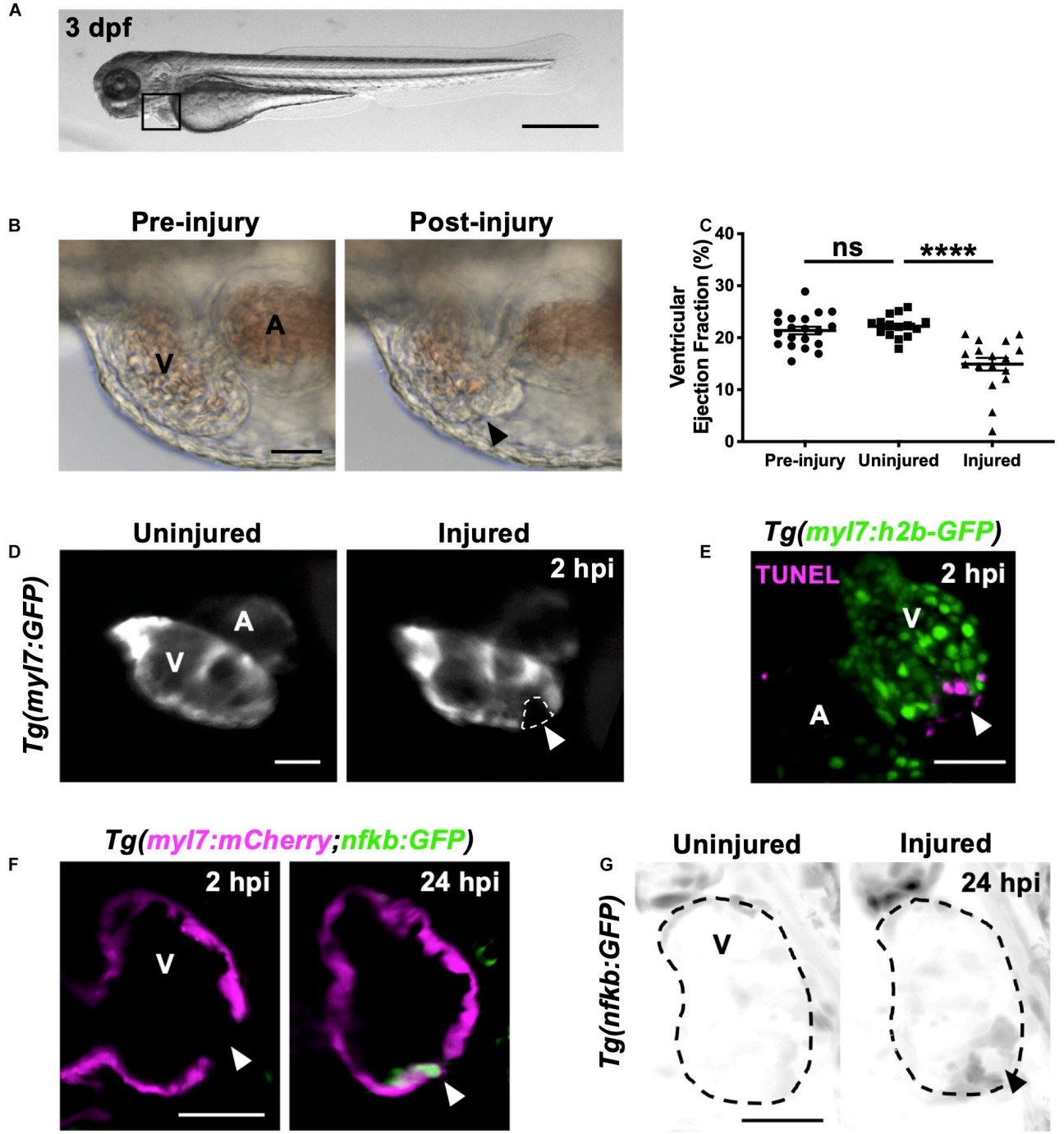

FIGURE 1 | Heart laser injury causes localized cardiomyocyte cell death. **(A)** Whole larva brightfield image of 3 dpf zebrafish with heart region indicated (black square), scale bar = 500 μm. **(B)** Brightfield images of a 3 dpf larval heart pre-laser injury (left) and 1-min post laser injury (right). The lesion is seen as a thickened and partially collapsed region at the ventricular apex (black arrowhead). **(C)** Ventricular ejection fraction before injury, and 2 hpi in injured and uninjured larvae. Error bars = SEM, n = 15–20 larvae, experimental n = 3. Unpaired t-test performed between groups where **** $p < 0.0001$. **(D)** Epifluorescence images of an uninjured and injured *Tg(myl7:GFP)* heart. Injury site is marked by a loss of myocardial GFP at the ventricular apex (white dashed line and arrowhead). **(E)** 3D LSFM image of a TUNEL stained injured *Tg(myl7:h2b-GFP)* heart at 2 hpi. Injury site is marked by a loss of nuclear myocardial GFP (white arrowhead) bordered by TUNEL positive cells (magenta). Image displayed as a maximum intensity projection (MIP). **(F)** LSFM single z-plane image of a *Tg(myl7:mCherry;nfkb:GFP)* ventricle at 2 and 24 hpi following heart injury. White arrowheads indicate loss of myocardial signal at 2 hpi and upregulation of *nfkb:GFP* in wound-bordering cardiomyocytes at 24 hpi. **(G)** 3D LSFM image of *Tg(nfkb:GFP)* ventricular expression at 24 hpi in uninjured and injured larvae (black arrowhead indicates ventricular apex injury site). Image displayed as a MIP (inverse color map). All scale bars = 50 μm unless stated otherwise. V, ventricle; A, atrium; ns, non-significant.

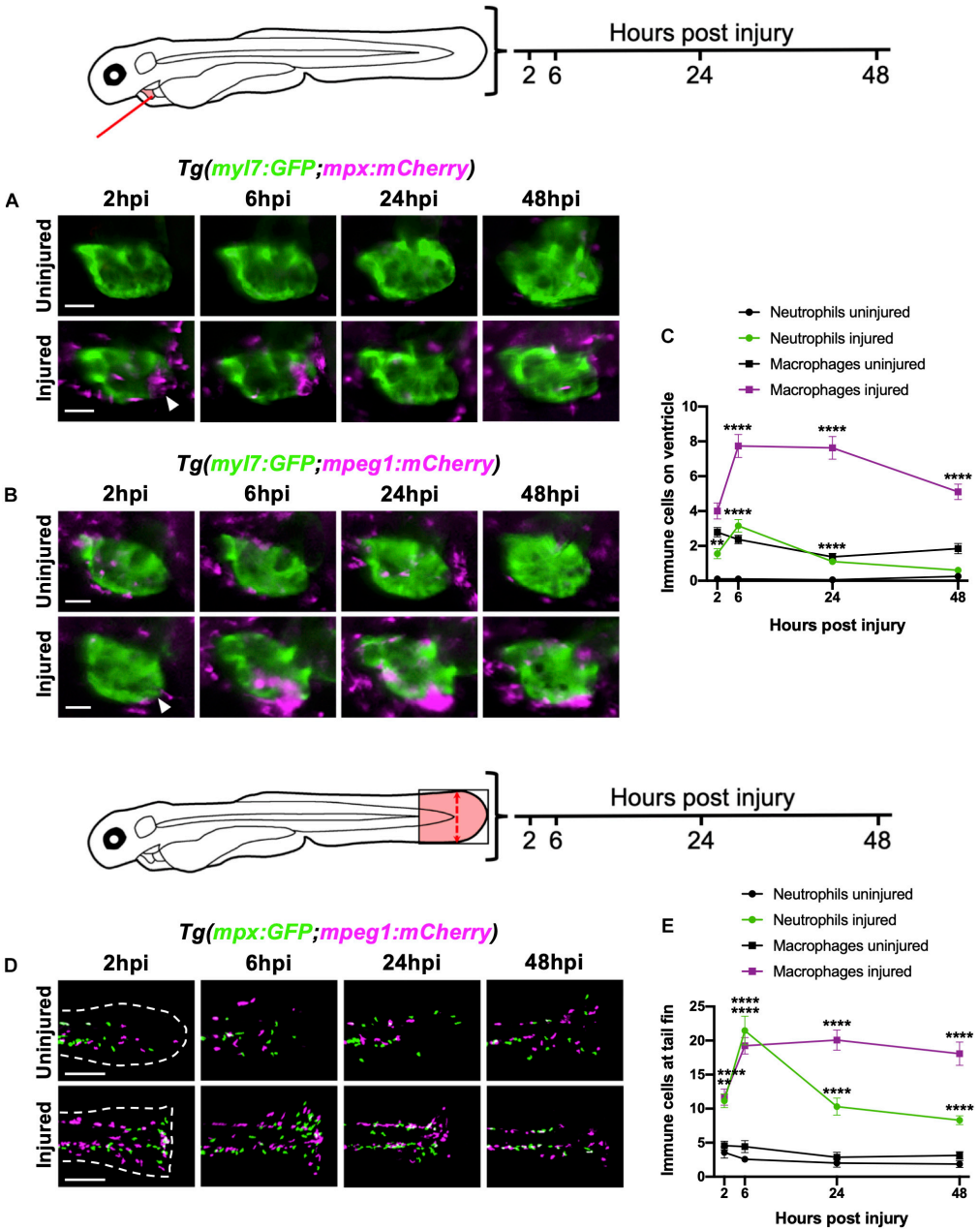

FIGURE 2 | Neutrophils and macrophages display distinct recruitment dynamics during heart injury comparable to tail fin injury. **(A)** Epifluorescence heart images of uninjured and injured *Tg(myl7:GFP;mpx:mCherry)* larvae displaying neutrophil accumulation at 2, 6, 24 and 48 hpi, scale bar = 50 μm. **(B)** Epifluorescence heart images of uninjured and injured *Tg(myl7:GFP;mpeg1:mCherry)* larvae displaying macrophage accumulation at 2, 6, 24 and 48 hpi, scale bar = 50 μm. Arrowheads indicate ventricular apex injury site. **(C)** Neutrophil and macrophage numbers on the ventricle at 2, 6, 24 and 48 hpi for uninjured and injured larvae. Error bars = SEM, n = 19 larvae, experimental n = 3. **(D)** Epifluorescence tail images of uninjured and injured *Tg(mpx:GFP;mpeg1:mCherry)* larvae displaying neutrophil (green) and macrophage (magenta) accumulation at the timepoints 2, 6, 24 and 48 hpi, scale bar = 60 μm. White dashed line indicates outline of tail fin. **(E)** Neutrophil and macrophage numbers at the tail fin at 2, 6, 24, and 48 hpi for uninjured and injured larvae. Error bars = SEM, n = 10 larvae for uninjured groups and n = 13 for transected groups, experimental n = 3. Two-way ANOVA and Sidak *post hoc* test performed for immune cell comparisons between uninjured and injured groups where ** $p < 0.001$, **** $p < 0.0001$. Immune cell counts were made from the region of interest (highlighted red) in the corresponding schematics.

model (Renshaw et al., 2006; Hoodless et al., 2016). Tail fins were transected at 3 dpf and immune cell recruitment quantified at the same timepoints. Similar immune cell dynamics were observed between both models, including a peak neutrophil response at 6 hpi that decreased at 24 hpi and 48 hpi, and a sustained macrophage response during 6–24 hpi, which decreased slightly by 48 hpi (**Figures 2D,E**). A notable difference between the two injury models was the magnitude of the immune response at

6 hpi, with a 7-fold increase in neutrophils and 2-fold increase in macrophages following tail transection. Additionally, tail inflammation resolved more slowly, with neutrophil numbers remaining relatively high at 48 hpi and macrophage numbers decreasing less steeply between 24 and 48 hpi (**Figure 2E**).

Heart Lesion Neutrophils and Macrophages Are Recruited From Both Local and Distal Immune Cell Reservoirs

To determine the origin of neutrophils and macrophages recruited to the heart following injury we used two photoconvertible lines *Tg(mpx:gal4;UAS:kaede)* and *Tg(csf1r:gal4;UAS:kaede)*, which allow spatiotemporal labeling of individual neutrophils and macrophages respectively (Holmes et al., 2012a). By choosing to convert the kaede fluorophore in specific regions of the larva, one can deduce at later timepoints, and in other tissues, whether any immune cells have originated from the converted region. We extended this technique by 'semi-converting' regions such that immune cells retain a roughly 1:1 ratio of unconverted and converted kaede, thus allowing assessment of the contribution of three regions simultaneously.

We divided each larva into three anatomical zones (1) head (proximal), (2) pericardium (local) and (3) trunk (distal) which were photoconverted fully, partially or left unconverted respectively. Cells were photoconverted one hour prior to injury and then imaged at 2 hpi and again at the peak immune response at 6 hpi (**Figure 3A**). At 2 hpi, the majority of both neutrophils and macrophages recruited to the heart were pericardial in origin (84 $\pm$ 6.9% and 82 $\pm$ 9.8% respectively), with a very small proportion originating from the head (10 $\pm$ 5.5% and 3.3 $\pm$ 3.3%, respectively) (**Figure 3B**). The most distal zone (the trunk) contributed very few neutrophils at 2 hpi, however a substantial proportion of heart recruited macrophages originated from the trunk (15 $\pm$ 7.6%). Later at 6hpi, we observed an increase in the proportion of trunk-derived neutrophils and macrophages (33 $\pm$ 7.7% and 29 $\pm$ 9.5%, respectively). Indeed, the absolute number of pericardium-derived immune cells did not increase at 6 hpi, and the overall increase in numbers for each cell type was largely due to the arrival of trunk-derived immune cells (**Supplementary Figure 3-supplement 1A**). Finally, whilst the proportion of neutrophils originating from the head remained low at 6 hpi, a substantial proportion of the peak macrophage response was head-derived (23 $\pm$ 9.9%, **Figure 3B**).

Heart Lesion Neutrophils and Macrophages Resolve by Local Dispersal

Wounding studies in larval zebrafish have previously shown that neutrophils primarily undergo reverse migration to resolve their numbers (Mathias et al., 2006; Holmes et al., 2012a,b; Ellett et al., 2015). To test the hypothesis that reverse migration contributes to resolution of immune cell numbers following heart injury, we again utilized photoconvertible lines *Tg(mpx:gal4;UAS:kaede)* and *Tg(csf1r:gal4;UAS:kaede)*. In this experiment, immune cells in the pericardial region were photoconverted at the peak response at 6 hpi. Larvae were subsequently re-imaged at 24 hpi to assess the location of any neutrophils or macrophages that may have reverse migrated from the injury (**Figure 3C**). Summarized by the heatmaps in **Figure 3D**, neutrophils can be seen to disperse in a posterior and dorsal direction away from the injury. In contrast, macrophages appear to disperse more evenly in all directions. Interestingly, neither cell type moves more than approximately 300 μm from the pericardial region despite our previous analysis demonstrating they can migrate much greater distances over a shorter timeframe during recruitment (**Figure 3B**). Notably, neither cell type reverse-migrates to any particular organ. Following tail resection, LSFM timelapse imaging suggests that a small number of neutrophils and macrophages undergo cell death at the wound (n = 6 timelapses up to 24 hpi) (**Supplementary Videos 4, 5**). However, only immune cell reverse migration was observed following heart injury (n = 12 timelapses up to 24 hpi).

Cxcr1/2 Is Required for Neutrophil Migration to the Lasered Heart

Following the discovery that both neutrophils and macrophages attend the heart lesion from local and distal sites, we posited that there are chemokine attractants coordinating this response. The best characterized of these chemokines in zebrafish is the Cxcl8-Cxcr1/2 axis, which is required for neutrophil mobility (Deng et al., 2013; Powell et al., 2017; Zuñiga-Traslaviña et al., 2017). We first validated a well-characterized Cxcr1/2 antagonist SB225002 following tail transection and confirmed that it decreased the peak neutrophil response but did not affect macrophage recruitment (**Supplementary Figures 3-supplement 1C,D**). To determine if Cxcr1/2 is involved in neutrophil or macrophage recruitment to the heart, we performed the same experiment in our heart injury model. The Cxcr1/2 antagonist decreased both neutrophil and macrophage presence at the heart lesion (**Figure 3E**). The neutrophil response to injury appeared entirely abolished (**Figure 3F**). Interestingly, macrophage dynamics were unaffected by the drug up until 6 hpi, but significantly decreased at 24 hpi and 48 hpi (**Figure 3G**). These later timepoints are when macrophages recruited from distal sites would normally reach the heart (**Figure 3B**), suggesting these immune cells are migrating to the injury site via the action of chemokine attractants.

Macrophages and Neutrophils Are Mobilized From the Caudal Hematopoietic Tissue Following Heart and Tail Fin Injury

Having established that a significant proportion of late-recruited immune cells are from the distal trunk region, we next tested if heart injury was able to mobilize the cells specifically from the caudal hematopoietic tissue (CHT). The CHT is the predominant source of immune cells in the trunk and is known to contribute to wound neutrophil numbers following tail fin injury (Yoo and Huttenlocher, 2011).

First, we sought to verify whether the tail fin injury, which recruits many more immune cells than our heart injury, was capable of inducing CHT emptying of immune cells. Comparison of the CHT in uninjured controls and tail transected

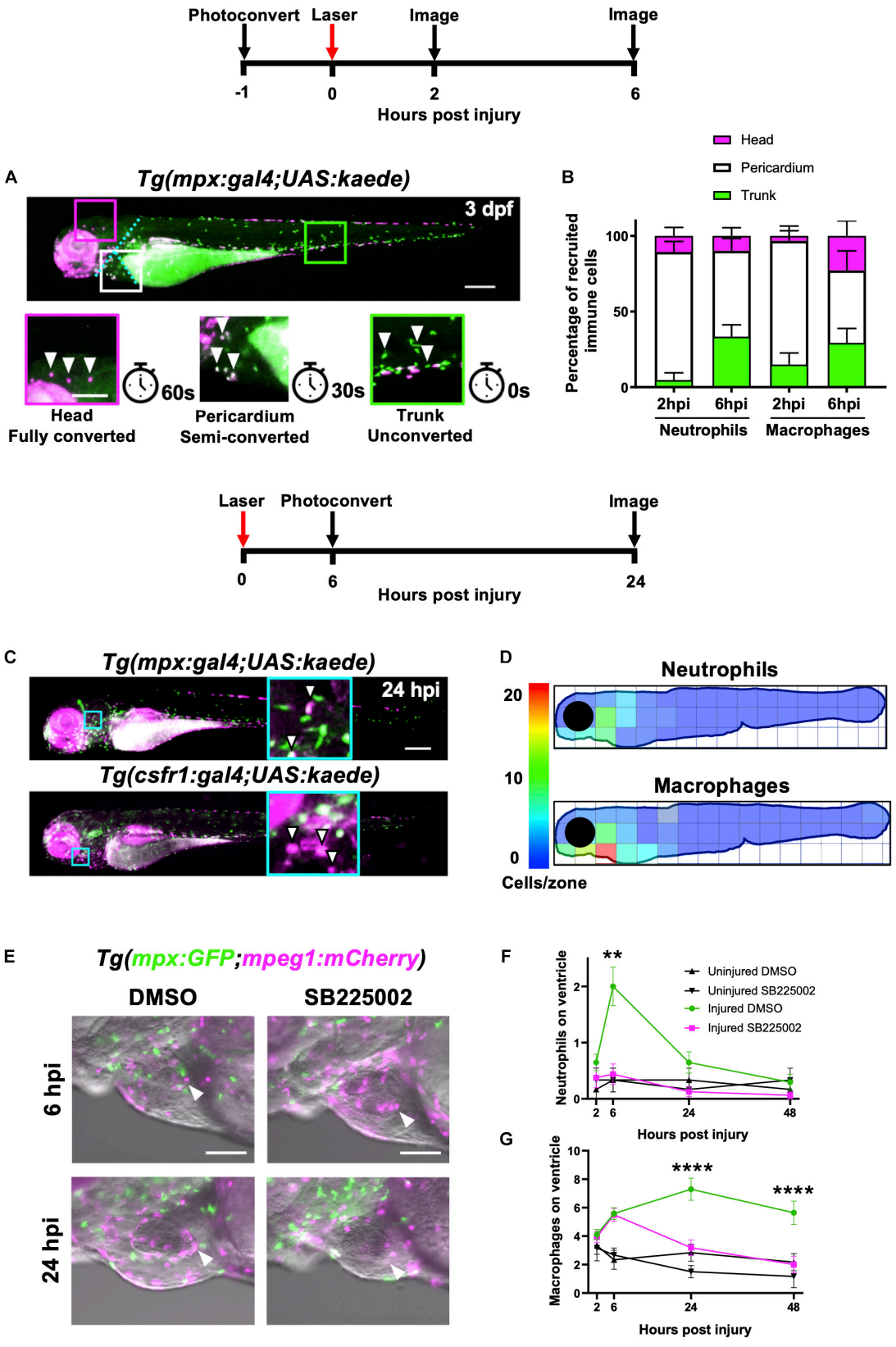

FIGURE 3 | Continued

FIGURE 3 | Heart injury recruits local immune cells from the pericardium and head but also cells from distal immune reservoirs. **(A)** Outline of experimental timeline to trace recruited immune cell tissue-origins. Whole body image of a *Tg(mpx:gal4;UAS:kaede)* larva where green cells, unconverted kaede; white cells (magenta and green), semi-converted kaede; and magenta cells, fully converted kaede. The larva is partitioned into three conversion areas marked by the cyan dotted line. Photoconversion of each area was achieved using a mercury lamp. Selected regions (boxes) within the three conversion areas are magnified in the lower panels along with the light exposure time for each level of conversion. White arrowheads, cells from each photoconverted region. Pigment in the eye and peripheries of the trunk autofluorescence magenta but are distinguishable from photoconverted cells because they are immobile. Upper panel scale bar = 200 μm and lower panel scale bar = 100 μm. **(B)** Percentage tissue origin of neutrophils and macrophages recruited to the injured ventricle at 2 and 6 hpi. Error bars = SEM, n = 11–21 larvae, experimental n = 3. **(C)** Outline of experimental timeline to trace immune cell reverse migration dispersal following heart injury. Whole body image of pericardially photoconverted *Tg(mpx:gal4;UAS:kaede)* (top panel) and *Tg(csf1r:gal4;UAS:kaede)* (bottom panel). Examples of converted cells (white arrow heads) are shown in magnified panels (cyan). Unconverted kaede (green), converted kaede (magenta), arrowheads, examples of converted cells, scale bar = 200 μm. **(D)** Heatmap of a 24 hpi larvae summarizing the dispersal of photoconversion-tracked neutrophils (top panel) and macrophages (bottom panel) following heart injury. Individual zone size = 31000 μm^2 and mean cell count normalized per zone, n = 17. **(E)** Epifluorescence images overlaid on a brightfield image showing neutrophil and macrophage numbers following laser heart injury in *Tg(mpx:GFP;mpeg1:mCherry)* larvae treated with Cxcr1/2 antagonist SB225002 (5 μM) or DMSO (0.1%) vehicle. Arrowheads, ventricular apex injury site. Scale bar = 100 μm. **(F)** Neutrophil numbers on the ventricle following laser injury in *Tg(mpx:GFP;mpeg1:mCherry)* larvae treated with Cxcr1/2 antagonist SB225002 (5 μM) or DMSO (0.1%) vehicle. **(G)** Macrophage numbers on the ventricle following laser injury in *Tg(mpx:GFP;mpeg1:mCherry)* larvae treated with Cxcr1/2 antagonist SB225002 (5 μM) or DMSO (0.1%) vehicle. Two-way ANOVA and Tukey *post hoc* test performed for immune cell comparisons between injured SB225002-treated and injured DMSO vehicle-treated larvae where ** $p < 0.01$ and **** $p < 0.0001$. Error bars = SEM, n = 17 larvae, experimental n = 3.

Tg(mpx:GFP;mpeg1:mCherry) larvae highlighted a reduction in the number of macrophages and neutrophils following injury (**Figure 4A**). The CHT depleted of neutrophils from 6–24 hpi, replenishing by 48 hpi. Macrophage CHT depletion was detected at 24 hpi and did not recover by 48 hpi (**Figure 4C**). Unlike tail injury, heart injury did not appear to stimulate a detectable decrease in the presence of CHT neutrophils (**Figures 4B,D**). However, heart injury caused a decrease in macrophage CHT presence at 24 and 48 hpi (**Figures 4B,D**), suggesting that macrophages migrate out of the CHT following heart injury.

Neutrophils Are Mobilized Into Peripheral Blood Following Heart and Tail Fin Injury

In response to cardiac and skin wounds, mammalian neutrophils and monocytes mobilize into the circulatory system in order to rapidly arrive at the site of injury (Anderson and Anderson, 1976). We tested if immune cells circulate in peripheral blood following heart injury, as this has been observed following tail transection (Zuñiga-Traslaviña et al., 2017).

Live epifluorescence imaging allowed us to easily observe and quantify the number of circulating neutrophils and macrophages following either tail or heart injury using the *Tg(mpx:GFP;mpeg1:mCherry)* line. Whilst there were almost no circulating macrophages or neutrophils during uninjured conditions, an increased number of both cell types were detected in circulation following tail transection at 6 hpi (4.3 ± 0.9 and 11.4 ± 2.7, respectively) (**Figure 4E**). Neutrophils were detected in the blood at 2 and 6 hpi whilst macrophages were only detected at 6 hpi. Similarly, we detected a number of neutrophils in the circulation of heart injured larvae, albeit fewer than in tail transected larvae (3.3 ± 0.9 vs 11.4 ± 2.7) (**Figure 4F**). In both injury models we observed trans-endothelial migration of neutrophils from the CHT into the cardinal vein, where they became spherical and began to roll or flow freely in the blood stream (**Supplementary Video 6**). We also observed rolling and egress of macrophages from the CHT following tail transection (**Supplementary Video 7**). Although we measured a reduction in CHT macrophages following heart injury, and acquired images of macrophages exiting the CHT into the cardinal vein (CV), there was not a statistically significant increase in circulatory macrophages at any time point (**Figure 4F**).

Neutrophils and Macrophages Use Vessels as Routes to Tail and Heart Injuries

Having shown that increased macrophage numbers at the heart lesion from 6 hpi were not accompanied by increased circulating macrophages, we next sought to determine if there were other routes and modes of immune cell migration from distal tissues.

Likely candidates were lymphatic vessels and peri-vascular surfaces, as these are known to be rich in adherent proteins and represent a ready-made transport network through the trunk musculature of the larva (von Andrian et al., 1993). To image both vascular and lymphatic networks in the same larva, we crossed two endothelial reporter lines to give *Tg(fli1:eGFP;kdrl:mCherry)* and injected high molecular weight blue fluorescent dextran to visualize any unmarked vessels and fluid spaces (**Figure 5A**). The vessels, known to run anteriorly posteriorly and ventrally dorsally, were indeed marked by all three of these labels. The anterior-posterior orientated vessels are the dorsal lateral anastomotic vessel (DLAV), dorsal aorta (DA) and CV, whilst the only ventro-dorsal vessels are the intersegmental vessels (ISV) that pattern the length of the larva (Isogai et al., 2001). Additionally, there are parachordal lymphatics (PCL) positioned parallel to the larval notochord (**Figure 5A**), as reported previously (Jung et al., 2017).

We injected high molecular weight dextran into *Tg(mpx:GFP;mpeg1:mCherry)* larvae to visualize all vessels and performed whole larva epifluorescence timelapse imaging. This facilitated simultaneous observation of all neutrophils and macrophages and directly confirmed their migration patterns through the trunk musculature for both injury models (**Supplementary Video 8**). In steady state, neutrophil presence outside the CHT was rarely observed and only macrophages were seen patrolling the musculature (**Figure 5B**). Temporal maximum intensity projections derived from superimposed epifluorescence images in uninjured larvae show neutrophils

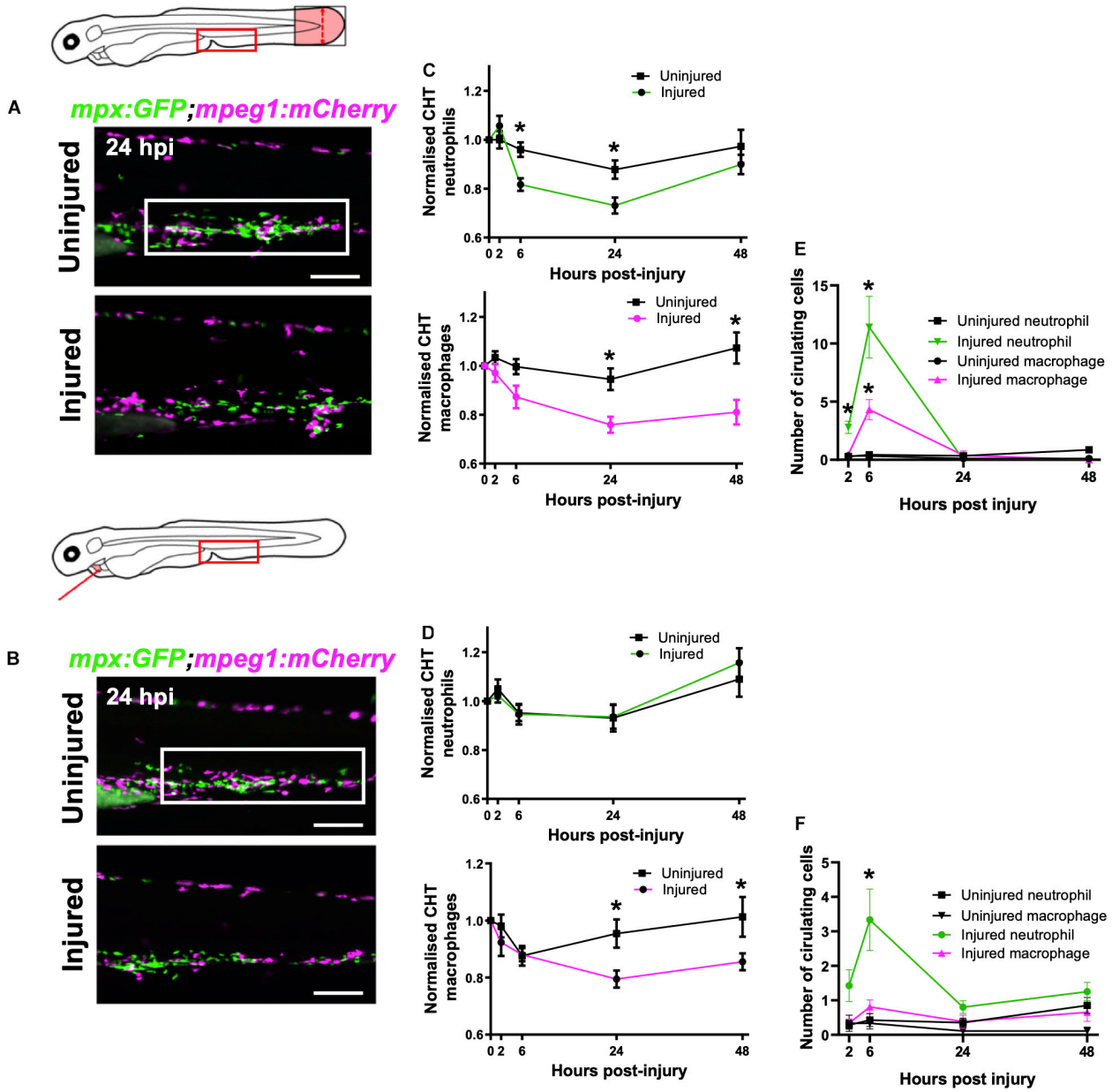

FIGURE 4 | Macrophages are mobilized from the CHT and neutrophils are mobilized into peripheral blood following tail and heart injury. **(A,B)** Epifluorescence images of *Tg(mpx:GFP;mpeg1:mCherry)* larval caudal hematopoietic tissue (CHT) at 24 hpi (macrophages, magenta and neutrophils, green) following tail transection **(A)** and laser heart injury **(B)**. White boxes, area of quantification. Scale bar = 200 μm. **(C,D)** Total CHT neutrophil and macrophage cell area based on normalized fluorescence using *Tg(mpx:GFP;mpeg1:mCherry)* larvae, n = 19 larvae, experimental n = 3. Values at each timepoint, cell type (neutrophil and macrophage) and injury model (heart laser and tail transection) are indicated. **(E)** Numbers of neutrophils and macrophages in the circulatory system following tail transection, n = 16 larvae, experimental n = 3. **(F)** Numbers of neutrophils and macrophages in the circulatory system following heart laser injury, n = 16 larvae, experimental n = 3. For all graphs, error bars, SEM and comparisons between uninjured, transected or laser injured groups was performed by Two-way ANOVA followed by Sidaks multiple comparison test where * $p < 0.05$.

and macrophages largely restricted to the CHT and head regions (**Figure 5C**).

Tail fin transection resulted in marked mobilization of macrophages and neutrophils from the CHT (**Figure 5C**). While the CHT of uninjured larvae appears as an intense white region of macrophage and neutrophil co-localization, transected larvae have neutrophils liberated dorsally and ventrally and migrating toward the tail transection. Quantification of vessel usage show that both cell types predominantly use the CV for migration in both uninjured and tail transection settings (**Figure 5D** and **Supplementary Figure 5-supplement 1B**). Neutrophils increase their use of PCL and the DA following injury to reach the

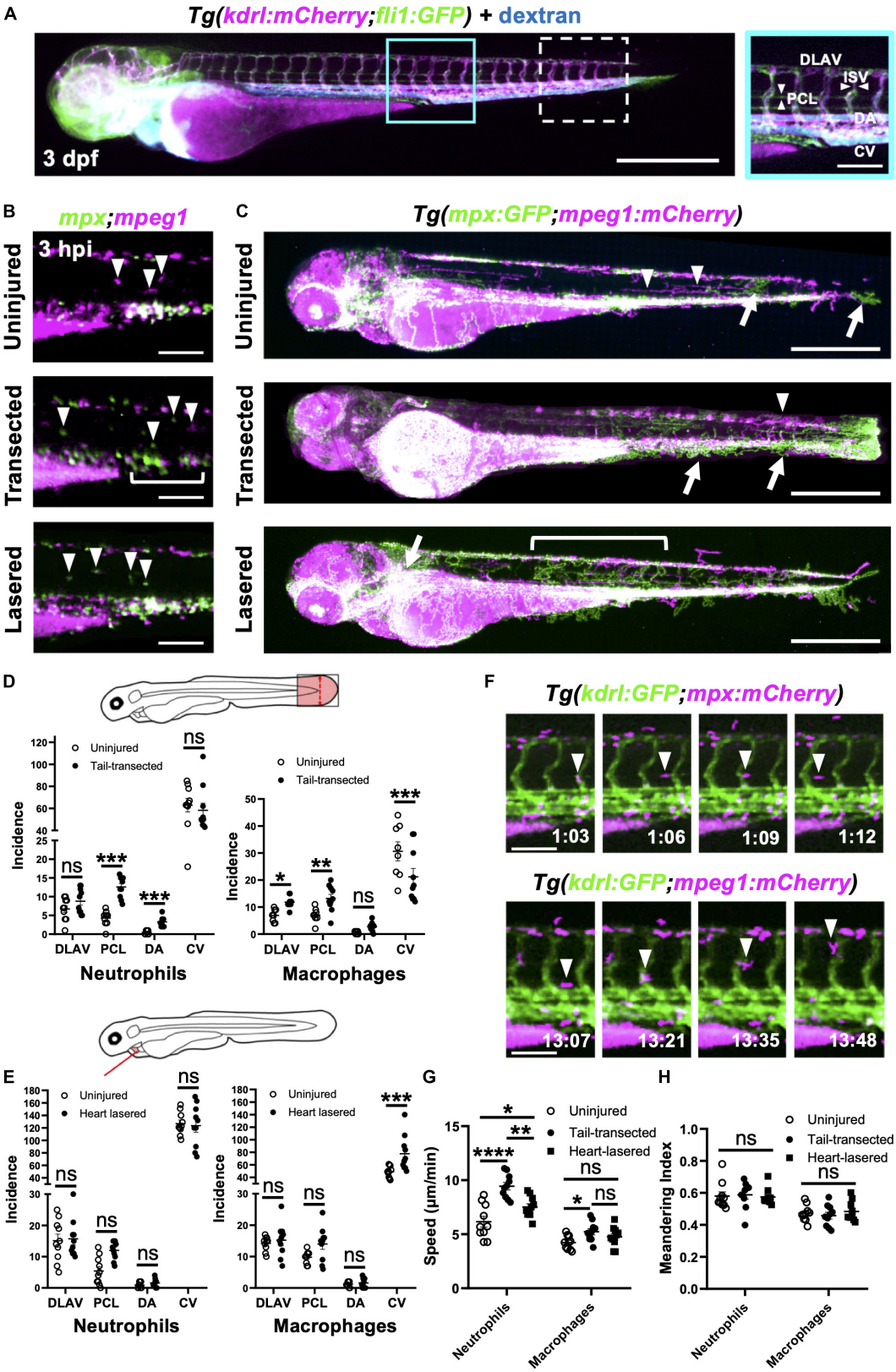

FIGURE 5 | Continued

FIGURE 5 | Neutrophils and macrophages utilize blood and lymphatic vessel surfaces for migration following injury. **(A)** Epifluorescence image of a 3dpf *Tg(kdrl:mCherry;fli1:eGFP)* whole larva injected with blue fluorescent 500 kDa dextran highlighting the entire cardiovascular network. Cyan box, region used for quantification for **(D)**, which is magnified in the right panel. White dashed box = region used for quantification for **(E)**. The right panel (**A** magnified) is annotated with vessels monitored for subsequent route use analysis. Left panel scale bar = 500 μm and the right panel scale bar = 100 μm. **(B)** Epifluorescence images of the peri-cloaca trunk region of *Tg(mpx:GFP;mpeg1:mCherry)* larvae at 3 hpi in uninjured, tail transected and heart lasered larvae. Neutrophils, green and macrophages, magenta. White bracket indicates a partially emptied CHT and white arrowheads CHT-liberated neutrophils and macrophages. Scale bar = 100 μm. **(C)** Epifluorescence images superimposed over 4–8 hpi to generate neutrophil (green) and macrophage (magenta) pseudotracks in whole *Tg(mpx:GFP;mpeg1:mCherry)* uninjured, tail transected and heart lasered larvae. White arrowheads highlight representative macrophage tracks, white arrows highlight representative neutrophil tracks and the white bracket highlights a region of neutrophil ventro-dorsal migration. Scale bar = 500 μm. **(D,E)** Incidence of vessel use by neutrophils or macrophages in larvae between 1–12 hpi following tail transection **(D)** or laser heart injury **(E)**. Injured groups were compared to uninjured groups using multiple *t*-tests with subsequent FDR correction using two stage step-up of Benjamini, Kreiger and Yekutieli, where $*p < 0.05$, $**p < 0.01$, and $*** p < 0.001$, $n = 10$ larvae analyzed per group. **(F)** Epifluorescence image sequence from heart lasered larvae showing a neutrophil migrating along the PCL (top) and a macrophage migrating up an ISV (bottom). Hours post injury as indicated. Scale bar = 100 μm. Neutrophil and macrophage speed **(G)** and meandering index **(H)** across the trunk 1.5–8 hpi in tail transected, heart lasered or uninjured larvae. Comparisons between groups were carried out using one-way ANOVA followed by Sidak-Holm multiple comparison test where $* p < 0.05$, $** p < 0.01$ and $**** p < 0.0001$, $n = 10$ larvae analyzed per group. Error bars for all graphs, SEM; Ns, non-significant; DLAV, dorsal lateral anastomotic vessel; PCL, parachordal lymphatic; DA, dorsal aorta; ISV, intersegmental vessels; and CV, cardinal vein.

tail wound. In contrast, macrophages take a more dorsal route, increasing their use of the PCL and the DLAV (**Figures 5C,D** and **Supplementary Video 8**).

Following heart injury, we observed more anterior-directed immune cell migration than in tail transected larvae (**Figure 5C**). In contrast to tail transection, macrophages begin to increase their use of the CV, taking a ventral route to the heart, occasionally using other vessels and the yolk sac (**Figures 5C,E**). Interestingly, neutrophils did not significantly increase their use of anterior-posterior oriented vessels in our quantification area (**Figure 5E** and **Supplementary Figure 5-supplement 1B**). Analysis of pseudotracks revealed this is because, following egress from the anterior pole of the CHT, neutrophils move dorsally via ISVs. It is only after that we observed neutrophils moving anteriorly via the DLAV and then through the perinephric region to the heart (**Figure 5C** and **Supplementary Video 8**). Close inspection of timelapses revealed that both macrophages and neutrophils migrate along the abluminal surface of vessels rather than inside them (**Figure 5F**).

In addition to vessel usage, we tested if other aspects of immune cell motility changed following injury, namely meandering and speed. Although macrophage speed only increased after tail transection, neutrophils significantly increase their speed following tail transection and to a lesser extent following heart injury (**Figure 5G** and **Supplementary Figure 5-supplement 1A**). Meandering index (MI) was unchanged for both cell types and in both injury settings (**Figure 5H**), indicating the increase in neutrophil speed is not an artifact of directionality. Taken together our data confirm that immune cells indeed use vessels as routes of migration and that there are unique patterns of use for each cell type and injury setting.

Neutrophils and Macrophages Migrate Onto the Heart via the Pericardium and Adopt Specific Migratory Behaviors Once at the Injury Site

Having shown that most neutrophils and macrophages are recruited to the heart locally (**Figures 3A,B**), we next wanted to identify how these cells migrate to the ventricle at a local scale. We used our optical gating system coupled with LSFM to acquire computationally frozen high-resolution 3D images of the beating heart (Taylor et al., 2011, 2012, 2019). We injected *Tg(kdrl:mCherry)* larvae intravenously with fluorescent dextran and applied our heartbeat-synchronized imaging to search for existing lymphatic or coronary vessels that could play a role in guiding immune cells to the injury site. We did not find the heart to have any supporting lymphatics or coronary vessels, only a thin layer of endocardium (**Figures 6A,B**). We next utilized the pan-chromatin *Tg(h2a:GFP)* line which labels all nuclei to visualize the whole pericardium. Analysis of 3D fluorescence image stacks by surface rendering confirmed no other cellular structures or routes between the pericardium and heart (**Figure 6C**).

We next performed heartbeat-synchronized imaging in injured *Tg(kdrl:mCherry;mpeg1:mCherry;mpx:GFP;h2a:GFP)* larvae, allowing neutrophil and macrophage chemotaxis to be tracked in 3D over several hours (Taylor et al., 2019). Timelapse imaging revealed that both cell types patrol the pericardium, with the majority of tracks concentrated around the bulbous arteriosus (**Figure 6D** and **Supplementary Video 9**). Tracking analysis also revealed that neutrophils and macrophages migrate to the injury site via adjacent points on the pericardial wall, typically on the ventricular side (**Figure 6D** and **Supplementary Video 9**).

To improve our understanding of neutrophil and macrophage behavior specifically at the heart lesion, we acquired 3D timelapse videos of *Tg(myl7:GFP;mpx:mCherry)* (**Figure 6E**) and *Tg(myl7:GFP;mpeg1:mCherry)* (**Figure 6F**) larvae up to 24 hpi. These timelapse videos demonstrated neutrophil wound swarming and macrophage accumulation at the wound, followed by reverse migration of both cell types (**Supplementary Videos 10, 11**). Quantification of individual cell behavior revealed that neutrophils migrated faster on the ventricle compared to macrophages following injury (4.3 ± 0.2 μm/min vs 2.1 ± 0.2 μm/min) and in uninjured larvae (4.1 ± 0.3 μm/min vs 2.4 ± 0.2 μm/min) (**Figure 6G**). However, neutrophil and macrophage speed following injury was no different to uninjured larvae (**Figure 6G**). Both neutrophils and macrophages reside on the ventricle for significantly longer periods of time following injury (**Supplementary Figure 6-supplement 1**). The duration of individual macrophage residency on the ventricle is 3-fold higher than neutrophils following injury (545 ± 28 min vs 178 ± 37 min) (**Supplementary Figure 6-supplement 1**). The speed and

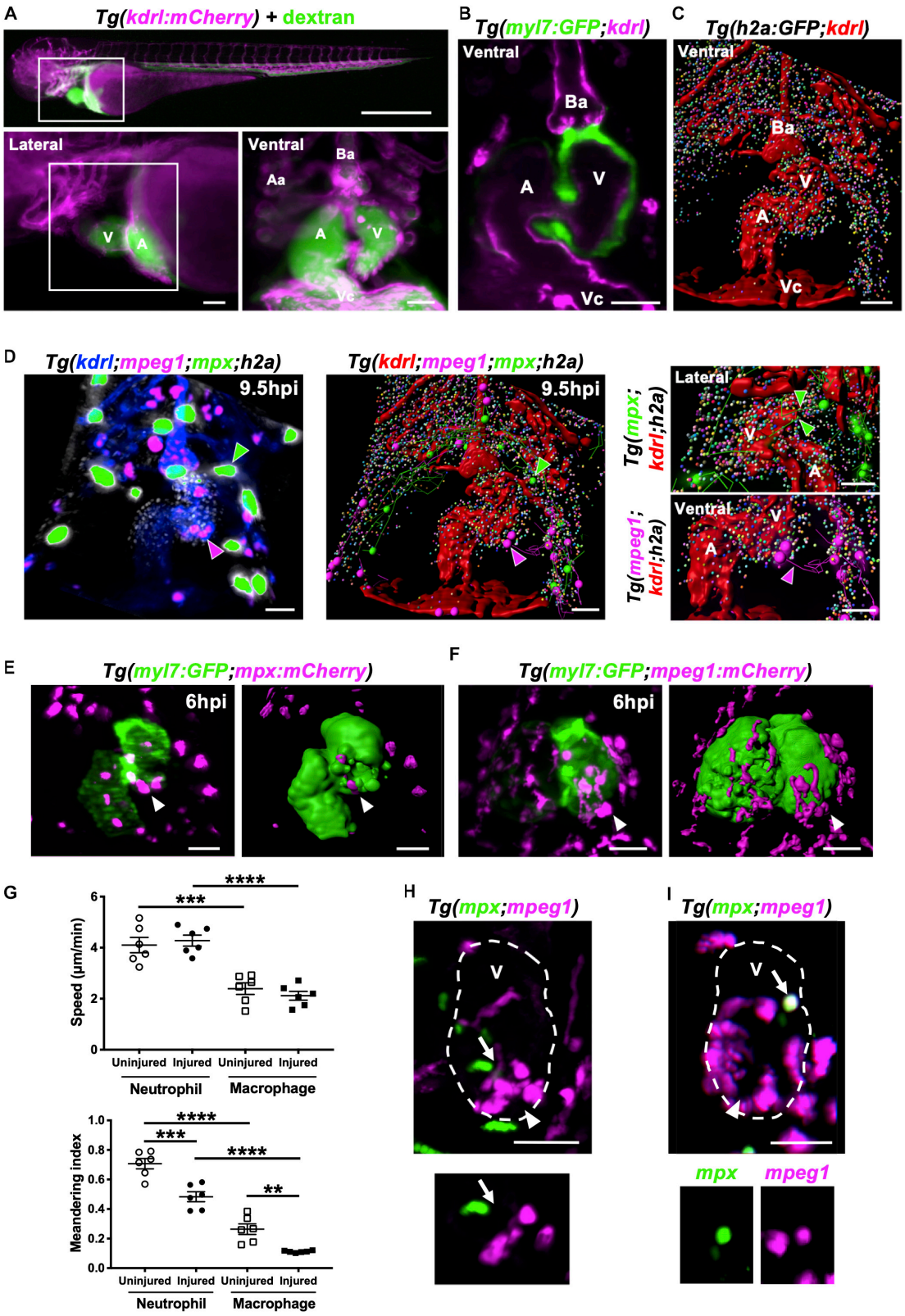

FIGURE 6 | Continued

FIGURE 6 | Neutrophils and macrophages migrate onto the ventricle via the pericardium and adopt specific migratory behaviors once on the ventricle following injury. **(A)** Epifluorescence image of *Tg(kdrl:mCherry)* larva injected with blue fluorescent 500 kDa dextran (colored green) to analyze the surrounding pericardium for vasculature (white box). Scale bar = 500 μm (top). Magnified epifluorescence image of the surrounding pericardium where white box indicates the nearby heart region (lower left). Magnified 3D LSFM image displaying the hearts vasculature (magenta) containing fluorescent dextran (green) (lower right). **(B)** LSFM *z*-plane of *Tg(myl7:GFP;kdrl:mCherry)* larva displaying the hearts myocardium and endothelium. **(C)** Surface rendered LSFM *z*-stack of *Tg(h2a:GFP;kdrl:mCherry)* larva displaying the hearts vasculature and surrounding pericardium. **(D)** LSFM fluorescence z-stack differentially color-labeled (left) and surface rendered z-stack (middle and right) of *Tg(kdrl:mCherry;mpeg1:mCherry;mpx:GFP;h2a:GFP)* larva displaying the heart vasculature (blue or red), pericardium (gray or multi-colored), neutrophils (green) and macrophages (magenta) at 9.5 hpi. Magnified view of neutrophil (right top) and macrophage (right bottom) tracks onto the ventricle. Green and magenta arrowheads indicate neutrophils and macrophages tracked to the ventricle respectively for 30 min from 9.5 hpi. **(E)** LSFM image (left) and surface render (right) of a *Tg(myl7:GFP;mpx:mCherry)* injured heart and recruited neutrophils at 6 hpi. **(F)** LSFM image (left) and surface render (right) of a *Tg(myl7:GFP;mpeg1:mCherry)* injured heart and recruited macrophages at 6 hpi. White arrowheads indicate recruited immune cells on the lesioned myocardium. **(G)** Ventricular recruited neutrophil and macrophage speed (top) and meandering index (distance traveled/displacement) (bottom) in heart lasered and uninjured larvae. Average cell behaviors are plotted per larva, $n = 5$ cells tracked per larva and $n = 6$ larvae per group. Error bars, SEM. One-way ANOVA and Tukey *post hoc* test performed for comparisons between mean behavioral values for each larva where $^{**}p < 0.01$, $^{***}p < 0.001$, and $^{****}p < 0.0001$. **(H)** LSFM image of a *Tg(mpx:GFP;mpeg1:mCherry)* injured ventricle displaying neutrophils and macrophages at 10 hpi. Arrow indicates a neutrophil and macrophage near the wound (top). LSFM *z*-plane image of the indicated neutrophil and macrophage. Arrow indicated at the same position (bottom). **(I)** LSFM image of a *Tg(mpx:GFP;mpeg1:mCherry)* injured ventricle displaying neutrophils and macrophages at 18 hpi. Arrow indicates a cell co-expressing *mpx:GFP* and *mpeg:mCherry* on the wounded ventricle (top and bottom). Arrowheads indicate the injury site. Outline of ventricle is indicated with a dashed line. All fluorescence images were acquired in 3D using LSFM and displayed as MIPs unless stated otherwise. All scale bar = 50 μm, unless stated otherwise. Ba, bulbus arteriosus; Aa, aortic arches; V, ventricle; A, atrium; Vc, venous cavernous.

duration in part explain the turnover of immune cells on the ventricle and therefore contribute to the overall recruitment dynamics following injury (**Figure 2**). Furthermore, neutrophils and macrophages recruited to the ventricle displayed greater meandering behavior following injury compared to uninjured larvae (0.48 ± 0.03 MI vs 0.71 ± 0.04 MI and 0.11 ± 0.003 MI vs 0.26 ± 0.04 MI). Additionally, macrophages were more meandering than neutrophils following injury (0.11 ± 0.003 MI vs 0.48 ± 0.03 MI) (**Figure 6G**). Taken together, these data demonstrate that both immune cells have distinct behavioral characteristics which become altered following heart injury.

Heartbeat-Synchronized LSFM Imaging of Neutrophils and Macrophages Following Injury Reveals an *mpx*:GFP+ *mpeg1*:mCherry+ Cell Population

We next tested if there were neutrophil-macrophage interactions on the heart following injury, such as macrophage efferocytosis of neutrophils as previously observed in other injury models (Meszaros et al., 1999; Ellett et al., 2011). LSFM timelapse experiments ($n = 6$ up to 24 hpi) using *Tg(mpx:GFP;mpeg1:mCherry)* larvae did not show any notable neutrophil-macrophage interactions on the heart (**Figure 6H** and **Supplementary Video 12**). Interestingly, we identified immune cells that were co-expressing the transgenes *mpx:*GFP and *mpeg1*:mCherry (**Figure 6I**). This observation prompted us to investigate these co-positive cells further as neutrophils are generally thought to be a homogenous cell type.

mpx:GFP+ *mpeg1*:mCherry+ Cells Are Neutrophils and Not Macrophages

We observed cells expressing both *mpx:*GFP and *mpeg1*:mCherry at and around the injured heart using both LSFM timelapse and epifluorescence microscopy (**Figure 7A**). This subset of cells represents 2.3 ± 1.0% of *mpx*:GFP+ or *mpeg1*:mCherry+ cells on the injured ventricle (**Figure 7B**). Co-positive cells are observed more frequently at tail transection wounds (**Figure 7C** and **Supplementary Figure 7-supplement 1A**), where they make up a much higher proportion of cells 14.4 ± 2.2% (**Figure 7D**). Hence, herein we chose the tail transection model to characterize the nature of these cells.

An important question is whether these cells are neutrophils or macrophages We first found indirect evidence that co-positive cells might be neutrophils through comparison with a similar reporter line with different versions of the same transgene *Tg(mpx:mCherry;mpeg1:GFP)*. Using this combination of transgenes, we observed very low numbers of wound-associated co-positive cells (1.9 ± 1.6%) (**Figure 7D**). Comparisons of the proportions of each cell type between these transgenic lines showed that whilst macrophage proportions were very similar between lines, the co-positive cell population observed in *Tg(mpx:GFP;mpeg1:mcherry)* arises at the expense of its neutrophil population. Likewise, it follows that some *mpeg1-mpx+* cells observed in *Tg(mpx:mCherry;mpeg1:GFP),* might be this same population of co-positive cells, albeit unmarked in this line.

Next, we assessed if co-positive cells were *csf1r+*, a gene not expressed in neutrophils and required for macrophage development (Sweet and Hume, 2003; Chitu and Stanley, 2006). Using *Tg(csf1r:gal4;UAS:mCherry-NTR;mpx:GFP)* larvae, we showed no co-expression of *mpx*:GFP and *csf1r*:mCherry-NTR in recruited cells following tail transection (**Figures 7E,F**). We can therefore deduce that co-positive cells also do not express *csf1r*, again suggesting that co-positive cells are more neutrophil-like in their fluorophore markers. Finally, we utilized our finding that the pharmacological Cxcr1/2 antagonist (SB225002) inhibits the recruitment of neutrophils but not macrophages following tail transection specifically (**Supplementary Figures 3-supplement 1C,D**). We reasoned that if co-positive cells were neutrophils then SB225002 should decrease their number at the wound but not if they are macrophages. Tail transected larvae treated with SB225002 did indeed exhibit decreased numbers of co-positive recruited cells at the wound, again suggesting that the co-positive cells are likely neutrophils (**Figure 7G** and **Supplementary Figure 7-supplement 1B**).

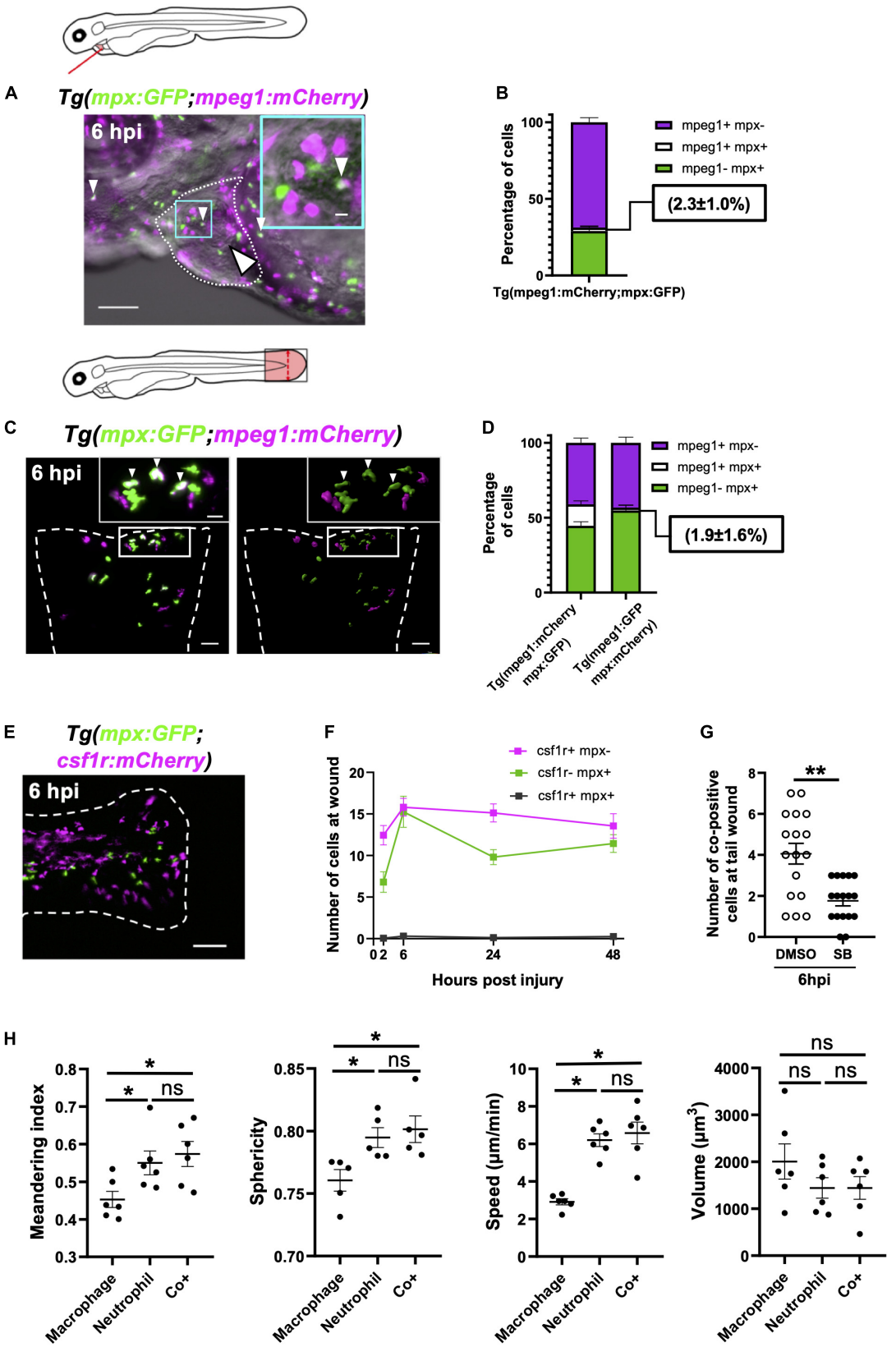

FIGURE 7 | Continued

FIGURE 7 | Immune cells co-positive for *mpeg1* and *mpx* expression are neutrophils not macrophages. **(A)** Epifluorescence timelapse still overlaid on a brightfield image displaying a heart lasered *Tg(mpx:GFP;mpeg1:mCherry)* larva at 6 hpi with neutrophils (green), macrophages (magenta) and co-positive cells (white). White dotted line, pericardial region; cyan square, magnified region; small arrowheads, co-positive cells; and the large arrowhead, injury site. Scale bar = 100 μm. **(B)** Percentage of *mpeg1*:mCherry+ *mpx*:GFP-, *mpeg1*:mCherry+ *mpx*:GFP+ and *mpeg1*:mCherry-*mpx*:GFP+ cell populations on the injured ventricle at 6 hpi, $n = 31$ larvae, experimental $n = 3$. **(C)** LSFM 3D images of a transected tail fin at 6 hpi from a *Tg(mpx:GFP;mpeg1:mCherry)* larva displayed as a MIP (left) and surface render (right) where *mpx*:GFP signal is colored green and *mpeg1*:mCherry signal in magenta. Arrowheads, co-positive cells; dashed line, wound edge; and white boxes, magnified panels. Scale bar = 50 μm for main panel and 20 μm for the magnified panel. **(D)** Percentage of *mpeg1*:mCherry+ *mpx*: GFP-, *mpeg1*:mCherry+ *mpx*:GFP+ and *mpeg1*:mCherry-*mpx*:GFP+ cell populations at the tail wound of *Tg(mpx:GFP;mpeg1:mCherry)* and *Tg(mpx:mCherry;mpeg1:GFP)* larvae at 6 hpi, $n = 24$ larvae, experimental $n = 3$. **(E)** Epifluorescence image of a transected tail fin at 6 hpi from a *Tg(mpx:GFP;csf1r:gal4;UAS:mCherry-NTR)* [abbreviated to *Tg(mpx:GFP;csf1r:mCherry)*] larva, showing a lack of co-expressing cells. Scale bar = 100 μm. **(F)** Number of *csf1r*:NTR-mCherry+ *mpx*: GFP-, *csf1r*:NTR-mCherry-*mpx*:GFP+ and *csf1r*:NTR-mCherry+ *mpx*:GFP+ cells at the tail transection wound at 2, 6, 24, and 48 hpi, $n = 16$ larvae, experimental $n = 3$. **(G)** Number of *mpx*:GFP+ *mpeg1*:mCherry+ co-positive cells at the tail transection wound at 6 hpi following treatment with Cxcr1/2 antagonist SB225002 (5 μM) or DMSO (0.1%) vehicle, $n = 17$ larvae, experimental $n = 3$. Comparison between treatments was conducted using a *t*-test where $^{**}\ p < 0.01$. **(H)** Graphs comparing macrophages, neutrophils and co-positive cells on the basis of meandering index, sphericity, speed and volume derived from 3D analysis of LSFM timelapses from transected *Tg(mpx:GFP;mpeg1:mCherry)* tail fins between 1–2 hpi. Comparisons between cell types was performed by One-way ANOVA followed by a *post hoc* two-stage step-up method of Benjamini, Krieger and Yekutieli FDR correction, $n = 6$ larvae analyzed per group where $^{*}\ p < 0.05$, ns, non-significant. Error bars, SEM for all graphs.

Co-positive Immune Cells Represent a Neutrophil Subset

In order to be confident that co-positive cells represent a subset of neutrophils, we excluded the most likely alternative explanations of their *mpx*:GFP+ *mpeg1*:mCherry+ expression. One such explanation is that co-positive cells represent neutrophils that have ingested *mpeg1*:mCherry+ macrophage cellular material. However, analysis of LSFM-acquired images at subcellular resolution refuted this hypothesis. We found co-positive cells to have a uniform intensity distribution of both fluorophores throughout the cytosol and found no phagosomes, suggesting endogenous expression (**Supplementary Figure 7-supplement 1C**). Next we tested if co-positive cells could represent activated or else developmentally immature neutrophils. Scans of different regions of 3 dpf larvae found these cells in non-hematopoietic tissues such as the perinephric region and brain in addition to the CHT (**Supplementary Figure 7-supplement 1D**). Furthermore, flow cytometry analysis of *mpx*:GFP+ and *mpeg1*:mCherry+ positive cells isolated from transected tailfins demonstrated that both *mpx*:GFP+ *mpeg1*:mCherry- and co-positive neutrophils degranulate following injury as evidenced by a trend for their side scatter to decrease (**Supplementary Figure 7-supplement 2C**). Taken together with the fact that co-positive cells attend wounds, it seems unlikely these cells are immature neutrophils. Furthermore, careful analysis of LSFM timelapse videos showed no instances of *mpx*:GFP+ *mpeg1*:mCherry- neutrophils transitioning to co-positive cells (**Supplementary Video 13**), nor was there any difference in forward scatter between cell types (**Supplementary Figure 7-supplement 2B**), suggesting that one is not simply an activated form of the other.

Having excluded likely alternative explanations, we proceeded to investigate differences in phenotype between single-positive neutrophils, macrophages and co-positive cells, and whether they might have a specialized role during inflammation. Our flow cytometry analysis did not show any difference in size (FSC) or granularity (SSC) between single-positive or co-positive neutrophils in steady state or injury setting (**Supplementary Figures 7-supplement 2A–C**). Hence, we took advantage of our unique ability to analyze the behavior of cells *in vivo* to assess if there were obvious behavioral or physical differences between single positive neutrophils, macrophages and co-positive cells. By tracking all three cell types in 3D timelapse to the transected tail fin, we were able to precisely measure speed, sphericity, meandering index and volume (**Supplementary Figures 7-supplement 3A–D**). No differences were found between co-positive cells and single-positive neutrophils for any of the measures (**Figure 7H**). However, several differences between macrophages and the other two cell types were found, again indicating that co-positive cells are neutrophils and not macrophages. Specifically, macrophages were found to be more meandering, less spherical, slower and tended to be larger than the other two cell types (**Figure 7H**). Though our data does not show any obvious structural or behavioral differences between single-positive and co-positive neutrophils, their unique molecular signature and presence at the wound indicate that they are playing a role in wound healing that is yet to be elucidated.

DISCUSSION

In this study, we provide a novel and in-depth characterization of innate immune cell migration in response to larval zebrafish heart injury. By simultaneously assessing multiple aspects of immune cell mobilization and comparing findings between tail transection and laser heart injury models, we have determined a potentially unifying multi-stage model of the wound immune response in zebrafish larvae (**Figure 8**).

We suggest that, as in mammalian tissue injury, there is an initial, early peak of neutrophil recruitment followed by a slower accumulation of macrophages. This is consistent with the adult zebrafish tail transection model (Petrie et al., 2014) and has also been observed in many others including larval spinal cord (Tsarouchas et al., 2018), larval trunk vasculature (Gurevich et al., 2018) and adult zebrafish heart injury (Bevan et al., 2019). Interestingly, the relative amplitude of the neutrophil and macrophage response differs between models, as does the duration of response. Whilst the duration can likely be attributed to injury size

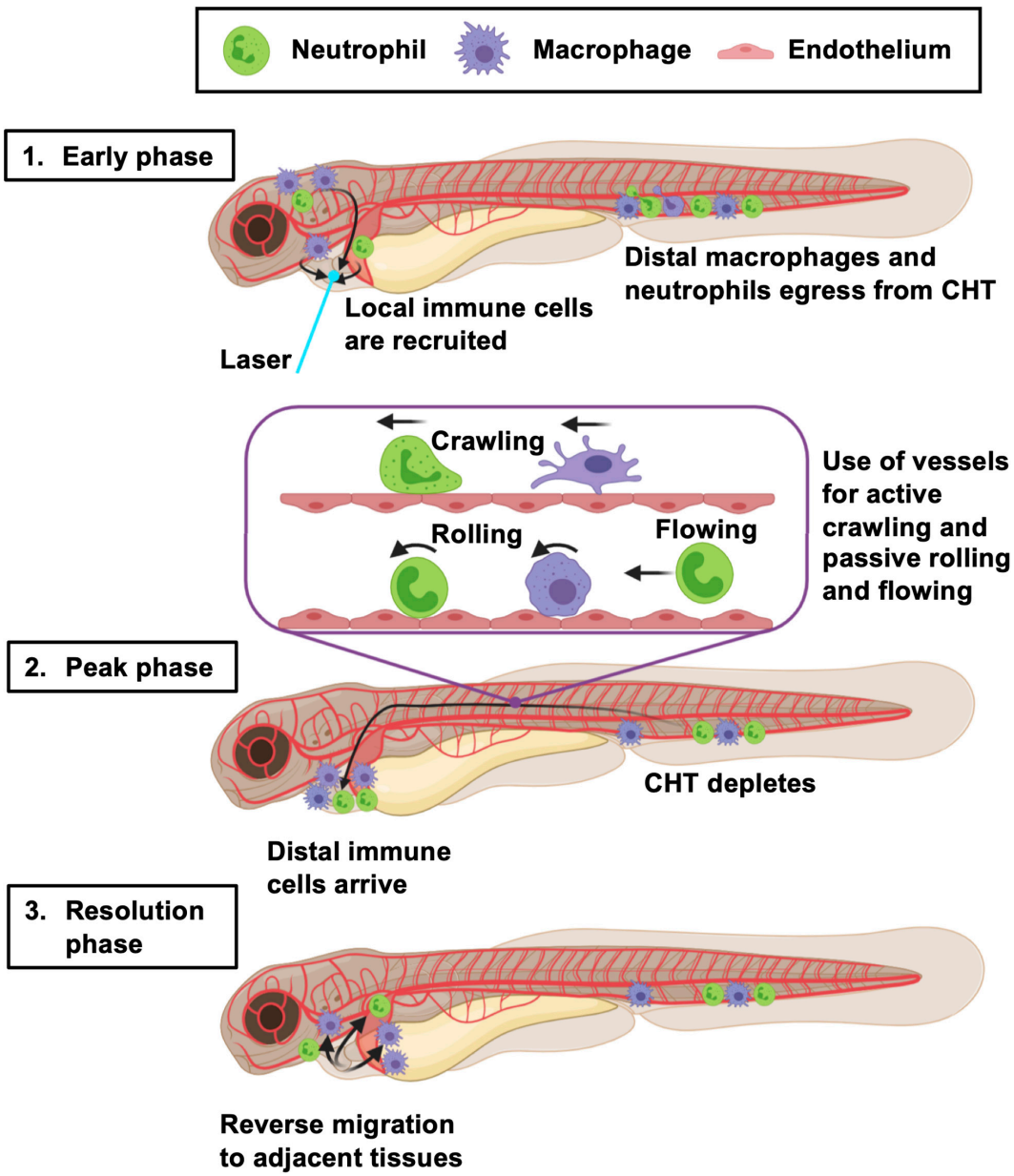

FIGURE 8 | Summary of the larval zebrafish immune response to heart injury. Following laser heart injury in the early phase (0–2 hpi), immune cells resident to nearby pericardial tissues are recruited to the ventricle. At the same time, distal neutrophils and macrophages begin to egress from the CHT into the vascular system. Distal macrophages and neutrophils subsequently utilize blood and lymphatic vessels to migrate to the injured heart, joining locally recruited immune cells during the peak phase (6–24 hpi). The majority of these cells actively crawl along the abluminal surface of vessels, but some also roll and flow along the inside of vessels. The resolution phase is characterized by reverse migration of immune cells to adjacent tissues (> 6 hpi). Created with Biorender.com.

(**Figure 2**), previous studies and our own preliminary data (unpublished) suggests the magnitude of the neutrophil response is at least in part dependent on sterility of the wound (Miskolci et al., 2019). This likely explains the limited neutrophil response in our laser injury model, which is largely sterile in comparison with the more external tail transection. This is an important consideration for groups attempting to model sterile injury using invasive procedures (Tsarouchas et al., 2018).

Our data show that, following laser heart injury, the initial response is dominated by neutrophils and macrophages recruited locally from the pericardial region. This contrasts with the later response where these locally recruited cells are joined by neutrophils and macrophages from more distal sites in the trunk and, in the case of macrophages, from the head. It is possible a fraction of macrophages migrating from the head to the heart injury are microglia as is the case in larval spinal cord injury, albeit a neural tissue (Tsarouchas et al., 2018). Similar examples

of long-range migration have been reported in tail transection studies, where some cells are known to originate from the CHT (Yoo and Huttenlocher, 2011). However, our study is the first to comprehensively determine the ontogeny of recruited larval immune cells, which is widely appreciated to influence repair and regeneration in other models (Ginhoux et al., 2016).

The method of inflammation resolution in the regenerative larva is highly relevant to understanding conditions permissive to tissue regeneration. In our heart injury model, we found no evidence of neutrophil cell death in live imaging, despite ourselves and others reporting this occasionally occurring following tail transection (**Supplementary Video 4** and Loynes et al., 2010; Hoodless et al., 2016). Our study suggests that the primary mode of resolution for both cell types in both injury models is reverse migration, previously only reported for neutrophils (Mathias et al., 2006). Following heart injury, neutrophils and macrophages dispersed randomly rather than gravitating to particular tissues. This finding is in agreement with others who have used mathematical models to demonstrate that random diffusion best describes neutrophil reverse migration (Holmes et al., 2012a,b).

In addition to determining the origin of recruited innate immune cells, we wanted to define their route of migration through the larvae. Mammals have circulating neutrophils and monocytes, supplied by the bone marrow, which can rapidly extravasate into injured tissues (Anderson and Anderson, 1976). Similarly, adult zebrafish have circulating hematopoietic lineage cells, albeit in low numbers and of kidney marrow origin (Willett et al., 1999). Our analysis of larvae in steady state confirmed that larvae usually have no circulating neutrophils or monocytes. However, we saw that in both injury models, neutrophils were indeed mobilized into the blood, but macrophages only did so following tail transection. We suspect that this difference in detection might reflect a difference in the magnitude of inflammatory response between the two injuries, as there were few circulating macrophages even in the larger response of the tail transection. Our timelapse videos of tissue macrophages entering the blood from the CHT demonstrates that it does occur, if rarely, and that perivascular crawling is the more common method of migration.

Notably, for all analyses comparing the two injury models, the laser heart injury seemed to be a milder version of the tail transection, possibly a direct consequence of injury size or increased bacterial load at the tail wound. For example, in addition to the number of neutrophils at the heart lesion being lower than that at the tail wound, fewer neutrophils are seen in circulation and no appreciable drop in CHT numbers was detectable. Nevertheless, our whole larva live imaging does suggest that the CHT is indeed the source of neutrophils suggesting that too few leave the CHT to cause a detectable reduction.

We hypothesized that neutrophils and macrophages might use additional routes and modes of migration to wounds other than circulating peripheral blood, and so performed whole larvae timelapse imaging. Our timelapse videos revealed that the majority of immune cells crawl along the outside of vessels. Interestingly, all vessel types were utilized, even developing lymphatics which were not yet fully patent. This live imaging directly confirmed the CHT as a major source of mobilized neutrophils and macrophages in both laser heart injury and tail transection. Others have reported the use of blood vessels (Manley et al., 2020), however our timelapse videos show this to be the *primary* mode of migration. We speculate that the immune adherence proteins found on endothelium might make these routes more tractable to migrating neutrophils and macrophages (von Andrian et al., 1993). Indeed, this could be an important mode of migration in larger adult wounds whose local scale is similar to that of a whole larva. Immune cells are often found adjacent to blood vessels in skin wounds, and assumed to be extravasating, but this could instead represent local migration. Additionally, we confirmed neutrophil migration to heart injury is Cxcr1/2 dependent and showed for the first time that recruitment of distal macrophages could also be Cxcr1/2 dependent. Interestingly a recent RNAseq analysis of larval zebrafish macrophages and neutrophils found Cxcr1 to only be expressed in the latter and Cxcr2 in neither (Rougeot et al., 2019). Thus suggesting that the decrease in macrophage numbers is likely an indirect, effect perhaps related to the reduced neutrophil presence at the lesion. We speculate that this may not have been observed in tail transection studies as this larger, non-sterile wound may have a greater array of compensatory chemoattractant signals than our sterile heart laser injury lesion. Antagonism of established chemokine axes such as CCL8-CXCR1/2 modulates local immune cell trafficking and might have implications for repair and revascularisation attempts in the human heart following myocardial infarction.

One of the key purposes of establishing a larval zebrafish model of myocardial infarction is to facilitate *in vivo* imaging live on the beating heart, as this is currently impossible using other models and other imaging modalities. The combination of heartbeat-synchronized LSFM imaging, injection of fluorescent dextran and use of a pan-nuclear reporter transgenic gave us unprecedented awareness of the local cardiac architecture in 3D timelapse. Despite the absence of supporting coronaries or lymphatics, we observed neutrophils and macrophages migrating onto the injured heart via adjacent pericardium and settling precisely over the lesion. The high temporal and spatial resolution facilitated characterization of immune cell behavior at the injured myocardium, where neutrophils and macrophages become more meandering and migrate further. Neutrophils and macrophages were not seen to interact with each other, thus excluding efferocytosis of neutrophils by macrophages as a form of inflammation resolution in this model.

Imaging neutrophils and macrophages simultaneously using timelapse LSFM led to the unexpected discovery that a small population of motile immune cells are marked by both the neutrophil marker *mpx* and macrophage marker *mpeg1*. Although, *mpeg1* is known to mark B-cells in the adult (Ferrero et al., 2020), in larvae these markers are considered mutually exclusive and a pan macrophage marker (Ellett et al., 2011). To our knowledge the only other evidence of such cells comes from the previously mentioned bulk RNAseq study characterizing

larval zebrafish macrophage and neutrophil gene expression (Rougeot et al., 2019). The RNAseq showed low levels of *mpx* expression in *mpeg1*+ cells which the authors reasonably interpreted as general overlap in gene expression between macrophages and neutrophils. The cellular level resolution of our study allows us to suggest that this low expression of *mpx* in *mpeg1*+ cells can be explained by the contribution of a small number of *mpx*+ *mpeg*+ neutrophils. We are confident that these cells are indeed neutrophils because their size, shape, chemokine requirements and behavior were all distinguishable from macrophages, but indistinguishable from neutrophils.

Furthermore, we were able to provide evidence against the most likely alternative explanations for co-positivity. Subcellular analysis of fluorophore distribution suggested that the *mpeg1*:mCherry signal was from endogenous expression rather than acquired by phagocytosis of macrophage material. Another possible explanation is that neutrophil *mpeg1*:mCherry expression delineates unactivated neutrophils and activated neutrophils. This seems unlikely as both types of neutrophil are found quiescent in the CHT, and both are found actively participating in the wound inflammatory environment. Additionally, our flow cytometry data indicated both types undergo degranulation upon wounding, suggesting neither represent a cell that was already activated. However, the fact that there is underlying transcriptional heterogeneity leading to differential expression of this gene, is contrary to the idea that neutrophils are all homogenous. Similarly this deduction holds true irrespective of whether co+ cells possess true *mpx mpeg1* co-expression or if it is unfaithful transgene expression. The fact remains that co-positivity only occurs in a subset of neutrophils suggesting an underlying heterogeneity in transcriptional regulation within larval zebrafish neutrophils. Furthermore, *mpeg1* has a specific immune function, as it encodes a pore protein for microbial defense (Benard et al., 2015) and hence these cells might provide enhanced anti-microbial activity in non-sterile wounds. The co-positive cells are an intriguing finding that might have been previously overlooked as *mpeg1*:mCherry and *mpx*:GFP transgenes are often not imaged simultaneously. Further investigation, ideally by single cell RNAseq, is required to understand how these cells might differ in function from single-positive neutrophils and to test for further innate immune cell heterogeneity.

In summary, we have validated a larval zebrafish model of heart injury suitable for the study of immune cell migration. Our work proposes a larval immune cell multi-stage recruitment model (**Figure 8**) whereby macrophages and neutrophils egress from the CHT to travel via the blood or vasculature to the injury site. Local immune cells from the initial wave of cells, are later joined by neutrophils and macrophages from more distal sites. Both macrophage and neutrophil numbers then resolve by reverse migration, randomly dispersing into adjacent tissues. We also highlight the presence of a neutrophil subtype defined by its expression of the macrophage marker *mpeg1*. Future studies will be required to understand the role of these immune cells in the injured larval zebrafish heart and whether they can be modulated to improve cardiac regeneration.

MATERIALS AND METHODS

Zebrafish Husbandry and Strains Used

Zebrafish husbandry, embryo collection and maintenance were conducted as per standard operating procedures. This was in accordance with the Animals (Scientific Procedures) Act, 1986 and approved by The University of Edinburgh Animal Welfare and Ethical Review Board in a United Kingdom Home Office-approved establishment. All experiments were performed on staged animals aged between 72–120 hpf (Kimmel et al., 1995). The following transgenic zebrafish were used: *Tg(myl7:eGFP)*^{twu26} (Huang et al., 2003), *Tg(myl7:h2b-GFP)*^{zf52} (Mickoleit et al., 2014), *Tg(myl7:DsRed2-NLS)*^{f2} (Rottbauer et al., 2002), *Tg(nfkb:eGFP)*^{i235} (Feng et al., 2012), *Tg(mpx:mCherry)*^{uwm7} (Yoo et al., 2010), *Tg(mpx:GFP)*^{i114} (Renshaw et al., 2006), *Tg(mpeg1:mCherry)*^{gl23} (Ellett et al., 2011), *Tg(mpx:gal4;UAS:Kaede)*^{i222} (Ellett et al., 2015), *Tg(fms:Gal4.VP16)*^{i186}, referred to as *csf1r:gal4* (Gray et al., 2011), *Tg(UAS-E1b:NfsB-mCherry)*^{c264}, abbreviated to *UAS:mCherry-NTR* (Davison et al., 2007), *Tg(fli1:eGFP)*^{y1tg} (Lawson and Weinstein, 2002), *Tg(kdrl:mCherry)*^{ci5} (Proulx et al., 2010), *Tg(kdrl:GFP)*^{la116} (Choi et al., 2007), and *Tg(h2a:GFP)* (Pauls et al., 2001). Adults were day-crossed as appropriate to yield desired combinations of transgenes in embryos. Embryos were treated with 0.003% phenylthiourea (Fisher Scientific, Hampshire, New Hampshire) at 7 hpf to prevent pigment formation and enhance image clarity (Karlsson et al., 2001). Fish were housed at 28.5°C in conditioned media and imaged at room temperature (23°C) on various microscopes (details below). When necessary, larvae were periodically anesthetized using 40 μg/ml tricaine methanesulfonate (Sigma Aldrich, St Louis, Missouri) before being transferred back to conditioned media.

Localized Ventricular Laser Ablation

A Zeiss Photo Activated Laser Microdissection (PALM) laser system (Zeiss, Oberkochen, Germany) (**Supplementary Figure 1-supplement 1**) was used to induce a localized injury at the ventricular apex of anesthetized 72 hpf larvae as initially reported recently (Taylor et al., 2019). Larvae were laterally mounted on a glass slide in 20 μl anesthetized conditioned media and the laser was fired through a 20X objective. Injuries were deemed successful when ventricular contractility noticeably decreased, the apex had shrunk, and the myocardial wall had swollen without causing cardiac rupture and subsequent erythrocyte leaking (**Figure 1B**). A successful injury resulted in the segment of dysfunctional tissue losing fluorescent myocardial transgenic signal (**Figure 1D**). Uninjured (control) larvae were treated in the same manner up to the point of laser injury, when they were individually separated into single wells of a 24-well plate and maintained in the same environmental conditions as injured fish.

Tail Fin Transection

The tail fin of anesthetized 72 hpf larvae was transected using a sterile scalpel, avoiding damage to the end of the notochord and vasculature (as depicted in the **Figure 2** schematic), and as

previously reported (Hoodless et al., 2016). Uninjured (control) fish were treated in the same manner up to the point of transection, when they were separated into a 24-well plate and maintained in the same environmental conditions as injured fish.

Epifluorescence Microscopy

A Leica M205 FA stereomicroscope (Leica, Wetzlar, Germany) with GFP, mCherry and BFP filters was used for all serial timepoint epifluorescence imaging experiments. To visualize neutrophil or macrophage presence at heart or tail wounds, larvae were anesthetized and mounted laterally on a glass slide in 50 μl of conditioned media. The number of immune cells on the heart were quantified by manually observing and counting cells moving synchronously with the beating heart. Heart images were acquired using 16X objective. The number of immune cells at the tail were quantified by counting from the caudal end of the vascular loop to the wound edge as performed by others (Miskolci et al., 2019). Tail images were acquired using 8X objective. CHT images were acquired using a 6X objective. Whole larvae images were acquired using 2.5X objective. The number of circulating immune cells were quantified by manually observing whole larvae for liberated cells which can be detected in real time migrating through or around the vasculature.

An EVOS Auto2 system (ThermoFisher, Waltham, MA, United States) with GFP, RFP and DAPI filters was used to image whole larvae in epifluorescence timelapse, in an automated manner at 28.5°C. Larvae were anesthetized and mounted laterally in a 6-well plate in 1% agarose. Three larvae were mounted per well. To ensure larvae remain immobilized, 500 μl of anesthetic solution was added to each well. Images of each well were acquired using a 2X objective at 1-minute intervals up to 24 hpi.

Light Sheet Fluorescence Microscopy (LSFM)

Individual larvae were prepared for LSFM by embedding in 1% low melting-point agarose (ThermoFisher, Waltham, Massachusetts) in anesthetized conditioned media inside FEP tubes (Adtech Polymer Engineering, Stroud, United Kingdom). This embedding reduced gradual drift of the embryo in the FEP tube, without causing developmental perturbations during long-term imaging. Larvae were used only once for a timelapse imaging experiment, and any repeats shown come from distinct individuals. Larvae were mounted head down such that the heart faces toward both illumination and imaging objectives to improve image clarity. All LSFM experiments were performed at room temperature (23°C). The setup of our custom-built LSFM system has been previously reported in detail (Taylor et al., 2019).

Optically Gated (Beat-Synchronized) Heart Imaging

Real time prospective optical gating and more recent adaptive prospective gating methods in conjunction with LSFM have been previously published (Taylor et al., 2011, 2012, 2019). In summary, the software permits real-time 3D imaging of the normally beating heart by determining the phase of the cardiac cycle using images acquired from a separate bright-field camera. The software checks subsequently acquired bright-field images against this reference image-set in real-time and activates the imaging laser at a user-designated phase of the cardiac cycle. This ensures the lightsheet only strikes the heart when it is in that desired phase of the cardiac cycle, illuminating each z-plane for a few milliseconds and limiting the impact of phototoxicity and photobleaching. Synchronization is maintained over tens of hours by periodically updating the reference images to account for changes in appearance of the heart during development/injury (Taylor et al., 2019). For timelapse imaging, the entire heart is scanned in 3D every 3 mins, with a z-plane spacing of 1 μm, and each image stack is stored as a.tif file. These images can be viewed as a maximum intensity projection images during acquisition in order to, if necessary, optimize the quality of subsequently acquired images.

Histological Cell Death Assays

To detect cell death at the injured ventricle, whole-mount larval TUNEL staining was performed. Larvae were fixed in 4% PFA for 30 mins and transferred to 1:10 dilution of PBS. Larvae were subsequently digested in 1 μg/ml Proteinase K for 1 h. Larvae were re-fixed in 4% PFA for 20 mins and subsequently washed in PBT. TUNEL staining was performed using ApopTag Red *In situ* kit (MilliporeSigma, Burlington, MA, United States) to label apoptotic cells, as described in (Buckley et al., 2017). Stained hearts were imaged using LSFM.

To corroborate these findings acridine orange staining was performed. Larvae were incubated in 10 ng/μl of Acridine orange solution (ThermoFisher, Waltham, MA, United States) in the dark for 20 min. Larvae were subsequently washed three times in conditioned media for 10 min and imaged using heartbeat synchronized LSFM.

For live staining with propidium iodide, larvae were injected intravenously with a 1 nl volume of 1 mg/ml PI (ThermoFisher, Waltham, MA, United States) in PBS immediately following laser injury (∼15 minutes post injury) and imaged using heartbeat synchronized LSFM.

Photoconversion of Neutrophils and Macrophages

We established a specific protocol for photoconversion of neutrophils and macrophages following laser heart injury, using *Tg(mpx:gal4;UAS:kaede)* and *Tg(csf1r:gal4;UAS:kaede)* larvae respectively on a Leica M205 FA epifluorescence stereomicroscope (Leica, Wetzlar, Germany). To increase throughput, we generated a digital reticule informing us of the beam location on the larva. The reticule was specifically positioned to target one of two different regions; the head and/or pericardium. Larvae were mounted laterally in 50 μl of conditioned media on a glass slide prior to photoconversion. The beam was focused through a Leica PLAN APO 2.0x CORR Objective with an eye piece magnification of x16. A Mercury Vapor Lamp (Leica, Wetzlar, Germany) at 50 W power was used in conjunction with a BFP filter to photoconvert kaede-labeled immune cells. Depending on the experiment, larvae were either

differentially photoconverted at 1 h prior to heart injury and imaged at 2 and 6 hpi (immune cell tissue origin assay), or their pericardiums were fully photoconverted at 6 hpi and imaged at 24 hpi (immune reverse migration assay). For the immune cell tissue origin experiment, the head was first fully photoconverted from green to red by exposing larvae for 60 s (until no green kaede signal was detectable above background). Next, the pericardium was semi-converted from green to brown (red and green) by exposing larvae for 30 s (immune cells retain 1:1 ratio of unconverted vs converted kaede fluorophore). The remainder of the larvae (which we term trunk) maintained endogenous green kaede fluorophore, hence producing three differentially labeled immune cell populations in the same larvae. Larvae were not imaged beyond 24 hpi because, shortly after this elapsed time, converted kaede fluorophore became difficult to detect in semi-converted cells. For the immune cell reverse migration experiment, the pericardium was fully photoconverted from green to red by exposing larvae for 60 s (until no green kaede signal was detectable above background). We confirmed that 93 $\pm$ 2.7% of pericardial immune cells photoconverted at 6 hpi were able to be traced at 24 hpi following their reverse migration, therefore validating the sensitivity of this technique (**Supplementary Figure 3-supplement 1B**). Larvae were imaged using both GFP and mCherry filters to detect level of photoconversion.

Pharmacological Cxcr1/2 Inhibition

Larvae were preincubated in 5 μM SB225002 (Sigma Aldrich, St. Louis, MO, United States) or 0.1% DMSO vehicle (Sigma Aldrich, St. Louis, MO, United States) dissolved in conditioned media at 70 hpf for two hours prior to heart or tail injury. Following injury, larvae were continuously bathed in drug or vehicle throughout the duration of the experiment.

Fluorescent Dextran Injection

Custom-synthesized molecular weight (500 kDa) pacific blue fluorophore-labeled dextran (Fina Biosolutions, Rockville, MD, United States) was injected into larvae at 1 hpi. Injections were administered in a 1 nL volume of 5% (w/v) dextran dissolved in phosphate-buffered saline and injected into the cardiac sinus venosus as described in more detail previously (Rider et al., 2018).

Image Analysis

Unless otherwise stated, images were prepared, processed and analyzed using ImageJ (Fiji) software (National Institutes of Health, Bethesda).

Ventricular Ejection Function

Tg(myl7:GFP) hearts were imaged using a Leica M205 FA epifluorescence stereomicroscope (Leica, Wetzlar, Germany) to capture when the ventricle was in diastole and systole. The ventricular area in diastole and systole was measured and ventricular ejection fraction calculated using the formula 100 X [(Diastolic Area – Systolic Area)/Diastolic Area] (Matrone et al., 2013).

Photoconverted Immune Cells

Epifluorescence images of photoconverted larvae were analyzed to quantify the number of immune cells that were fully converted (red), semi-converted (red and green) or unconverted (green) on the heart or to identify immune cell locations in the whole larvae following heart injury. More specifically, for the latter reverse migration (immune cell location) assay, each larva was divided into 48 equally sized square zones (3 rows of 16, individual zone size = 31000 μm^2). The number of photoconverted immune cells within each square zone at 24 hpi was quantified per larvae, averaged and normalized per zone to generate a heat map (**Figure 3D**).

Immune Cell CHT Quantity

The number of immune cells specifically within the CHT (as depicted in **Figure 4**) were quantified across timepoints and normalized to baseline preinjury (0 hpi) for each larva. Quantification was performed in a semi-automated fashion using a custom FIJI. In brief, a rectangular region of interest (766 μm × 151 μm) is generated and positioned over the CHT. This region is cropped, and brightness/contrast enhanced to identify all neutrophils or macrophages. Background signal is subtracted, then an unsharp mask and watershed segmentation are applied. The 'Analyze Particles' plugin is run to measure the area of segmented neutrophils or macrophages in the CHT.

EVOS Whole Larva Imaging Analysis

Timelapse images were analyzed using the FIJI plugin Trackmate (Tinevez et al., 2017) automating the tracking of neutrophils and macrophages. Detection parameters: LOG detector, diameter 14 μm and threshold 5 μm. Tracking was performed using Simple Linear Assignment Problem (LAP) algorithms with parameters: linking distance 27 μm, max closing distance 15 μm and gap closing max frame gap 2. The dataset was then handled one of two ways depending on the analysis.

Analysis 1 - vessel use incidence: the incidence of use of each vessel for lasered datasets was obtained manually by plotting a line along the dorso-ventral axis one somite anterior to the cloaca and counting how many cells pass the line over the time frame 1–12 hpi for each vessel. Detecting and ringing each cell using Trackmate aids counting. The same method was used for tail transection datasets except the dorso-ventral line was drawn four somites back from the tail fin. The reasoning behind using different sites for quantification is that the majority of migrating cells will be coming from the CHT, which is located between the two different wound sites we studied, and hence cells are expected to move in opposite directions depending on the injury model.

Analysis 2 - cell behavior: tracked cells were filtered to a range of 1.5–8 hpi and restricted to the trunk region of the larva. Non-migrating cells were then excluded from the analysis based on displacement. Remaining tracks were used for plots of speed and meandering index. Meandering index was calculated using the Trackmate output data 'Displacement', 'Duration' and 'Speed.' Where Meandering index = Displacement/(Duration/Speed).

Surface Rendering of Heart, Vasculature, Nuclei and Tracking of Immune Cells Following Heart Injury

Light sheet fluorescence microscopy *z*-stacks of the myocardium, endocardium, immune cells and nuclei were surface-rendered using Imaris software (Bitplane, Zurich, Switzerland). Rendered immune cells were tracked during the indicated time course using an autoregressive motion algorithm, and individual tracks were surface rendered for display using Imaris.

Differentially Color-Labeling Cell Types Imaged in the Same Fluorescent Channel

To distinguish *kdrl:mCherry* fluorescence from *mpeg1:mCherry* fluorescence, a sequential subtraction of two frames difference was performed across the image sequence to produce a magenta channel where only moving cells were visible. This distinguished moving macrophages (magenta) from the static endothelium (blue). To distinguish *mpx:GFP* fluorescence from *h2a:GFP* fluorescence, a threshold was applied across the image sequence, creating a mask for brighter *mpx:GFP* neutrophils only. The brightness/contrast of *h2a:GFP* fluorescence (gray) was altered so that it was visible when overlaid with the *mpx:GFP* fluorescent mask (green). All channels were combined to create a composite image displayed in **Figure 6D**.

Ventricle-Recruited Immune Cell Behavior Analysis

Light sheet fluorescence microscopy timelapses of the myocardium and neutrophils or macrophages were processed as maximum intensity projections. The Fiji plugin MTrackJ (Meijering, 2006) was used to manually track the migration of immune cells from the moment they migrate onto the ventricular myocardium until the moment they reverse-migrate off the ventricular myocardium or, as is commonly the case for macrophages, until the end of the timelapse.

Immune Cell Behavior Analysis Following Tail Transection Using LSFM Timelapses

LSFM timelapses of the transected tail fin acquired at scan intervals of 1 min were analyzed using Imaris (Bitplane, Zurich, Switzerland). Default and suggested parameters were used for supervised tracking by the autoregressive motion algorithm. Co-positive cells were designated as cells with a mpx:mpeg1 ratio less than 3:1 and greater than 1.33:1. Gating the cells by ratios overcomes the variability in absolute intensity as cells move through different area of tissue and take on different shapes. Plotted values are calculated from the averages of all cells in a particular larva 2–3 hpi following tail transection.

Fluorescence Intensity Plots of Immune Cell *z*-Planes

LSFM z-stacks of transected tail fins were analyzed in Fiji using the plot profile function to measure the intensity of the desired fluorophore across a manually drawn line.

Flow Cytometry

Larvae were euthanized using 0.3 mg/ml tricaine methanesulfonate at 24 h post injury (4 dpf) and transferred into 1 ml of enzyme digestion mix consisting of Collagenase V (Sigma Aldrich, St. Louis, MO, United States), Collagenase D (Roche, Basel, Switzerland), Dispase (ThermoFisher, Waltham, MA, United States) and DNase (Roche, Basel, Switzerland). A single-cell suspension in RPMI+ 10% FBS was achieved through mechanical homogenization and filtering through a 40 μm cell strainer. The cells were resuspended in HBSS (−/−)+ 15 mM HEPES+ 25 μM D-Glucose) and filtered through a 40 μm cell strainer. Lastly, DAPI (1:1000) was added to the sample which was subsequently analyzed by flow cytometry. Samples were kept on ice throughout and were analyzed by flow cytometry at 4°C. Analysis and visualization of data was performed using FCS Express 7 software (*De Novo* Software, Pasadena, CA, United States).

Statistical Analysis

Graphs and statistics were curated in GraphPad Prism 8 software (GraphPad Software, San Diago, CA, United States). Data were analyzed by student *t*-test, one-way ANOVA or two-way ANOVA followed by an appropriate multiple comparison *post hoc* test. All statistical tests, *p*-values and *n* numbers used are given in figure legends.

DATA AVAILABILITY STATEMENT

All datasets presented in this study are included in the article/**Supplementary Material**.

ETHICS STATEMENT

The animal study was reviewed and approved by The University of Edinburgh Animal Welfare and Ethical Review Board.

AUTHOR CONTRIBUTIONS

AK, FAB, and MAD conceived and designed the study. AK, FAB, MEMO, and CB carried out all experiments. Image analysis was performed by AK, FAB, and CB. LSFM-related technical assistance was provided by JMT. AK and FAB wrote the manuscript. CB, JMT, CST, JJM, AGR, and MAD edited the manuscript. MAD, AGR, and CST supervised the study. All authors contributed to the article and approved the submitted version.

FUNDING

This work was funded by a British Heart Foundation (BHF) CoRE award (RE/13/3/30183), Medical Research

Scotland studentship (PhD-1049-2016), NC3R studentship (NC/P002196/1), BHF New Horizons grant (NH/14/2/31074), and a Medical Research Council UK award (MR/K013386/1).

ACKNOWLEDGMENTS

We thank the BVS Aquatics Facility Staff for their expert animal care during the course of this study. We also thank the SCRM Flow Cytometry facility, in particular Fiona Rossi, for sample processing and analysis.

SUPPLEMENTARY MATERIAL

The Supplementary Material for this article can be found online at: https://www.frontiersin.org/articles/10.3389/fcell.2020.579943/full#supplementary-material

REFERENCES

Adamo, L., Rocha-Resende, C., Prabhu, S., and Mann, D. (2020). Reappraising the role of inflammation in heart failure. *Nat. Rev. Cardiol.* 17, 269–285. doi: 10.1038/s41569-019-0315-x

Anderson, A. O., and Anderson, N. D. (1976). Lymphocyte emigration from high endothelial venules in rat lymph nodes. *Immunology* 31, 731–748.

Barros-Becker, F., Lam, P., Fisher, R., and Huttenlocher, A. (2017). Live imaging reveals distinct modes of neutrophil and macrophage migration within interstitial tissues. *J. Cell Sci.* 130, 3801–3808. doi: 10.1242/jcs.206128

Benard, E. L., Racz, P. I., Rougeot, J., Nezhinsky, A. E., Verbeek, F. J., Spaink, H. P., et al. (2015). Macrophage-expressed perforins mpeg1 and mpeg1. 2 have an anti-bacterial function in zebrafish. *J. Innate Immun.* 7, 136–152. doi: 10.1159/000366103

Bevan, L., Lim, Z. W., Venkatesh, B., Riley, P. R., Martin, P., and Richardson, R. J. (2019). Specific macrophage populations promote both cardiac scar deposition and subsequent resolution in adult zebrafish. *Cardiovasc. Res.* 116, 1357–1371.

Buckley, C., Carvalho, M., Young, L., Rider, S., McFadden, C., Berlage, C., et al. (2017). Precise spatio-temporal control of rapid optogenetic cell ablation with mem-KillerRed in Zebrafish. *Sci. Rep.* 7:5096.

Chitu, V., and Stanley, E. R. (2006). Colony-stimulating factor-1 in immunity and inflammation. *Curr. Opin. Immunol.* 18, 39–48. doi: 10.1016/j.coi.2005.11.006

Choi, J., Dong, L., Ahn, J., Dao, D., Hammerschmidt, M., and Chen, J. (2007). FoxH1 negatively modulates flk1 gene expression and vascular formation in zebrafish. *Dev. Biol.* 304, 735–744. doi: 10.1016/j.ydbio.2007.01.023

Davison, J., Akitake, C., Goll, M., Rhee, J., Gosse, N., Baier, H., et al. (2007). Transactivation from Gal4-VP16 transgenic insertions for tissue-specific cell labeling and ablation in zebrafish. *Dev. Biol.* 304, 811–824. doi: 10.1016/j.ydbio.2007.01.033

Deng, Q., Sarris, M., Bennin, D. A., Green, J. M., Herbomel, P., and Huttenlocher, A. (2013). Localized bacterial infection induces systemic activation of neutrophils through Cxcr2 signaling in zebrafish. *J. Leukocyte Biol.* 93, 761–769.

Dewald, O., Zymek, P., Winkelmann, K., Koerting, A., Ren, G., Abou-Khamis, T., et al. (2005). CCL2/Monocyte chemoattractant protein-1 regulates inflammatory responses critical to healing myocardial infarcts. *Circ. Res.* 96, 881–889. doi: 10.1161/01.RES.0000163017.13772.3a

Ellett, F., Elks, P., Robertson, A., Ogryzko, N., and Renshaw, S. (2015). Defining the phenotype of neutrophils following reverse migration in zebrafish. *J. Leukocyte Biol.* 98, 975–981. doi: 10.1189/jlb.3MA0315-105R

Ellett, F., Pase, L., Hayman, J. W., Andrianopoulos, A., and Lieschke, G. J. (2011). mpeg1 promoter transgenes direct macrophage-lineage expression in zebrafish. *Blood J. Am. Soc. Hematol.* 117, e49–e56. doi: 10.1182/blood-2010-10-314120

Feng, Y., Renshaw, S., and Martin, P. (2012). Live imaging of tumor initiation in Zebrafish larvae reveals a trophic role for leukocyte-derived PGE2. *Curr. Biol.* 22, 1253–1259. doi: 10.1016/j.cub.2012.05.010

Ferrero, G., Gomez, E., lyer, S., Rovira, M., Miserocchi, M., Langenau, D. M., et al. (2020). The macrophage-expressed gene (mpeg) 1 identifies a subpopulation of B cells in the adult zebrafish. *J. Leukocyte Biol.* 107, 431–443.

Ginhoux, F., Schultze, J. L., Murray, P. J., Ochando, J., and Biswas, S. K. (2016). New insights into the multidimensional concept of macrophage ontogeny, activation and function. *Nat. Immunol.* 17, 34–40. doi: 10.1038/ni.3324

Gonzalez-Rosa, J., Martin, V., Peralta, M., Torres, M., and Mercader, N. (2011). Extensive scar formation and regression during heart regeneration after cryoinjury in zebrafish. *Development* 138, 1663–1674. doi: 10.1242/dev.060897

Gray, C., Loynes, C., Whyte, M., Crossman, D., Renshaw, S., and Chico, T. (2011). Simultaneous intravital imaging of macrophage and neutrophil behaviour during inflammation using a novel transgenic zebrafish. *Thromb. Haemost.* 105, 811–819. doi: 10.1160/TH10-08-0525

Gurevich, D. B., Severn, C. E., Twomey, C., Greenhough, A., Cash, J., Toye, A. M., et al. (2018). Live imaging of wound angiogenesis reveals macrophage orchestrated vessel sprouting and regression. *EMBO J.* 37:e97786.

Holmes, G., Anderson, S., Dixon, G., Robertson, A., Reyes-Aldasoro, C., Billings, S., et al. (2012a). Repelled from the wound, or randomly dispersed? Reverse migration behaviour of neutrophils characterized by dynamic modelling. *J. R. Soc. Interface* 9, 3229–3239. doi: 10.1098/rsif.2012.0542

Holmes, G., Dixon, G., Anderson, S., Reyes-Aldasoro, C., Elks, P., Billings, S., et al. (2012b). Drift-diffusion analysis of neutrophil migration during inflammation resolution in a Zebrafish Model. *Adv. Hematol.* 2012, 1–8.

Hoodless, L., Lucas, C., Duffin, R., Denvir, M., Haslett, C., Tucker, C., et al. (2016). Genetic and pharmacological inhibition of CDK9 drives neutrophil apoptosis to resolve inflammation in zebrafish in vivo. *Sci. Rep.* 5:36980.

Horckmans, M., Ring, L., Duchene, J., Santovito, D., Schloss, M., Drechsler, M., et al. (2016). Neutrophils orchestrate post-myocardial infarction healing by polarizing macrophages towards a reparative phenotype. *Eur. Heart J.* 38, 187–197.

Huang, C. J., Tu, C. T., Hsiao, C. D., Hsieh, F. J., and Tsai, H. J. (2003). Germ-line transmission of a myocardium-specific GFP transgene reveals critical regulatory elements in the cardiac myosin light chain 2 promoter of zebrafish. *Dev Dyn.* 228, 30–40. doi: 10.1002/dvdy.10356

Isogai, S., Horiguchi, M., and Weinstein, B. (2001). The vascular anatomy of the developing zebrafish: an atlas of embryonic and early larval development. *Dev. Biol.* 230, 278–301. doi: 10.1006/dbio.2000.9995

Jung, H., Castranova, D., Swift, M., Pham, V., Venero Galanternik, M., Isogai, S., et al. (2017). Development of the larval lymphatic system in zebrafish. *Development* 144, 2070–2081.

Karlsson, J., von Hofsten, J., and Olsson, P. (2001). Generating transparent zebrafish: a refined method to improve detection of gene expression during embryonic development. *Mar. Biotechnol.* 3, 0522–0527. doi: 10.1007/s1012601-0053-4

Karra, R., Knecht, A. K., Kikuchi, K., and Poss, K. D. (2015). Myocardial NF-κB activation is essential for zebrafish heart regeneration. *Proc. Nat. Acad. Sci. U.S.A.* 112, 13255–13260. doi: 10.1073/pnas.1511209112

Kimmel, C., Ballard, W., Kimmel, S., Ullmann, B., and Schilling, T. (1995). Stages of embryonic development of the zebrafish. *Dev. Dyn.* 203, 253–310. doi: 10.1002/aja.1002030302

Lai, S., Marín-Juez, R., and Stainier, D. (2018). Immune responses in cardiac repair and regeneration: a comparative point of view. *Cell. Mol. Life Sci.* 76, 1365–1380. doi: 10.1007/s00018-018-2995-5

Lawson, N., and Weinstein, B. (2002). In vivo imaging of embryonic vascular development using transgenic zebrafish. *Dev. Biol.* 248, 307–318. doi: 10.1006/dbio.2002.0711

Loynes, C. A., Martin, J. S., Robertson, A., Trushell, D. M., Ingham, P. W., Whyte, M. K., et al. (2010). Pivotal advance: pharmacological manipulation of inflammation resolution during spontaneously resolving tissue neutrophilia in the zebrafish. *J. Leukocyte Biol.* 87, 203–212. doi: 10.1189/jlb.0409255

Ma, Y., Yabluchanskiy, A., and Lindsey, M. (2013). Neutrophil roles in left ventricular remodeling following myocardial infarction. *Fibrogen. Tissue Repair* 6:11. doi: 10.1186/1755-1536-6-11

Manley, H. R., Potter, D. L., Heddleston, J. M., Chew, T. L., Keightley, M. C., and Lieschke, G. J. (2020). Frontline science: dynamic cellular and subcellular features of migrating leukocytes revealed by in vivo lattice lightsheet microscopy. *J. Leukocyte Biol.* 108, 455–468. doi: 10.1002/JLB.3HI0120-589R

Mathias, J. R., Perrin, B. J., Liu, T. X., Kanki, J., Look, A. T., and Huttenlocher, A. (2006). Resolution of inflammation by retrograde chemotaxis of neutrophils in transgenic zebrafish. *J. Leukocyte Biol.* 80, 1281–1288.

Matrone, G., Maqsood, S., Taylor, J., Mullins, J., Tucker, C., and Denvir, M. (2014). Targeted laser ablation of the zebrafish larval heart induces models of heart block. Valvular regurgitation, and outflow tract obstruction. *Zebrafish* 11, 536–541. doi: 10.1089/zeb.2014.1027

Matrone, G., Taylor, J., Wilson, K., Baily, J., Love, G., Girkin, J., et al. (2013). Laser-targeted ablation of the zebrafish embryonic ventricle: a novel model of cardiac injury and repair. *Int. J. Cardiol.* 168, 3913–3919.

Matrone, G., Wilson, K., Maqsood, S., Mullins, J., Tucker, C., and Denvir, M. (2015). CDK9 and its repressor LARP7 modulate cardiomyocyte proliferation and response to injury in the zebrafish heart. *J. Cell Sci.* 128, 4560–4571. doi: 10.1242/jcs.175018

Meijering, E. (2006). *MTrackJ: A Java Program for Manual Object Tracking.* Rotterdam: University Medical Center Rotterdam.

Meszaros, A., Reichner, J., and Albina, J. (1999). Macrophage phagocytosis of wound neutrophils. *J. Leukocyte Biol.* 65, 35–42. doi: 10.1002/jlb.65.1.35

Mickoleit, M., Schmid, B., Weber, M., Fahrbach, F., Hombach, S., Reischauer, S., et al. (2014). High-resolution reconstruction of the beating zebrafish heart. *Nat. Methods* 11, 919–922. doi: 10.1038/nmeth.3037

Miskolci, V., Squirrell, J., Rindy, J., Vincent, W., Sauer, J. D., Gibson, A., et al. (2019). Distinct inflammatory and wound healing responses to complex caudal fin injuries of larval zebrafish. *eLife* 8:e45976. doi: 10.7554/eLife.45976

Nahrendorf, M., Swirski, F., Aikawa, E., Stangenberg, L., Wurdinger, T., Figueiredo, J., et al. (2007). The healing myocardium sequentially mobilizes two monocyte subsets with divergent and complementary functions. *J. Exp. Med.* 204, 3037–3047.

Pauls, S., Geldmacher-Voss, B., and Campos-Ortega, J. (2001). A zebrafish histone variant H2A.F/Z and a transgenic H2A.F/Z:GFP fusion protein for in vivo studies of embryonic development. *Dev. Genes Evol.* 211, 603–610. doi: 10.1007/s00427-001-0196-x

Petrie, T. A., Strand, N. S., Tsung-Yang, C., Rabinowitz, J. S., and Moon, R. T. (2014). Macrophages modulate adult zebrafish tail fin regeneration. *Development* 141, 2581–2591. doi: 10.1242/dev.098459

Powell, D., Tauzin, S., Hind, L. E., Deng, Q., Beebe, D. J., and Huttenlocher, A. (2017). Chemokine signaling and the regulation of bidirectional leukocyte migration in interstitial tissues. *Cell Rep.* 19, 1572–1585. doi: 10.1016/j.celrep.2017.04.078

Proulx, K., Lu, A., and Sumanas, S. (2010). Cranial vasculature in zebrafish forms by angioblast cluster-derived angiogenesis. *Dev. Biol.* 348, 34–46. doi: 10.1016/j.ydbio.2010.08.036

Renshaw, S., Loynes, C., Trushell, D., Elworthy, S., Ingham, P., and Whyte, M. (2006). A transgenic zebrafish model of neutrophilic inflammation. *Blood* 108, 3976–3978. doi: 10.1182/blood-2006-05-024075

Rider, S. A., Bruton, F. A., Collins, R. G., Conway, B. R., and Mullins, J. J. (2018). The efficacy of puromycin and adriamycin for induction of glomerular failure in larval zebrafish validated by an assay of glomerular permeability dynamics. *Zebrafish* 15, 234–242. doi: 10.1089/zeb.2017.1527

Ridker, P., Everett, B., Thuren, T., MacFadyen, J., Chang, W., Ballantyne, C., et al. (2017). Antiinflammatory therapy with canakinumab for atherosclerotic disease. *N. Engl. J. Med.* 377, 1119–1131.

Rosowski, E. (2020). Determining macrophage versus neutrophil contributions to innate immunity using larval zebrafish. *Dis. Models Mech.* 13:dmm041889. doi: 10.1242/dmm.041889

Rottbauer, W., Saurin, A., Lickert, H., Shen, X., Burns, C., Wo, Z., et al. (2002). Reptin and pontin antagonistically regulate heart growth in zebrafish embryos. *Cell* 111, 661–672.

Rougeot, J., Torraca, V., Zakrzewska, A., Kanwal, Z., Jansen, H. J., Sommer, F., et al. (2019). RNAseq profiling of leukocyte populations in zebrafish larvae reveals a cxcl11 chemokine gene as a marker of macrophage polarization during mycobacterial infection. *Front. Immunol.* 10:832. doi: 10.3389/fimmu.2019.00832

Sweet, M. J., and Hume, D. A. (2003). CSF-1 as a regulator of macrophage activation and immune responses. *Arch. Immunol. Ther. Exp. Engl. Ed.* 51, 169–178.

Tardif, J., Kouz, S., Waters, D., Bertrand, O., Diaz, R., Maggioni, A., et al. (2019). Efficacy and safety of low-dose colchicine after myocardial infarction. *N. Engl. J. Med.* 381, 2497–2505.

Taylor, J., Girkin, J., and Love, G. (2012). High-resolution 3D optical microscopy inside the beating zebrafish heart using prospective optical gating. *Biomed. Opt. Express* 3, 3043–3053. doi: 10.1364/BOE.3.003043

Taylor, J., Nelson, C., Bruton, F., Baghbadrani, A., Buckley, C., Tucker, C., et al. (2019). Adaptive prospective optical gating enables day-long 3D time-lapse imaging of the beating embryonic zebrafish heart. *Nat. Commun.* 10:5173.

Taylor, J., Saunter, C., Love, G., Girkin, J., Henderson, D., and Chaudhry, B. (2011). Real-time optical gating for three-dimensional beating heart imaging. *J. Biomed. Opt.* 16:116021.

Tillmanns, J., Carlsen, H., Blomhoff, R., Valen, G., Calvillo, L., Ertl, G., et al. (2006). Caught in the act: in vivo molecular imaging of the transcription factor NF-κB after myocardial infarction. *Biochem. Biophys. Res. Commun.* 342, 773–774.

Tinevez, J. Y., Perry, N., Schindelin, J., Hoopes, G. M., Reynolds, G. D., Laplantine, E., et al. (2017). TrackMate: an open and extensible platform for singleparticle tracking. *Methods* 115, 80–90.

Tsarouchas, T. M., Wehner, D., Cavone, L., Munir, T., Keatinge, M., Lambertus, M., et al. (2018). Dynamic control of proinflammatory cytokines Il-1β and Tnf-α by macrophages in zebrafish spinal cord regeneration. *Nat. Communi.* 9, 1–17.

von Andrian, U. H., Chambers, J. D., Berg, E. L., Michie, S. A., Brown, D. A., Karolak, D., et al. (1993). L-selectin mediates neutrophil rolling in inflamed venules through sialyl LewisX-dependent and-independent recognition pathways. *Blood* 82, 182–191. doi: 10.1182/blood.V82.1.182.bloodjournal821182

Willett, C. E., Cortes, A., Zuasti, A., and Zapata, A. G. (1999). Early hematopoiesis and developing lymphoid organs in the zebrafish. *Dev. Dyn.* 214, 323–336. doi: 10.1002/(SICI)1097-0177(199904)214:4<323::AID-AJA5>3.0.CO;2-3

Yoo, S., Deng, Q., Cavnar, P., Wu, Y., Hahn, K., and Huttenlocher, A. (2010). Differential regulation of protrusion and polarity by PI(3)K during neutrophil motility in live zebrafish. *Dev. Cell* 18, 226–236.

Yoo, S. K., and Huttenlocher, A. (2011). Spatiotemporal photolabeling of neutrophil trafficking during inflammation in live zebrafish. *J. Leukoc. Biol.* 89, 661–667. doi: 10.1189/jlb.1010567

Zuñiga-Traslaviña, C., Bravo, K., Reyes, A., and Feijóo, C. (2017). Cxcl8b and Cxcr2 regulate neutrophil migration through bloodstream in zebrafish. *J. Immunol. Res.* 2017, 1–11. doi: 10.1155/2017/6530531

Conflict of Interest: The authors declare that the research was conducted in the absence of any commercial or financial relationships that could be construed as a potential conflict of interest.

Copyright © 2020 Kaveh, Bruton, Buckley, Oremek, Tucker, Mullins, Taylor, Rossi and Denvir. This is an open-access article distributed under the terms of the Creative Commons Attribution License (CC BY). The use, distribution or reproduction in other forums is permitted, provided the original author(s) and the copyright owner(s) are credited and that the original publication in this journal is cited, in accordance with accepted academic practice. No use, distribution or reproduction is permitted which does not comply with these terms.

3.4. Discussion

In this study, comprehensive live *in vivo* imaging provided a detailed characterisation of neutrophil and macrophage migration to heart injury in larval zebrafish. All major stages of the immune cell journey were mapped, from egress out of primary haematopoietic sites, to use of the vascular network as a migratory highway and the eventual reverse migration away from the heart. I demonstrated that larval zebrafish have negligible circulating immune cells but, like mammals, they are mobilised from haematopoietic sites into the peripheral blood following heart injury, where they can crawl, roll and freely-flow. Furthermore, the ontogeny of wound-recruited immune cells was assessed using a novel photoconversion strategy, finding the initial immune cell response to be locally derived and later, distally derived. This is important as ontology is recognised as a key determinant of immune cell phenotypes in relation to repair and regeneration (Ginhoux et al., 2016). Additionally, whole larva timelapse imaging demonstrated that both neutrophils and macrophages use the outside surface of blood vessels as a primary network for migration to the site of injury. I also built on our previously published work (Taylor et al., 2019), performing heart-synchronised imaging of wound-recruited immune cell behaviour live *in vivo* on the beating heart. This allowed us to show that neutrophils display dynamic swarm-like behaviour at the cardiac lesion. Macrophages, which are behaviourally less dynamic, are recruited to the injured heart more slowly and in greater numbers. These recruitment dynamics are consistent with mammalian cardiac injury (Epelman et al., 2015). We found that the neutrophil and macrophage response at the injured heart resolves entirely by reverse migration and not by cell death. Resolution of immune cell numbers is considered mandatory for proper tissue healing (Ortega-Gomez et al., 2013) and neutrophil reverse migration in larval zebrafish can be promoted pharmacologically (Robertson et al., 2014). However, there are currently no studies that report the effect of enhanced neutrophil resolution on tissue repair/regeneration in zebrafish. This could be addressed by pharmacologically targeting the peak neutrophil response following cardiac injury in our model. Finally, high

resolution LSFM imaging identified a novel neutrophil subset expressing the macrophage marker *mpeg1* that migrates to both heart and tail fin injuries. This highlights previously unrecognised heterogeneity in neutrophils and is an important practical consideration for researchers using *mpeg1* expression to exclusively identify macrophages. In summary, this study offers important insights into all stages of neutrophil and macrophage migration following larval zebrafish cardiac injury, providing a foundation to modulate these cells during cardiac repair/regeneration.

Chapter 4. The effect of CDK9 inhibitor treatment on the innate inflammatory and regenerative response following larval zebrafish cardiac injury

4.1. Introduction

Extensive work from our group and others has shown that CDK9 inhibitor compounds selectively induce neutrophil apoptosis, reduce neutrophil infiltration and promote the resolution of inflammation *in vitro* and *in vivo* (Rossi et al., 2006; Loynes et al., 2010; Leitch et al., 2012; Wang et al., 2012; Lucas et al., 2014; and Hoodless et al., 2016). Unlike most other CDKs, CDK9 specifically regulates transcription of primary inflammatory response genes via RNA Polymerase II. These include inflammatory cytokines and the neutrophil pro-survival protein, Mcl-1 (Sundar et al., 2020; Eyvazi et al., 2019 and Lucas et al., 2014). Acute inhibition of CDK9 therefore provides a therapeutic opportunity to preferentially suppress the transcription of short-lived inflammatory disease drivers. Two potent CDK9 inhibitors, AT7519 and Flavopiridol (FVP), have been widely used in clinical trials as anti-cancer therapies (Mahadevan et al., 2011; Chen et al., 2014; Luke et al., 2012 and Awan et al., 2016). These compounds have the potential to modify inflammatory and repair responses following cardiac injury. Our group has shown that AT7519 and FVP drive neutrophil apoptosis in a CDK9-dependent manner to resolve inflammation following tail fin resection in larval zebrafish (Hoodless et al., 2016). It is not yet understood how CDK9 inhibitors influence tissue inflammation and repair/regeneration. We recently characterised neutrophil and macrophage migratory responses in a larval zebrafish cardiac injury model using bespoke live imaging (Taylor et al., 2019 and Kaveh et al., 2020). We found a conserved sequence of events marked by an early and acute phase of neutrophil recruitment followed by sustained macrophage recruitment (Kaveh et al., 2020). In this chapter, I use our established zebrafish cardiac injury model to investigate whether CDK9 inhibitor (CDK9i) treatment with AT7519 or FVP resolves

neutrophil infiltration and examine whether this regulates downstream macrophage involvement and cardiac regeneration.

4.2. CDK9i treatment resolves neutrophil infiltration by promoting reverse migration from the cardiac injury site

I have previously characterised cardiac injury, neutrophil recruitment and resolution following ventricular laser injury in larval zebrafish. I found peak neutrophil infiltration occurs at 6 hours post injury (hpi) and neutrophil numbers entirely resolve by 48 hpi (Kaveh et al., 2020). Two CDK9 inhibitors, AT7519 and Flavopiridol (FVP), have been shown to resolve wound-recruited neutrophils by inducing apoptosis following larval zebrafish tail fin resection (Hoodless et al., 2016). To avoid disrupting the onset of inflammation in our cardiac injury model and encourage the resolution of peak neutrophilic inflammation, *Tg(myl7:GFP;mpx:mCherry)* larvae were treated continuously with AT7519 or FVP from 4 hpi. Larvae were subsequently imaged at 6 hpi and 24 hpi using epifluorescence microscopy to quantify ventricular neutrophil numbers (**Figure 4.1A**). Following recruitment to the injured ventricular apex at 4 hpi, neutrophil numbers increased in DMSO vehicle-treated larvae at 6 hpi (**Figure 4.1B** and **C**). In contrast, fewer ventricular neutrophils were present in larvae treated with 50µM AT7519 or 3µM FVP at 6 hpi (1.8 ± 0.3 vs 3.6 ± 0.5 and 1.8 ± 0.4 vs 3.7 ± 0.6) (**Figure 4.1B** and **C**). Neutrophil presence decreased in all groups at 24 hpi, indicating neutrophil numbers had mostly resolved (**Figure 4.1B** and **C**). To determine whether this drug-induced reduction in cardiac-neutrophil numbers was due to cell death or reverse migration, timelapse images were acquired using heartbeat-synchronised light sheet fluorescence microscopy (LSFM) (Taylor et al., 2019). Live imaging demonstrated that neutrophils gradually accumulate and display swarm-like behaviour at the cardiac injury site in DMSO vehicle-treated larvae (Supplementary Video 1), as previously shown (Kaveh et al., 2020). This is displayed in **Figure 4.1D** where neutrophil

migration is temporally colour coded between 4 hpi and 6 hpi. Following treatment with AT7519 (Supplementary Video 2) or FVP (Supplementary Video 3), recruited neutrophils reverse migrate to the pericardium by 6 hpi, and can do so anteriorly or posteriorly from the ventricle (**Figure 4.1D** and **F**). These data demonstrate that CDK9i drug treatment accelerates the resolution of peak neutrophilic inflammation at the cardiac injury site dynamically by reverse migration. As our timelapse imaging can account for every wound-recruited immune cell, these findings exclude neutrophil apoptosis or the efferocytosis of apoptotic neutrophils as a resolution mechanism with CDK9i treatment in this model.

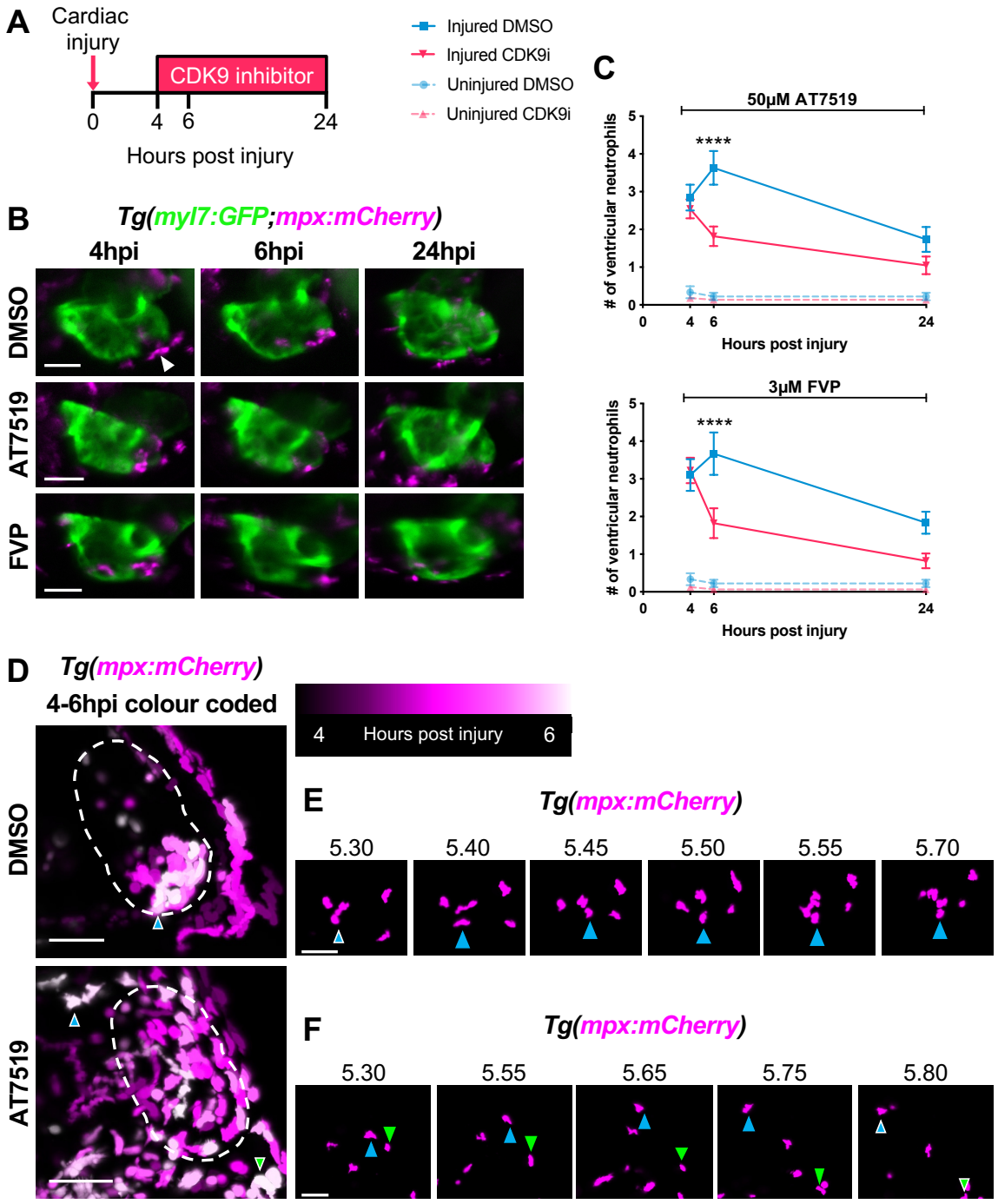

Figure 4.1: CDK9i treatment following cardiac injury resolves neutrophil infiltration by promoting reverse migration. (A) Experimental timeline indicating cardiac injury, CDK9i treatment and imaging timepoints. **(B)** Epifluorescence images of *Tg(myl7:GFP;mpx:mCherry)* larvae displaying neutrophil presence on the injured ventricle at 4 hpi (prior to treatment), and at 6 hpi and 24 hpi with 0.3% DMSO vehicle (top panel), 50μM AT7519 (middle panel) or 3μM FVP (bottom panel). Arrowhead indicates ventricular apex injury site marked by a loss of myocardial GFP and neutrophil accumulation. **(C)** Number of ventricular neutrophils at 4 hpi, 6 hpi and 24 hpi with 50μM AT7519 (top graph) or 3μM FVP (bottom graph) treatment. Error bars = SEM, *n* = 19 larvae, experimental *n* = 3. Two-way ANOVA and Bonferroni *post hoc* test performed for comparisons between cardiac-injured DMSO vehicle or CDK9i

treatment groups where **** $p < 0.0001$. **(D)** LSFM images of neutrophil (*mpx:mCherry*) migration temporally colour coded between 4 hpi and 6 hpi with 0.1% DMSO vehicle (top) or 50µM AT7519 (bottom). White dashed line indicates outline of ventricle. Arrowhead indicates starting position of neutrophil (DMSO vehicle) or ending position of neutrophils (AT7519) relative to image panels in **(E)** and **(F)** respectively. **(E)** LSFM timelapse-derived images of ventricular neutrophil migration with DMSO vehicle (0.1%), hpi indicated above each image. Blue arrowhead tracks an individual neutrophil migrating across the ventricular apex. **(F)** LSFM timelapse-derived images of neutrophil migration from ventricle to pericardium with AT7519 (50µM) treatment, hpi indicated above each image. Blue and green arrowheads track individual neutrophils reverse migrating anteriorly and posteriorly to the pericardium respectively. LSFM fluorescence images were acquired in 3D and maximum intensity projections were used for temporal colour code analysis **(D)** or are individually displayed **(E and F)**. All scale bars = 50 µm.

4.3. Continuous CDK9i treatment reduces macrophage retention by promoting reverse migration from the injured heart

Having established that CDK9i treatment induces neutrophil reverse migration following cardiac injury, macrophage involvement was next examined. We have previously described macrophage recruitment dynamics in this model. Unlike the neutrophil response, macrophage recruitment occurs up to 24 hpi, with their numbers decreasing but not returning to baseline by 48 hpi (Kaveh et al., 2020). To test the effect of CDK9i treatment during the macrophage response to cardiac injury, *Tg(myl7:GFP;mpeg1:mCherry)* larvae were treated continuously with AT7519 or FVP from 4 hpi and subsequently imaged at 6 hpi, 24 hpi and 48 hpi (**Figure 4.2A**). In the presence of AT7519 or FVP, macrophage numbers were unaffected until 24 hpi, at which point significantly fewer ventricular macrophages were present with AT7519 (8.3 ± 0.6 vs 10.9 ± 0.7) or FVP (3.7 ± 0.7 vs 10.6 ± 0.9) (**Figure 4.2B**). This attenuated macrophage presence was more pronounced with FVP, where ventricular macrophage numbers were as low as uninjured larvae (**Figure 4.2B**). At 48 hpi, ventricular macrophage numbers remained diminished with FVP treatment (3.7 ± 0.6 vs 8.7 ± 0.9), similarly AT7519-treated larvae displayed a further decrease in cardiac-recruited macrophages (4.9 ± 0.6 vs 8.0 ± 0.8) (**Figure**

4.2B). LSFM timelapse imaging indicated that cardiac-recruited macrophages gradually undergo reverse migration in the presence of FVP, as opposed to being retained on the injured ventricle in control conditions (Supplementary Video 4, Supplementary Video 5 and **Figure 4.2C**).

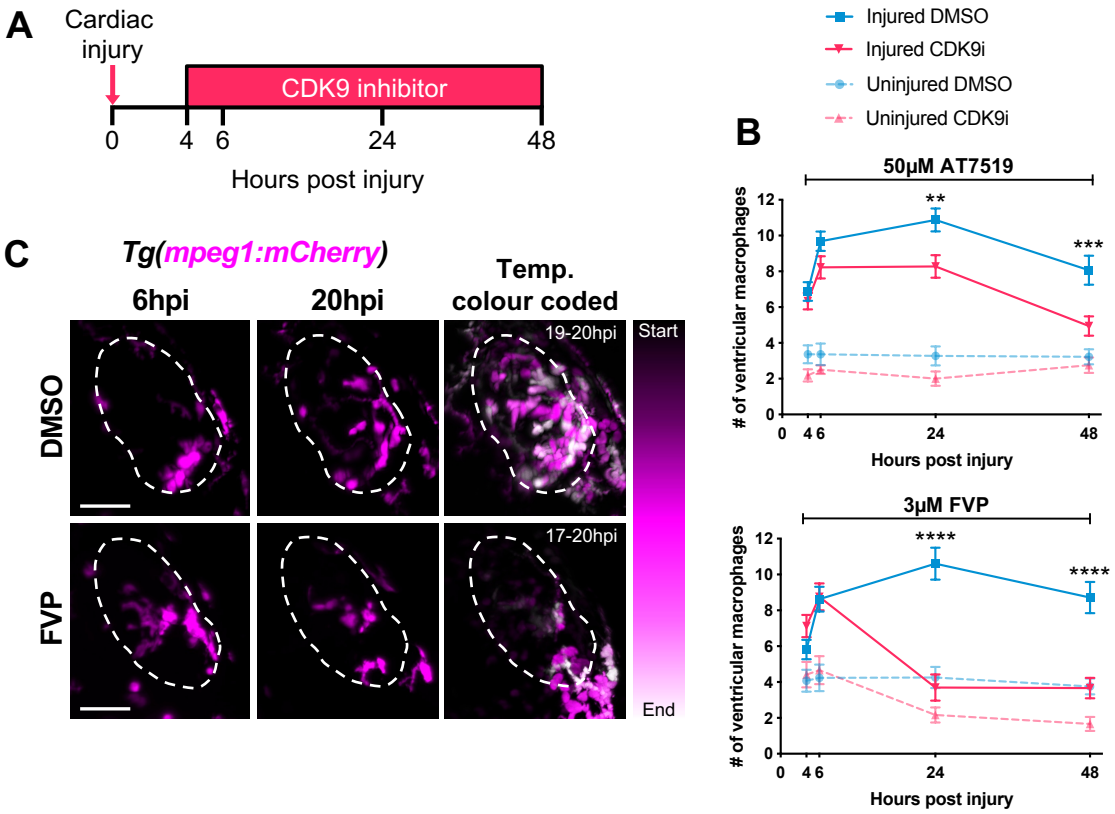

Figure 4.2: Continuous CDK9i treatment reduces macrophage retention on the injured ventricle. **(A)** Experimental timeline indicating cardiac injury, continuous CDK9i treatment and imaging timepoints. **(B)** Number of ventricular macrophages at 4 hpi, 6 hpi, 24 hpi and 48 hpi with ≤0.3% DMSO vehicle, 50μM AT7519 (top graph) or 3μM FVP (bottom graph) treatment. Error bars = SEM, *n* = 16 larvae, experimental *n* = 3. Two-way ANOVA and Bonferroni *post hoc* test performed for comparisons between cardiac-injured DMSO vehicle or CDK9i treatment groups where ** $p < 0.01$, *** $p < 0.001$, and **** $p < 0.0001$. **(C)** LSFM timelapse-derived images of cardiac-injured *Tg(mpeg1:mCherry)* larvae displaying ventricular macrophage presence at 6 hpi (left panel) and 20 hpi (middle panel) with 0.3% DMSO vehicle or 3μM FVP. LSFM timelapse images of macrophage (*mpeg1:mCherry*) migration temporally colour coded with DMSO vehicle (0.3%) or FVP (3μM) treatment (right panel). Start and end timepoint (hpi) of colour code is indicated. White dashed line indicates outline of ventricle. LSFM fluorescence images

were acquired in 3D and maximum intensity projections are used for timepoint display or temporal colour code analysis **(C)**. All scale bars = 50 µm.

4.4. Continuous CDK9i treatment impairs cardiac contractility

While examining the macrophage response with CDK9i treatment, it became apparent that ventricular contractility was being compromised at the later timepoints. Ventricular ejection fraction was indeed diminished with FVP at 24 hpi and 48 hpi, and with AT7519 at 48 hpi, in both uninjured and cardiac-injured larvae (**Figure 4.3**). Contrastingly, DMSO vehicle-treated cardiac-injured larvae displayed an almost complete functional recovery of ejection fraction by 48 hpi (**Figure 4.3**).

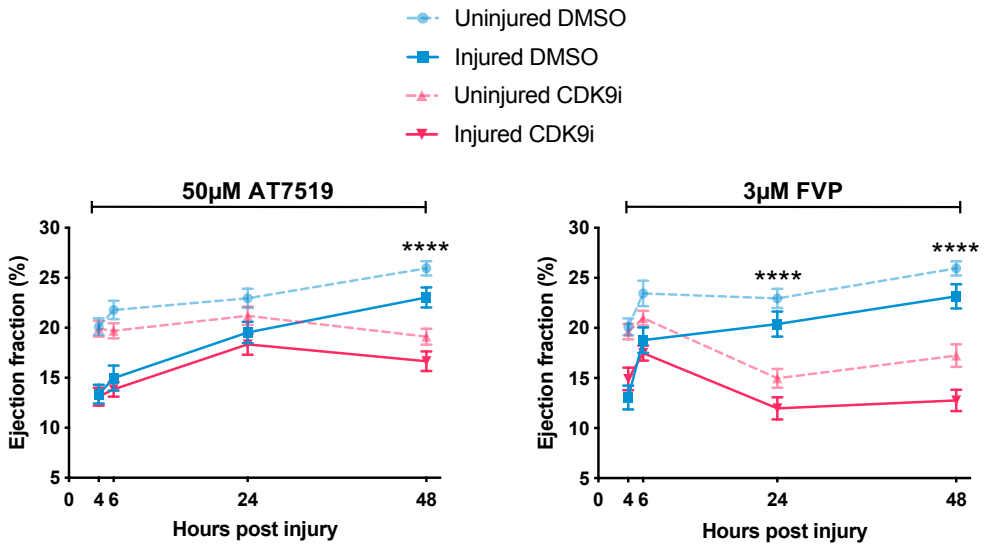

Figure 4.3: Continuous CDK9i treatment reduces ventricular contractility. Ventricular ejection fraction (%) at 4 hpi, 6 hpi, 24 hpi and 48 hpi with ≤0.3% DMSO vehicle, 50µM AT7519 (left graph) or 3µM FVP (right graph). Error bars = SEM, *n* = 18 larvae, experimental *n* = 3. Two-way ANOVA and Bonferroni *post hoc* test performed for comparisons between DMSO vehicle or CDK9i treatment groups, where **** $p < 0.0001$.

4.5. Continuous CDK9i treatment disrupts cardiomyocyte number expansion

To identify if impaired cardiac contractility is associated with a change in cardiomyocyte numbers, ventricular cardiomyocyte nuclei were quantified using *Tg(myl7:DsRed2-NLS)* larvae and LSFM. No differences were observed between treatment groups at 24 hours post treatment (hpt) (**Figure 4.4A** and **B**). At 48 hpt, however, fewer ventricular cardiomyocytes were observed in the presence of AT7519 (251.6 ± 17.5 vs 272.7 ± 14.9) and FVP (241.7 ± 21.6 vs 269.3 ± 17.3) compared to DMSO vehicle (**Figure 4.4A** and **B**). These data indicate that continuous CDK9i treatment suppresses the developmental expansion of cardiomyocyte numbers.

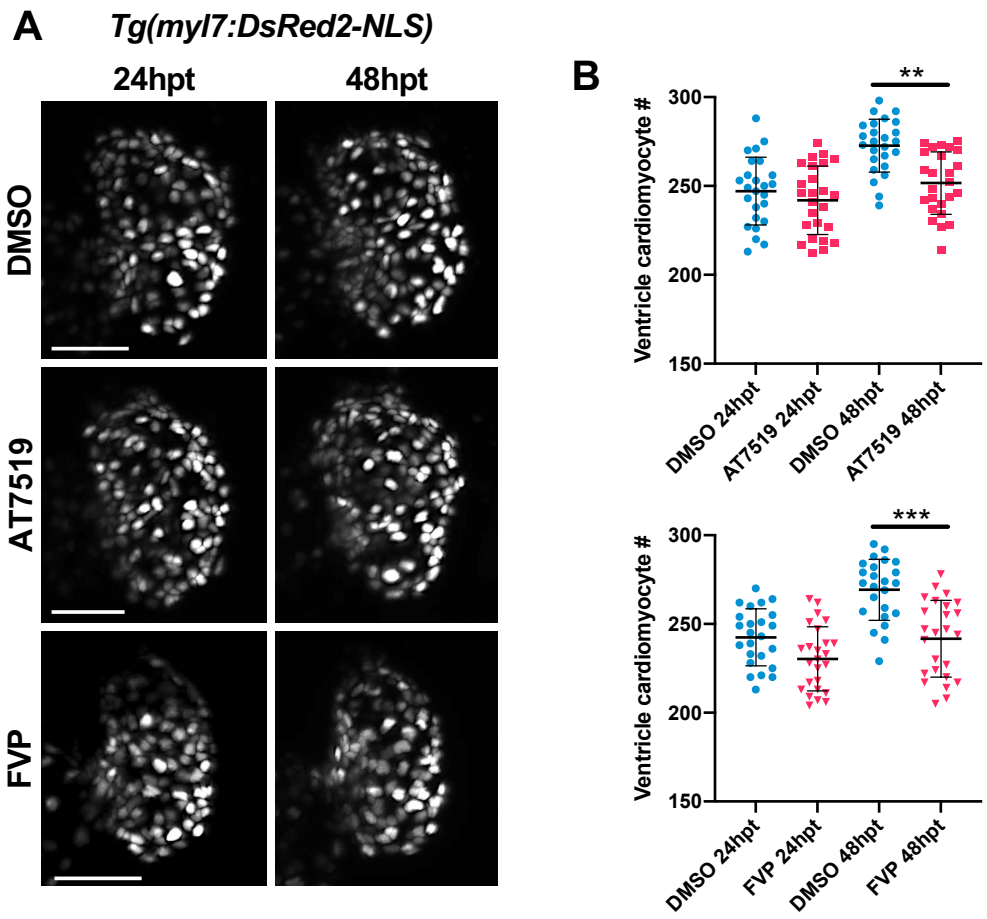

Figure 4.4: Continuous CDK9i treatment reduces cardiomyocyte number expansion. (A) LSFM images of *Tg(myl7:DsRed2-NLS)* larvae displaying ventricular cardiomyocyte nuclei at 24 hours post treatment (hpt) and 48 hpt with 0.3% DMSO vehicle (top panel), 50µM AT7519 (middle panel) or 3µM FVP (bottom panel). **(B)** Number of ventricular cardiomyocytes at 24 hpt and 48 hpt with ≤0.3% DMSO vehicle, 50µM AT7519 (top graph) or 3µM FVP (bottom graph). Error bars = SD, *n* = 25 larvae, experimental *n* = 3. One-way ANOVA and Tukey *post hoc* test performed for comparisons between DMSO vehicle or CDK9i treatment groups where ** $p < 0.01$ and *** $p < 0.001$. LSFM fluorescence images were acquired in 3D and maximum intensity projections are used for timepoint display **(A)**. All scale bars = 50 µm.

4.6. Continuous CDK9i treatment does not affect global macrophage numbers but causes neutropenia

Having identified undesirable cardiac effects with continuous CDK9i treatment, I tested if these compounds altered whole-body macrophage or neutrophil numbers by serially imaging *Tg(mpeg1:mCherry)* or *Tg(mpx:mCherry)* larvae. Across all experimental timepoints and treatment groups, whole-body macrophage numbers were unaffected and increased steadily, as expected with normal development (**Figure 4.5A**). However, at 48 hpi, significantly fewer neutrophils were present globally with AT7519 (253.7 ± 17.7 vs 318.1 ± 18.8) and FVP (218.8 ± 15.9 vs 280.9 ± 8.7) compared to their DMSO vehicle-treated counterparts (**Figure 4.5B** and **C**). Closer examination of CDK9i-treated neutropenic larvae revealed the presence of condensed and rounded neutrophils – two established phenotypic hallmarks of an apoptotic cell (**Figure 4.5D**). Thus, these data suggest that continuous exposure to CDK9 inhibitors causes neutrophil but not macrophage apoptosis, corroborating previous studies (Lucas et al., 2014 and Hoodless et al., 2016).

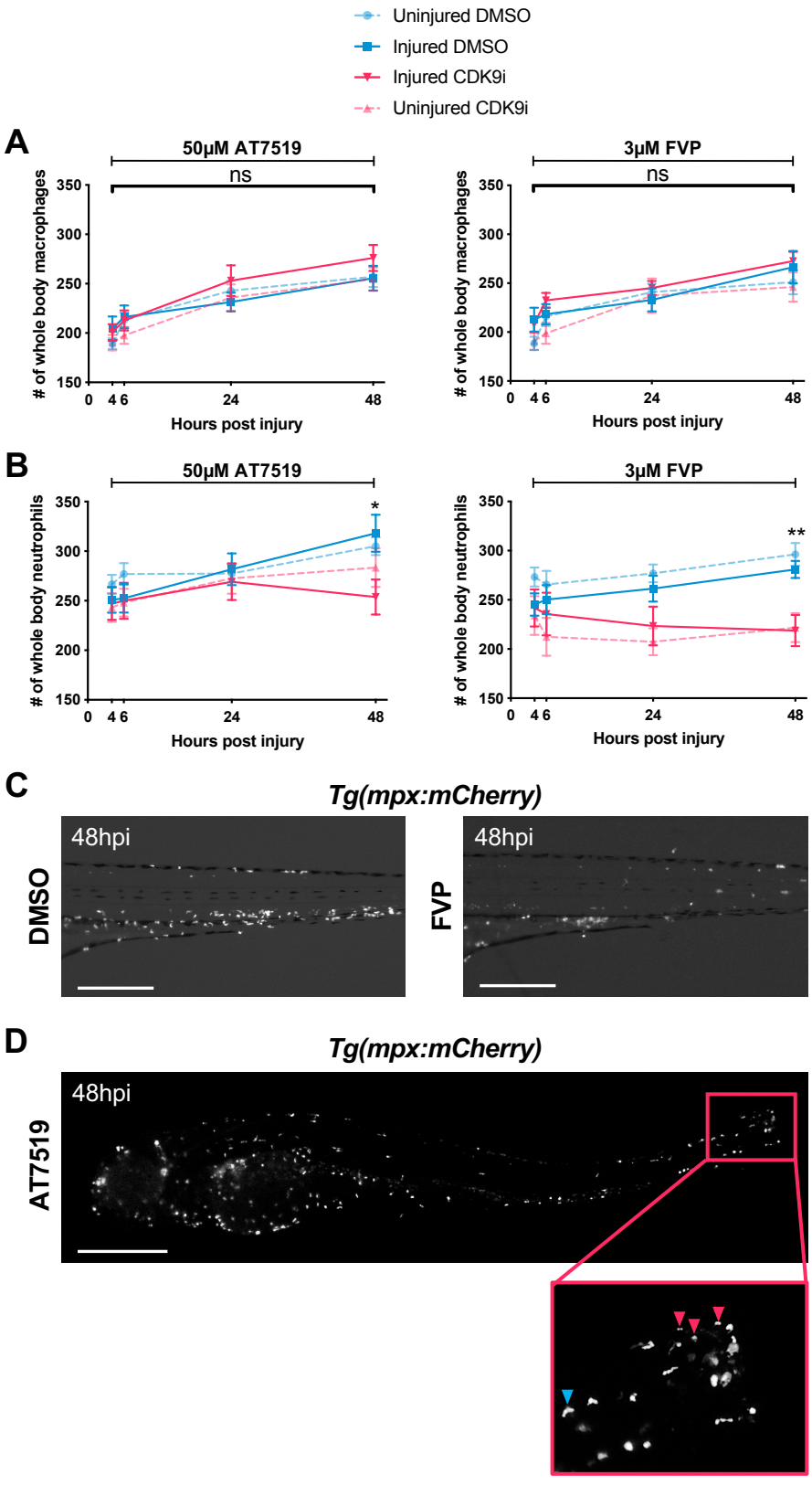

Figure 4.5: Continuous CDK9i treatment does not affect global macrophage numbers but causes neutropenia. (A) Number of whole-body macrophages at 4 hpi, 6 hpi, 24 hpi and 48 hpi, with ≤0.3% DMSO vehicle, 50μM AT7519 (left graph) or 3μM FVP (right graph). Error bars = SEM, *n* = 18 larvae, experimental *n* = 3. Two-way ANOVA and Bonferroni *post hoc* test performed for comparisons between

DMSO vehicle or CDK9i treatment groups. Ns, non-significant. **(B)** Number of whole-body neutrophils at 4 hpi, 6 hpi, 24 hpi and 48 hpi with ≤0.3%, DMSO vehicle, 50μM AT7519 (left graph) or 3μM FVP (right graph). Error bars = SEM, n = 16 larvae, experimental n = 3. Two-way ANOVA and Bonferroni *post hoc* test performed for comparisons between DMSO vehicle or CDK9i treatment groups, where * $p < 0.05$ and ** $p < 0.01$. **(C)** Epifluorescence image of *Tg(mpx:mCherry)* neutrophils within the caudal hematopoietic region at 48 hpi following treatment with 0.3% DMSO vehicle (left) or 3μM FVP (right). Scale bars = 300 μm. **(D)** Epifluorescence image of *Tg(mpx:mCherry)* neutrophils within a whole larva at 48 hpi following treatment with 50μM AT7519. Scale bar = 500 μm. Red box indicates area of magnified view below whole larva image. Within magnified view: blue arrowhead indicates a non-apoptotic neutrophil and red arrowheads indicate apoptotic (condensed and rounded) neutrophils.

4.7. Transient CDK9i treatment resolves neutrophilic inflammation without causing neutropenia or impairing cardiac contractility

To avoid the adverse cardiac effects and neutropenia apparent at the later timepoints with CDK9i treatment, the duration of treatment was modified. I have previously shown that peak neutrophilic inflammation at 6 hpi resolves by treating larvae with AT7519 or FVP from 4 hpi (**Figure 4.1**). Therefore, a shorter treatment was adopted where larvae were specifically treated with AT7519 or FVP for two hours from 4 hpi (**Figure 4.6A**). I first confirmed that following transient (pulsed) CDK9i treatment cardiac-recruited neutrophil numbers were reduced, which was not associated with neutropenia across all timepoints (**Figure 4.6B**). I next assessed ventricular ejection fraction as this was noticeably diminished at 24 hpi and/or 48 hpi during continuous CDK9i treatments (**Figure 4.3**). Following transient CDK9i treatment with AT7519 or FVP, ejection fraction remained unchanged between treatment groups, with no significant differences across all timepoints following injury (**Figure 4.6C**).

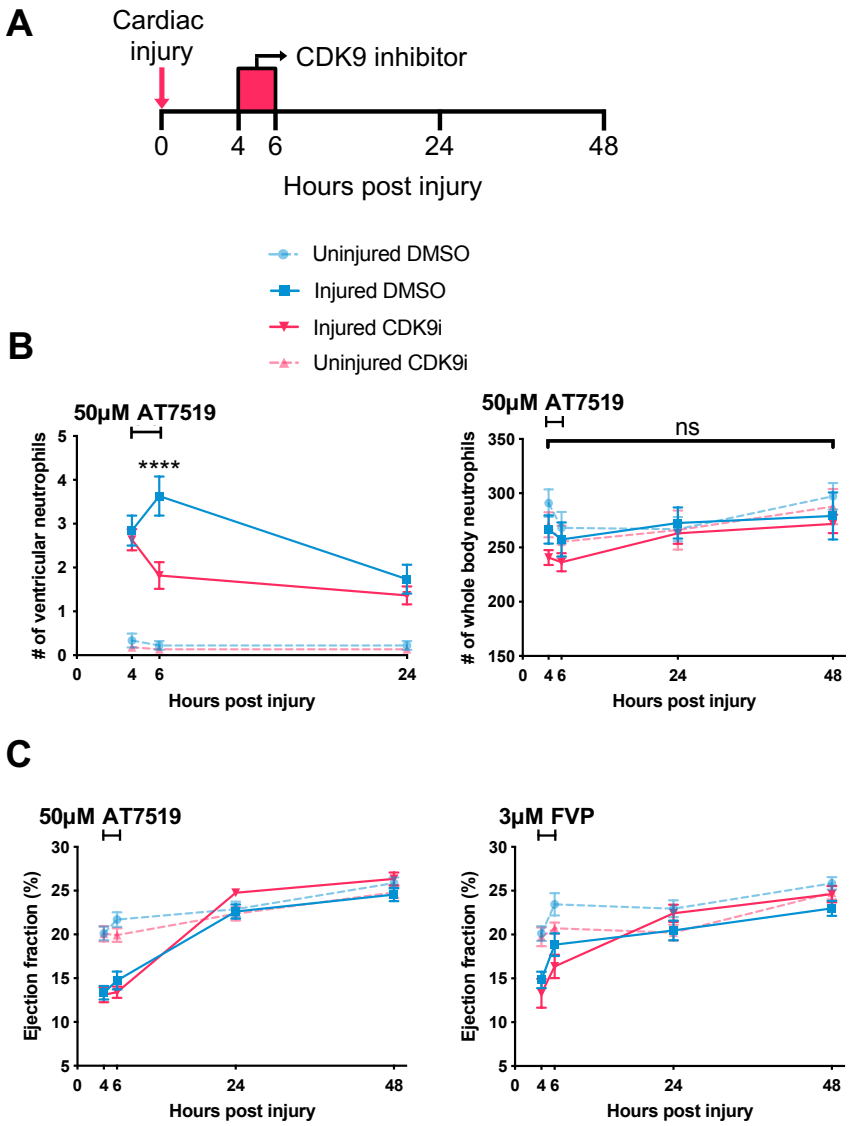

Figure 4.6: Transient CDK9i treatment resolves neutrophilic inflammation without causing neutropenia or impairing cardiac contractility. (A) Experimental timeline indicating cardiac injury, transient CDK9i treatment and imaging timepoints. **(B)** Number of ventricular neutrophils at 4 hpi, 6 hpi and 24 hpi following transient 50μM AT7519 treatment. Error bars = SEM, *n* = 18 larvae, experimental *n* = 3. Two-way ANOVA and Bonferroni *post hoc* test performed for comparisons between cardiac-injured DMSO vehicle or CDK9i treatment groups where **** $p < 0.0001$ (left). Number of whole-body neutrophils at 4 hpi, 6 hpi, 24 hpi and 48 hpi following transient treatment with 0.1% DMSO vehicle or 50μM AT7519 (right). Error bars = SEM, *n* = 18 larvae, experimental *n* = 3. Two-way ANOVA and Bonferroni *post hoc* test performed for comparisons between treatment groups. Ns, non-significant. **(C)** Ventricular ejection fraction (%) at 4 hpi, 6 hpi, 24 hpi and 48 hpi following transient treatment with ≤0.3% DMSO vehicle, 50μM AT7519 (left graph) or 3μM FVP (right graph). Error bars = SEM, *n* = 18 larvae, experimental *n* = 3. Two-way ANOVA and Bonferroni *post hoc* test performed for comparisons between DMSO vehicle or CDK9i treatment groups. No statistical differences were observed between injured DMSO vehicle and CDK9i treatment groups across all timepoints.

4.8. Transient CDK9i treatment retains cardiac macrophage numbers following injury and AT7519 enhances wound-macrophage *TNF* expression

As macrophages are essential for myocardial repair (Ma et al., 2018), I next tested whether the revised transient CDK9i treatment (**Figure 4.7A**) alters ventricular macrophage wound accumulation and/or polarisation. Unlike in mammalian models, only one macrophage polarisation marker has been reliably reported in larval zebrafish and this is TNF. These studies revealed that *TNF*$^{+}$ macrophages have pro-regenerative properties following spinal cord, somitic muscle and tail fin injury (Tsarouchas et al., 2018; Gurevich et al., 2018 and Nguyen-Chi et al., 2017). As such, the hearts of *Tg(mpeg1:mCherry;TNFa:GFP)* larvae were analysed using LSFM following cardiac injury. Unlike continuous CDK9i treatment, ventricular macrophage retention was unaffected following transient treatment with AT7519 or FVP (**Figure 4.7B, C** and **E**). Furthermore, following transient AT7519 treatment, a significant increase in ventricular *TNF*$^{+}$ macrophages was observed at 24 hpi compared to their DMSO vehicle-treated counterparts (8.8 ± 4.8 vs 4.0 ± 3.7), which returned to baseline at 48 hpi (5.0 ± 4.1 vs 4.0 ± 3.4) (**Figure 4.7B** and **D**). Interestingly, this was not detected following transient FVP treatment, as no statistical differences were observed in ventricular *TNF*$^{+}$ macrophage numbers at 24 hpi (5.2 ± 5.3 vs 3.2 ± 3.2) (**Figure 4.7B** and **E**). The increase in *TNF*$^{+}$ cardiac macrophages following transient AT7519 treatment is injury-specific, as the same phenotype was not observed when applied to uninjured larvae (**Figure 4.7F**). LSFM timelapse imaging demonstrated that *TNF*$^{+}$ macrophages migrate onto the injured ventricle or, more commonly, wound-proximal macrophages upregulate *TNF* (Supplementary Video 6 and **Figure 4.7G**). Together these data demonstrate that transient CDK9i treatment does not affect cardiac macrophage wound accumulation, and AT7519 in particular enhances *TNF* expression in wound-associated macrophages.

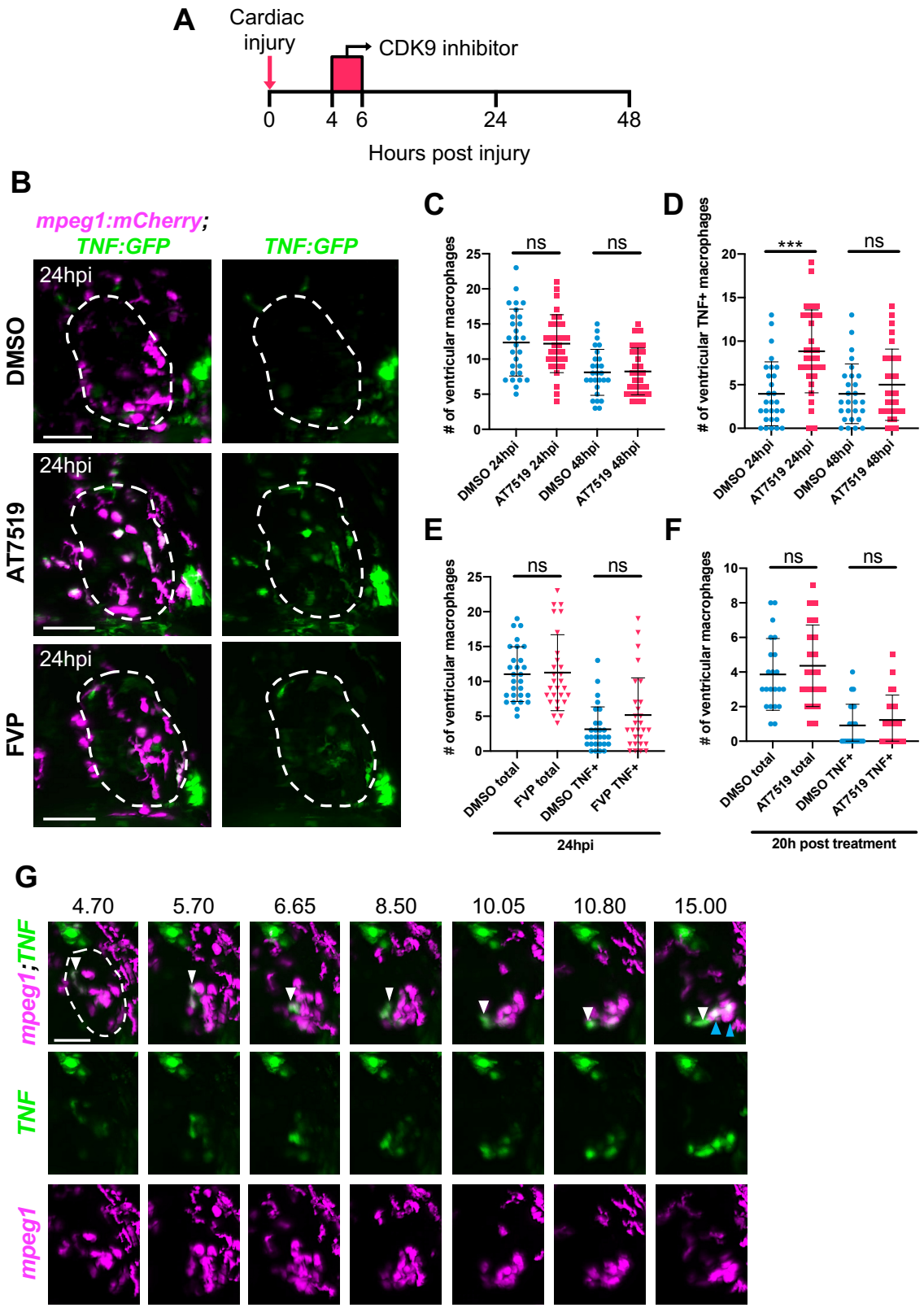

Figure 4.7: Transient CDK9i treatment does not affect cardiac macrophage numbers and AT7519 enhances wound-macrophage *TNF* polarisation following injury. (A) Experimental timeline indicating cardiac injury, transient CDK9i treatment and imaging timepoints. **(B)** LSFM images of *Tg(mpeg1:mCherry;TNFa:GFP)* larvae displaying macrophage accumulation and *TNF* expression on

the injured ventricle at 24 hpi following transient treatment with 0.3% DMSO vehicle (top panel), 50µM AT7519 (middle panel) or 3µM FVP (bottom panel). Number of ventricular macrophages **(C)** and ventricular *TNF*+ macrophages **(D)** at 24 hpi and 48 hpi following transient AT7519 (50µM) treatment. **(E)** Number of ventricular macrophages (total and *TNF*+) at 24 hpi following transient FVP (3µM) treatment. **(C, D and E)** Error bars = SD, *n* = 28 larvae, experimental *n* = 3. One-way ANOVA and Tukey *post hoc* test performed for comparisons between treatment groups where *** $p < 0.001$ and Ns, non-significant. **(F)** Number of ventricular macrophages (total and *TNF*+) at 20 hpt following transient treatment with 0.1% DMSO vehicle or 50µM AT7519 in uninjured larvae. Error bars = SD, *n* = 23 larvae, experimental *n* = 3. One-way ANOVA and Tukey *post hoc* test performed for comparisons between treatment groups. Ns, non-significant. **(G)** LSFM timelapse-derived images displaying macrophage migration and *TNF* expression at the injured ventricle, hpi indicated above each image. White arrowhead (top panel, all timepoints) tracks an individual *TNF*+ macrophage migrating to the ventricular apex. Blue arrowheads (top panel, at 15.00 hpi) indicate two macrophages that have upregulated their *TNF* expression at the injured ventricular apex. LSFM fluorescence images were acquired in 3D and maximum intensity projections are displayed. White dashed line indicates outline of ventricle. All scale bars = 50 µm.

4.9. Transient AT7519 but not Flavopiridol treatment enhances cardiomyocyte number expansion following injury

I next tested whether the differing regulation of macrophage *TNF* polarisation following transient AT7519 or FVP treatment (**Figure 4.7**) influenced cardiomyocyte numbers. Following transient treatment with AT7519 or FVP (**Figure 4.8A**), LSFM scans of *Tg(myl7:DsRed2-NLS)* larvae indicated no change in ventricular cardiomyocyte numbers at 24 hpi (**Figure 4.8C**). At 48 hpi, however, ventricular cardiomyocyte numbers were significantly elevated following AT7519 treatment (321.6 ± 31.7 vs 292.7 ± 23.5) (**Figure 4.8B** and **C**), indicating an increase in cardiomyocyte number expansion. At 48 hpi following FVP treatment no difference in cardiomyocyte numbers was present (298.0 ± 22.5 vs 298.8 ± 25.8) (**Figure 4.8B** and **C**). This AT7519-specific increase in cardiomyocyte numbers was injury-specific as uninjured larvae displayed no change in ventricular cardiomyocyte numbers following the same treatment (**Figure 4.8D**).

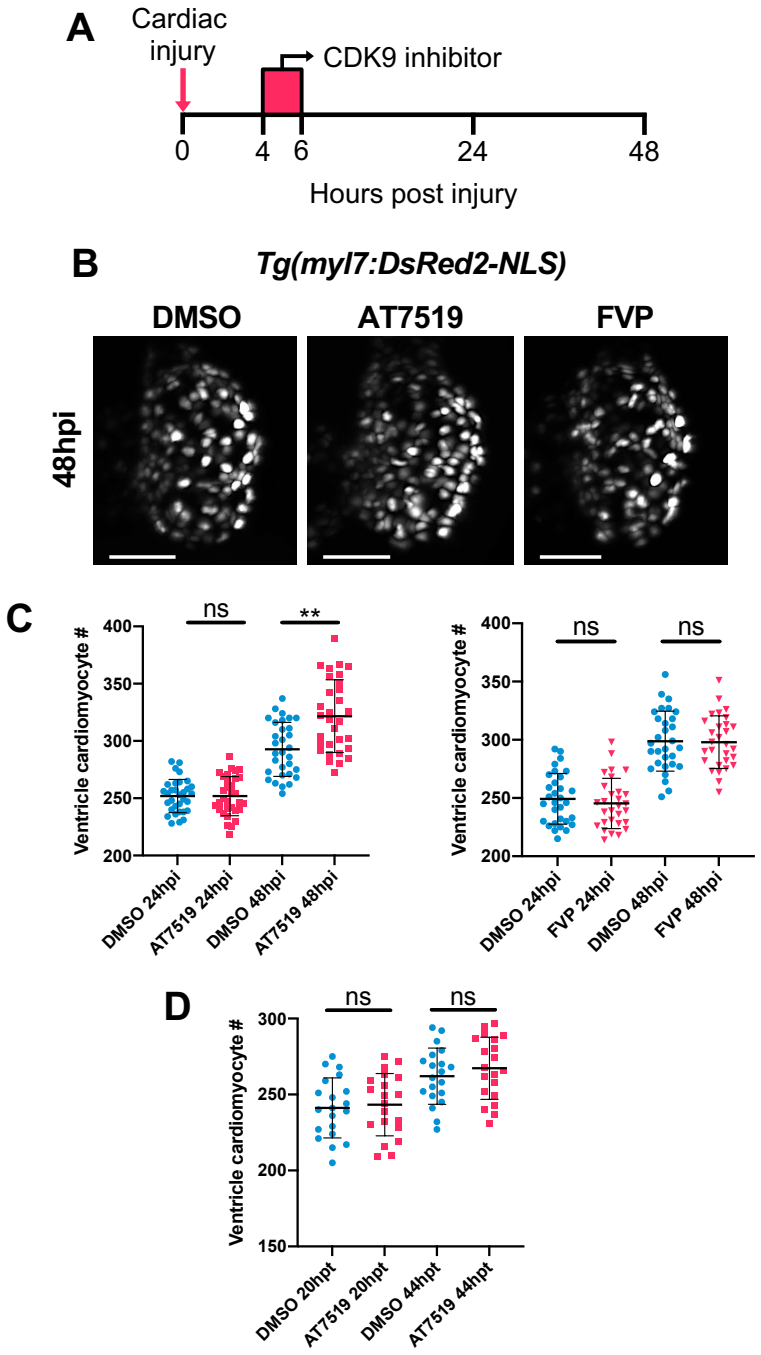

Figure 4.8: Transient AT7519 treatment enhances cardiomyocyte number expansion following injury. (A) Experimental timeline indicating cardiac injury, transient CDK9i treatment and imaging timepoints. **(B)** LSFM images of *Tg(myl7:DsRed2-NLS)* larvae displaying ventricular cardiomyocyte nuclei at 48 hpi following transient treatment with 0.3% DMSO vehicle (left panel), 50µM AT7519 (middle panel) or 3µM FVP (right panel). **(C)** Number of ventricular cardiomyocytes at 24 hpi and 48 hpi following transient treatment with ≤0.3% DMSO vehicle, 50µM AT7519 (left graph) or 3µM FVP (right graph). Error bars = SD, $n = 29$ larvae, experimental $n = 3$. One-way ANOVA and Tukey *post hoc* test performed for comparisons between DMSO vehicle or CDK9i treatment groups where ** $p < 0.01$. **(D)** Number of ventricular cardiomyocytes in uninjured larvae at 20 hpt and 44 hpt following transient treatment with

0.1% DMSO vehicle or 50µM AT7519. Error bars = SD, *n* = 21 larvae, experimental *n* = 3. One-way ANOVA and Tukey *post hoc* test performed for comparisons between treatment groups. Ns, non-significant. LSFM fluorescence images were acquired in 3D and maximum intensity projections **(B)** are displayed. All scale bars = 50 µm. Ns, non-significant.

4.10. Transient AT7519 treatment accelerates structural myocardial regeneration following injury

I have previously shown that laser injury induces cardiomyocyte death locally at the ventricular apex (Kaveh et al., 2020). In order to determine whether the increase in cardiomyocyte numbers identified with transient AT7519 treatment is associated with improved structural myocardial regeneration (**Appendix Figure 1**), LSFM scans of cardiac-injured *Tg(myl7:GFP)* larvae were acquired and the ventricular wound area was quantified (**Figure 4.9A**). At 24 hpi, myocardial wound area was similar between DMSO vehicle-treated and AT7519-treated groups (109.2 ± 84.8µm^2 vs 100.9 ± 59.3µm^2) (**Figure 4.9B** and **C**). At 48 hpi, both groups displayed a reduction in wound area, although the DMSO vehicle group trended towards a larger wound area compared to the AT7519 group (53.1 ± 57.6µm^2 vs 29.9 ± 30.2µm^2) (**Figure 4.9B** and **C**). To better understand the rate of wound regression in these groups, percentage myocardial wound closure between 24 hpi and 48 hpi was analysed. This indicated a clear increase in myocardial wound closure following AT7519 treatment compared to controls (69.6% vs 21.2%) (**Figure 4.9D**), highlighting an acceleration in the rate of myocardial wound regression. To closely examine how the myocardial wound structurally regenerates, LSFM timelapse images were acquired. Live heartbeat-synchronised timelapse imaging revealed that wound-proximal cardiomyocytes protrude into, and subsequently bridge across, the injured myocardium to regenerate the damaged tissue (Supplementary Video 7 and **Figure 4.9B** and **E**).

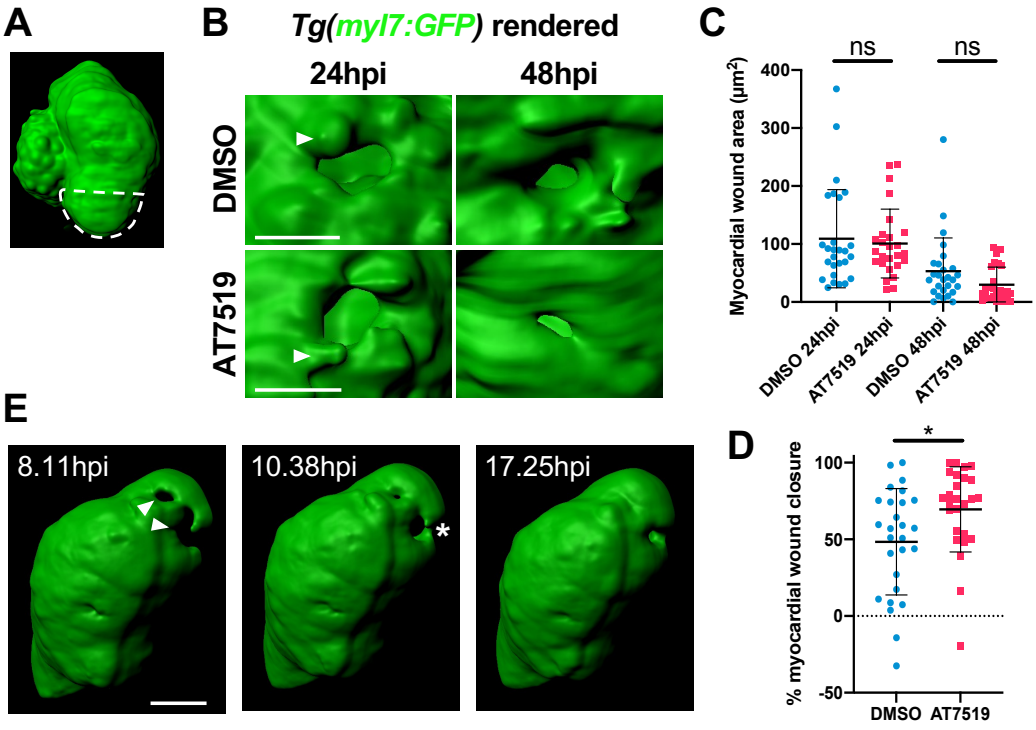

Figure 4.9: Transient AT7519 treatment accelerates the rate of myocardial wound regeneration following injury. (A) Surface rendered LSFM image of a *Tg(myl7:GFP)* heart. White dashed line outlines the ventricular apex. **(B)** Surface rendered LSFM image of a *Tg(myl7:GFP)* ventricular apex wound at 24 hpi and 48 hpi, following transient treatment with 0.1% DMSO vehicle (top panel) or 50μM AT7519 (bottom panel). Arrowheads indicate cardiomyocyte protrusions adjacent to the myocardial wound (*myl7:GFP* negative). Scale bars = 20 μm. **(C)** Myocardial wound area (μm²) at 24 hpi and 48 hpi following transient treatment with 0.1% DMSO vehicle or 50μM AT7519. Error bars = SD, *n* = 27 larvae, experimental *n* = 3. One-way ANOVA and Tukey *post hoc* test performed for comparisons between treatment groups. **(D)** Myocardial wound closure (%) between 24 hpi and 48 hpi following transient treatment with 0.1% DMSO vehicle or 50μM AT7519. Error bars = SD, *n* = 27 larvae, experimental *n* = 3. Mann–Whitney *U*-test performed for comparison between treatment groups where * $p < 0.05$. **(E)** Surface rendered LSFM timelapse-derived images of an injured *myl7:GFP* ventricle, hpi indicated. Arrowheads indicate the myocardial wound (*myl7:GFP* negative). Asterisk indicates cardiomyocytes bridging across the myocardial wound. LSFM fluorescence images were acquired in 3D and surface renders **(A, B and E)** are displayed. Unless stated, all scale bars = 50 μm. Ns, non-significant.

4.11. Discussion

Resolving inflammation is a promising therapeutic approach to promote tissue repair/regeneration following injury. CDK9 inhibitor compounds, currently deployed in clinical trials as anti-cancer treatments, can be applied experimentally to curtail early neutrophilic inflammation (Rossi et al., 2006; Lucas et al., 2014; Hoodless et al., 2016 and Cartwright et al., 2019). This study is the first to examine the effect of CDK9 inhibitors, AT7519 and FVP, during the inflammatory and regeneration response following tissue injury *in vivo*. Using a larval zebrafish model of cardiac injury combined with high resolution live imaging, I determined that AT7519 and FVP resolve neutrophilic inflammation at the injured heart via reverse migration, but differentially regulate macrophage polarisation and myocardial regeneration.

As previously shown in various models of injury and infection *in vivo* (Rossi et al., 2006; Loynes et al., 2010; Leitch et al., 2012; Lucas et al., 2013; Lucas et al., 2014; Hoodless et al., 2016 and Barth et al., 2020), I found CDK9 inhibitors to enhance the resolution of neutrophilic inflammation following heart injury in larval zebrafish. Numerous studies have demonstrated that CDK9 inhibitors induce neutrophil apoptosis via downregulation of Mcl-1 (Moulding et al., 1998; Rossi, et al., 2006; Leitch et al., 2012; Wang et al., 2012; Lucas et al., 2013; Lucas et al., 2014 and Dorward et al., 2017). Here, I show that AT7519 and FVP promote neutrophil resolution from the cardiac lesion *via* reverse migration (**Figure 4.1**). Despite previously observing increased neutrophil apoptosis following tail fin resection with CDK9i treatment (Hoodless et al., 2016), there was no evidence of such events at the injured heart. Reverse migration is the primary inflammatory cell resolution mechanism in this model, most likely due to the size and sterility of the myocardial laser wound (Kaveh et al., 2020). A wound of such scale would release fewer chemoattractant signals such as reactive oxygen species, cytokines and chemokines responsible for regulating neutrophil wound retention (Yoo et al., 2011; Yan

et al., 2014; Powell et al., 2017; Coombs et al., 2019; Isles et al., 2019). Expression of these inflammatory mediators could indeed be modulated in the presence of AT7519 or FVP, as documented in other studies (Santo et al., 2010 and Yik et al., 2014). Consequently, this could alter the chemoattractant gradient, desensitising wound-swarming neutrophils and inducing their reverse migration. Similarly, other compounds that cause neutrophil apoptosis in mammalian systems have been shown to promote neutrophil reverse migration following tail fin wounding in larval zebrafish (Robertson et al., 2014). Additional research is needed to better understand how CDK9 inhibitors regulate the aforementioned inflammatory signals to induce neutrophil reverse chemotaxis from sterile wounds (Hind and Huttenlocher, 2018).

The majority of CDK9 inhibitors act by competitively inhibiting the ATP-binding domain which is conserved between all CDKs (Krystof et al., 2012). Consequently, long-term exposure to CDK9 inhibitor compounds can cause undesirable effects due to inhibition of other CDKs, many of which are cell-cycle regulators, such as CDK2 (Azevedo et al., 1996 and Wyatt et al., 2008). We showed that continuous AT7519 or FVP treatments result in developmental and injury-associated adverse effects including reduced cardiomyocyte number expansion, ventricular ejection fraction, macrophage wound-retention and neutropenia (**Figure 4.2**; **Figure 4.3**; **Figure 4.4** and **Figure 4.5**). By limiting the CDK9i treatment period to a two-hour window, I was able to enhance neutrophil resolution while avoiding the adverse effects (**Figure 4.6**). Principally this approach is more clinically relevant compared to continuous treatments. Using the transient treatment, ventricular macrophage accumulation was unaffected (**Figure 4.7**), suggesting prolonged neutrophil swarming is not required for macrophage retention and/or recruitment. In addition, I observed an unexpected difference between CDK9i treatments where AT7519, but not FVP, increased the polarisation of wound-macrophages to a *TNF*$^{+}$ phenotype (**Figure 4.7**). FVP has been shown to inhibit TNF activation and signaling in other models of inflammation (Takada and Aggarwal, 2004; Haque et al., 2011 and

Schmerwitz et al., 2011), whereas AT7519 does not disrupt *TNF* activity (Lucas et al., 2014). Therefore, a plausible explanation could be that FVP suppresses *TNF* upregulation in wound-associated macrophages. Moreover, using LSFM timelapse imaging I directly observed a migratory *TNF*$^{+}$ macrophage settle at the injury site, neighbouring two wound-associated macrophages. Within six hours, the two proximal and originally *TNF*^{low} macrophages markedly upregulate their TNF expression (**Figure 4.7**). This observation suggests that paracrine signaling from nearby inflammatory cells encourages *TNF* upregulation in macrophages. As such, macrophage *TNF* expression may also be upregulated by prolonged contact/proximity with swarming neutrophils at the injured ventricle. Studies using macrophage-null zebrafish have reported elevated and sustained neutrophil responses to wounding (Shiau et al., 2015; Tsarouchas et al., 2018 and Tauzin et al., 2014), suggesting macrophages promote timely neutrophil resolution. Therefore, during AT7519 or FVP treatment, wound-associated macrophages could encourage the reverse migration of infiltrating neutrophils via contact-mediated inhibition or paracrine signaling, as suggested by others in larval zebrafish (Tauzin et al., 2014 and Loynes et al., 2018).

Cellular mechanisms regulating immune cell involvement after wounding have been largely characterised in murine models and are not entirely recapitulated in zebrafish. For example, neutrophil apoptosis, subsequent macrophage efferocytosis and polarisation have not been reported following wounding in larval zebrafish (Starnes and Huttenlocher, 2012; Robertson et al., 2014; Loynes et al., 2018 and Kaveh et al., 2020). Instead, the role of immune cells is more dynamic and closely coupled to molecular signaling (Loynes et al., 2018; Coombs et al., 2019 and Tsarouchas et al., 2018). Larval zebrafish studies have described that *TNF*$^{+}$ macrophages have pro-regenerative roles following tissue wounding (Nguyen-Chi et al., 2017; Tsarouchas et al., 2018 and Gurevich et al., 2018). A recent single-cell RNA sequencing study found wound-associated *TNF*$^{+}$ macrophages express high levels of traditional M1 and M2 markers

(Cavone et al., 2021), suggesting they are a genuine pro-regenerative subtype in larval zebrafish. Our data show that cardiac-injured larvae transiently treated with AT7519, but not FVP, exhibit enhanced cardiomyocyte number expansion two-days post injury (**Figure 4.8**), one day after the peak *TNF*$^{+}$ macrophage response (**Figure 4.7**). One mechanism for this pro-regenerative effect could be that cardiac *TNF*$^{+}$ macrophages secrete mitogens, such as VEGF, as is the case during skeletal muscle wounding angiogenesis (Gurevich et al., 2018). Similarly, TNF itself could act as a mitogen via activation of histone proteins in progenitor cells, as described during spinal cord regeneration (Cavone et al., 2021). Alternatively, *TNF*$^{+}$ macrophages could stimulate other cardiac cell types, such as the endocardium or epicardium to promote cardiomyocyte proliferation. In order to address this, macrophage ablation experiments and/or transcriptomic sequencing of heart cells (endocardium, myocardium and epicardium), macrophages and neutrophils would be required.

Our data indicate that increased cardiomyocyte numbers following transient AT7519 treatment correlates with accelerated myocardial wound closure, to the point of almost complete regeneration (**Figure 4.9**). This was not, however, associated with enhanced cardiac function, which recovered rapidly in both AT7519-treated and control larvae. Cardiomyocyte proliferation is a prerequisite for cardiac regeneration in many animal models (Godwin et al., 2017; Chablais et al., 2011; Curado et al., 2007 and Porrello et al., 2013), suggesting that cardiomyocyte proliferation, potentially enhanced by *TNF*$^{+}$ macrophages in our model, could be driving myocardial wound closure. Furthermore, 4D LSFM imaging during myocardial regeneration revealed a novel observation where wound-bordering cardiomyocytes protrude into and subsequently bridge across the wound, gradually sealing it (**Figure 4.9** and Supplementary Video 7). Cardiomyocyte bridging has previously been reported following transplantation of neonatal rat cardiomyocytes to infarcted hearts *in vitro* (Sekine et al., 2006), however to our knowledge, this is the first time such an event has been observed live in the

beating heart. Extracellular matrix proteins, such as collagen, could form a scaffold to facilitate cardiomyocyte wound bridging, as similar mechanisms occur in the injured hearts of adult zebrafish (Simoes et al., 2020). Future research should address whether macrophages are required for injury-associated cardiomyocyte proliferation and wound regression via cardiomyocyte bridging. Performing high resolution live imaging and complementary sequencing experiments in this model would reveal the cell types and signaling molecules that regulate cardiac regeneration during different stages of the injury response.

Chapter 5. Identifying novel CDK9 inhibitor compounds

5.1. Introduction

The vast majority of CDK9 inhibitors act by competitively inhibiting the ATP-binding domain of CDK9 (**Figure 1.2**), which is structurally conserved between CDKs (Krystof et al., 2012). Therefore, CDK9 inhibitor compounds can cause non-specific adverse effects due to inhibition of other CDKs responsible for cell cycle regulation, such as CDK2 (Azevedo et al., 1996 and Wyatt et al., 2008). In the previous chapter, I showed that continuously treating larval zebrafish with AT7519 or FVP results in developmental and injury-associated adverse effects, specifically reduced cardiomyocyte numbers, ventricular ejection fraction, macrophage wound-retention, in addition to neutropenia. By limiting the CDK9i treatment period to a two-hour window, I was able to enhance neutrophil resolution while avoiding all adverse effects, also revealing that AT7519 can cause pro-regenerative effects. To mitigate the risk of adverse effects associated with CDK9i treatment, there is a need to seek and develop CDK9 inhibitors that display a higher level of selectivity, while maintaining a high degree of potency (Krystof et al., 2012). Identifying highly selective and potent CDK9 inhibitors could have important clinical implications for treating a range of inflammatory disorders associated with acute or chronic neutrophilic inflammation (Rossi et al., 2007). Newly developed CDK9 inhibitor compounds are typically tested for potency and selectivity using various *in vitro* assays, with little or no *in vivo* validation (Albert et al., 2014 and Olson et al., 2018). Hence, *in vitro* and *in vivo* based experimental approaches could be used in tandem to efficiently validate and streamline promising CDK9 inhibitors for use in certain disease scenarios. The larval zebrafish and isolated human neutrophils are highly amenable to combinatory drug screening studies (Lucas et al., 2013 and Robertson et al., 2014); thus, both models can be used to identify efficacious CDK9 inhibitors in a relatively high throughput manner. In this chapter, I develop an *in vivo*

assay to assess CDK9 inhibitor selectivity in larval zebrafish, perform an *in silico* similarity screen to identify efficacious and novel CDK9 inhibitors, and validate the biological efficacy of Flavopiridol in an *in vitro* human neutrophil apoptosis assay.

5.2. A zebrafish selectivity assay demonstrates AT7519 is a more selective CDK9 inhibitor than Flavopiridol

In the previous chapter, I showed that AT7519 and FVP promote wound-neutrophil reverse migration, and that transient treatment with AT7519, but not FVP, increased macrophage polarisation, enhanced cardiomyocyte number expansion and accelerated myocardial regeneration. To better understand the differential pro-regenerative effects observed with AT7519 and FVP treatment, I explored the selectivity of these two CDK9 inhibitor compounds in larval zebrafish. Previous drug screening studies have indicated that AT7519 is a more selective CDK9 inhibitor compared to first-generation CDK9 inhibitors such as FVP (Santo et al., 2010 and Liu et al., 2011). Thus, I hypothesised that FVP is a less selective CDK9 inhibitor compared to AT7519. I formally tested the Cdk9 selectivity of these inhibitors *in vivo* using stable *cdk9* knockout zebrafish previously generated using CRISPR/Cas9 (Hoodless et al., 2016). Homozygous *cdk9* mutant zebrafish larvae are phenotypically distinguishable at 3 dpf (Hoodless et al., 2016), therefore they can be reliably selected at this stage. Compared to their heterozygous and wild-type siblings, homozygous *cdk9* mutants display a curved body axis, shorter body length and smaller eye diameter (**Figure 5.1A**). No phenotypic differences are identifiable between heterozygous mutants and their wild-type siblings during larval stages (**Figure 5.1A**), which was confirmed by genotyping (**Figure 5.1B**). I reasoned that a truly specific CDK9 inhibitor compound would not have any effect on *cdk9*$^{-/-}$ knockout zebrafish larvae. To test this, I continuously treated 3 dpf homozygous *cdk9* mutants with DMSO vehicle, AT7519 or FVP and quantified heart rate between treatments as a readout for overall health

across 48 hours. A decline in heart rate with AT7519 or FVP treatment compared to vehicle would indicate the drugs are acting in a Cdk9-independent manner, thus allowing real-time examination of CDK9 inhibitor selectivity *in vivo*. First, larvae were treated at equal 1µM concentrations of AT7519 or FVP (or DMSO vehicle) so that CDK9i treatments were fair and comparable. Between 2 hpt and 48 hpt, all treatment groups displayed a gradual reduction in heart rate, which was associated with decreased survival from 24 hpt (**Figure 5.1C** and **E**). At 24 hpt, compared to the DMSO vehicle group, FVP-treated, but not AT7519-treated, mutant larvae displayed a significant reduction in heart rate (22.5 ± 8.9 vs 80.4 ± 6.6 and 63.2 ± 8.6 vs 80.4 ± 6.6), associated with increased mortality (64.3% vs 14.3%) (**Figure 5.1C** and **E**). The heart rates of larvae treated with AT7519 were unchanged across all timepoints and displayed a more gradual reduction, similar to their DMSO vehicle-treated counterparts (**Figure 5.1C** and **E**). To draw direct comparisons between drug selectivity and the differential phenotypes observed, I applied the drug concentrations established originally for resolving neutrophilic inflammation (50µM for AT7519 and 3µM for FVP). Using these concentrations, FVP-treated mutant larvae displayed significantly lowered heart rates from 2 hpt (90.0 ± 6.7 vs 117.1 ± 6.2) until 12 hpt (64.3 ± 6.5 vs 99.6 ± 4.9) compared to their DMSO vehicle-treated and AT7519-treated counterparts, which showed no differences across these timepoints (**Figure 5.1D**). Until 12 hpt, this FVP-induced reduction in heart rate was not due to a change in survival (**Figure 5.1F**). At 24 hours post FVP treatment, only 14% of larvae survived, of which displayed dramatically diminished heart rates (**Figure 5.1D** and **F**). In contrast, at 24 hours post AT7519 treatment survival only decreased to 93%, but the heart rates of these larvae were lower compared to their DMSO vehicle-treated counterparts (60.0 ± 9.0 vs 88.2 ± 8.7) (**Figure 5.1D** and **F**). At 48 hpt, no larvae survived with FVP and AT7519, whereas 36% of DMSO vehicle-treated survived (**Figure 5.1D** and **F**). In summary, I have developed a proof-of-concept assay using knockout larval zebrafish mutants to examine real-time drug selectivity. The assay indicated whether AT7519 or FVP exhibit Cdk9-independent effects up to 48 hpt, with FVP

displaying significant off-target effects from 2 hpt. Overall, these comparative data suggest that AT7519 is a particularly selective CDK9 inhibitor *in vivo*.

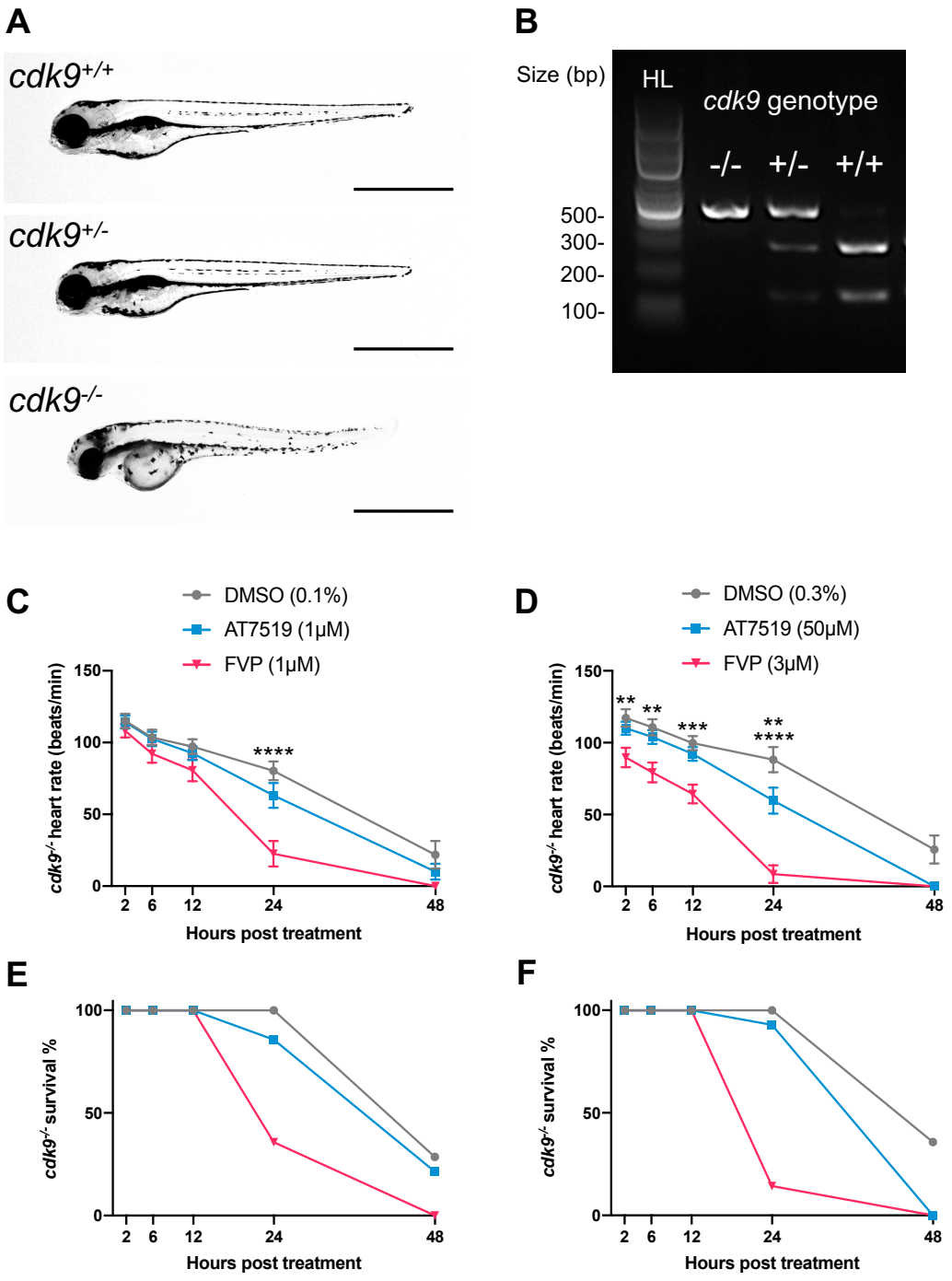

Figure 5.1: AT7519 is a more selective CDK9 inhibitor than Flavopiridol. (A) Brightfield image of a *cdk9*$^{+/+}$ (top), *cdk9*$^{+/-}$ (middle) and *cdk9*$^{-/-}$ (bottom) whole zebrafish larva at 4 dpf. Scale bars = 1 mm. **(B)** Restriction enzyme digest gel displaying band sizes and *cdk9* genotypes of zebrafish. Hyperladder (HL) bands and individual genotype bands (in order: *cdk9*$^{-/-}$, *cdk9*$^{+/-}$ and *cdk9*$^{+/+}$) are indicated. Heart rate (beats/min) **(C)** and survival % **(E)** of *cdk9*$^{-/-}$ larvae at 2 hpt, 6 hpt, 12 hpt, 24 hpt and 48 hpt with 0.1%,

DMSO vehicle, 1μM AT7519 or 1μM FVP treatment. Heart rate (beats/min) **(D)** and survival % **(F)** of *cdk9*$^{-/-}$ larvae at 2 hpt, 6 hpt, 12 hpt, 24 hpt and 48 hpt with 0.3% DMSO vehicle, 50μM AT7519 or 3μM FVP treatment. **(C and D)** Error bars = SEM, $n = 15$ larvae, experimental $n = 3$. Two-way ANOVA and Bonferroni *post hoc* test performed for comparisons between DMSO vehicle or CDK9i treatment groups where ** $p < 0.01$, *** $p < 0.001$ and **** $p < 0.0001$.

5.3. Generating a focussed compound library to identify novel and efficacious CDK9 inhibitors from BioAscent's 125k library

This aspect of my PhD was undertaken in collaboration with drug discovery contract research organisation, BioAscent Discovery Ltd. BioAscent offer a modern, automated compound management, screening and logistic facility to pharmaceutical companies and academic institutions. They provide access to 125,000+ intellectual property free, lead-like and drug-like pharmaceutical compounds, including widely diverse and target-specific compounds. Specifically, 27.5% of BioAscent's 125k compound library consists of specialised kinase-like inhibitors. In addition to supplying compound collections, BioAscent offer multiple biochemical, biophysical and cellular assay development services to perform high throughput screening. Thus, I planned to use BioAscent's diverse 125k compound library and screening services to identify novel and efficacious CDK9 inhibitor compounds. These compounds would serve as medicinal chemistry starting points to further test and optimise to improve potency and selectivity. I have already identified AT7519 to be a considerably selective CDK9 inhibitor that resolves neutrophilic inflammation and enhances cardiomyocyte regeneration. As such, I performed an extensive literature search to identify other potent and selective CDK9 inhibitor drugs that have been developed. These compounds were selected based on published IC50 values and include: LDC000067, MC180295, AZD4573, NVP-2 and iCDK9 (**Table 2.5**) (Albert et al., 2014; Zhang et al., 2018; Cidado et al., 2020; Olson et al., 2018 and Lu et al., 2015). Including AT7519 (Squires et al., 2009), I used the chemical structure of these six compounds and performed a computational 3D similarity search of BioAscent's diverse 125k compound

library (as described in **section 2.8.2**). The top 1000 BioAscent compounds ranked by 3D (USRCAT) similarity against each of the six query compounds were selected. Duplicated compounds (molecules that appeared in two or more query lists) were identified and shortlisted (as described in **section 2.8.2**). This ligand-based computational screening approach was used to generate a focussed library containing potentially novel compounds that display structural similarity against known efficacious CDK9 inhibitors, to subsequently screen, validate and optimise *in vitro*.

Table 5.1: Number of duplicated BioAscent compounds identified between CDK9 inhibitor query compounds.

Query compound	**AT7519**	**LDC000067**	**MC180295**	**AZD4573**	**NVP-2**	**iCDK9**
Number of duplicated BioAscent compounds	3	28	30	258	511	531

In total, 622 ranked BioAscent compounds were duplicated between two or more of the six query compounds and were shortlisted for further study. The number of duplicated BioAscent compounds identified for each of the six query compounds is indicated in **Table 5.1**. No ranked BioAscent compound was identified between more than three query compounds. All shortlisted (duplicated) BioAscent compound structures were manually inspected and any compound that displayed pan-assay interference features was removed to yield a final CDK9 inhibitor-like focussed library (as described in **section 2.8.3**). Focussed library compounds were ranked by their average 3D (USCRAT) similarity score to matched query compounds. The final focussed library consists of 598 BioAscent compounds (**Table 5.2**).

Table 5.2: Final focussed library consisting of shortlisted BioAscent compounds ranked by average 3D (USRCAT) similarity to matched query CDK9 inhibitors.

Rank (average USRCAT similarity)	BioAscent molecular ID	Matched query CDK9 inhibitors
1	BCC0086345	iCDK9, NVP-2
2	BCC0111704	iCDK9, NVP-2
3	BCC0099608	iCDK9, NVP-2
4	BCC0041524	iCDK9, NVP-2
5	BCC0101331	iCDK9, NVP-2
6	BCC0084752	iCDK9, NVP-2
7	BCC0019985	iCDK9, NVP-2
8	BCC0066023	iCDK9, NVP-2
9	BCC0075739	iCDK9, NVP-2
10	BCC0090134	iCDK9, NVP-2
11	BCC0022882	iCDK9, NVP-2
12	BCC0016291	iCDK9, NVP-2
13	BCC0011524	iCDK9, NVP-2
14	BCC0088459	iCDK9, NVP-2
15	BCC0016781	iCDK9, NVP-2
16	BCC0074366	iCDK9, NVP-2
17	BCC0011780	iCDK9, NVP-2
18	BCC0040983	iCDK9, NVP-2
19	BCC0083911	iCDK9, NVP-2
20	BCC0095259	iCDK9, NVP-2
21	BCC0064678	iCDK9, NVP-2
22	BCC0112898	iCDK9, NVP-2
23	BCC0015033	iCDK9, NVP-2
24	BCC0022651	iCDK9, NVP-2
25	BCC0026787	iCDK9, NVP-2
26	BCC0088215	iCDK9, NVP-2
27	BCC0114004	iCDK9, NVP-2
28	BCC0044835	AZD4573, iCDK9, NVP-2
29	BCC0124309	AZD4573, iCDK9
30	BCC0014215	iCDK9, NVP-2
31	BCC0039710	iCDK9, NVP-2
32	BCC0024727	AZD4573, iCDK9, NVP-2
33	BCC0007598	iCDK9, NVP-2
34	BCC0090698	iCDK9, NVP-2
35	BCC0116652	iCDK9, NVP-2
36	BCC0098832	iCDK9, NVP-2
37	BCC0046200	iCDK9, NVP-2
38	BCC0050821	iCDK9, NVP-2
39	BCC0090375	iCDK9, NVP-2
40	BCC0114557	AZD4573, iCDK9, NVP-2
41	BCC0104820	iCDK9, NVP-2
42	BCC0017240	AZD4573, iCDK9, NVP-2
43	BCC0021396	iCDK9, NVP-2
44	BCC0090669	iCDK9, NVP-2
45	BCC0027755	iCDK9, NVP-2
46	BCC0039382	iCDK9, NVP-2
47	BCC0016436	iCDK9, NVP-2
48	BCC0110014	iCDK9, NVP-2
49	BCC0025010	iCDK9, NVP-2
50	BCC0013735	iCDK9, NVP-2
51	BCC0035974	iCDK9, NVP-2
52	BCC0117061	AZD4573, iCDK9, NVP-2
53	BCC0051967	iCDK9, NVP-2
54	BCC0100229	iCDK9, NVP-2
55	BCC0088011	iCDK9, NVP-2
56	BCC0016476	iCDK9, NVP-2
57	BCC0121244	iCDK9, NVP-2
58	BCC0090917	iCDK9, NVP-2
59	BCC0002440	iCDK9, NVP-2
60	BCC0120543	iCDK9, NVP-2
61	BCC0011473	iCDK9, NVP-2
62	BCC0005648	iCDK9, NVP-2
63	BCC0002332	AZD4573, iCDK9, NVP-2
64	BCC0002287	iCDK9, NVP-2
65	BCC0117892	iCDK9, NVP-2
66	BCC0086763	iCDK9, NVP-2
67	BCC0022851	iCDK9, NVP-2
68	BCC0094647	iCDK9, NVP-2
69	BCC0088044	iCDK9, NVP-2
70	BCC0064676	iCDK9, NVP-2
71	BCC0039674	iCDK9, NVP-2
72	BCC0002135	iCDK9, NVP-2
73	BCC0049165	iCDK9, NVP-2
74	BCC0013544	AZD4573, iCDK9, NVP-2
75	BCC0089181	iCDK9, NVP-2
76	BCC0010714	iCDK9, NVP-2
77	BCC0010875	iCDK9, NVP-2
78	BCC0103978	AZD4573, iCDK9, NVP-2
79	BCC0055944	AZD4573, NVP-2
80	BCC0089146	iCDK9, NVP-2
81	BCC0089577	iCDK9, NVP-2
82	BCC0091868	iCDK9, NVP-2
83	BCC0014494	iCDK9, NVP-2
84	BCC0077725	iCDK9, NVP-2
85	BCC0088460	iCDK9, NVP-2
86	BCC0017132	iCDK9, NVP-2
87	BCC0113227	AZD4573, iCDK9, NVP-2
88	BCC0024799	AZD4573, NVP-2
89	BCC0101704	iCDK9, NVP-2
90	BCC0107048	iCDK9, NVP-2

Table 5.2 (continued)

91	BCC0124823	AZD4573, iCDK9, NVP-2
92	BCC0055068	iCDK9, NVP-2
93	BCC0010622	AZD4573, NVP-2
94	BCC0002291	LDC000067, MC180295
95	BCC0017419	iCDK9, NVP-2
96	BCC0087172	iCDK9, NVP-2
97	BCC0027467	iCDK9, NVP-2
98	BCC0120465	iCDK9, NVP-2
99	BCC0028671	AZD4573, iCDK9, NVP-2
100	BCC0119697	AZD4573, iCDK9, NVP-2
101	BCC0004638	iCDK9, NVP-2
102	BCC0006520	iCDK9, NVP-2
103	BCC0051439	iCDK9, NVP-2
104	BCC0076435	iCDK9, NVP-2
105	BCC0013573	AZD4573, iCDK9, NVP-2
106	BCC0007728	AZD4573, NVP-2
107	BCC0004766	iCDK9, NVP-2
108	BCC0122755	iCDK9, NVP-2
109	BCC0114379	iCDK9, NVP-2
110	BCC0003434	AZD4573, iCDK9, NVP-2
111	BCC0003740	iCDK9, NVP-2
112	BCC0024045	iCDK9, NVP-2
113	BCC0039952	iCDK9, NVP-2
114	BCC0044831	AZD4573, iCDK9, NVP-2
115	BCC0040742	iCDK9, NVP-2
116	BCC0003986	iCDK9, NVP-2
117	BCC0110745	AZD4573, NVP-2
118	BCC0012452	LDC000067, MC180295
119	BCC0002858	AZD4573, iCDK9, NVP-2
120	BCC0100024	AZD4573, iCDK9, NVP-2
121	BCC0065389	iCDK9, NVP-2
122	BCC0087668	iCDK9, NVP-2
123	BCC0039692	iCDK9, NVP-2
124	BCC0028231	AZD4573, NVP-2
125	BCC0007215	iCDK9, NVP-2
126	BCC0044186	AZD4573, NVP-2
127	BCC0090675	AZD4573, iCDK9, NVP-2
128	BCC0074886	AZD4573, iCDK9, NVP-2
129	BCC0010470	AZD4573, iCDK9, NVP-2
130	BCC0005363	iCDK9, NVP-2
131	BCC0008012	AZD4573, iCDK9, NVP-2
132	BCC0120370	iCDK9, NVP-2
133	BCC0053836	iCDK9, NVP-2
134	BCC0044464	iCDK9, NVP-2
135	BCC0089542	AZD4573, iCDK9
136	BCC0023780	AZD4573, iCDK9, NVP-2
137	BCC0038856	iCDK9, NVP-2
138	BCC0079043	iCDK9, NVP-2
139	BCC0000843	iCDK9, NVP-2
140	BCC0010669	iCDK9, NVP-2
141	BCC0093281	iCDK9, NVP-2
142	BCC0021972	iCDK9, NVP-2
143	BCC0121087	AZD4573, iCDK9, NVP-2
144	BCC0124861	AZD4573, iCDK9, NVP-2
145	BCC0035788	iCDK9, NVP-2
146	BCC0052050	AZD4573, iCDK9, NVP-2
147	BCC0092132	iCDK9, NVP-2
148	BCC0008303	iCDK9, NVP-2
149	BCC0112932	iCDK9, NVP-2
150	BCC0118105	AZD4573, iCDK9, NVP-2
151	BCC0015538	AZD4573, iCDK9
152	BCC0123332	iCDK9, NVP-2
153	BCC0123200	AZD4573, iCDK9, NVP-2
154	BCC0002438	AZD4573, NVP-2
155	BCC0023901	iCDK9, NVP-2
156	BCC0069834	iCDK9, NVP-2
157	BCC0080156	iCDK9, NVP-2
158	BCC0070201	LDC000067, MC180295
159	BCC0054442	iCDK9, NVP-2
160	BCC0020287	LDC000067, MC180295
161	BCC0090813	AZD4573, iCDK9, NVP-2
162	BCC0112902	iCDK9, NVP-2
163	BCC0110623	LDC000067, MC180295
164	BCC0039696	iCDK9, NVP-2
165	BCC0024515	AZD4573, iCDK9, NVP-2
166	BCC0034509	AZD4573, iCDK9, NVP-2
167	BCC0101714	iCDK9, NVP-2
168	BCC0035516	AZD4573, iCDK9, NVP-2
169	BCC0008290	AZD4573, NVP-2
170	BCC0094322	iCDK9, NVP-2
171	BCC0093643	AZD4573, iCDK9, NVP-2
172	BCC0011136	iCDK9, NVP-2
173	BCC0083679	iCDK9, NVP-2
174	BCC0082990	iCDK9, NVP-2
175	BCC0122336	AZD4573, NVP-2
176	BCC0001772	AZD4573, NVP-2
177	BCC0036237	iCDK9, NVP-2

Table 5.2 (continued)

178	BCC0116924	iCDK9, NVP-2
179	BCC0039953	iCDK9, NVP-2
180	BCC0112799	AZD4573, iCDK9, NVP-2
181	BCC0005226	AZD4573, iCDK9
182	BCC0052129	iCDK9, NVP-2
183	BCC0028993	iCDK9, NVP-2
184	BCC0020771	AZD4573, iCDK9, NVP-2
185	BCC0001378	AZD4573, iCDK9
186	BCC0018218	iCDK9, NVP-2
187	BCC0105546	LDC000067, MC180295
188	BCC0039834	iCDK9, NVP-2
189	BCC0122924	iCDK9, NVP-2
190	BCC0116714	iCDK9, NVP-2
191	BCC0070604	AZD4573, NVP-2
192	BCC0080033	iCDK9, NVP-2
193	BCC0002410	AZD4573, iCDK9, NVP-2
194	BCC0003397	AZD4573, NVP-2
195	BCC0011090	AZD4573, iCDK9, NVP-2
196	BCC0010245	AZD4573, iCDK9, NVP-2
197	BCC0123188	AZD4573, iCDK9
198	BCC0026434	AZD4573, iCDK9
199	BCC0116948	AZD4573, iCDK9
200	BCC0015024	iCDK9, NVP-2
201	BCC0000624	AZD4573, NVP-2
202	BCC0053686	AZD4573, iCDK9, NVP-2
203	BCC0024423	AZD4573, iCDK9
204	BCC0103090	AZD4573, iCDK9
205	BCC0010177	iCDK9, NVP-2
206	BCC0123378	iCDK9, NVP-2
207	BCC0123707	iCDK9, NVP-2
208	BCC0117750	AZD4573, iCDK9
209	BCC0090031	iCDK9, NVP-2
210	BCC0111168	LDC000067, MC180295
211	BCC0017081	iCDK9, NVP-2
212	BCC0053711	iCDK9, NVP-2
213	BCC0089165	iCDK9, NVP-2
214	BCC0116700	AZD4573, iCDK9, NVP-2
215	BCC0120988	AZD4573, iCDK9, NVP-2
216	BCC0053049	iCDK9, NVP-2
217	BCC0020397	AZD4573, iCDK9
218	BCC0018543	AZD4573, iCDK9
219	BCC0116383	iCDK9, NVP-2
220	BCC0117315	iCDK9, NVP-2
221	BCC0051682	AZD4573, NVP-2
222	BCC0045410	iCDK9, NVP-2
223	BCC0065910	AZD4573, iCDK9, NVP-2
224	BCC0084345	iCDK9, NVP-2
225	BCC0022016	iCDK9, NVP-2
226	BCC0012367	AZD4573, iCDK9
227	BCC0109212	iCDK9, NVP-2
228	BCC0016320	AZD4573, NVP-2
229	BCC0082309	AZD4573, iCDK9, NVP-2
230	BCC0010204	iCDK9, NVP-2
231	BCC0105984	iCDK9, NVP-2
232	BCC0088938	iCDK9, NVP-2
233	BCC0120631	AZD4573, iCDK9, NVP-2
234	BCC0000570	AZD4573, iCDK9, NVP-2
235	BCC0094613	iCDK9, NVP-2
236	BCC0090830	iCDK9, NVP-2
237	BCC0122709	AZD4573, iCDK9
238	BCC0066780	iCDK9, NVP-2
239	BCC0113188	AZD4573, iCDK9, NVP-2
240	BCC0002140	AZD4573, iCDK9, NVP-2
241	BCC0087598	iCDK9, NVP-2
242	BCC0058452	iCDK9, NVP-2
243	BCC0072613	iCDK9, NVP-2
244	BCC0061119	AZD4573, NVP-2
245	BCC0016369	iCDK9, NVP-2
246	BCC0103187	AZD4573, iCDK9, NVP-2
247	BCC0110313	iCDK9, NVP-2
248	BCC0090704	iCDK9, NVP-2
249	BCC0123302	AZD4573, iCDK9, NVP-2
250	BCC0004227	AZD4573, iCDK9, NVP-2
251	BCC0003193	AZD4573, iCDK9, NVP-2
252	BCC0124855	iCDK9, NVP-2
253	BCC0028250	AZD4573, iCDK9, NVP-2
254	BCC0119215	AZD4573, iCDK9, NVP-2
255	BCC0111789	AZD4573, iCDK9, NVP-2
256	BCC0113103	AZD4573, iCDK9, NVP-2
257	BCC0113285	iCDK9, NVP-2
258	BCC0116436	AZD4573, iCDK9
259	BCC0032371	iCDK9, NVP-2
260	BCC0090647	AZD4573, iCDK9, NVP-2
261	BCC0116805	AZD4573, iCDK9
262	BCC0007416	iCDK9, NVP-2
263	BCC0045330	iCDK9, NVP-2
264	BCC0020047	iCDK9, NVP-2

Table 5.2 (continued)

265	BCC0068251	iCDK9, NVP-2
266	BCC0072920	iCDK9, NVP-2
267	BCC0084770	AZD4573, NVP-2
268	BCC0001366	AZD4573, NVP-2
269	BCC0055848	AZD4573, iCDK9
270	BCC0018856	iCDK9, NVP-2
271	BCC0018806	iCDK9, NVP-2
272	BCC0021739	iCDK9, NVP-2
273	BCC0017743	AZD4573, iCDK9, NVP-2
274	BCC0114531	iCDK9, NVP-2
275	BCC0106996	iCDK9, NVP-2
276	BCC0001722	AZD4573, iCDK9, NVP-2
277	BCC0121004	iCDK9, NVP-2
278	BCC0122363	LDC000067, MC180295
279	BCC0049924	AZD4573, iCDK9
280	BCC0010817	AZD4573, iCDK9
281	BCC0051455	AZD4573, iCDK9, NVP-2
282	BCC0105361	AZD4573, iCDK9, NVP-2
283	BCC0116257	iCDK9, NVP-2
284	BCC0119832	iCDK9, NVP-2
285	BCC0005488	AZD4573, NVP-2
286	BCC0099908	iCDK9, NVP-2
287	BCC0087025	AZD4573, iCDK9
288	BCC0083725	iCDK9, NVP-2
289	BCC0093145	iCDK9, NVP-2
290	BCC0005878	iCDK9, NVP-2
291	BCC0005193	iCDK9, NVP-2
292	BCC0034652	iCDK9, NVP-2
293	BCC0122280	iCDK9, NVP-2
294	BCC0116634	AZD4573, iCDK9, NVP-2
295	BCC0121522	AZD4573, iCDK9, NVP-2
296	BCC0060485	AZD4573, iCDK9
297	BCC0053051	iCDK9, NVP-2
298	BCC0124000	AZD4573, iCDK9, NVP-2
299	BCC0114418	AZD4573, NVP-2
300	BCC0124121	AZD4573, iCDK9, NVP-2
301	BCC0074516	iCDK9, NVP-2
302	BCC0044180	AZD4573, iCDK9, NVP-2
303	BCC0122443	AZD4573, iCDK9, NVP-2
304	BCC0077107	iCDK9, NVP-2
305	BCC0064398	iCDK9, NVP-2
306	BCC0098728	iCDK9, NVP-2
307	BCC0079321	iCDK9, NVP-2
308	BCC0028932	iCDK9, NVP-2
309	BCC0004371	AZD4573, iCDK9, NVP-2
310	BCC0010521	iCDK9, NVP-2
311	BCC0048923	iCDK9, NVP-2
312	BCC0010115	iCDK9, NVP-2
313	BCC0106660	AZD4573, iCDK9
314	BCC0101715	iCDK9, NVP-2
315	BCC0020706	AZD4573, iCDK9
316	BCC0001206	AZD4573, iCDK9
317	BCC0005846	AZD4573, iCDK9, NVP-2
318	BCC0025011	iCDK9, NVP-2
319	BCC0123722	AZD4573, iCDK9, NVP-2
320	BCC0114679	AZD4573, iCDK9
321	BCC0106995	iCDK9, NVP-2
322	BCC0064978	AZD4573, iCDK9
323	BCC0003181	AZD4573, iCDK9, NVP-2
324	BCC0122120	AZD4573, NVP-2
325	BCC0090763	iCDK9, NVP-2
326	BCC0070764	AZD4573, NVP-2
327	BCC0014153	iCDK9, NVP-2
328	BCC0122126	AZD4573, NVP-2
329	BCC0021773	AZD4573, iCDK9, NVP-2
330	BCC0055719	AZD4573, iCDK9, NVP-2
331	BCC0120353	AZD4573, NVP-2
332	BCC0114113	AZD4573, NVP-2
333	BCC0044572	iCDK9, NVP-2
334	BCC0002441	iCDK9, NVP-2
335	BCC0027034	LDC000067, MC180295
336	BCC0016088	iCDK9, NVP-2
337	BCC0040804	iCDK9, NVP-2
338	BCC0077618	AZD4573, NVP-2
339	BCC0009308	AZD4573, iCDK9, NVP-2
340	BCC0038711	iCDK9, NVP-2
341	BCC0005029	iCDK9, NVP-2
342	BCC0103921	AZD4573, iCDK9, NVP-2
343	BCC0065931	iCDK9, NVP-2
344	BCC0012491	iCDK9, NVP-2
345	BCC0084909	iCDK9, NVP-2
346	BCC0023877	iCDK9, NVP-2
347	BCC0033738	LDC000067, MC180295
348	BCC0044614	iCDK9, NVP-2
349	BCC0010485	AZD4573, iCDK9, NVP-2
350	BCC0000683	iCDK9, NVP-2
351	BCC0027648	AZD4573, iCDK9, NVP-2
352	BCC0014688	AZD4573, iCDK9, NVP-2

Table 5.2 (continued)

353	BCC0040643	iCDK9, NVP-2
354	BCC0024981	AZD4573, iCDK9, NVP-2
355	BCC0025004	iCDK9, NVP-2
356	BCC0002301	iCDK9, NVP-2
357	BCC0012021	AZD4573, iCDK9, NVP-2
358	BCC0008790	iCDK9, NVP-2
359	BCC0071408	iCDK9, NVP-2
360	BCC0004487	AZD4573, iCDK9, NVP-2
361	BCC0100618	iCDK9, NVP-2
362	BCC0044515	AZD4573, iCDK9
363	BCC0047887	AZD4573, NVP-2
364	BCC0007791	iCDK9, NVP-2
365	BCC0008879	iCDK9, NVP-2
366	BCC0090535	iCDK9, NVP-2
367	BCC0025986	iCDK9, NVP-2
368	BCC0000173	AZD4573, iCDK9
369	BCC0086400	AZD4573, iCDK9
370	BCC0073066	AZD4573, iCDK9, NVP-2
371	BCC0124192	AZD4573, MC180295
372	BCC0118087	iCDK9, NVP-2
373	BCC0123009	AZD4573, NVP-2
374	BCC0039735	iCDK9, NVP-2
375	BCC0111502	iCDK9, NVP-2
376	BCC0022413	iCDK9, NVP-2
377	BCC0001425	iCDK9, NVP-2
378	BCC0122973	AZD4573, NVP-2
379	BCC0121186	AZD4573, iCDK9, NVP-2
380	BCC0005392	iCDK9, NVP-2
381	BCC0115939	AZD4573, iCDK9, NVP-2
382	BCC0049320	iCDK9, NVP-2
383	BCC0112672	AZD4573, iCDK9
384	BCC0110708	iCDK9, NVP-2
385	BCC0082994	iCDK9, NVP-2
386	BCC0090969	AZD4573, NVP-2
387	BCC0004089	AZD4573, NVP-2
388	BCC0012288	AZD4573, iCDK9, NVP-2
389	BCC0112141	iCDK9, NVP-2
390	BCC0113169	iCDK9, NVP-2
391	BCC0118864	AZD4573, iCDK9, NVP-2
392	BCC0039431	iCDK9, NVP-2
393	BCC0018584	AZD4573, iCDK9
394	BCC0111773	iCDK9, NVP-2
395	BCC0112695	AZD4573, iCDK9, NVP-2
396	BCC0006591	AZD4573, iCDK9
397	BCC0054508	LDC000067, MC180295
398	BCC0023829	AZD4573, iCDK9, NVP-2
399	BCC0042883	iCDK9, NVP-2
400	BCC0047820	iCDK9, NVP-2
401	BCC0061499	AZD4573, iCDK9
402	BCC0121761	LDC000067, MC180295
403	BCC0014613	AZD4573, NVP-2
404	BCC0095265	iCDK9, NVP-2
405	BCC0119987	AZD4573, iCDK9, NVP-2
406	BCC0107331	iCDK9, NVP-2
407	BCC0112256	AZD4573, NVP-2
408	BCC0027962	iCDK9, NVP-2
409	BCC0033182	AZD4573, iCDK9
410	BCC0089486	AZD4573, iCDK9
411	BCC0087168	iCDK9, NVP-2
412	BCC0025129	AZD4573, iCDK9, NVP-2
413	BCC0022058	iCDK9, NVP-2
414	BCC0123992	AZD4573, iCDK9, NVP-2
415	BCC0114412	LDC000067, MC180295
416	BCC0113315	iCDK9, NVP-2
417	BCC0026329	AZD4573, iCDK9, NVP-2
418	BCC0013839	iCDK9, NVP-2
419	BCC0082304	iCDK9, NVP-2
420	BCC0102620	iCDK9, NVP-2
421	BCC0105362	AZD4573, iCDK9, NVP-2
422	BCC0116819	iCDK9, NVP-2
423	BCC0042713	iCDK9, NVP-2
424	BCC0076036	AZD4573, iCDK9
425	BCC0022828	AZD4573, NVP-2
426	BCC0043888	iCDK9, NVP-2
427	BCC0113602	AZD4573, iCDK9
428	BCC0039786	iCDK9, NVP-2
429	BCC0010686	iCDK9, NVP-2
430	BCC0101304	iCDK9, NVP-2
431	BCC0027191	iCDK9, NVP-2
432	BCC0042499	iCDK9, NVP-2
433	BCC0060607	iCDK9, NVP-2
434	BCC0000787	AZD4573, iCDK9, NVP-2
435	BCC0051940	AZD4573, NVP-2
436	BCC0112986	iCDK9, NVP-2
437	BCC0090831	AZD4573, AT7519
438	BCC0124043	iCDK9, NVP-2
439	BCC0083300	AZD4573, NVP-2
440	BCC0084847	iCDK9, NVP-2
441	BCC0124089	AZD4573, iCDK9, NVP-2
442	BCC0027606	iCDK9, NVP-2

Table 5.2 (continued)

443	BCC0026128	AZD4573, iCDK9, NVP-2
444	BCC0013076	iCDK9, NVP-2
445	BCC0121743	LDC000067, AZD4573
446	BCC0124851	AZD4573, iCDK9
447	BCC0079065	iCDK9, NVP-2
448	BCC0020433	LDC000067, MC180295
449	BCC0038593	AZD4573, NVP-2
450	BCC0115303	MC180295, AT7519
451	BCC0112969	iCDK9, NVP-2
452	BCC0011158	AZD4573, NVP-2
453	BCC0069630	iCDK9, NVP-2
454	BCC0077847	AZD4573, iCDK9
455	BCC0060465	iCDK9, NVP-2
456	BCC0011146	iCDK9, NVP-2
457	BCC0030550	iCDK9, NVP-2
458	BCC0121274	AZD4573, NVP-2
459	BCC0004401	iCDK9, NVP-2
460	BCC0110762	AZD4573, iCDK9, NVP-2
461	BCC0083914	iCDK9, NVP-2
462	BCC0020926	iCDK9, NVP-2
463	BCC0043933	AZD4573, NVP-2
464	BCC0017541	LDC000067, MC180295
465	BCC0057436	AZD4573, NVP-2
466	BCC0011142	AZD4573, iCDK9, NVP-2
467	BCC0028220	AZD4573, iCDK9, NVP-2
468	BCC0013327	AZD4573, iCDK9, NVP-2
469	BCC0119517	iCDK9, NVP-2
470	BCC0116382	AZD4573, iCDK9, NVP-2
471	BCC0029051	LDC000067, MC180295
472	BCC0079901	iCDK9, NVP-2
473	BCC0015082	AZD4573, iCDK9
474	BCC0034623	iCDK9, NVP-2
475	BCC0103794	AZD4573, iCDK9
476	BCC0011414	AZD4573, iCDK9
477	BCC0089896	iCDK9, NVP-2
478	BCC0048956	AZD4573, iCDK9, NVP-2
479	BCC0028854	LDC000067, MC180295
480	BCC0021305	LDC000067, MC180295
481	BCC0100768	AZD4573, iCDK9, NVP-2
482	BCC0051510	AZD4573, NVP-2
483	BCC0106288	iCDK9, NVP-2
484	BCC0112330	iCDK9, NVP-2
485	BCC0040942	iCDK9, NVP-2
486	BCC0008272	LDC000067, MC180295
487	BCC0117801	iCDK9, NVP-2
488	BCC0016857	LDC000067, MC180295
489	BCC0020186	LDC000067, MC180295
490	BCC0124853	iCDK9, NVP-2
491	BCC0004045	AZD4573, iCDK9, NVP-2
492	BCC0116075	AZD4573, iCDK9
493	BCC0043781	AZD4573, NVP-2
494	BCC0101712	AZD4573, iCDK9
495	BCC0024033	iCDK9, NVP-2
496	BCC0022158	AZD4573, iCDK9, NVP-2
497	BCC0003217	AZD4573, NVP-2
498	BCC0112590	LDC000067, MC180295
499	BCC0111939	iCDK9, NVP-2
500	BCC0021154	iCDK9, NVP-2
501	BCC0057028	iCDK9, NVP-2
502	BCC0007055	iCDK9, NVP-2
503	BCC0000004	iCDK9, NVP-2
504	BCC0004804	MC180295, AT7519
505	BCC0122427	AZD4573, iCDK9
506	BCC0063915	AZD4573, iCDK9
507	BCC0095670	AZD4573, iCDK9
508	BCC0022215	AZD4573, iCDK9
509	BCC0016271	iCDK9, NVP-2
510	BCC0084768	AZD4573, NVP-2
511	BCC0093602	AZD4573, iCDK9
512	BCC0054417	AZD4573, iCDK9
513	BCC0010440	AZD4573, iCDK9, NVP-2
514	BCC0073738	iCDK9, NVP-2
515	BCC0109641	LDC000067, MC180295
516	BCC0004880	AZD4573, iCDK9
517	BCC0097550	iCDK9, NVP-2
518	BCC0045666	AZD4573, iCDK9
519	BCC0105778	iCDK9, NVP-2
520	BCC0082062	iCDK9, NVP-2
521	BCC0101716	iCDK9, NVP-2
522	BCC0018627	AZD4573, iCDK9
523	BCC0005568	AZD4573, iCDK9, NVP-2
524	BCC0022085	AZD4573, iCDK9
525	BCC0117963	AZD4573, NVP-2
526	BCC0023449	iCDK9, NVP-2
527	BCC0111211	iCDK9, NVP-2
528	BCC0014631	AZD4573, NVP-2
529	BCC0044659	AZD4573, NVP-2
530	BCC0090948	AZD4573, NVP-2
531	BCC0079052	iCDK9, NVP-2
532	BCC0082992	iCDK9, NVP-2
533	BCC0041466	AZD4573, iCDK9
534	BCC0022207	iCDK9, NVP-2
535	BCC0044796	AZD4573, iCDK9

Table 5.2 (continued)

536	BCC0049706	AZD4573, iCDK9
537	BCC0099609	iCDK9, NVP-2
538	BCC0044125	iCDK9, NVP-2
539	BCC0109826	LDC000067, MC180295
540	BCC0005368	AZD4573, iCDK9
541	BCC0118694	iCDK9, NVP-2
542	BCC0085595	AZD4573, NVP-2
543	BCC0087142	AZD4573, iCDK9
544	BCC0087622	iCDK9, NVP-2
545	BCC0008534	iCDK9, NVP-2
546	BCC0089579	AZD4573, iCDK9, NVP-2
547	BCC0107304	AZD4573, iCDK9
548	BCC0102887	AZD4573, NVP-2
549	BCC0056138	iCDK9, NVP-2
550	BCC0025491	AZD4573, iCDK9
551	BCC0040061	iCDK9, NVP-2
552	BCC0117915	AZD4573, iCDK9
553	BCC0013005	AZD4573, iCDK9
554	BCC0100297	AZD4573, NVP-2
555	BCC0005479	AZD4573, iCDK9
556	BCC0088814	iCDK9, NVP-2
557	BCC0099591	iCDK9, NVP-2
558	BCC0100824	iCDK9, NVP-2
559	BCC0087922	AZD4573, iCDK9
560	BCC0016783	iCDK9, NVP-2
561	BCC0020229	AZD4573, iCDK9
562	BCC0083925	AZD4573, NVP-2
563	BCC0032303	iCDK9, NVP-2
564	BCC0123675	iCDK9, NVP-2
565	BCC0050361	AZD4573, NVP-2
566	BCC0018651	AZD4573, iCDK9, NVP-2
567	BCC0016217	AZD4573, iCDK9
568	BCC0069495	iCDK9, NVP-2
569	BCC0018155	iCDK9, NVP-2
570	BCC0013144	AZD4573, iCDK9, NVP-2
571	BCC0040918	AZD4573, iCDK9
572	BCC0084869	AZD4573, iCDK9
573	BCC0051512	AZD4573, NVP-2
574	BCC0018215	iCDK9, NVP-2
575	BCC0081981	AZD4573, NVP-2
576	BCC0016828	AZD4573, iCDK9, NVP-2
577	BCC0001252	AZD4573, iCDK9, NVP-2
578	BCC0026724	iCDK9, NVP-2
579	BCC0116116	AZD4573, iCDK9
580	BCC0051791	iCDK9, NVP-2
581	BCC0039846	iCDK9, NVP-2
582	BCC0088311	iCDK9, NVP-2
583	BCC0014704	iCDK9, NVP-2
584	BCC0009072	iCDK9, NVP-2
585	BCC0099947	iCDK9, NVP-2
586	BCC0004055	iCDK9, NVP-2
587	BCC0089433	iCDK9, NVP-2
588	BCC0077927	LDC000067, MC180295
589	BCC0017213	AZD4573, iCDK9, NVP-2
590	BCC0047793	iCDK9, NVP-2
591	BCC0025180	AZD4573, iCDK9
592	BCC0002333	iCDK9, NVP-2
593	BCC0010198	AZD4573, iCDK9
594	BCC0105245	LDC000067, MC180295
595	BCC0076298	iCDK9, NVP-2
596	BCC0012675	LDC000067, MC180295
597	BCC0067799	AZD4573, iCDK9
598	BCC0019578	AZD4573, iCDK9

Table 5.3: Breakdown of BioAscent compound duplication between matched query CDK9 inhibitors.

Matched query CDK9 inhibitors	BioAscent compound duplication count	% of total
iCDK9, NVP-2	323	54.01
AZD4573, iCDK9, NVP-2	111	18.6
AZD4573, iCDK9	75	12.5
AZD4573, NVP-2	57	9.53
LDC000067, MC180295	27	4.52
MC180295, AT7519	2	0.334
AZD4573, AT7519	1	0.167
AZD4573, MC180295	1	0.167
LDC000067, AZD4573	1	0.167
Grand Total	**598**	

As displayed in **Table 5.3**, the majority of duplicated BioAscent compounds were shared between iCDK9 and NVP-2. Additionally, BioAscent compounds identified between iCDK9 and NVP-2 generally ranked highly by 3D similarity score (**Table 5.2**). BioAscent duplications between AZD4573, iCDK9 and NVP-2 were the second most frequent. BioAscent compound duplications were less frequent between other query CDK9 inhibitor compounds (<5%). There were no BioAscent compound duplications between the following query compounds:

1. AT7519, iCDK9, NVP-2 and LDC000067
2. MC180295, iCDK9 and NVP-2
3. LDC000067, iCDK9 and NVP-2.

The final focussed library contains 598 compounds which were all manually examined and selected for subsequent assay screening to establish CDK9 inhibition activity. While this was my original plan, due to the COVID-19 pandemic, I was not able to visit BioAscent's commercial site to develop, validate and perform the assay using their screening facilities. However, as the

focussed compound library has been established, the CDK9 inhibition screen could be performed at a later date when practically feasible.

5.4. Testing the biological efficacy of Flavopiridol in a human neutrophil apoptosis assay

It is important to identify whether compounds that resolve neutrophilic inflammation in larval zebrafish also do so in mammals. The Rossi laboratory has documented that AT7519 promotes neutrophil resolution by inducing neutrophil apoptosis in different murine models (Cartwright et al., 2019; Lucas et al., 2014 and Barth et al., 2020). Importantly, these pro-resolving effects are conserved in humans, as AT7519 also induces human neutrophil apoptosis (Dorward et al., 2017 and Gray et al., 2018), highlighting its translatable potential for treating neutrophilic disorders. I wanted to verify the human neutrophil assay with a view of using it to assess the biological efficacy of hit BioAscent compounds identified from the CDK9 inhibition screen. Our laboratory has not yet validated the efficacy of Flavopiridol to induce human neutrophil apoptosis, as such I performed this experiment to serve as a positive control. Human neutrophils were freshly isolated from the whole blood of healthy volunteers. Isolated neutrophils were treated with FVP or DMSO vehicle and apoptosis was assessed by flow cytometry using annexin V (labels apoptotic cells) and propidium iodide (labels necrotic cells) staining at 22 hours post culture. Flow cytometry indicated that in the control group 36% of neutrophils were early apoptotic, 43% were late apoptotic/necrotic and 21% were viable. Contrastingly, in the FVP-treated group 43% of neutrophils were early apoptotic, 53% were late apoptotic/necrotic and 4% were viable (**Figure 5.2A** and **B**). Light microscopy indicated that FVP-treated neutrophils displayed marked apoptotic morphology, with smaller and condensed/rounded nuclei compared to the control group (**Figure 5.2A**). Treatment with pan caspase inhibitor, Q-VD-OPh, increased neutrophil viability to greater than 90% both in the control and FVP-treated group (**Figure 5.2A** and **B**).

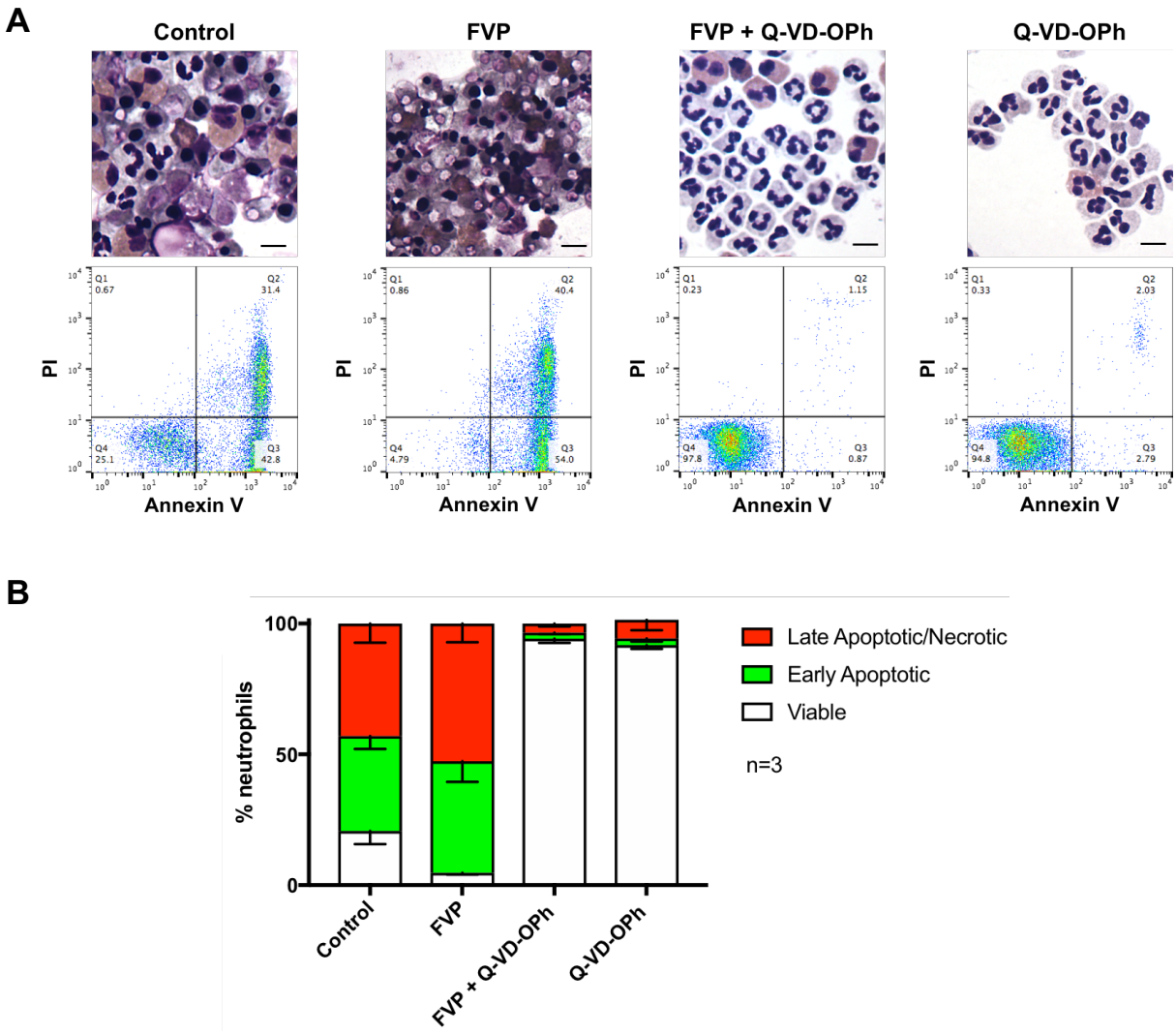

Figure 5.2: The effect of Flavopiridol in a human neutrophil apoptosis assay. (A) Cytocentrifuge stained preparations following 22 hours culture with the associated treatment and corresponding flow cytometry plots displaying cell viability (AnnV–ve/PI–ve, lower left quadrant), early apoptosis (AnnV+ve/PI–ve, lower right quadrant) and late apoptosis/necrosis (AnnV+ve/PI+ve, upper right quadrant). Scale bar = 10µm. **(B)** % of viable, early apoptotic and late apoptotic/necrotic human neutrophils following 22 hours culture in each treatment group. Data are representative of three separate replicates and presented as mean ± SEM.

5.5. Discussion

In this chapter, I hypothesised that the adverse effects observed with continuous CDK9i treatment, and the differing regenerative effects identified with transient AT7519 and FVP treatment were due to non-specific binding. To test this, I developed a larval zebrafish CDK9 inhibitor selectivity assay using homozygous knockout *cdk9* mutants and heart rate as a surrogate measurement for overall health. The assay revealed that AT7519 and FVP accelerate the decline of heart rate in knockout mutants from one-day post treatment (**Figure 5.1**), which coincides with the onset of adverse phenotypes, indicating that both compounds were acting in a Cdk9-independent manner. However, this does not rule out the adverse effects being partially Cdk9-dependent, as vehicle-treated knockout mutants also displayed a decline in heart rate, albeit more gradual. Of the two CDK9 inhibitors, FVP showed more notable off-target effects in the selectivity assay (**Figure 5.1**), a likely cause for the prominent adverse phenotypes observed (**Figure 4.2** and **Figure 4.3**), which have also been reported *in vitro* (Garriga et al., 2010 and Liu et al., 2011). Additionally, the selectivity assay revealed that from two hours post treatment (the duration of transient treatment), FVP exhibited significantly less Cdk9 selectivity compared to AT7519 (**Figure 5.1**). This finding supports the hypothesis that FVP suppresses *TNF* upregulation in wound-associated macrophages, providing a potential explanation for why AT7519 enhanced cardiomyocyte regeneration and FVP did not. Indeed, this larval zebrafish knockout screening approach could be applied to other druggable targets and used to identify uniquely selective inhibitors in a high throughput manner and across relatively short timescales (≤2 hours) *in vivo*.

I went on to perform a ligand-based computational similarity screen of BioAscent's 125k library using six potent and selective CDK9 inhibitors (AT7519, LDC000067, MC180295, AZD4573, NVP-2 and iCDK9), with the aim of identifying novel and efficacious CDK9 inhibitor-like compounds for subsequent downstream testing. The *in silico* similarity screen indicated that

the majority of shortlisted compounds shared 3D structural homology with NVP-2 and iCDK9 (**Table 5.2**). NVP-2 and iCDK9 are two of the most potent and selective CDK9 inhibitors developed to date, with a CDK9 IC50 of 0.5nM and <0.4nM respectively (Olson et al., 2018 and Lu et al., 2015). Therefore, BioAscent compounds that share high structural similarity with NVP-2 and iCDK9 (**Table 2.5**) may also display high inhibitory efficacy against CDK9. However, rather than predicting, a CDK9 inhibition assay is ultimately required to directly assess the efficacy of shortlisted BioAscent compounds. Such a screen was in the process of being planned for the focussed library (**Table 5.2**), but due to the unforeseen COVID-19 pandemic, this was not possible to perform. A caveat of our computational screening approach is that it is biased towards known CDK9 inhibitors and therefore may not identify compounds with completely novel mechanisms of action. However, allosteric CDK9 inhibitors, which bind an alternate site that is not the ATP binding domain have thus far not been developed, due to difficulty with targeting non-ATP binding domain sites on CDK9 (Mariaule and Belmont, 2014 and Boffo et al., 2018). As the focussed compound library has already been generated (**Table 5.2**), the following workflow was developed in conjunction with scientists at BioAscent to identify, validate and subsequently optimise hit compounds (**Table 5.4**).

Table 5.4: BioAscent compound screening, triage and optimisation workflow to identify efficacious and potentially novel CDK9 inhibitors.

Step	Description
1. CDK9 inhibition screening assay	Developing and validating a biochemical screening assay to assess CDK9 inhibition.
2. Screening the focussed compound library to identify initial hits	Selecting statistically relevant actives from initial screen and repeating screen to confirm actives and eliminate statistical false positives.
3. Deselection and orthogonal testing	Confirming selected hits in a different assay.
4. Determining dose-response curves	Testing selected hits over ranging concentrations to determine IC50 values and thus potency.
5. Target engagement and mode of action assays	Using biophysical techniques to determine reversibility, competitivity and kinetics of selected hits.
6. Chemoinformatic assessment	Closely analysing hit compounds to ensure they do not have undesirable physicochemical properties.
7. Synthesising authentic hit compounds	Confirming chemical structure and retesting in previous assays to confirm biological activity with confidence.
8. Hit ranking and clustering	Ranking and clustering hit compounds for e.g., affinity, selectivity, solubility, permeability and stability.
9. Optimising identified hit series further	Chemically modifying hit structures to increase compound potency and selectivity against CDK9.

During the outlined workflow (**Table 5.4**), any promising hits identified could be computationally re-screened against BioAscent's extensive 125k library to identify structurally similar compounds that may have not been shortlisted in the initial virtual ligand-based screen. Alternatively, specific scaffold or substructure based computational searches could be performed to identify compounds enriched for desirable pharmacophores and/or physicochemical properties. The final stages of the drug screening workflow (following step 9 in **Table 5.4**), would involve testing the biological efficacy of lead compounds using the *in vitro* and *in vivo* model systems described.

Finally, I tested the effect of Flavopiridol in a human neutrophil apoptosis assay *in vitro*. Due to the 22-hour incubation period and short lifespan of isolated neutrophils (Kennedy and DeLeo, 2009), both control- and FVP-treated neutrophils displayed considerable levels of caspase-dependent apoptosis, although this appeared to increase in the presence of FVP (**Figure 5.2**). If repeated, this assay will be performed with a shorter incubation time (6 hours), prior to cultured human neutrophils undergoing constitutive apoptosis (Dorward et al., 2017 and Gray et al., 2018). In addition to the newly proposed larval zebrafish CDK9 selectivity assay (**Figure 5.1**), the human neutrophil apoptosis assay (**Figure 5.2**) could form part of a drug discovery pipeline to validate the biological efficacy of novel CDK9 inhibitors in future work.

Chapter 6. General discussion

6.1. Neutrophil and macrophage responses in zebrafish models of cardiac injury and regeneration

Unlike adult mammalian species, zebrafish possess a remarkable capacity to regenerate their hearts following injury via cardiomyocyte proliferation (Jopling et al., 2010). Two important innate immune cells, the neutrophil and macrophage, have recently been implicated in regulating heart regeneration in adult zebrafish. These studies have found that sustained neutrophil retention at the injured heart inhibits cardiomyocyte proliferation, promotes cardiomyocyte apoptosis and delays scar regression (Xu et al., 2019). Similarly, reduced macrophage recruitment prolongs neutrophil retention, which impairs cardiomyocyte proliferation, neovascularisation and scar resolution (Lai et al., 2017). These findings indicate that the innate immune response is specifically coupled to efficient cardiomyocyte regeneration following injury, with neutrophil accumulation likely playing a detrimental role in this process. Due to their unique amenability for live *in vivo* imaging and pharmacological/genetic manipulation, the larval zebrafish is rapidly being recognised as a powerful model system to investigate innate immune cells during tissue regeneration. Unlike adult zebrafish, larval zebrafish are small in size, transparent and easy to handle, making them ideal for live imaging screening studies. Furthermore, it can take up to three months for zebrafish to reach adulthood, and due to difficulties with live imaging of immune cells at adult stages, experimentation often involves surgery, tissue fixation and antibody staining. These procedures are generally more time-consuming and heart regeneration takes at least two months in adult zebrafish; therefore, statistical power is much harder to achieve in a timely manner. It should be noted that larval zebrafish up to 5 dpf are not protected under the ASPA 1986 act which regulates the use of animals in research. The Denvir laboratory had established a 3 dpf cardiac laser injury model in zebrafish to study myocardial repair/regeneration within a two-day window (Matrone et al.,

2013 and Matrone et al., 2015). Throughout the course of this study, I used the larval zebrafish model of cardiac injury (**Appendix Figure 1** and **Appendix Figure 2**). This is in agreement with the NC3R guidelines as it allowed us to replace the use of adult zebrafish with larval zebrafish.

The inflammatory response to cardiac laser injury had yet to be established in the larval zebrafish model (Matrone et al., 2013 and Matrone et al., 2015). Therefore, I initially developed bespoke live imaging techniques to characterise local and systemic immune cell responses following cardiac injury (Taylor et al., 2019 and Kaveh et al., 2020). Consistent with adult zebrafish and mammalian models of cardiac injury, we found there is an acute wave of neutrophil recruitment followed by sustained macrophage recruitment over the two-day injury model, where both immune cells infiltrate the myocardial laser lesion (Kaveh et al., 2020). Of particular importance was the development of a tri-hue photoconversion strategy that allowed the ontogeny of wound-recruited immune cells to be mapped. Using this method, I found that both cell types are initially recruited locally from nearby tissues and are later mobilised from the haematopoietic tissue into peripheral blood (Kaveh et al., 2020), similar to mammalian models of cardiac injury. The ontogeny of immune cells is less well defined following adult zebrafish heart injury, largely due to technical challenges presented by immune cell tracking in adult species. Recent cardiac cryoinjury studies in adult zebrafish have focussed on the role of macrophage subpopulations during heart regeneration. Bevan et al. (2020) found that *TNF*$^{+}$ macrophages prolong scar retention, whereas *TNF*$^{-}$ macrophages promote scar removal during regeneration. My data suggests that *TNF*$^{+}$ macrophages have a pro-proliferative role in the injured larval zebrafish heart, which was recently supported in the larval zebrafish spinal cord by single-cell RNA sequencing (Cavone et al., 2021). Together, these findings indicate a potential transition in TNF macrophage function during development from a more plastic/mitogenic to differentiated/hypertrophic role. Furthermore, a wt1b^{+} macrophage

population has also been shown to have pro-regenerative properties following adult zebrafish heart and tail fin wounding, potentially via regulation of wound-macrophage migration and retention (Sanz-Morejon et al., 2019). Given that immune cell phenotypes can regulate regenerative outcomes, immune cell phenotyping in the injured zebrafish heart requires further study to establish a library of markers and their regenerative roles in the larvae and adult.

In contrast to the study of macrophages during zebrafish heart regeneration, neutrophils are generally less well understood. For example, there is a lack of known neutrophil phenotypes in the injured adult zebrafish heart. Using our comparative injury model approach to characterise immune cell migration, I found unexcepted *mpeg1* heterogeneity in wound-recruited larval zebrafish neutrophils at the heart and tail fin (Kaveh et al., 2020). Moreover, wound-recruited neutrophils have been shown to upregulate *il-1β* at the spinal cord lesion in larval zebrafish, which in excess, is associated with impaired regeneration (Tsarouchas et al., 2018). To explore the heterogeneity of neutrophil inflammatory phenotypes, I examined transgenic zebrafish expressing *mpx* and *il-1β*, *tnf* and *nfκb* following tail resection, as this model displays a robust neutrophil recruitment response. However, I did not find any of these inflammatory mediators to be highly expressed in tail wound-recruited neutrophils at 6 hpi, 24 hpi and 48 hpi (**Appendix Figure 3**). As the spinal cord lesion is an invasive and open wound, neutrophil-specific expression of *il-1β* could be correlated with injury site sterility. This concept could be further explored at the wounded heart and/or tail fin by enhancing the bacterial burden and examining neutrophil inflammatory phenotypes and regeneration using high resolution LSFM or confocal imaging. Nevertheless, we and others have shown that wound-recruited neutrophils are not transcriptionally homogenous, which is an overly simplistic dogma.

Furthermore, I have shown that reverse migration is the *primary* mechanism for neutrophil resolution following cardiac and tail fin injury in larval zebrafish. Tail resection studies in larval zebrafish have shown that neutrophil reverse migration is best described by stochastic dispersal, likely as a result of neutrophils becoming desensitised to local chemotactic gradients (Robertson et al., 2014 and Holmes et al., 2012). More recent tail fin wounding studies in larval zebrafish have explored mechanisms governing neutrophil reverse migration, which indeed appears primarily chemokine dependent. Isles et al. (2019) found that genetic and pharmacological inhibition of Cxcl12a and Cxcr4b, which form a signaling axis, enhances reverse migration. Similarly, the Cxcl8a/Cxcr2 axis is also required for neutrophil reverse migration (Powell et al., 2017). Coombs et al. (2019) dissected the molecular mechanism of Cxcr2 during neutrophil retention and reverse chemotaxis following wounding. The authors found that sustained expression of Cxcr2 on the plasma membrane of neutrophils is required to promote neutrophil bidirectional motility and subsequent reverse migration from wounds (Coombs et al., 2019). Importantly, this study is the first to provide a molecular mechanism for how neutrophil reverse chemotaxis is regulated, as it was previously undetermined why certain chemokine receptors stimulate reverse migration while others do not. Together, these studies support the dogma that neutrophil reverse migration is induced following neutrophil chemokine receptor (e.g., Cxcr4b or Cxcr2) binding to chemokine ligand (e.g., Cxcl12a or Cxcl8a/b) gradients, with the latter upregulated at the wound site (Isles et al., 2019; Powell et al., 2017 and Coombs et al., 2019). Reverse chemotaxis may well be an important neutrophil resolution mechanism following cardiac injury in adult zebrafish and mammals, as shown following sterile liver injury in adult mice (Wang et al., 2017). Investigating the mechanisms underlying reverse migration is a promising approach for enhancing neutrophil resolution without compromising host defence.

6.2. Role of CDK9 during cardiac development and injury-induced inflammation

As a core transcriptional regulator, CDK9 is functionally implicated in many physiological and pathological related settings (Bacon and Orso et al., 2019). In the context of the larval zebrafish, morpholino knockdown of *cdk9* impairs cardiac structure and function and downregulates cardiomyocyte proliferation, highlighting its transcriptional importance in the developing heart (Matrone et al., 2015). Cardiac expression of *cdk9* in zebrafish peaks at 96 hpf, coinciding with high rates of developmental cardiomyocyte proliferation (Matrone et al., 2015). Both *cdk9* expression and cardiomyocyte proliferation decrease at adulthood in zebrafish, which is comparable to the neonatal and adult mouse (Matrone et al., 2015 and Sano et al., 2002). Consistent with the aforementioned observations, I found that continuous CDK9i treatment with FVP or AT7519 reduces cardiac contractility and cardiomyocyte number expansion. Although homozygous *cdk9* mutants displayed abnormal global phenotypes (**Appendix Figure 4**), their heart rates, which gradually deteriorated (**Figure 5.1C** and **D)**, are markedly lower than that of wild-type zebrafish (**Appendix Figure 2**). These data suggest that CDK9 is required to maintain cardiac electrophysiology, which when perturbed could be a molecular mechanism that causes drug-induced cardiotoxicity (Mamoshina et al., 2021). Recently it was shown that developmental cardiomyocyte contractility causes cardiomyocyte delamination during cardiac trabeculation in zebrafish (Priya et al., 2020). Thus, perhaps continuous CDK9 inhibition disturbs the contractile actomyosin machinery, which may lead to downstream defects in cardiac function and cardiomyocyte number expansion. Combined, these data support the notion that CDK9 is crucial for maintaining cardiac function during cardiac development. Interestingly, the functional role of CDK9 switches during adulthood in mammals to promoting cardiac hypertrophy, and ectopic CDK9 activation causes heart failure in mice (Sano et al., 2002 and Sano et al., 2004). As such, CDK9 inhibitors have also been proposed as a therapy to treat pathological cardiac hypertrophy (Krystof et al., 2010), although this has not been tested preclinically or clinically.

In this project, I was specifically interested in targeting the neutrophil response to cardiac injury. It was previously unknown whether therapeutically enhancing neutrophil resolution influences cardiac regeneration. The larval zebrafish permits unparalleled imaging of inflammatory and regenerative responses following injury, while allowing high throughput *in vivo* drug screening, a unique feat not possible in other animal models. Therefore, I utilised our characterised larval zebrafish cardiac injury model to investigate whether CDK9 inhibitor treatment resolves neutrophilic inflammation, and importantly, whether this modulates cardiac regeneration. Our group has previously shown that CDK9 inhibitor treatment with AT7519 and FVP resolves neutrophilic inflammation via the induction of apoptosis following tail resection in larval zebrafish (Hoodless et al., 2016). In this study, I have shown that both AT7519 and FVP promote neutrophil reverse migration from the cardiac injury site during the peak inflammatory response. Numerous studies have reported that CDK9 inhibitors induce neutrophil apoptosis, however, it was not previously known that these compounds can also promote neutrophil reverse migration from smaller and more sterile wounds. This finding may open new avenues for exploring CDK9 inhibitor treatment in settings of acute inflammation, as these drugs are often studied in models of non-resolving inflammation (Cartwright et al., 2019).

As discussed above, neutrophil reverse migration is primarily chemokine-dependent following larval zebrafish wounding (Isles et al., 2019; Powell et al., 2017 and Coombs et al., 2019). Thus, FVP and AT7519 could have inhibited neutrophil-specific chemokine signaling at the cardiac lesion to promote reverse migration. Indeed, other inflammatory mediators present at the wound site and shown to regulate neutrophil wound retention in larval zebrafish could have been supressed by CDK9 inhibition. These include reactive oxygen species, specifically hydrogen peroxide, and cytokines such as *il-1β* (Yoo et al., 2010 and Yan et al., 2014). Continuous treatment with both FVP and AT7519 also caused a loss of macrophage retention at the injured heart by promoting their reverse migration. Similar to neutrophil reverse

migration, wound-recruited macrophages may have also sensed a dampened chemotactic gradient at the injured heart with CDK9i treatment. Alternatively, the loss of cardiac macrophage retention could have been secondary to the impaired cardiac function that was apparent at the later timepoints. Nevertheless, the effect of CDK9i treatment on injury-induced expression of inflammatory mediators and chemoattractants warrants further study. Furthermore, continuous CDK9i treatment caused neutrophils, but not macrophages, to undergo cell death during steady state, and thus was associated with neutropenia. Continuous CDK9i treatment may also cause apoptosis of other non-immune cell types, however this was not tested. Roscovitine has been shown to protect against doxorubicin-induced cardiomyocyte apoptosis and contractile dysfunction in rodent models (Xia et al., 2018), perhaps suggesting that AT7519 or FVP may not encourage cardiomyocyte death in our zebrafish model.

To maximise the potent pro-resolving effects of CDK9i treatment on cardiac-infiltrating neutrophils, while minimising unwanted perturbations to cardiac physiology, macrophage recruitment and host defence, a shorter pulsed (i.e., transient) treatment was adopted. This transient CDK9i treatment resolved neutrophilic inflammation at the injured heart, while circumventing all adverse effects, indicating that prolonged neutrophil infiltration is not necessary for sufficient macrophage recruitment/retention and heart repair/regeneration. When comparing the macrophage response to cardiac injury following transient CDK9i treatment, I found an unexpected differential effect where AT7519, but not FVP, enhanced *TNF* expression specifically in wound-associated macrophages. Interestingly, this increase in *TNF*$^{+}$ macrophage presence following transient AT7519 treatment was associated with increased cardiomyocyte numbers and accelerated myocardial wound regeneration. However, these cardiomyocyte-specific regenerative effects were not observed following transient FVP treatment. My data suggests that this may be due to a lack of CDK9 selectivity caused by FVP during the transient treatment, which AT7519 did not exhibit. As such, it is plausible that FVP

may have suppressed *TNF* expression in wound-adjacent macrophages, subsequently halting downstream mitogenic signaling in the injured heart. Therefore, not only timing and duration of CDK9i treatment are crucial for targeting the acute inflammatory response, but CDK9 inhibitor selectivity is also paramount, especially when assessing tightly regulated and dynamic cellular events such as regeneration. My findings that timely AT7519 treatment resolves neutrophilic inflammation and promotes cardiac regeneration in larval zebrafish ultimately warrants its experimental validation in mammalian models that more closely mimic human myocardial infarction. This is pertinent for two reasons: 1) prolonged neutrophilic inflammation following MI, for example during I/R injury, is detrimental for cardiac repair outcomes (Frangogiannis et al., 2002 and Vinten-Johansen, 2004), and 2) tissue reparative macrophage polarisation is considered of key factor importance in promoting myocardial repair (Frangogiannis, 2015 and Ma et al., 2018).

6.3. Testing the efficacy of CDK9 inhibitors *in vivo* and *in vitro*

One of the most important outcomes of this project was the development and validation of a real-time drug selectivity assay in larval zebrafish *in vivo*, as previously this has only been achieved *in vitro* (Anastassiadis et al., 2011). Using homozygous *cdk9* mutants and heart rate as an accessible readout for drug selectivity, I found that AT7519 is a significantly more selective CDK9 inhibitor compared to FVP. Similar to the way in which morpholinos are tested in stable mutants to determine off-target effects in zebrafish (Stainier et al., 2017), the same principle can be applied to inhibitor drugs using the proposed selectivity assay. Therefore, this proposed method has the potential to be widely used as an effective tool for zebrafish drug screening studies. Importantly, the findings derived from this experiment offer a plausible explanation for the pro-regenerative effects observed with AT7519, and not FVP, highlighting the potential promise of AT7519 in a clinical setting. Due to structural homology between

kinases, CDK9 inhibitors can be promiscuous in their pharmacological activity by inhibiting other CDKs at varying potencies (Krystof et al., 2012). Some CDK9 inhibitors, such as Flavopiridol, have caused undesirable side effects in clinical trials including diarrhoea, fatigue, and hematologic toxicities (Lanasa et al., 2015 and Morales and Giordano, 2016). As I have also shown differing regenerative and selectivity responses between FVP and AT7519, there is a need to develop more efficacious CDK9 inhibitors to maximise potential therapeutic benefits. Developing an allosteric pharmacological CDK9 inhibitor that does not inhibit the ATP-binding site of other CDKs has thus far been unachievable (Mariaule and Belmont, 2014 and Boffo et al., 2018). Hence, we set out to identify novel CDK9 inhibitor-like molecules that could be optimised to improve selectivity and potency. To address this, I performed an *in silico* similarity screen of BioAscent's 125k diverse compound library using six potent and selective CDK9 inhibitors (AT7519, LDC000067, MC180295, AZD4573, NVP-2 and iCDK9). During the computational screening, we shortlisted BioAscent compounds that displayed the highest 3D structural similarity between the known CDK9 inhibitors. I was planning to screen these shortlisted compounds in a high throughput CDK9 inhibition assay to determine potencies and identify potential hits. However, this was not possible due to the COVID-19 pandemic. As the CDK9 inhibition screen has commercial potential, our scientific collaborators at BioAscent were still interesting in developing the assay. Thus, our curated focussed library could still be screened in the future.

In order to validate the biological efficacy of CDK9i treatment on isolated human neutrophils, I performed an *in vitro* apoptosis assay using Flavopiridol. As reported with other CDK9 inhibitors (Dorward et al., 2017; Leitch et al., 2010 and Lucas et al., 2013), I found that FVP promotes human neutrophil apoptosis *in vitro*, which was reversed with pan caspase inhibition. The Rossi laboratory is capable of performing this assay on approximately ten different compounds during one experiment in a given day. Therefore, any hits identified from the

BioAscent CDK9 inhibition screen could be screened with human neutrophils relatively quickly to examine apoptotic and pro-resolving potencies *in vitro*. The following pipeline could be used to discern the most promising CDK9 inhibitor compounds following initial hit identification with BioAscent:

1. Human neutrophil apoptosis assay
2. Larval zebrafish CDK9 inhibitor selectivity assay
3. Larval zebrafish neutrophil resolution assay
4. Larval zebrafish tissue repair/regeneration assay

Hit compounds that are found to promote human neutrophil apoptosis *in vitro* could then be tested in our newly proposed larval zebrafish selectivity assay *in vivo*. As this assay is designed to identify selective CDK9 inhibitors, any compounds that lack CDK9 selectivity (similar to FVP) could be excluded at this stage. Subsequent experimentation using shortlisted selective CDK9 inhibitors could involve examination of wound inflammation and regeneration in larval zebrafish *in vivo*. It is preferable to have a refined number of compounds (ideally no more than three) to test in these experiments as they involve high resolution serial or timelapse imaging of dynamic cellular events, and thus are not as high throughput. In addition to our heart injury model, the drug screening pipeline described could be applied to other wounding/regeneration models associated with neutrophilic inflammation in larval zebrafish, such as the tail fin, spinal cord, brain, liver and somitic muscle (Li et al., 2012; Tsarouchas et al., 2018; Herzog et al., 2019; Stoddard et al., 2019 and Gurevich et al., 2018). Excluding the larval zebrafish selectivity assay, the above pipeline could also be used for phenotypic screening to identify compounds that promote neutrophil resolution and tissue repair/regeneration agnostic of a specific target.

6.4. Future directions

To better appreciate the expression profile of infiltrating immune cells and heart cells following injury in our model, transcriptomic, epigenomic and/or proteomic studies are required. Single-cell RNA sequencing and ATAC sequencing experiments have recently been performed in adult and embryonic zebrafish hearts (Honkoop et al., 2019 and Yuan et al., 2018); thus, these methods are likely to be feasible in larval zebrafish. Importantly, these techniques would shed light on macrophage and neutrophil heterogeneity in the regenerating heart. I have shown that immune cell heterogeneity can change dynamically over a one-day period (**Figure 4.7**); however, we were limited by the lack of characterised immune cell subsets in larval zebrafish. Therefore, immune cell heterogeneity requires further investigation, and I believe that our cardiac injury model could be uniquely harnessed to achieve that. Such experimentation in our highly regenerative model could identify unique molecular crosstalk between immune and cardiac cells, potentially providing a roadmap to novel treatment strategies that promote regeneration of the mammalian myocardium. Perhaps a specific population of recruited immune cells initiate injury-associated cardiomyocyte dedifferentiation and proliferation, for example.

To better understand the requirement of immune cells during cardiac injury and regeneration (cellular debridement, cardiomyocyte proliferation and myocardial wound closure), cell-specific ablation experiments would need to be performed. The role of macrophages in our model is being investigated in a separate study using *irf8* (macrophage null) mutants (Shiau et al., 2015), and macrophage nitroreductase/metronidazole ablation (Gray et al., 2011). The results of this study will be particularly important, especially since I found that transient AT7519 treatment increased cardiac *TNF* macrophage presence, which was associated with improved cardiomyocyte regeneration. To confirm if this pro-regenerative effect is macrophage dependent, AT7519 could be transiently administered in *irf8* mutant zebrafish and

cardiomyocyte regeneration assessed. Importantly, the functional role of neutrophils could also be studied in our cardiac injury model using *csf3r* mutants which are neutrophil deplete (Pazhakh et al., 2017), or *drf* mutants which are *mpx* deficient (Pase et al., 2012). Similarly, neutrophils could be temporally ablated by treating *mpx:NTR-mCherry* larvae with metronidazole (Britto et al., 2018). The advantages of cell-specific nitroreductase/metronidazole ablation are that it is not confounded by developmental mutations or complete lack of immune cells, and it can be controlled in a time-dependent manner. However, a caveat is that at high doses the pro-drug metronidazole can cause off-target effects (Curado et al., 2007).

As my CDK9 inhibitor findings are mostly from a developing zebrafish model, it would be important to validate AT7519 treatment in an adult zebrafish or mammalian model of myocardial infarction. It will be particularly important to determine whether AT7519 polarises macrophages to a reparative phenotype and how this regulates cardiac fibrosis, scar resolution, angiogenesis and function. Furthermore, it will be necessary to identify whether AT7519 affects other immune cell types absent in our model. Namely monocytes, B cells, T cells and eosinophils – all of which are known to play important roles during myocardial injury and repair (Hofmann and Frantz, 2015 and Toor et al., 2017). AT7519 could be a particularly effective treatment in clinical settings where MI is followed by prolonged coronary reperfusion injury, as there is a profound secondary influx of neutrophils (Vinten-Johansen, 2004; Niccoli et al., 2009 and Mangold et al., 2015). This can occur following percutaneous coronary intervention, a standard clinical procedure for opening an acutely occluded coronary artery following MI. Thus, AT7519 could be transiently administered at the time of PCI via a drug eluting-stent, or as an intra-coronary bolus injection, to resolve locally recruited neutrophils and promote downstream mechanisms that modulate myocardial repair.

6.5. Concluding remarks

The larval zebrafish is a powerful model system to study inflammatory and regenerative processes following wounding *in vivo*. During the course of this study, a series of live imaging techniques were developed to characterise local and systemic immune cell migration responses to cardiac injury in larval zebrafish. Immune cell recruitment and resolution kinetics were found to be comparable to mammalian models of cardiac injury. Additionally, the immune response was found to precede heart repair/regeneration, which is comparable to adult zebrafish cardiac injury. Our amenable model was used to investigate the effect of CDK9i treatment on the resolution of neutrophilic inflammation and cardiac regeneration. AT7519 and FVP were found to resolve neutrophil infiltration by inducing reverse migration from the cardiac injury site. However, AT7519, unlike FVP, showed promise as a highly selective CDK9 inhibitor by harnessing macrophage polarisation and promoting cardiomyocyte regeneration. As such, future research should establish whether selective CDK9 inhibitors, such as AT7519, have analogous reparative effects on macrophage polarisation and infarct healing in mammalian models of MI associated with neutrophilic inflammation. This could ultimately reveal the clinical potential of selective CDK9 inhibition as an immunomodulatory therapy for myocardial infarction.

References

Abbate, A. *et al.* (2011) 'Alterations in the Interleukin-1/Interleukin-1 Receptor Antagonist Balance Modulate Cardiac Remodeling following Myocardial Infarction in the Mouse', *PLOS ONE*, 6(11), p. e27923. doi: 10.1371/journal.pone.0027923.

Albert, T. K. *et al.* (2014) 'Characterization of molecular and cellular functions of the cyclin-dependent kinase CDK9 using a novel specific inhibitor', *British Journal of Pharmacology*, 171(1), pp. 55–68. doi: 10.1111/bph.12408.

Alessandri, A. L. *et al.* (2011) 'Induction of Eosinophil Apoptosis by the Cyclin-Dependent Kinase Inhibitor AT7519 Promotes the Resolution of Eosinophil-Dominant Allergic Inflammation', *PLOS ONE*, 6(9), p. e25683. doi: 10.1371/journal.pone.0025683.

Anastassiadis, T. *et al.* (2011) 'Comprehensive assay of kinase catalytic activity reveals features of kinase inhibitor selectivity', *Nature biotechnology*, 29(11), pp. 1039–1045. doi: 10.1038/nbt.2017.

Anderson, J. L. and Morrow, D. A. (2017) 'Acute Myocardial Infarction', *The New England Journal of Medicine*, 376(21), pp. 2053–2064. doi: 10.1056/NEJMra1606915.

Arruda-Olson, A. M. *et al.* (2009) 'Neutrophilia predicts death and heart failure after myocardial infarction: a community-based study', *Circulation. Cardiovascular Quality and Outcomes*, 2(6), pp. 656–662. doi: 10.1161/CIRCOUTCOMES.108.831024.

Arslan, F. *et al.* (2010) 'Myocardial ischemia/reperfusion injury is mediated by leukocytic toll-like receptor-2 and reduced by systemic administration of a novel anti-toll-like receptor-2 antibody', *Circulation*, 121(1), pp. 80–90. doi: 10.1161/CIRCULATIONAHA.109.880187.

Awan, F. T. *et al.* (2016) 'A phase 1 clinical trial of flavopiridol consolidation in chronic lymphocytic leukemia patients following chemoimmunotherapy', *Annals of Hematology*, 95(7), pp. 1137–1143. doi: 10.1007/s00277-016-2683-1.

Azevedo, W. F. D. *et al.* (1996) 'Structural basis for specificity and potency of a flavonoid inhibitor of human CDK2, a cell cycle kinase', *Proceedings of the National Academy of Sciences*, 93(7), pp. 2735–2740. doi: 10.1073/pnas.93.7.2735.

Bacon, C. W. and D'Orso, I. (2018) 'CDK9: a signaling hub for transcriptional control', *Transcription*, 10(2), pp. 57–75. doi: 10.1080/21541264.2018.1523668.

Baell, J. B. and Holloway, G. A. (2010) 'New Substructure Filters for Removal of Pan Assay Interference Compounds (PAINS) from Screening Libraries and for Their Exclusion in Bioassays', *Journal of Medicinal Chemistry*, 53(7), pp. 2719–2740. doi: 10.1021/jm901137j.

Barth, N. D. *et al.* (2020) 'A fluorogenic cyclic peptide for imaging and quantification of drug-induced apoptosis', *Nature Communications*, 11(1), p. 4027. doi: 10.1038/s41467-020-17772-7.

Baumli, S. *et al.* (2008) 'The structure of P-TEFb (CDK9/cyclin T1), its complex with flavopiridol and regulation by phosphorylation', *The EMBO journal*, 27(13), pp. 1907–1918. doi: 10.1038/emboj.2008.121.

Bennett, C. M. *et al.* (2001) 'Myelopoiesis in the zebrafish, Danio rerio', *Blood*, 98(3), pp. 643–651. doi: 10.1182/blood.v98.3.643.

Bentzon Jacob Fog *et al.* (2014) 'Mechanisms of Plaque Formation and Rupture', *Circulation Research*, 114(12), pp. 1852–1866. doi: 10.1161/CIRCRESAHA.114.302721.

Bevan, L. *et al.* (2020) 'Specific macrophage populations promote both cardiac scar deposition and subsequent resolution in adult zebrafish', *Cardiovascular Research*, 116(7), pp. 1357–1371. doi: 10.1093/cvr/cvz221.

Bianchi, M. E. (2007) 'DAMPs, PAMPs and alarmins: all we need to know about danger', *Journal of Leukocyte Biology*, 81(1), pp. 1–5. doi: 10.1189/jlb.0306164.

Boffo, S. *et al.* (2018) 'CDK9 inhibitors in acute myeloid leukemia', *Journal of experimental & clinical cancer research: CR*, 37(1), p. 36. doi: 10.1186/s13046-018-0704-8.

Bournazou, I. *et al.* (2009) 'Apoptotic human cells inhibit migration of granulocytes via release of lactoferrin', *The Journal of Clinical Investigation*, 119(1), pp. 20–32. doi: 10.1172/JCI36226.

Bratton, D. L. and Henson, P. M. (2011) 'Neutrophil clearance: when the party is over, clean-up begins', *Trends in Immunology*, 32(8), pp. 350–357. doi: 10.1016/j.it.2011.04.009.

Britto, D. D. *et al.* (2018) 'Macrophages enhance Vegfa-driven angiogenesis in an embryonic zebrafish tumour xenograft model', *Disease Models & Mechanisms*, 11(12). doi: 10.1242/dmm.035998.

Buckley, C. *et al.* (2017) 'Precise spatio-temporal control of rapid optogenetic cell ablation with mem-KillerRed in Zebrafish', *Scientific Reports*, 7(1), p. 5096. doi: 10.1038/s41598-017-05028-2.

Buckley, C. D. *et al.* (2013) 'The resolution of inflammation', *Nature Reviews. Immunology*, 13(1), pp. 59–66. doi: 10.1038/nri3362.

Bujak, M. *et al.* (2008) 'Interleukin-1 receptor type I signaling critically regulates infarct healing and cardiac remodeling', *The American Journal of Pathology*, 173(1), pp. 57–67. doi: 10.2353/ajpath.2008.070974.

Cartwright, J. A., Lucas, C. D. and Rossi, A. G. (2019) 'Inflammation Resolution and the Induction of Granulocyte Apoptosis by Cyclin-Dependent Kinase Inhibitor Drugs', *Frontiers in Pharmacology*, 10. doi: 10.3389/fphar.2019.00055.

Cassandri, M. *et al.* (2020) 'CDK9 as a Valuable Target in Cancer: From Natural Compounds Inhibitors to Current Treatment in Pediatric Soft Tissue Sarcomas', *Frontiers in Pharmacology*, 11. doi: 10.3389/fphar.2020.01230.

Cavone, L. *et al.* (2020) 'A Unique Macrophage Subpopulation Signals Directly to Progenitor Cells to Promote Regenerative Neurogenesis in the Zebrafish Spinal Cord'. SSRN Scholarly Paper. Social Science Research Network. doi: 10.2139/ssrn.3712669.

Cereto-Massagué, A. *et al.* (2015) 'Molecular fingerprint similarity search in virtual screening', *Methods*, 71, pp. 58–63. doi: 10.1016/j.ymeth.2014.08.005.

Chablais, F. *et al.* (2011) 'The zebrafish heart regenerates after cryoinjury-induced myocardial infarction', *BMC Developmental Biology*, 11(1), p. 21. doi: 10.1186/1471-213X-11-21.

Chao, J. R. *et al.* (1998) 'mcl-1 is an immediate-early gene activated by the granulocyte-macrophage colony-stimulating factor (GM-CSF) signaling pathway and is one component of the GM-CSF viability response', *Molecular and Cellular Biology*, 18(8), pp. 4883–4898. doi: 10.1128/mcb.18.8.4883.

Chao, S.-H. *et al.* (2000) 'Flavopiridol Inhibits P-TEFb and Blocks HIV-1 Replication', *Journal of Biological Chemistry*, 275(37), pp. 28345–28348. doi: 10.1074/jbc.C000446200.

Chen, A. T. and Zon, L. I. (2009) 'Zebrafish blood stem cells', *Journal of Cellular Biochemistry*, 108(1), pp. 35–42. doi: https://doi.org/10.1002/jcb.22251.

Chen, B. and Frangogiannis, N. G. (2021) 'Chemokines in Myocardial Infarction', *Journal of Cardiovascular Translational Research*, 14(1), pp. 35–52. doi: 10.1007/s12265-020-10006-7.

Chen, E. X. *et al.* (2014) 'A Phase I study of cyclin-dependent kinase inhibitor, AT7519, in patients with advanced cancer: NCIC Clinical Trials Group IND 177', *British Journal of Cancer*, 111(12), pp. 2262–2267. doi: 10.1038/bjc.2014.565.

Chen, M.-C. *et al.* (2000) 'Cloning and Characterization of a Novel Nuclear Bcl-2 Family Protein, zfMcl-1a, in Zebrafish Embryo', *Biochemical and Biophysical Research Communications*, 279(2), pp. 725–731. doi: 10.1006/bbrc.2000.3977.

Chia, S. *et al.* (2009) 'Association of leukocyte and neutrophil counts with infarct size, left ventricular function and outcomes after percutaneous coronary intervention for ST-elevation myocardial infarction', *The American Journal of Cardiology*, 103(3), pp. 333–337. doi: 10.1016/j.amjcard.2008.09.085.

Choi, J. *et al.* (2007) 'FoxH1 negatively modulates flk1 gene expression and vascular formation in zebrafish', *Developmental Biology*, 304(2), pp. 735–744. doi: 10.1016/j.ydbio.2007.01.023.

Cidado, J. *et al.* (2020) 'AZD4573 Is a Highly Selective CDK9 Inhibitor That Suppresses MCL-1 and Induces Apoptosis in Hematologic Cancer Cells', *Clinical Cancer Research: An Official Journal of the American Association for Cancer Research*, 26(4), pp. 922–934. doi: 10.1158/1078-0432.CCR-19-1853.

Coombs, C. *et al.* (2019) 'Chemokine receptor trafficking coordinates neutrophil clustering and dispersal at wounds in zebrafish', *Nature Communications*, 10(1), p. 5166. doi: 10.1038/s41467-019-13107-3.

Cordeiro, J. V. and Jacinto, A. (2013) 'The role of transcription-independent damage signals in the initiation of epithelial wound healing', *Nature Reviews. Molecular Cell Biology*, 14(4), pp. 249–262. doi: 10.1038/nrm3541.

Curado, S. *et al.* (2007) 'Conditional targeted cell ablation in zebrafish: A new tool for regeneration studies', *Developmental Dynamics*, 236(4), pp. 1025–1035. doi: https://doi.org/10.1002/dvdy.21100.

Daseke, M. J. *et al.* (2019) 'Neutrophil proteome shifts over the myocardial infarction time continuum', *Basic Research in Cardiology*, 114(5), p. 37. doi: 10.1007/s00395-019-0746-x.

Daseke, M. J. *et al.* (2020) 'Exogenous IL-4 shuts off pro-inflammation in neutrophils while stimulating anti-inflammation in macrophages to induce neutrophil phagocytosis following myocardial infarction', *Journal of Molecular and Cellular Cardiology*, 145, pp. 112–121. doi: 10.1016/j.yjmcc.2020.06.006.

Daseke, M. J. *et al.* (2021) 'Neutrophil signaling during myocardial infarction wound repair', *Cellular Signalling*, 77, p. 109816. doi: 10.1016/j.cellsig.2020.109816.

Davison, J. M. *et al.* (2007) 'Transactivation from Gal4-VP16 transgenic insertions for tissue-specific cell labeling and ablation in zebrafish', *Developmental Biology*, 304(2), pp. 811–824. doi: 10.1016/j.ydbio.2007.01.033.

de Jong, J. L. O. and Zon, L. I. (2005) 'Use of the zebrafish system to study primitive and definitive hematopoiesis', *Annual Review of Genetics*, 39, pp. 481–501. doi: 10.1146/annurev.genet.39.073003.095931.

de Oliveira, S. *et al.* (2014) 'ATP modulates acute inflammation in vivo through dual oxidase 1-derived H2O2 production and NF-κB activation', *Journal of Immunology*, 192(12), pp. 5710–5719. doi: 10.4049/jimmunol.1302902.

de Oliveira, S. *et al.* (2015) 'Duox1-derived H2O2 modulates Cxcl8 expression and neutrophil recruitment via JNK/c-JUN/AP-1 signaling and chromatin modifications', *Journal of Immunology*, 194(4), pp. 1523–1533. doi: 10.4049/jimmunol.1402386.

Deng, Q. *et al.* (2013) 'Localized bacterial infection induces systemic activation of neutrophils through Cxcr2 signaling in zebrafish', *Journal of Leukocyte Biology*, 93(5), pp. 761–769. doi: 10.1189/jlb.1012534.

de Preux Charles, A.-S. *et al.* (2016) 'Distinct effects of inflammation on preconditioning and regeneration of the adult zebrafish heart', *Open Biology*, 6(7). doi: 10.1098/rsob.160102.

Dewald, O. *et al.* (2005) 'CCL2/Monocyte Chemoattractant Protein-1 regulates inflammatory responses critical to healing myocardial infarcts', *Circulation Research*, 96(8), pp. 881–889. doi: 10.1161/01.RES.0000163017.13772.3a.

Dorward, D. A. *et al.* (2017) 'The cyclin-dependent kinase inhibitor AT7519 accelerates neutrophil apoptosis in sepsis-related acute respiratory distress syndrome', *Thorax*, 72(2), pp. 182–185. doi: 10.1136/thoraxjnl-2016-209229.

Duffin, R. *et al.* (2009) 'The CDK inhibitor, R-roscovitine, promotes eosinophil apoptosis by down-regulation of Mcl-1', *FEBS letters*, 583(15), pp. 2540–2546. doi: 10.1016/j.febslet.2009.07.017.

Duffin, R. *et al.* (2010) 'Targeting granulocyte apoptosis: mechanisms, models, and therapies', *Immunological Reviews*, 236, pp. 28–40. doi: 10.1111/j.1600-065X.2010.00922.x.

Dzhagalov, I., St John, A. and He, Y.-W. (2007) 'The antiapoptotic protein Mcl-1 is essential for the survival of neutrophils but not macrophages', *Blood*, 109(4), pp. 1620–1626. doi: 10.1182/blood-2006-03-013771.

Ebejer, J.-P., Morris, G. M. and Deane, C. M. (2012) 'Freely available conformer generation methods: how good are they?', *Journal of Chemical Information and Modeling*, 52(5), pp. 1146–1158. doi: 10.1021/ci2004658.

Edwards, S. W. *et al.* (2004) 'Regulation of neutrophil apoptosis by Mcl-1', *Biochemical Society Transactions*, 32(Pt3), pp. 489–492. doi: 10.1042/BST0320489.

Ellett, F. *et al.* (2011) 'mpeg1 promoter transgenes direct macrophage-lineage expression in zebrafish', *Blood*, 117(4), pp. e49–e56. doi: 10.1182/blood-2010-10-314120.

Ellett, F. *et al.* (2015) 'Defining the phenotype of neutrophils following reverse migration in zebrafish', *Journal of Leukocyte Biology*, 98(6), pp. 975–981. doi: 10.1189/jlb.3MA0315-105R.

Enyedi, B., Jelcic, M. and Niethammer, P. (2016) 'The Cell Nucleus Serves as a Mechanotransducer of Tissue Damage-Induced Inflammation', *Cell*, 165(5), pp. 1160–1170. doi: 10.1016/j.cell.2016.04.016.

Epelman, S., Liu, P. P. and Mann, D. L. (2015) 'Role of Innate and Adaptive Immunity in Cardiac Injury and Repair', *Nature reviews. Immunology*, 15(2), pp. 117–129. doi: 10.1038/nri3800.

Eyvazi, S. *et al.* (2019) 'CDK9 as an Appealing Target for Therapeutic Interventions', *Current Drug Targets*, 20(4), pp. 453–464. doi: 10.2174/1389450119666181026152221.

Falco, G. D. *et al.* (2002) 'Cdk9, a member of the cdc2-like family of kinases, binds to gp130, the receptor of the IL-6 family of cytokines', *Oncogene*, 21(49), pp. 7464–7470. doi: 10.1038/sj.onc.1205967.

Fang James C. (2005) 'Angiotensin-Converting Enzyme Inhibitors or β-Blockers in Heart Failure', *Circulation*, 112(16), pp. 2380–2382. doi: 10.1161/CIRCULATIONAHA.105.586545.

Feng, Y., Renshaw, S. and Martin, P. (2012) 'Live Imaging of Tumor Initiation in Zebrafish Larvae Reveals a Trophic Role for Leukocyte-Derived PGE2', *Current Biology*, 22(13), pp. 1253–1259. doi: 10.1016/j.cub.2012.05.010.

Filippi, M.-D. (2019) 'Neutrophil transendothelial migration: updates and new perspectives', *Blood*, 133(20), pp. 2149–2158. doi: 10.1182/blood-2018-12-844605.

Frangogiannis, N. G. *et al.* (1998) 'Resident cardiac mast cells degranulate and release preformed TNF-alpha, initiating the cytokine cascade in experimental canine myocardial ischemia/reperfusion', *Circulation*, 98(7), pp. 699–710. doi: 10.1161/01.cir.98.7.699.

Frangogiannis, N. G. (2012) 'Matricellular Proteins in Cardiac Adaptation and Disease', *Physiological Reviews*, 92(2), pp. 635–688. doi: 10.1152/physrev.00008.2011.

Frangogiannis, N. G. (2014) 'The inflammatory response in myocardial injury, repair, and remodelling', *Nature Reviews. Cardiology*, 11(5), pp. 255–265. doi: 10.1038/nrcardio.2014.28.

Frangogiannis, N. G. (2015) 'Emerging roles for macrophages in cardiac injury: cytoprotection, repair, and regeneration', *The Journal of Clinical Investigation*, 125(8), pp. 2927–2930. doi: 10.1172/JCI83191.

Frangogiannis, N. G., Smith, C. W. and Entman, M. L. (2002) 'The inflammatory response in myocardial infarction', *Cardiovascular Research*, 53(1), pp. 31–47. doi: 10.1016/s0008-6363(01)00434-5.

Frantz, S. and Nahrendorf, M. (2014) 'Cardiac macrophages and their role in ischaemic heart disease', *Cardiovascular Research*, 102(2), pp. 240–248. doi: 10.1093/cvr/cvu025.

Fu, N. Y. *et al.* (2015) 'EGF-mediated induction of Mcl-1 at the switch to lactation is essential for alveolar cell survival', *Nature Cell Biology*, 17(4), pp. 365–375. doi: 10.1038/ncb3117.

Furze, R. C. and Rankin, S. M. (2008) 'Neutrophil mobilization and clearance in the bone marrow', *Immunology*, 125(3), pp. 281–288. doi: 10.1111/j.1365-2567.2008.02950.x.

García-Prieto, J. *et al.* (2017) 'Neutrophil stunning by metoprolol reduces infarct size', *Nature Communications*, 8, p. 14780. doi: 10.1038/ncomms14780.

Garlichs, C. D. *et al.* (2004) 'Delay of neutrophil apoptosis in acute coronary syndromes', *Journal of Leukocyte Biology*, 75(5), pp. 828–835. doi: https://doi.org/10.1189/jlb.0703358.

Garriga, J. *et al.* (2010) 'Selective control of gene expression by CDK9 in human cells', *Journal of cellular physiology*, 222(1), pp. 200–208. doi: 10.1002/jcp.21938.

Geissmann, F., Jung, S. and Littman, D. R. (2003) 'Blood monocytes consist of two principal subsets with distinct migratory properties', *Immunity*, 19(1), pp. 71–82. doi: 10.1016/s1074-7613(03)00174-2.

Ginhoux, F. *et al.* (2016) 'New insights into the multidimensional concept of macrophage ontogeny, activation and function', *Nature Immunology*, 17(1), pp. 34–40. doi: 10.1038/ni.3324.

Godwin, J. W. *et al.* (2017) 'Heart regeneration in the salamander relies on macrophage-mediated control of fibroblast activation and the extracellular landscape', *npj Regenerative Medicine*, 2(1), pp. 1–11. doi: 10.1038/s41536-017-0027-y.

González-Rosa, J. M. *et al.* (2011) 'Extensive scar formation and regression during heart regeneration after cryoinjury in zebrafish', *Development*, 138(9), pp. 1663–1674. doi: 10.1242/dev.060897.

González-Rosa, J. M., Burns, C. E. and Burns, C. G. (2017) 'Zebrafish heart regeneration: 15 years of discoveries', *Regeneration*, 4(3), pp. 105–123. doi: 10.1002/reg2.83.

Gordon, S. and Martinez, F. O. (2010) 'Alternative Activation of Macrophages: Mechanism and Functions', *Immunity*, 32(5), pp. 593–604. doi: 10.1016/j.immuni.2010.05.007.

Gordon, S. and Taylor, P. R. (2005) 'Monocyte and macrophage heterogeneity', *Nature Reviews Immunology*, 5(12), pp. 953–964. doi: 10.1038/nri1733.

Gray, C. *et al.* (2011) 'Simultaneous intravital imaging of macrophage and neutrophil behaviour during inflammation using a novel transgenic zebrafish', *Thrombosis and Haemostasis*, 105(5), pp. 811–819. doi: 10.1160/TH10-08-0525.

Gray, R. D. *et al.* (2018) 'Delayed neutrophil apoptosis enhances NET formation in cystic fibrosis', *Thorax*, 73(2), pp. 134–144. doi: 10.1136/thoraxjnl-2017-210134.

Gurevich, D. B. *et al.* (2018) 'Live imaging of wound angiogenesis reveals macrophage orchestrated vessel sprouting and regression', *The EMBO Journal*, 37(13). doi: 10.15252/embj.201797786.

Hall, C. and Crosier, P. (2010) 'Editorial: Maintaining the balance—fishing for drugs to treat persistent neutrophilic inflammation', *Journal of Leukocyte Biology*, 87(2), pp. 189–191. doi: https://doi.org/10.1189/jlb.0909647.

Haque, A. *et al.* (2011) 'Flavopiridol inhibits lipopolysaccharide-induced TNF-α production through inactivation of nuclear factor-κB and mitogen-activated protein kinases in the MyD88-dependent pathway', *Microbiology and Immunology*, 55(3), pp. 160–167. doi: https://doi.org/10.1111/j.1348-0421.2010.00304.x.

Harel-Adar, T. *et al.* (2011) 'Modulation of cardiac macrophages by phosphatidylserine-presenting liposomes improves infarct repair', *Proceedings of the National Academy of Sciences*, 108(5), pp. 1827–1832. doi: 10.1073/pnas.1015623108.

Harvie, E. A. and Huttenlocher, A. (2015) 'Neutrophils in host defense: new insights from zebrafish', *Journal of Leukocyte Biology*, 98(4), pp. 523–537. doi: 10.1189/jlb.4MR1114-524R.

Hasegawa, T. *et al.* (2015) 'A diffusible signal derived from hematopoietic cells supports the survival and proliferation of regenerative cells during zebrafish fin fold regeneration', *Developmental Biology*, 399(1), pp. 80–90. doi: 10.1016/j.ydbio.2014.12.015.

Hasegawa, T. *et al.* (2017) 'Transient inflammatory response mediated by interleukin-1β is required for proper regeneration in zebrafish fin fold', *eLife*, 23(6). doi: 10.7554/eLife.22716.

Hatori, N. *et al.* (1991) 'Beneficial effects of coronary venous retroinfusion but not left atrial administration of superoxide dismutase on myocardial necrosis in pigs', *European Heart Journal*, 12(3), pp. 442–450. doi: 10.1093/oxfordjournals.eurheartj.a059915.

Henry, K. M. *et al.* (2013) 'Zebrafish as a model for the study of neutrophil biology', *Journal of Leukocyte Biology*, 94(4), pp. 633–642. doi: https://doi.org/10.1189/jlb.1112594.

Herskowitz, A. *et al.* (1995) 'Cytokine mRNA expression in postischemic/reperfused myocardium', *The American Journal of Pathology*, 146(2), pp. 419–428.

Herzog, C. *et al.* (2019) 'Rapid clearance of cellular debris by microglia limits secondary neuronal cell death after brain injury in vivo', *Development*, 146(9). doi: 10.1242/dev.174698.

Heusch, G. (2020) 'Myocardial ischaemia-reperfusion injury and cardioprotection in perspective', *Nature Reviews. Cardiology*, 17(12), pp. 773–789. doi: 10.1038/s41569-020-0403-y.

Heymans, S. *et al.* (1999) 'Inhibition of plasminogen activators or matrix metalloproteinases prevents cardiac rupture but impairs therapeutic angiogenesis and causes cardiac failure', *Nature Medicine*, 5(10), pp. 1135–1142. doi: 10.1038/13459.

Hilgendorf, I. *et al.* (2014) 'Ly-6Chigh monocytes depend on Nr4a1 to balance both inflammatory and reparative phases in the infarcted myocardium', *Circulation Research*, 114(10), pp. 1611–1622. doi: 10.1161/CIRCRESAHA.114.303204.

Hind, L. E. and Huttenlocher, A. (2018) 'Neutrophil Reverse Migration and a Chemokinetic Resolution', *Developmental Cell*, 47(4), pp. 404–405. doi: 10.1016/j.devcel.2018.11.004.

Hofmann Ulrich and Frantz Stefan (2015) 'Role of Lymphocytes in Myocardial Injury, Healing, and Remodeling After Myocardial Infarction', *Circulation Research*, 116(2), pp. 354–367. doi: 10.1161/CIRCRESAHA.116.304072.

Holmes, G. R. *et al.* (2012) 'Repelled from the wound, or randomly dispersed? Reverse migration behaviour of neutrophils characterized by dynamic modelling', *Journal of The Royal Society Interface*, 9(77), pp. 3229–3239. doi: 10.1098/rsif.2012.0542.

Honkoop, H. *et al.* (2019) 'Single-cell analysis uncovers that metabolic reprogramming by ErbB2 signaling is essential for cardiomyocyte proliferation in the regenerating heart', *eLife*, 8. doi: 10.7554/eLife.50163.

Hoodless, L. J. *et al.* (2016) 'Genetic and pharmacological inhibition of CDK9 drives neutrophil apoptosis to resolve inflammation in zebrafish in vivo', *Scientific Reports*, 6(1), p. 36980. doi: 10.1038/srep36980.

Horckmans, M. *et al.* (2017) 'Neutrophils orchestrate post-myocardial infarction healing by polarizing macrophages towards a reparative phenotype', *European Heart Journal*, 38(3), pp. 187–197. doi: 10.1093/eurheartj/ehw002.

Howe, K. *et al.* (2013) 'The zebrafish reference genome sequence and its relationship to the human genome', *Nature*, 496(7446), pp. 498–503. doi: 10.1038/nature12111.

Hu, Z. *et al.* (2016) 'Inhibition of CDK9 prevents mechanical injury-induced inflammation, apoptosis and matrix degradation in cartilage explants', *European cells & materials*, 30, pp. 200–209. doi: 10.22203/ecm.v030a14.

Huang, C.-J. *et al.* (2003) 'Germ-line transmission of a myocardium-specific GFP transgene reveals critical regulatory elements in the cardiac myosin light chain 2 promoter of zebrafish', *Developmental Dynamics*, 228(1), pp. 30–40. doi: 10.1002/dvdy.10356.

Huang, S. and Frangogiannis, N. G. (2018) 'Anti-inflammatory therapies in myocardial infarction: failures, hopes and challenges', *British Journal of Pharmacology*, 175(9), pp. 1377–1400. doi: 10.1111/bph.14155.

Huang, W.-C. *et al.* (2013) 'Treatment of Glucocorticoids Inhibited Early Immune Responses and Impaired Cardiac Repair in Adult Zebrafish', *PLoS ONE*, 8(6). doi: 10.1371/journal.pone.0066613.

Huynh, M.-L. N., Fadok, V. A. and Henson, P. M. (2002) 'Phosphatidylserine-dependent ingestion of apoptotic cells promotes TGF-beta1 secretion and the resolution of inflammation', *The Journal of Clinical Investigation*, 109(1), pp. 41–50. doi: 10.1172/JCI11638.

Isles, H. M. *et al.* (2019) 'The CXCL12/CXCR4 Signaling Axis Retains Neutrophils at Inflammatory Sites in Zebrafish', *Frontiers in Immunology*, 10. doi: 10.3389/fimmu.2019.01784.

Jolly, S. R. *et al.* (1986) 'Reduction of myocardial infarct size by neutrophil depletion: Effect of duration of occlusion', *American Heart Journal*, 112(4), pp. 682–690. doi: 10.1016/0002-8703(86)90461-8.

Jopling, C. *et al.* (2010) 'Zebrafish heart regeneration occurs by cardiomyocyte dedifferentiation and proliferation', *Nature*, 464(7288), pp. 606–609. doi: 10.1038/nature08899.

Jordan, J. E., Zhao, Z.-Q. and Vinten-Johansen, J. (1999) 'The role of neutrophils in myocardial ischemia–reperfusion injury', *Cardiovascular Research*, 43(4), pp. 860–878. doi: 10.1016/S0008-6363(99)00187-X.

Jourdan, M. *et al.* (2000) 'Regulation of Bcl-2-family proteins in myeloma cells by three myeloma survival factors: interleukin-6, interferon-alpha and insulin-like growth factor 1', *Cell Death & Differentiation*, 7(12), pp. 1244–1252. doi: 10.1038/sj.cdd.4400758.

Kain, V. *et al.* (2015) 'Resolvin D1 activates the inflammation resolving response at splenic and ventricular site following myocardial infarction leading to improved ventricular function', *Journal of Molecular and Cellular Cardiology*, 84, pp. 24–35. doi: 10.1016/j.yjmcc.2015.04.003.

Karlsson, J., von Hofsten, J. and Olsson, P. E. (2001) 'Generating transparent zebrafish: a refined method to improve detection of gene expression during embryonic development', *Marine Biotechnology*, 3(6), pp. 522–527. doi: 10.1007/s1012601-0053-4.

Kaveh, A. *et al.* (2020) 'Live Imaging of Heart Injury in Larval Zebrafish Reveals a Multi-Stage Model of Neutrophil and Macrophage Migration', *Frontiers in Cell and Developmental Biology*, 8, p. 579943. doi: 10.3389/fcell.2020.579943.

Kennedy, A. D. and DeLeo, F. R. (2009) 'Neutrophil apoptosis and the resolution of infection', *Immunologic Research*, 43(1–3), pp. 25–61. doi: 10.1007/s12026-008-8049-6.

Kimmel, C. B. *et al.* (1995) 'Stages of embryonic development of the zebrafish', *Developmental Dynamics: An Official Publication of the American Association of Anatomists*, 203(3), pp. 253–310. doi: 10.1002/aja.1002030302.

Kobayashi, S. D. *et al.* (2005) 'Spontaneous neutrophil apoptosis and regulation of cell survival by granulocyte macrophage-colony stimulating factor', *Journal of Leukocyte Biology*, 78(6), pp. 1408–1418. doi: https://doi.org/10.1189/jlb.0605289.

Kohoutek, J. *et al.* (2009) 'Cyclin T2 is essential for mouse embryogenesis', *Molecular and Cellular Biology*, 29(12), pp. 3280–3285. doi: 10.1128/MCB.00172-09.

Kratz, E. *et al.* (2006) 'Functional characterization of the Bcl-2 gene family in the zebrafish', *Cell Death & Differentiation*, 13(10), pp. 1631–1640. doi: 10.1038/sj.cdd.4402016.

Kryštof, V., Baumli, S. and Fürst, R. (2012) 'Perspective of Cyclin-dependent kinase 9 (CDK9) as a Drug Target', *Current Pharmaceutical Design*, 18(20), pp. 2883–2890. doi: 10.2174/138161212800672750.

Kurrelmeyer, K. M. *et al.* (2000) 'Endogenous tumor necrosis factor protects the adult cardiac myocyte against ischemic-induced apoptosis in a murine model of acute myocardial infarction', *Proceedings of the National Academy of Sciences*, 97(10), pp. 5456–5461. doi: 10.1073/pnas.070036297.

Laflamme, M. A. and Murry, C. E. (2005) 'Regenerating the heart', *Nature Biotechnology*, 23(7), pp. 845–856. doi: 10.1038/nbt1117.

Lahiri, K. *et al.* (2005) 'Temperature Regulates Transcription in the Zebrafish Circadian Clock', *PLOS Biology*, 3(11), p. e351. doi: 10.1371/journal.pbio.0030351.

Lai, S.-L. *et al.* (2017) 'Reciprocal analyses in zebrafish and medaka reveal that harnessing the immune response promotes cardiac regeneration', *eLife*, 20(6). doi: 10.7554/eLife.25605.

Lam, P. and Huttenlocher, A. (2013) 'Interstitial leukocyte migration in vivo', *Current opinion in cell biology*, 25(5), pp. 650–658. doi: 10.1016/j.ceb.2013.05.007.

Lämmermann, T. *et al.* (2013) 'Neutrophil swarms require LTB4 and integrins at sites of cell death in vivo', *Nature*, 498(7454). doi: 10.1038/nature12175.

Lanasa, M. C. *et al.* (2015) 'Final Results of EFC6663: A Multicenter, International, Phase 2 Study of Alvocidib for Patients with Fludarabine-Refractory Chronic Lymphocytic Leukemia', *Leukemia research*, 39(5), pp. 495–500. doi: 10.1016/j.leukres.2015.02.001.

Lawson, N. D. and Weinstein, B. M. (2002) 'In vivo imaging of embryonic vascular development using transgenic zebrafish', *Developmental Biology*, 248(2), pp. 307–318. doi: 10.1006/dbio.2002.0711.

Le Gouill, S. *et al.* (2004) 'Mcl-1 regulation and its role in multiple myeloma', *Cell Cycle*, 3(10), pp. 1259–1262. doi: 10.4161/cc.3.10.1196.

Leitch, A. E. *et al.* (2010) 'The cyclin-dependent kinase inhibitor R-roscovitine down-regulates Mcl-1 to override pro-inflammatory signalling and drive neutrophil apoptosis', *European Journal of Immunology*, 40(4), pp. 1127–1138. doi: 10.1002/eji.200939664.

Leitch, A. E. *et al.* (2012) 'Cyclin-dependent kinases 7 and 9 specifically regulate neutrophil transcription and their inhibition drives apoptosis to promote resolution of inflammation', *Cell Death and Differentiation*, 19(12), pp. 1950–1961. doi: 10.1038/cdd.2012.80.

Lewis, E. F. *et al.* (2003) 'Predictors of late development of heart failure in stable survivors of myocardial infarction: the CARE study', *Journal of the American College of Cardiology*, 42(8), pp. 1446–1453. doi: 10.1016/s0735-1097(03)01057-x.

Li, D. *et al.* (2019) 'ARAF recurrent mutation causes central conducting lymphatic anomaly treatable with a MEK inhibitor', *Nature Medicine*, 25(7), pp. 1116–1122. doi: 10.1038/s41591-019-0479-2.

Li, J. *et al.* (2019) 'Transcription modulation by CDK9 regulates inflammatory genes and RIPK3-MLKL-mediated necroptosis in periodontitis progression', *Scientific Reports*, 9(1), p. 17369. doi: 10.1038/s41598-019-53910-y.

Li, L. *et al.* (2012) 'Live Imaging Reveals Differing Roles of Macrophages and Neutrophils during Zebrafish Tail Fin Regeneration', *Journal of Biological Chemistry*, 287(30), pp. 25353–25360. doi: 10.1074/jbc.M112.349126.

Lichtenauer, M., Mildner, M., Baumgartner, A., *et al.* (2011) 'Intravenous and intramyocardial injection of apoptotic white blood cell suspensions prevents ventricular remodelling by increasing elastin expression in cardiac scar tissue after myocardial infarction', *Basic Research in Cardiology*, 106(4), pp. 645–655. doi: 10.1007/s00395-011-0173-0.

Lichtenauer, M., Mildner, M., Hoetzenecker, K., *et al.* (2011) 'Secretome of apoptotic peripheral blood cells (APOSEC) confers cytoprotection to cardiomyocytes and inhibits tissue remodelling after acute myocardial infarction: a preclinical study', *Basic Research in Cardiology*, 106(6), pp. 1283–1297. doi: 10.1007/s00395-011-0224-6.

Lieschke, G. J. *et al.* (2001) 'Morphologic and functional characterization of granulocytes and macrophages in embryonic and adult zebrafish', *Blood*, 98(10), pp. 3087–3096. doi: 10.1182/blood.v98.10.3087.

Lieschke, G. J. *et al.* (2002) 'Zebrafish SPI-1 (PU.1) marks a site of myeloid development independent of primitive erythropoiesis: implications for axial patterning', *Developmental Biology*, 246(2), pp. 274–295. doi: 10.1006/dbio.2002.0657.

Lieschke, G. J. and Currie, P. D. (2007) 'Animal models of human disease: zebrafish swim into view', *Nature Reviews Genetics*, 8(5), pp. 353–367. doi: 10.1038/nrg2091.

Litt, M. R. *et al.* (1989) 'Neutrophil depletion limited to reperfusion reduces myocardial infarct size after 90 minutes of ischemia. Evidence for neutrophil-mediated reperfusion injury', *Circulation*, 80(6), pp. 1816–1827. doi: 10.1161/01.cir.80.6.1816.

Liu, X. *et al.* (2012) 'CDKI-71, a novel CDK9 inhibitor, is preferentially cytotoxic to cancer cells compared to flavopiridol', *International Journal of Cancer*, 130(5), pp. 1216–1226. doi: 10.1002/ijc.26127.

London, A. *et al.* (2011) 'Neuroprotection and progenitor cell renewal in the injured adult murine retina requires healing monocyte-derived macrophages', *The Journal of Experimental Medicine*, 208(1), pp. 23–39. doi: 10.1084/jem.20101202.

Loynes, C. A. *et al.* (2010) 'Pivotal Advance: Pharmacological manipulation of inflammation resolution during spontaneously resolving tissue neutrophilia in the zebrafish', *Journal of Leukocyte Biology*, 87(2), pp. 203–212. doi: 10.1189/jlb.0409255.

Loynes, C. A. *et al.* (2018) 'PGE2 production at sites of tissue injury promotes an anti-inflammatory neutrophil phenotype and determines the outcome of inflammation resolution in vivo', *Science Advances*, 4(9), p. 8320. doi: 10.1126/sciadv.aar8320.

Lu, H. *et al.* (2015) 'Compensatory induction of MYC expression by sustained CDK9 inhibition via a BRD4-dependent mechanism', *eLife*, 4, p. e06535. doi: 10.7554/eLife.06535.

Lucas, C. D. *et al.* (2013) 'Flavones induce neutrophil apoptosis by down-regulation of Mcl-1 via a proteasomal-dependent pathway', *The FASEB Journal*, 27(3), pp. 1084–1094. doi: https://doi.org/10.1096/fj.12-218990.

Lucas, C. D. *et al.* (2014) 'Downregulation of Mcl-1 has anti-inflammatory pro-resolution effects and enhances bacterial clearance from the lung', *Mucosal Immunology*, 7(4), pp. 857–868. doi: 10.1038/mi.2013.102.

Luke, J. J. *et al.* (2012) 'The Cyclin-Dependent Kinase Inhibitor Flavopiridol Potentiates Doxorubicin Efficacy in Advanced Sarcomas: Preclinical Investigations and Results of a Phase I Dose-Escalation Clinical Trial', *Clinical Cancer Research*, 18(9), pp. 2638–2647. doi: 10.1158/1078-0432.CCR-11-3203.

Ma, Y. *et al.* (2016) 'Temporal neutrophil polarization following myocardial infarction', *Cardiovascular Research*, 110(1), pp. 51–61. doi: 10.1093/cvr/cvw024.

Ma, Y., Mouton, A. J. and Lindsey, M. L. (2018) 'Cardiac macrophage biology in the steady-state heart, the aging heart, and following myocardial infarction', *Translational research*, 191, pp. 15–28. doi: 10.1016/j.trsl.2017.10.001.

Ma, Y., Yabluchanskiy, A. and Lindsey, M. L. (2013) 'Neutrophil roles in left ventricular remodeling following myocardial infarction', *Fibrogenesis & Tissue Repair*, 6(1), p. 11. doi: 10.1186/1755-1536-6-11.

Maekawa, N. *et al.* (2002) 'Improved myocardial ischemia/reperfusion injury in mice lacking tumor necrosis factor-alpha', *Journal of the American College of Cardiology*, 39(7), pp. 1229–1235. doi: 10.1016/s0735-1097(02)01738-2.

Mahadevan, D. *et al.* (2011) 'A phase I pharmacokinetic and pharmacodynamic study of AT7519, a cyclin-dependent kinase inhibitor in patients with refractory solid tumors', *Annals of Oncology: Official Journal of the European Society for Medical Oncology*, 22(9), pp. 2137–2143. doi: 10.1093/annonc/mdq734.

Mahler, D. A. *et al.* (2004) 'Efficacy and safety of a monoclonal antibody recognizing interleukin-8 in COPD: a pilot study', *Chest*, 126(3), pp. 926–934. doi: 10.1378/chest.126.3.926.

Malumbres, M. (2014) 'Cyclin-dependent kinases', *Genome Biology*, 15(6), p. 122. doi: 10.1186/gb4184.

Malumbres, M. and Barbacid, M. (2005) 'Mammalian cyclin-dependent kinases', *Trends in Biochemical Sciences*, 30(11), pp. 630–641. doi: 10.1016/j.tibs.2005.09.005.

Mamoshina, P., Rodriguez, B. and Bueno-Orovio, A. (2021) 'Toward a broader view of mechanisms of drug cardiotoxicity', *Cell Reports Medicine*, 2(3), p. 100216. doi: 10.1016/j.xcrm.2021.100216.

Mangold Andreas *et al.* (2015) 'Coronary Neutrophil Extracellular Trap Burden and Deoxyribonuclease Activity in ST-Elevation Acute Coronary Syndrome Are Predictors of ST-Segment Resolution and Infarct Size', *Circulation Research*, 116(7), pp. 1182–1192. doi: 10.1161/CIRCRESAHA.116.304944.

Mann, D. L. (2011) 'The emerging role of innate immunity in the heart and vascular system: for whom the cell tolls', *Circulation Research*, 108(9), pp. 1133–1145. doi: 10.1161/CIRCRESAHA.110.226936.

Mariaule, G. and Belmont, P. (2014) 'Cyclin-dependent kinase inhibitors as marketed anticancer drugs: where are we now? A short survey', *Molecules*, 19(9), pp. 14366–14382. doi: 10.3390/molecules190914366.

Matrone, G. *et al.* (2013) 'Laser-targeted ablation of the zebrafish embryonic ventricle: a novel model of cardiac injury and repair', *International Journal of Cardiology*, 168(4), pp. 3913–3919. doi: 10.1016/j.ijcard.2013.06.063.

Matrone, G. *et al.* (2015) 'CDK9 and its repressor LARP7 modulate cardiomyocyte proliferation and response to injury in the zebrafish heart', *Journal of Cell Science*, 128(24), pp. 4560–4571. doi: 10.1242/jcs.175018.

McDonald, B. *et al.* (2010) 'Intravascular danger signals guide neutrophils to sites of sterile inflammation', *Science*, 330(6002), pp. 362–366. doi: 10.1126/science.1195491.

McSweeney, S. J. *et al.* (2010) 'Improved heart function follows enhanced inflammatory cell recruitment and angiogenesis in 11βHSD1-deficient mice post-MI', *Cardiovascular Research*, 88(1), pp. 159–167. doi: 10.1093/cvr/cvq149.

Medenwald, D. *et al.* (2014) 'Inflammation and Prolonged QT Time: Results from the Cardiovascular Disease, Living and Ageing in Halle (CARLA) Study', *PLoS ONE*, 9(4). doi: 10.1371/journal.pone.0095994.

Meijering, E., Dzyubachyk, O. and Smal, I. (2012) 'Methods for cell and particle tracking', *Methods in Enzymology*, 504, pp. 183–200. doi: 10.1016/B978-0-12-391857-4.00009-4.

Mickoleit, M. *et al.* (2014) 'High-resolution reconstruction of the beating zebrafish heart', *Nature Methods*, 11(9), pp. 919–922. doi: 10.1038/nmeth.3037.

Milot, E. and Filep, J. G. (2011) 'Regulation of neutrophil survival/apoptosis by Mcl-1', *TheScientificWorldJournal*, 11, pp. 1948–1962. doi: 10.1100/2011/131539.

Miskolci, V. *et al.* (2019) 'Distinct inflammatory and wound healing responses to complex caudal fin injuries of larval zebrafish', *eLife*, 8, p. e45976. doi: 10.7554/eLife.45976.

Montecucco Fabrizio *et al.* (2010) 'Single Administration of the CXC Chemokine-Binding Protein Evasin-3 During Ischemia Prevents Myocardial Reperfusion Injury in Mice', *Arteriosclerosis, Thrombosis, and Vascular Biology*, 30(7), pp. 1371–1377. doi: 10.1161/ATVBAHA.110.206011.

Morales, F. and Giordano, A. (2016) 'Overview of CDK9 as a target in cancer research', *Cell Cycle*, 15(4), pp. 519–527. doi: 10.1080/15384101.2016.1138186.

Moris, D. *et al.* (2017) 'The role of reactive oxygen species in myocardial redox signaling and regulation', *Annals of Translational Medicine*, 5(16). doi: 10.21037/atm.2017.06.17.

Moulding, D. A. *et al.* (1998) 'Mcl-1 expression in human neutrophils: regulation by cytokines and correlation with cell survival', *Blood*, 92(7), pp. 2495–2502.

Murray, P. J. and Wynn, T. A. (2011) 'Protective and pathogenic functions of macrophage subsets', *Nature Reviews Immunology*, 11(11), pp. 723–737. doi: 10.1038/nri3073.

Nahrendorf, M. *et al.* (2007) 'The healing myocardium sequentially mobilizes two monocyte subsets with divergent and complementary functions', *The Journal of Experimental Medicine*, 204(12), pp. 3037–3047. doi: 10.1084/jem.20070885.

Nathan, C. and Ding, A. (2010) 'Nonresolving inflammation', *Cell*, 140(6), pp. 871–882. doi: 10.1016/j.cell.2010.02.029.

Nguyen-Chi, M. *et al.* (2015) 'Identification of polarized macrophage subsets in zebrafish', *eLife*, 4, p. e07288. doi: 10.7554/eLife.07288.

Nguyen-Chi, M. *et al.* (2017) 'TNF signaling and macrophages govern fin regeneration in zebrafish larvae', *Cell Death & Disease*, 8(8), pp. e2979–e2979. doi: 10.1038/cddis.2017.374.

Ni, W. *et al.* (2020) 'Cyclin-Dependent Kinase 9 (CDK9) Inhibitor Atuveciclib Suppresses Intervertebral Disk Degeneration via the Inhibition of the NF-κB Signaling Pathway', *Frontiers in Cell and Developmental Biology*, 8. doi: 10.3389/fcell.2020.579658.

Niccoli, G. *et al.* (2009) 'Myocardial No-Reflow in Humans', *Journal of the American College of Cardiology*, 54(4), pp. 281–292. doi: 10.1016/j.jacc.2009.03.054.

Niethammer, P. *et al.* (2009) 'A tissue-scale gradient of hydrogen peroxide mediates rapid wound detection in zebrafish', *Nature*, 459(7249), pp. 996–999. doi: 10.1038/nature08119.

Niethammer, P. (2016) 'The Early Wound Signals', *Current opinion in genetics & development*, 40, pp. 17–22. doi: 10.1016/j.gde.2016.05.001.

Oka, T. *et al.* (2012) 'Mitochondrial DNA That Escapes from Autophagy Causes Inflammation and Heart Failure', *Nature*, 485(7397), pp. 251–255. doi: 10.1038/nature10992.

Olson, C. M. *et al.* (2018) 'Pharmacological perturbation of CDK9 using selective CDK9 inhibition or degradation', *Nature Chemical Biology*, 14(2), pp. 163–170. doi: 10.1038/nchembio.2538.

Ortega-Gómez, A., Perretti, M. and Soehnlein, O. (2013) 'Resolution of inflammation: an integrated view', *EMBO molecular medicine*, 5(5), pp. 661–674. doi: 10.1002/emmm.201202382.

Oyama, J. *et al.* (2004) 'Reduced myocardial ischemia-reperfusion injury in toll-like receptor 4-deficient mice', *Circulation*, 109(6), pp. 784–789. doi: 10.1161/01.CIR.0000112575.66565.84.

Panahi, M. *et al.* (2018) 'Immunomodulatory interventions in myocardial infarction and heart failure: a systematic review of clinical trials and meta-analysis of IL-1 inhibition', *Cardiovascular Research*, 114(11), pp. 1445–1461. doi: 10.1093/cvr/cvy145.

Pase, L. *et al.* (2012) 'Neutrophil-Delivered Myeloperoxidase Dampens the Hydrogen Peroxide Burst after Tissue Wounding in Zebrafish', *Current Biology*, 22(19), pp. 1818–1824. doi: 10.1016/j.cub.2012.07.060.

Patton, E. E. and Tobin, D. M. (2019) 'Spotlight on zebrafish: the next wave of translational research', *Disease Models & Mechanisms*, 12(3). doi: 10.1242/dmm.039370.

Pauls, S., Geldmacher-Voss, B. and Campos-Ortega, J. A. (2001) 'A zebrafish histone variant H2A.F/Z and a transgenic H2A.F/Z:GFP fusion protein for in vivo studies of embryonic development', *Development Genes and Evolution*, 211(12), pp. 603–610. doi: 10.1007/s00427-001-0196-x.

Pazhakh, V. *et al.* (2017) 'A GCSFR/CSF3R zebrafish mutant models the persistent basal neutrophil deficiency of severe congenital neutropenia', *Scientific Reports*, 7(1), p. 44455. doi: 10.1038/srep44455.

Peal, D. S. *et al.* (2011) 'Novel chemical suppressors of long QT syndrome identified by an in vivo functional screen', *Circulation*, 123(1), pp. 23–30. doi: 10.1161/CIRCULATIONAHA.110.003731.

Peng, J. *et al.* (1998) 'Identification of multiple cyclin subunits of human P-TEFb', *Genes & Development*, 12(5), pp. 755–762.

Peoples, J. N. *et al.* (2019) 'Mitochondrial dysfunction and oxidative stress in heart disease', *Experimental & Molecular Medicine*, 51(12), pp. 1–13. doi: 10.1038/s12276-019-0355-7.

Pesce, J. T. *et al.* (2009) 'Arginase-1-expressing macrophages suppress Th2 cytokine-driven inflammation and fibrosis', *PLoS pathogens*, 5(4), p. e1000371. doi: 10.1371/journal.ppat.1000371.

Petrie, T. A. *et al.* (2014) 'Macrophages modulate adult zebrafish tail fin regeneration', *Development*, 141(13), pp. 2581–2591. doi: 10.1242/dev.098459.

Porrello, E. R. *et al.* (2013) 'Regulation of neonatal and adult mammalian heart regeneration by the miR-15 family', *Proceedings of the National Academy of Sciences*, 110(1), pp. 187–192. doi: 10.1073/pnas.1208863110.

Poss, K. D., Wilson, L. G. and Keating, M. T. (2002) 'Heart Regeneration in Zebrafish', *Science*, 298(5601), pp. 2188–2190. doi: 10.1126/science.1077857.

Powell, D. *et al.* (2017) 'Chemokine Signaling and the Regulation of Bidirectional Leukocyte Migration in Interstitial Tissues', *Cell Reports*, 19(8), pp. 1572–1585. doi: 10.1016/j.celrep.2017.04.078.

Power, R. M. and Huisken, J. (2017) 'A guide to light-sheet fluorescence microscopy for multiscale imaging', *Nature Methods*, 14(4), pp. 360–373. doi: 10.1038/nmeth.4224.

Price, D. H. (2000) 'P-TEFb, a Cyclin-Dependent Kinase Controlling Elongation by RNA Polymerase II', *Molecular and Cellular Biology*, 20(8), pp. 2629–2634.

Priya, R. *et al.* (2020) 'Tension heterogeneity directs form and fate to pattern the myocardial wall', *Nature*, 588(7836), pp. 130–134. doi: 10.1038/s41586-020-2946-9.

Proulx, K., Lu, A. and Sumanas, S. (2010) 'Cranial vasculature in zebrafish forms by angioblast cluster-derived angiogenesis', *Developmental Biology*, 348(1), pp. 34–46. doi: 10.1016/j.ydbio.2010.08.036.

Renshaw, S. A. *et al.* (2006) 'A transgenic zebrafish model of neutrophilic inflammation', *Blood*, 108(13), pp. 3976–3978. doi: 10.1182/blood-2006-05-024075.

Renshaw, S. A. and Trede, N. S. (2012) 'A model 450 million years in the making: zebrafish and vertebrate immunity', *Disease Models & Mechanisms*, 5(1), pp. 38–47. doi: 10.1242/dmm.007138.

Reynaud, E. G. *et al.* (2008) 'Light sheet-based fluorescence microscopy: more dimensions, more photons, and less photodamage', *HFSP Journal*, 2(5), pp. 266–275. doi: 10.2976/1.2974980.

Ridker, P. M. *et al.* (2017) 'Antiinflammatory Therapy with Canakinumab for Atherosclerotic Disease', *New England Journal of Medicine*, 377(12), pp. 1119–1131. doi: 10.1056/NEJMoa1707914.

Rieger, S. and Sagasti, A. (2011) 'Hydrogen Peroxide Promotes Injury-Induced Peripheral Sensory Axon Regeneration in the Zebrafish Skin', *PLOS Biology*, 9(5), p. e1000621. doi: 10.1371/journal.pbio.1000621.

Roberts, A. B. *et al.* (1986) 'Transforming growth factor type beta: rapid induction of fibrosis and angiogenesis in vivo and stimulation of collagen formation in vitro', *Proceedings of the National Academy of Sciences*, 83(12), pp. 4167–4171. doi: 10.1073/pnas.83.12.4167.

Robertson, A. L. *et al.* (2014) 'A zebrafish compound screen reveals modulation of neutrophil reverse migration as an anti-inflammatory mechanism', *Science Translational Medicine*, 6(225), p. 225ra29. doi: 10.1126/scitranslmed.3007672.

Robertson, A. L. *et al.* (2016) 'Identification of benzopyrone as a common structural feature in compounds with anti-inflammatory activity in a zebrafish phenotypic screen', *Disease Models & Mechanisms*, 9(6), pp. 621–632. doi: 10.1242/dmm.024935.

Roh, J. S. and Sohn, D. H. (2018) 'Damage-Associated Molecular Patterns in Inflammatory Diseases', *Immune Network*, 18(4). doi: 10.4110/in.2018.18.e27.

Romano, G. (2013) 'Deregulations in the Cyclin-Dependent Kinase-9-Related Pathway in Cancer: Implications for Drug Discovery and Development', *ISRN Oncology*, 2013. doi: 10.1155/2013/305371.

Romson, J. L. *et al.* (1983) 'Reduction of the extent of ischemic myocardial injury by neutrophil depletion in the dog', *Circulation*, 67(5), pp. 1016–1023. doi: 10.1161/01.cir.67.5.1016.

Rosales, C. (2018) 'Neutrophil: A Cell with Many Roles in Inflammation or Several Cell Types?', *Frontiers in Physiology*, 9. doi: 10.3389/fphys.2018.00113.

Rosowski, E. E. (2020) 'Determining macrophage versus neutrophil contributions to innate immunity using larval zebrafish', *Disease Models & Mechanisms*, 13(1). doi: 10.1242/dmm.041889.

Rossi, A. G. *et al.* (2006) 'Cyclin-dependent kinase inhibitors enhance the resolution of inflammation by promoting inflammatory cell apoptosis', *Nature Medicine*, 12(9), pp. 1056–1064. doi: 10.1038/nm1468.

Rossi, A. G. *et al.* (2007) 'Modulation of granulocyte apoptosis can influence the resolution of inflammation', *Biochemical Society Transactions*, 35(2), pp. 288–291. doi: 10.1042/BST0350288.

Rottbauer, W. *et al.* (2002) 'Reptin and Pontin Antagonistically Regulate Heart Growth in Zebrafish Embryos', *Cell*, 111(5), pp. 661–672. doi: 10.1016/S0092-8674(02)01112-1.

Sager, H. B. *et al.* (2015) 'Targeting Interleukin-1β Reduces Leukocyte Production After Acute Myocardial Infarction', *Circulation*, 132(20), pp. 1880–1890. doi: 10.1161/CIRCULATIONAHA.115.016160.

Sano, M. *et al.* (2002) 'Activation and function of cyclin T-Cdk9 (positive transcription elongation factor-b) in cardiac muscle-cell hypertrophy', *Nature Medicine*, 8(11), pp. 1310–1317. doi: 10.1038/nm778.

Sano, M. *et al.* (2004) 'Activation of cardiac Cdk9 represses PGC-1 and confers a predisposition to heart failure', *The EMBO Journal*, 23(17), pp. 3559–3569. doi: 10.1038/sj.emboj.7600351.

Santo, L. *et al.* (2010) 'AT7519, A novel small molecule multi-cyclin-dependent kinase inhibitor, induces apoptosis in multiple myeloma via GSK-3beta activation and RNA polymerase II inhibition', *Oncogene*, 29(16), pp. 2325–2336. doi: 10.1038/onc.2009.510.

Sanz-Morejón, A. *et al.* (2019) 'Wilms Tumor 1b Expression Defines a Pro-regenerative Macrophage Subtype and Is Required for Organ Regeneration in the Zebrafish', *Cell Reports*, 28(5), pp. 1296-1306.e6. doi: 10.1016/j.celrep.2019.06.091.

Sanz-Morejón, A. and Mercader, N. (2020) 'Recent insights into zebrafish cardiac regeneration', *Current Opinion in Genetics & Development*, 64, pp. 37–43. doi: 10.1016/j.gde.2020.05.020.

Savage, N. D. L. *et al.* (2008) 'Human Anti-Inflammatory Macrophages Induce Foxp3+GITR+CD25+ Regulatory T Cells, Which Suppress via Membrane-Bound TGFβ-1', *The Journal of Immunology*, 181(3), pp. 2220–2226. doi: 10.4049/jimmunol.181.3.2220.

Savill, J. *et al.* (2002) 'A blast from the past: clearance of apoptotic cells regulates immune responses', *Nature Reviews. Immunology*, 2(12), pp. 965–975. doi: 10.1038/nri957.

Schloss, M. J. *et al.* (2016) 'The time-of-day of myocardial infarction onset affects healing through oscillations in cardiac neutrophil recruitment', *EMBO molecular medicine*, 8(8), pp. 937–948. doi: 10.15252/emmm.201506083.

Schmerwitz Ulrike K. *et al.* (2011) 'Flavopiridol Protects Against Inflammation by Attenuating Leukocyte-Endothelial Interaction via Inhibition of Cyclin-Dependent Kinase 9', *Arteriosclerosis, Thrombosis, and Vascular Biology*, 31(2), pp. 280–288. doi: 10.1161/ATVBAHA.110.213934.

Schreyer, A. M. and Blundell, T. (2012) 'USRCAT: real-time ultrafast shape recognition with pharmacophoric constraints', *Journal of Cheminformatics*, 4, p. 27. doi: 10.1186/1758-2946-4-27.

Schumacher, D. *et al.* (2021) 'Phosphatidylserine Supplementation as a Novel Strategy for Reducing Myocardial Infarct Size and Preventing Adverse Left Ventricular Remodeling', *International Journal of Molecular Sciences*, 22(9), p. 4401. doi: 10.3390/ijms22094401.

Schwab, J. M. *et al.* (2007) 'Resolvin E1 and protectin D1 activate inflammation-resolution programmes', *Nature*, 447(7146), pp. 869–874. doi: 10.1038/nature05877.

Sekine, H. *et al.* (2006) 'Cardiomyocyte Bridging Between Hearts and Bioengineered Myocardial Tissues With Mesenchymal Transition of Mesothelial Cells', *The Journal of Heart and Lung Transplantation*, 25(3), pp. 324–332. doi: 10.1016/j.healun.2005.09.017.

Shiau, C. E. *et al.* (2015) 'Differential Requirement for irf8 in Formation of Embryonic and Adult Macrophages in Zebrafish', *PLOS ONE*, 10(1), p. e0117513. doi: 10.1371/journal.pone.0117513.

Shimokado, K. *et al.* (1985) 'A significant part of macrophage-derived growth factor consists of at least two forms of PDGF', *Cell*, 43(1), pp. 277–286. doi: 10.1016/0092-8674(85)90033-9.

Shore, S. M. *et al.* (2003) 'Identification of a novel isoform of Cdk9', *Gene*, 307, pp. 175–182. doi: 10.1016/s0378-1119(03)00466-9.

Shore, S. M. *et al.* (2005) 'Characterization of Cdk9(55) and differential regulation of two Cdk9 isoforms', *Gene*, 350(1), pp. 51–58. doi: 10.1016/j.gene.2005.01.015.

Silber, S. *et al.* (2005) 'Guidelines for percutaneous coronary interventions. The Task Force for Percutaneous Coronary Interventions of the European Society of Cardiology', *European Heart Journal*, 26(8), pp. 804–847. doi: 10.1093/eurheartj/ehi138.

Simões, F. C. *et al.* (2020) 'Macrophages directly contribute collagen to scar formation during zebrafish heart regeneration and mouse heart repair', *Nature Communications*, 11(1), p. 600. doi: 10.1038/s41467-019-14263-2.

Soehnlein, O. and Lindbom, L. (2010) 'Phagocyte partnership during the onset and resolution of inflammation', *Nature Reviews. Immunology*, 10(6), pp. 427–439. doi: 10.1038/nri2779.

Squires, M. S. *et al.* (2009) 'Biological characterization of AT7519, a small-molecule inhibitor of cyclin-dependent kinases, in human tumor cell lines', *Molecular Cancer Therapeutics*, 8(2), pp. 324–332. doi: 10.1158/1535-7163.MCT-08-0890.

Stainier, D. Y. R. *et al.* (2017) 'Guidelines for morpholino use in zebrafish', *PLOS Genetics*, 13(10), p. e1007000. doi: 10.1371/journal.pgen.1007000.

Starnes, T. W. and Huttenlocher, A. (2012) 'Neutrophil Reverse Migration Becomes Transparent with Zebrafish', *Advances in Hematology*, 2012, p. e398640. doi: 10.1155/2012/398640.

Stein, M. *et al.* (1992) 'Interleukin 4 potently enhances murine macrophage mannose receptor activity: a marker of alternative immunologic macrophage activation', *The Journal of Experimental Medicine*, 176(1), pp. 287–292. doi: 10.1084/jem.176.1.287.

Stoddard, M. *et al.* (2019) 'Live imaging of leukocyte recruitment in a zebrafish model of chemical liver injury', *Scientific Reports*, 9(1), p. 28. doi: 10.1038/s41598-018-36771-9.

Streisinger, G. *et al.* (1981) 'Production of clones of homozygous diploid zebra fish (Brachydanio rerio)', *Nature*, 291(5813), pp. 293–296. doi: 10.1038/291293a0.

Su, Y. and Richmond, A. (2015) 'Chemokine Regulation of Neutrophil Infiltration of Skin Wounds', *Advances in Wound Care*, 4(11), pp. 631–640. doi: 10.1089/wound.2014.0559.

Sugimoto, M. A. *et al.* (2016) 'Resolution of Inflammation: What Controls Its Onset?', *Frontiers in Immunology*, 7, p. 160. doi: 10.3389/fimmu.2016.00160.

Sundar, V. *et al.* (2021) 'Transcriptional cyclin-dependent kinases as the mediators of inflammation-a review', *Gene*, 769, p. 145200. doi: 10.1016/j.gene.2020.145200.

Swirski, F. K. and Nahrendorf, M. (2013) 'Leukocyte behavior in atherosclerosis, myocardial infarction, and heart failure', *Science*, 339(6116), pp. 161–166. doi: 10.1126/science.1230719.

Takada, Y. and Aggarwal, B. B. (2004) 'Flavopiridol Inhibits NF-κB Activation Induced by Various Carcinogens and Inflammatory Agents through Inhibition of IκBα Kinase and p65

Phosphorylation: Abrogation Of Cyclin D1, Cyclooxygenase-2, And Matrix Metalloprotease-9', *Journal of Biological Chemistry*, 279(6), pp. 4750–4759. doi: 10.1074/jbc.M304546200.

Talman, V. and Ruskoaho, H. (2016) 'Cardiac fibrosis in myocardial infarction-from repair and remodeling to regeneration', *Cell and Tissue Research*, 365(3), pp. 563–581. doi: 10.1007/s00441-016-2431-9.

Tardif, J.-C. *et al.* (2019) 'Efficacy and Safety of Low-Dose Colchicine after Myocardial Infarction', *New England Journal of Medicine*, 381(26), pp. 2497–2505. doi: 10.1056/NEJMoa1912388.

Tauzin, S. *et al.* (2014) 'Redox and Src family kinase signaling control leukocyte wound attraction and neutrophil reverse migration', *Journal of Cell Biology*, 207(5), pp. 589–598. doi: 10.1083/jcb.201408090.

Taylor, J. M. *et al.* (2011) 'Real-time optical gating for three-dimensional beating heart imaging', *Journal of Biomedical Optics*, 16(11), p. 116021. doi: 10.1117/1.3652892.

Taylor, J. M. *et al.* (2019) 'Adaptive prospective optical gating enables day-long 3D time-lapse imaging of the beating embryonic zebrafish heart', *Nature Communications*, 10(1), p. 5173. doi: 10.1038/s41467-019-13112-6.

Taylor, J. M., Girkin, J. M. and Love, G. D. (2012) 'High-resolution 3D optical microscopy inside the beating zebrafish heart using prospective optical gating', *Biomedical Optics Express*, 3(12), pp. 3043–3053. doi: 10.1364/BOE.3.003043.

Taylor, J. S. *et al.* (2003) 'Genome Duplication, a Trait Shared by 22,000 Species of Ray-Finned Fish', *Genome Research*, 13(3), pp. 382–390. doi: 10.1101/gr.640303.

Tibes, R. and Bogenberger, J. M. (2019) 'Transcriptional Silencing of MCL-1 Through Cyclin-Dependent Kinase Inhibition in Acute Myeloid Leukemia', *Frontiers in Oncology*, 9, p. 1205. doi: 10.3389/fonc.2019.01205.

Timmers, L. *et al.* (2008) 'Toll-like receptor 4 mediates maladaptive left ventricular remodeling and impairs cardiac function after myocardial infarction', *Circulation Research*, 102(2), pp. 257–264. doi: 10.1161/CIRCRESAHA.107.158220.

Tinevez, J.-Y. *et al.* (2017) 'TrackMate: An open and extensible platform for single-particle tracking', *Methods*, 115, pp. 80–90. doi: 10.1016/j.ymeth.2016.09.016.

Toor, I. S. *et al.* (2020) 'Eosinophil Deficiency Promotes Aberrant Repair and Adverse Remodeling Following Acute Myocardial Infarction', *JACC: Basic to Translational Science*, 5(7), pp. 665–681. doi: 10.1016/j.jacbts.2020.05.005.

Traver, D. *et al.* (2003) 'The zebrafish as a model organism to study development of the immune system', *Advances in Immunology*, 81, pp. 253–330.

Trede, N. S. *et al.* (2004) 'The Use of Zebrafish to Understand Immunity', *Immunity*, 20(4), pp. 367–379. doi: 10.1016/S1074-7613(04)00084-6.

Tsarouchas, T. M. *et al.* (2018) 'Dynamic control of proinflammatory cytokines Il-1β and Tnf-α by macrophages in zebrafish spinal cord regeneration', *Nature Communications*, 9(1), p. 4670. doi: 10.1038/s41467-018-07036-w.

Tucker, B. and Lardelli, M. (2007) 'A rapid apoptosis assay measuring relative acridine orange fluorescence in zebrafish embryos', *Zebrafish*, 4(2), pp. 113–116. doi: 10.1089/zeb.2007.0508.

van der Laan, A. M. *et al.* (2014) 'Monocyte subset accumulation in the human heart following acute myocardial infarction and the role of the spleen as monocyte reservoir', *European Heart Journal*, 35(6), pp. 376–385. doi: 10.1093/eurheartj/eht331.

van Hout, G. P. J. *et al.* (2015) 'Elevated mean neutrophil volume represents altered neutrophil composition and reflects damage after myocardial infarction', *Basic Research in Cardiology*, 110(6), p. 58. doi: 10.1007/s00395-015-0513-6.

Vinten-Johansen, J. (2004) 'Involvement of neutrophils in the pathogenesis of lethal myocardial reperfusion injury', *Cardiovascular Research*, 61(3), pp. 481–497. doi: 10.1016/j.cardiores.2003.10.011.

Vogel, C.-W. (2020) 'The Role of Complement in Myocardial Infarction Reperfusion Injury: An Underappreciated Therapeutic Target', *Frontiers in Cell and Developmental Biology*, 8. doi: 10.3389/fcell.2020.606407.

Walter, W. *et al.* (2018) 'Deciphering the Dynamic Transcriptional and Post-transcriptional Networks of Macrophages in the Healthy Heart and after Myocardial Injury', *Cell Reports*, 23(2), pp. 622–636. doi: 10.1016/j.celrep.2018.03.029.

Wang, J. *et al.* (2017) 'Visualizing the function and fate of neutrophils in sterile injury and repair', *Science*, 358(6359), pp. 111–116. doi: 10.1126/science.aam9690.

Wang, K. *et al.* (2012) 'Cyclin-dependent kinase 9 activity regulates neutrophil spontaneous apoptosis', *PloS One*, 7(1), p. e30128. doi: 10.1371/journal.pone.0030128.

Westerfield, M. (2007) The Zebrafish Book. A Guide for the Laboratory Use of Zebrafish (Danio rerio), 5th Edition. University of Oregon Press, Eugene.

Wood, D. J. and Endicott, J. A. (2018) 'Structural insights into the functional diversity of the CDK-cyclin family', *Open Biology*, 8(9). doi: 10.1098/rsob.180112.

Wyatt, P. G. *et al.* (2008) 'Identification of N-(4-piperidinyl)-4-(2,6-dichlorobenzoylamino)-1H-pyrazole-3-carboxamide (AT7519), a novel cyclin dependent kinase inhibitor using fragment-based X-ray crystallography and structure based drug design', *Journal of Medicinal Chemistry*, 51(16), pp. 4986–4999. doi: 10.1021/jm800382h.

Xia, P. *et al.* (2018) 'Inhibition of cyclin-dependent kinase 2 protects against doxorubicin-induced cardiomyocyte apoptosis and cardiomyopathy', *The Journal of Biological Chemistry*, 293(51), pp. 19672–19685. doi: 10.1074/jbc.RA118.004673.

Xiang, W., Yang, C.-Y. and Bai, L. (2018) 'MCL-1 inhibition in cancer treatment', *OncoTargets and therapy*, 11, pp. 7301–7314. doi: 10.2147/OTT.S146228.

Xie, Y., Meijer, A. H. and Schaaf, M. J. M. (2021) 'Modeling Inflammation in Zebrafish for the Development of Anti-inflammatory Drugs', *Frontiers in Cell and Developmental Biology*, 8. doi: 10.3389/fcell.2020.620984.

Xu, S., Liu, C., *et al.* (2019) 'Excessive inflammation impairs heart regeneration in zebrafish breakdance mutant after cryoinjury', *Fish & Shellfish Immunology*, 89, pp. 117–126. doi: 10.1016/j.fsi.2019.03.058.

Xu, S., Xie, F., *et al.* (2019) 'Prolonged neutrophil retention in the wound impairs zebrafish heart regeneration after cryoinjury', *Fish & Shellfish Immunology*, 94, pp. 447–454. doi: 10.1016/j.fsi.2019.09.030.

Xue, S. *et al.* (2019) 'CDK9 attenuation exerts protective effects on catabolism and hypertrophy in chondrocytes and ameliorates osteoarthritis development', *Biochemical and Biophysical Research Communications*, 517(1), pp. 132–139. doi: 10.1016/j.bbrc.2019.07.032.

Yan, B. *et al.* (2014) 'Il-1β and Reactive Oxygen Species Differentially Regulate Neutrophil Directional Migration and Basal Random Motility in a Zebrafish Injury–Induced Inflammation Model', *The Journal of Immunology*, 192(12), pp. 5998–6008. doi: 10.4049/jimmunol.1301645.

Yik, J. H. N. *et al.* (2014) 'Cyclin-Dependent Kinase 9 Inhibition Protects Cartilage From the Catabolic Effects of Proinflammatory Cytokines', *Arthritis & Rheumatology*, 66(6), pp. 1537–1546. doi: https://doi.org/10.1002/art.38378.

Yoo, S. K. *et al.* (2010) 'Differential regulation of protrusion and polarity by PI3K during neutrophil motility in live zebrafish', *Developmental Cell*, 18(2), pp. 226–236. doi: 10.1016/j.devcel.2009.11.015.

Yoo, S. K. *et al.* (2011) 'Lyn is a redox sensor that mediates leukocyte wound attraction in vivo', *Nature*, 480(7375), pp. 109–112. doi: 10.1038/nature10632.

Yoo, S. K. *et al.* (2012) 'Early redox, Src family kinase, and calcium signaling integrate wound responses and tissue regeneration in zebrafish', *Journal of Cell Biology*, 199(2), pp. 225–234. doi: 10.1083/jcb.201203154.

Yuan, X. *et al.* (2018) 'Heart enhancers with deeply conserved regulatory activity are established early in zebrafish development', *Nature Communications*, 9(1), p. 4977. doi: 10.1038/s41467-018-07451-z.

Zanandrea, R., Bonan, C. D. and Campos, M. M. (2020) 'Zebrafish as a model for inflammation and drug discovery', *Drug Discovery Today*, 25(12), pp. 2201–2211. doi: 10.1016/j.drudis.2020.09.036.

Zhang, H. *et al.* (2018) 'Targeting CDK9 Reactivates Epigenetically Silenced Genes in Cancer', *Cell*, 175(5), pp. 1244-1258.e26. doi: 10.1016/j.cell.2018.09.051.

Zhang, Q. *et al.* (2010) 'Circulating mitochondrial DAMPs cause inflammatory responses to injury', *Nature*, 464(7285), pp. 104–107. doi: 10.1038/nature08780.

Zuñiga-Traslaviña, C. *et al.* (2017) 'Cxcl8b and Cxcr2 Regulate Neutrophil Migration through Bloodstream in Zebrafish', *Journal of Immunology Research*, p. 6530531. doi: 10.1155/2017/6530531.

Supplementary Videos

The supplementary videos associated with Chapter 3 (Live imaging of heart injury in larval zebrafish reveals a multi-stage model of neutrophil and macrophage migration) are published and available online: https://www.frontiersin.org/articles/10.3389/fcell.2020.579943/full#supplementary-material.

The following link is to view/download the supplementary videos associated with Chapter 4 (The effect of CDK9 inhibitor treatment on the innate inflammatory and regenerative response following larval zebrafish cardiac injury): https://www.dropbox.com/sh/blyre53zgpwl9an/AADeoCKQD27Mf30SD7kt_jVKa?dl=0.

The caption for each Chapter 4 supplementary video is given below.

Supplementary Video 1: Neutrophil infiltration following cardiac injury with DMSO vehicle

LSFM heartbeat-synchronised timelapse of a *Tg(mpx:mCherry)* larva treated with DMSO vehicle showing neutrophils infiltrating the cardiac injury site between 4 hpi and 6 hpi. 3D images are displayed as maximum intensity projections. Dotted line indicates outline of ventricle.

Supplementary Video 2: Neutrophil reverse migration following cardiac injury with AT7519 treatment

LSFM heartbeat-synchronised timelapse of a *Tg(mpx:mCherry)* larva treated with AT7519 showing wound-recruited neutrophils undergoing reverse migration from the injured heart between 4 hpi and 6 hpi. 3D images are displayed as maximum intensity projections. Dotted line indicates outline of ventricle.

Supplementary Video 3: Neutrophil reverse migration following cardiac injury with Flavopiridol treatment

LSFM heartbeat-synchronised timelapse of a *Tg(mpx:mCherry)* larva treated with Flavopiridol showing wound-recruited neutrophils undergoing reverse migration from the injured heart between 4 hpi and 6 hpi. 3D images are displayed as maximum intensity projections. Dotted line indicates outline of ventricle.

Supplementary Video 4: Macrophage reverse migration following cardiac injury with Flavopiridol treatment

LSFM heartbeat-synchronised timelapse of a *Tg(mpeg1:mCherry)* larva treated with Flavopiridol showing wound-recruited macrophages undergoing reverse migration from the injured heart between 4 hpi and 21 hpi. 3D images are displayed as maximum intensity projections. Dotted line indicates outline of ventricle.

Supplementary Video 5: Macrophage wound retention following cardiac injury with DMSO vehicle

LSFM heartbeat-synchronised timelapse of a *Tg(mpeg1:mCherry)* larva treated with DMSO vehicle showing wound-recruited macrophages being retained on the injured heart between 4 hpi and 20 hpi. 3D images are displayed as maximum intensity projections. Dotted line indicates outline of ventricle.

Supplementary Video 6: Wound-associated macrophages upregulate *TNF* expression following cardiac injury

LSFM heartbeat-synchronised timelapse of a *Tg(mpeg1:mCherry;TNFa:GFP)* larva showing wound-adjacent macrophages upregulating *TNF* expression at the cardiac injury site between 4 hpi and 15 hpi. 3D images are displayed as maximum intensity projections. Dotted line indicates outline of ventricle.

Supplementary Video 7: Myocardial regeneration via cardiomyocyte protrusion and bridging following cardiac injury

LSFM heartbeat-synchronised timelapse of a *Tg(myl7:GFP)* larva showing myocardial regeneration occurring via cardiomyocyte protrusion and bridging between 6 hpi and 17 hpi. 3D images were surface rendered.

Appendix 1

Subsidiary data and images that I acquired during this project, which are not enclosed in the main thesis chapters, are included in this appendix chapter.

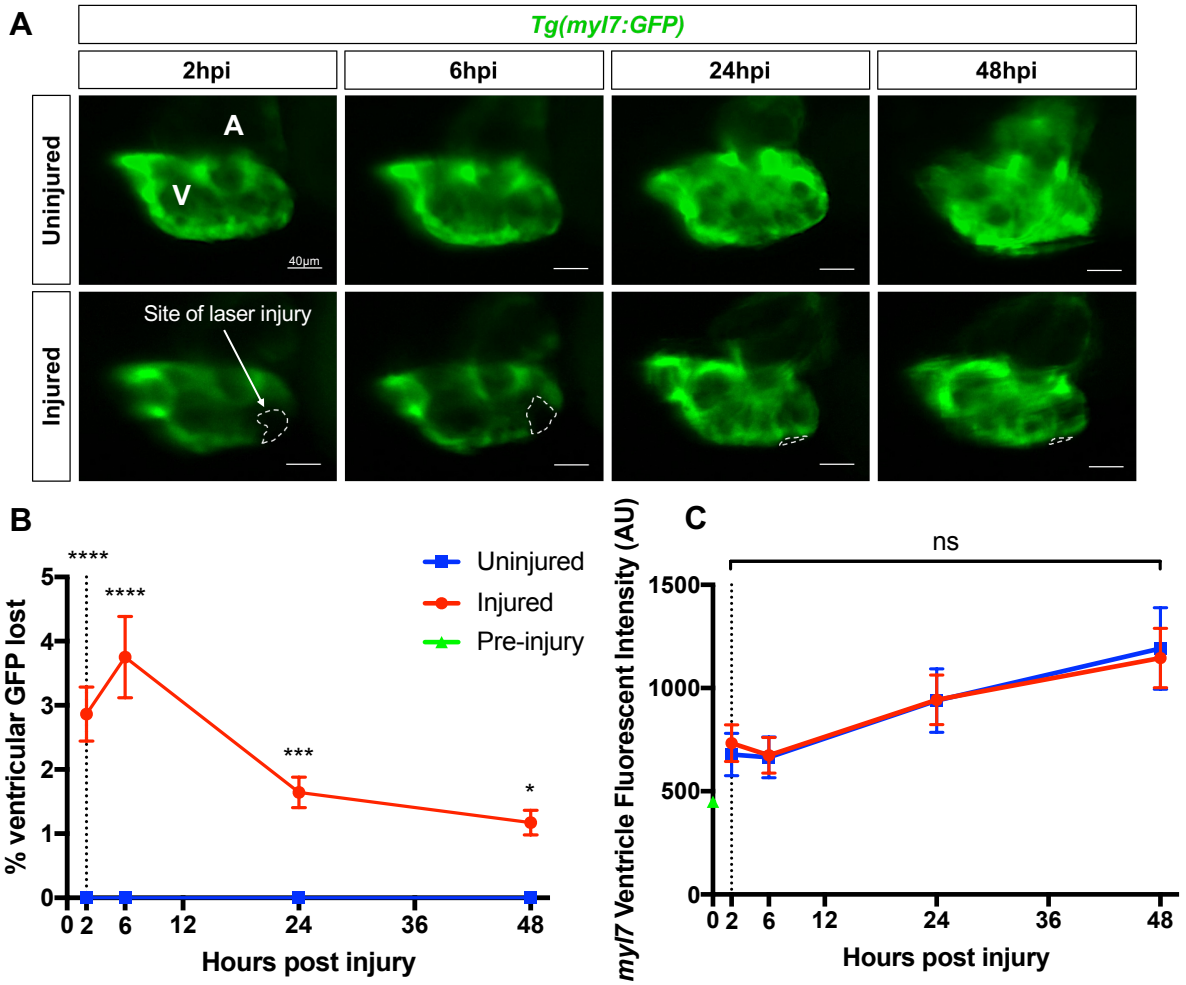

Appendix Figure 1: Ventricular apex laser injury causes the localised loss of myocardium that regenerates. (A) Epifluorescence images of uninjured and injured *Tg(myl7:GFP)* hearts, **(B)** % ventricular *myl7:GFP* lost and **(C)** *myl7:GFP* ventricle fluorescent intensity at 2 hpi, 6 hpi, 24 hpi and 48 hpi. Error bars = SEM, $n = 19$ larvae, experimental $n = 3$. Two-way ANOVA and Bonferroni *post hoc* test performed for comparisons between uninjured and injured groups, where * $p < 0.05$, *** $p < 0.001$, **** $p < 0.0001$ and ns = non-significant. The myocardial wound (*myl7:GFP* negative) in **(A)** is indicated with a dashed line. V = ventricle, A = atrium, AU = arbitrary units. Scale bars = 40 μm.

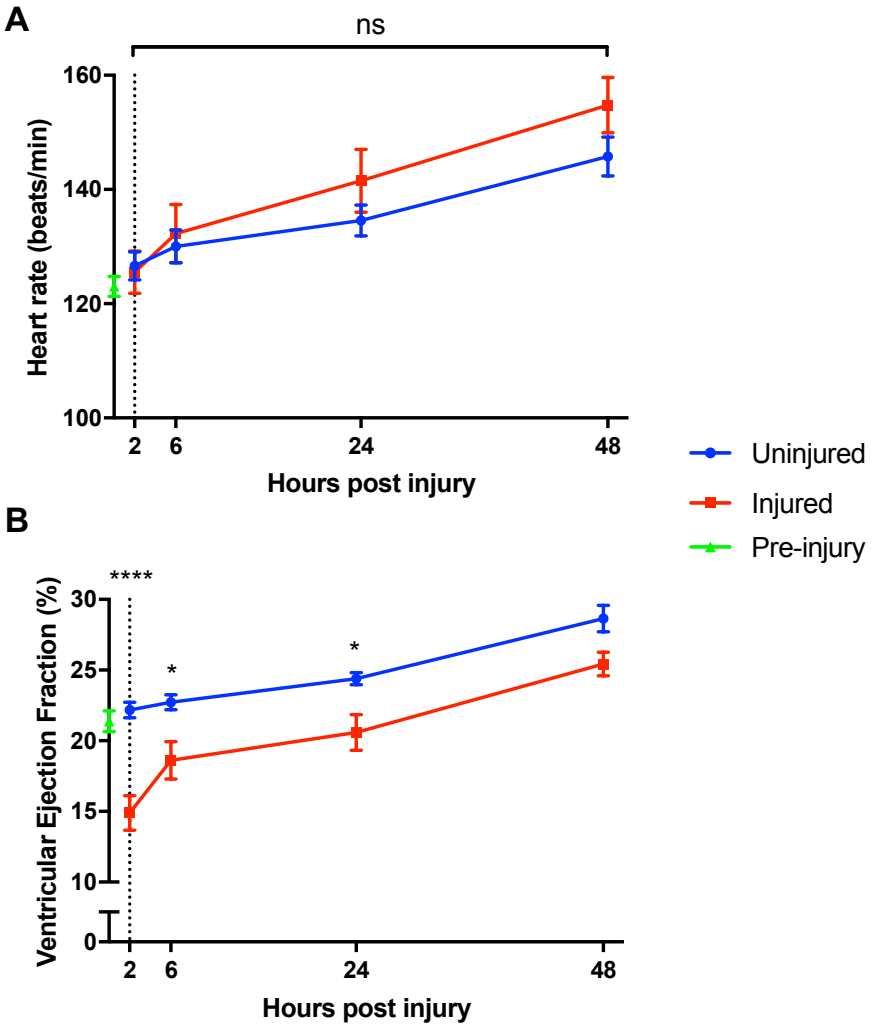

Appendix Figure 2: Assessment of cardiac function following injury. (A) Heart rate (beats/minute) and **(B)** Ventricular ejection fraction (%) of uninjured and injured larvae prior to laser injury, at 2 hpi, 6 hpi, 24 hpi and 48 hpi. Error bars = SEM, n = 20 larvae, experimental n = 3. Two-way ANOVA and Bonferroni *post hoc* test performed for comparisons between uninjured and injured groups, where * $p < 0.05$, **** $p < 0.0001$ and ns = non-significant.

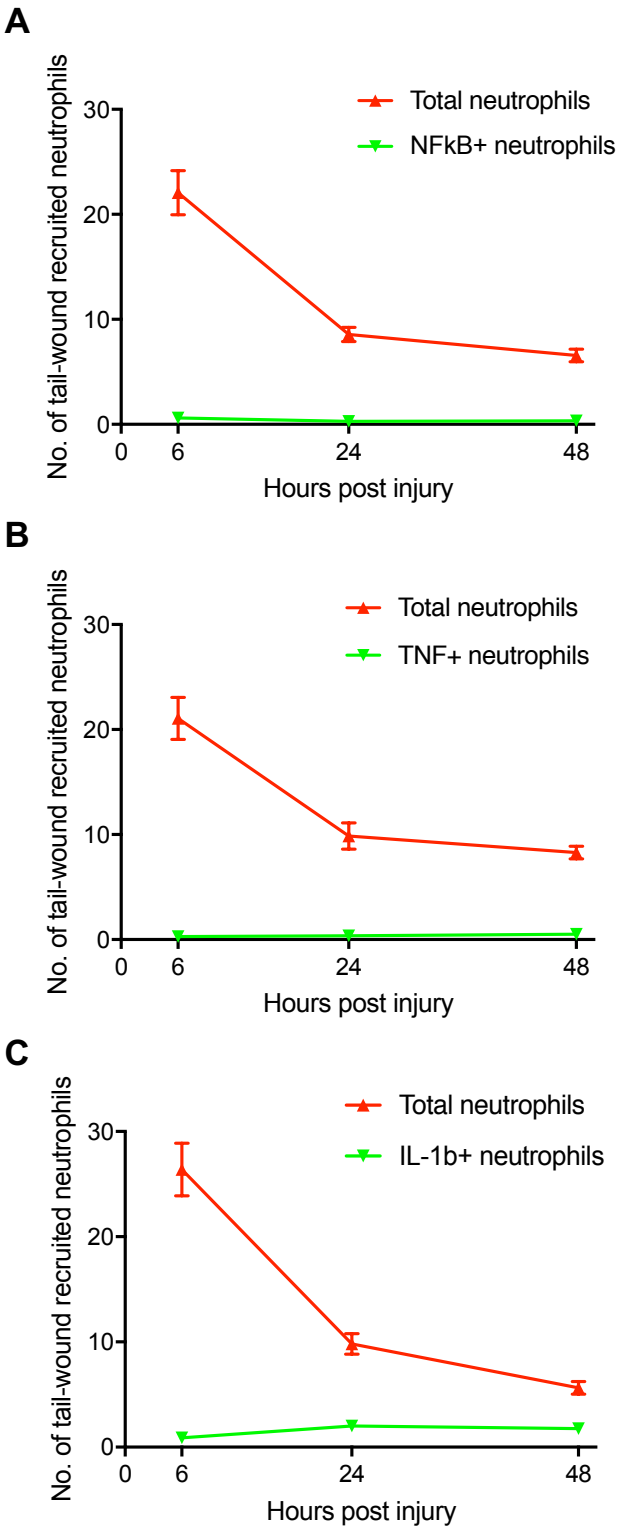

Appendix Figure 3: Tail-wound recruited neutrophils do not highly express or upregulate *nfκb*, *tnf* or *il-1b*. Number of tail-wound recruited neutrophils that express **(A)** *nfκb:GFP*, **(B)** *TNF:GFP* or **(C)** *il-1b:GFP* as detected using epifluorescence microscopy at 6 hpi, 24 hpi and 48 hpi. Error bars = SEM, *n* = 15 larvae, experimental *n* = 2.

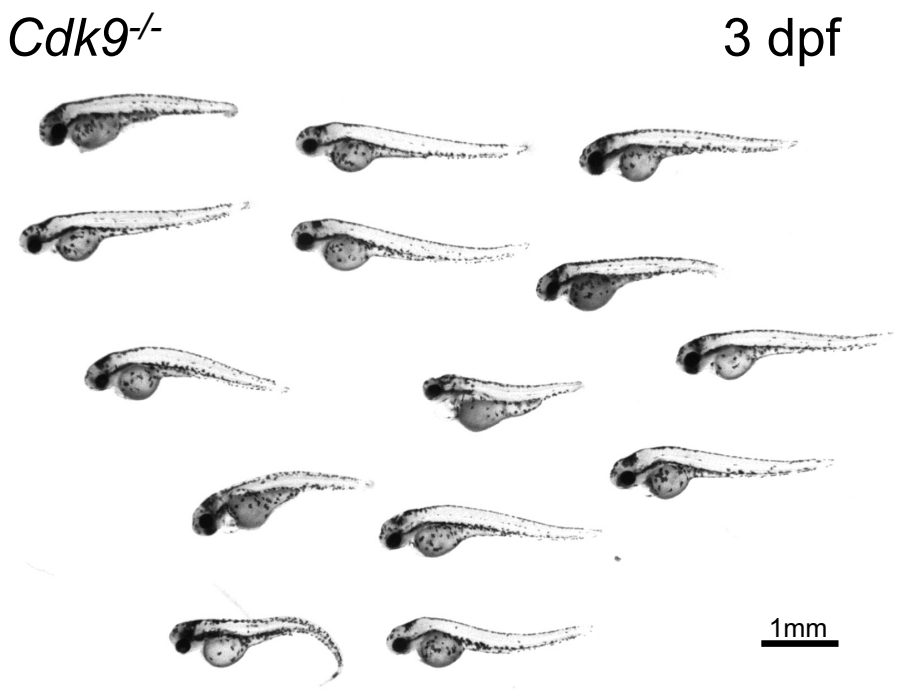

Appendix Figure 4: Homozygous *cdk9* mutant zebrafish display an apparent abnormal phenotype from 3 dpf. All larvae imaged were retrospectively genotyped and confirmed to be *cdk9* homozygous mutants. Scale bar length indicated.

Appendix 2

The following publication, which I contributed towards, is enclosed in this appendix chapter.

Taylor JM, Nelson CJ, Bruton FA, **Kaveh A**, Buckley C, Tucker CS, Rossi AG, Mullins JJ, Denvir MA. **Adaptive prospective optical gating enables day-long 3D time-lapse imaging of the beating embryonic zebrafish heart**. Nat Commun. 2019 Nov 15;10(1):5173. doi: 10.1038/s41467-019-13112-6.

This is an open-access article distributed under a Creative Commons Attribution 4.0 International License.

Contributions

JMT and CJN developed the synchronisation algorithms, software, electronics and optics. CJN, FAB, AK and CB performed the experiments and quantitative analysis, conceived individual experiments and developed the protocols. JMT, MAD, JJM, AGR, CST conceived the study and supervised the research. The manuscript was written with input from all authors.

nature COMMUNICATIONS

ARTICLE

There are amendments to this paper

https://doi.org/10.1038/s41467-019-13112-6 OPEN

Adaptive prospective optical gating enables day-long 3D time-lapse imaging of the beating embryonic zebrafish heart

Jonathan M. Taylor [1*], Carl J. Nelson [1], Finnius A. Bruton [2], Aryan Kaveh [2], Charlotte Buckley [2], Carl S. Tucker[2], Adriano G. Rossi[3], John J. Mullins[2] & Martin A. Denvir[2]

Three-dimensional fluorescence time-lapse imaging of the beating heart is extremely challenging, due to the heart's constant motion and a need to avoid pharmacological or phototoxic damage. Although real-time triggered imaging can computationally "freeze" the heart for 3D imaging, no previous algorithm has been able to maintain phase-lock across developmental timescales. We report a new algorithm capable of maintaining day-long phase-lock, permitting routine acquisition of synchronised 3D + time video time-lapse datasets of the beating zebrafish heart. This approach has enabled us for the first time to directly observe detailed developmental and cellular processes in the beating heart, revealing the dynamics of the immune response to injury and witnessing intriguing proliferative events that challenge the established literature on cardiac trabeculation. Our approach opens up exciting new opportunities for direct time-lapse imaging studies over a 24-hour time course, to understand the cellular mechanisms underlying cardiac development, repair and regeneration.

[1] School of Physics and Astronomy, University of Glasgow, Glasgow, UK. [2] British Heart Foundation Centre for Cardiovascular Science, Queen's Medical Research Institute, University of Edinburgh, Edinburgh, UK. [3] Centre for Inflammation Research, University of Edinburgh Medical School, Teviot Place, Edinburgh EH8 9AG, UK. *email: jonathan.taylor@glasgow.ac.uk

The ability to image an embryo at a cellular and subcellular level is crucial for understanding the dynamic processes and interactions underpinning development[1–6]. The ideal imaging system would acquire high-resolution three-dimensional (3D) images of specific organs and structures continuously over relevant time periods, typically hours or days, without causing tissue damage or interfering with the anatomical or physiological state of the organism. While light sheet microscopy has emerged as a valuable in vivo imaging solution to this challenge[7,8], imaging the complex 3D structure of the beating heart has additional challenges due to its constant cyclic motion at rates of 120–180 beats per minute. This problem can in principle be overcome by using synchronisation techniques to acquire 3D images free from motion artefacts[9–11]. However, to date, only some aspects of this problem have been solved at any one time. Imaging of the developing fish and chick heart has been previously reported for: single 3D snapshots at selected intervals[11], 3D images of a single cardiac cycle[12,13], sampling of a limited number of time points during development[9,14], and 2D time-lapse video[15]. Temporarily stopping the heart using high-dose anaesthetic has also been used to acquire 3D image sequences of the heart[16] but such approaches can significantly alter the physiological state of the heart[17] and the wider embryo[18], particularly when performed repeatedly in the same embryo at multiple timepoints. No method exists that can sustain day-long synchronised 3D imaging at the sufficiently short time-lapse intervals required to reliably track mobile cells and visualise specific cellular and subcellular events in the unperturbed heart.

The challenges of time-lapse 3D cardiac imaging can be understood on three key timescales. Within one cardiac cycle there are rapid changes in shape and size of the heart over less than a second. From one cardiac cycle to the next the heart adopts a highly repeatable sequence of shapes, although there can be subtle changes in rhythm from one beat to the next. However, on longer timescales dramatic structural and functional changes occur at a cellular and whole-organ level, especially during development where the heart undergoes significant morphological changes. It is important to be able to maintain stable imaging over all of these timescales in order to fully understand the biological processes of interest. For example, cell shape changes and immune cell migration takes place over minutes, while cell proliferation and acute inflammatory responses occur over hours. At a whole-heart level, developmental processes such as cardiac morphogenesis take 2–3 days to complete, and injury-associated inflammation also takes several days to resolve. Synchronisation algorithms for day-long imaging must eliminate intra-beat motion, visualise inter-beat motion, and be tolerant of morphological changes on developmental timescales. It is also crucial that they do not require an increased phototoxic laser exposure compared to time-lapse imaging in non-moving tissue.

We have previously demonstrated prospective optical gating in the beating zebrafish heart[10,11], stroboscopically building up a synchronised 3D *z*-stack of the heart at a single time point without motion artefacts (i.e. the imaging is phase-locked) such that the heart is at exactly the same phase in the cardiac cycle when every plane is imaged (Fig. 1a, b, Supplementary Video 1). In contrast to alternative retrospective optical gating approaches requiring several orders of magnitude more fluorescence images to be acquired[9], we only needed to acquire one single fluorescence image per *z*-plane per timepoint. Thus, in the same way that light sheet microscopy eliminates redundant excitation of fluorescence in the spatial domain, the philosophy of our prospective approach is to eliminate redundant excitation in the time domain (Fig. 1c). However, our previous algorithm relied on the assumption of quasi-periodic, stereotypical motion across all cardiac cycles in the experiment. This assumption is drastically violated on developmental timescales, as the heart changes in position, size and shape: correct phase-lock is lost within approximately 1 h (Fig. 1d, e), making it impossible until now to maintain live time-lapse imaging of the heart across developmental timescales.

We have now developed new algorithms to overcome this barrier and achieve day-long, synchronised 3D time-lapse imaging in the beating heart, involving both algorithmic and optical advances. By implementing these on a light sheet fluorescence microscope (Supplementary Fig. 1) we have been able, for the first time, to image a live, physiologically unperturbed, beating zebrafish heart over 24 h. This novel capability has allowed us to track cardiac developmental morphogenesis and patterning with high temporal and spatial resolution in 3D, and track individual motile cells, including cardiomyocytes and inflammatory cells associated with heart development and heart injury for the first time. The established understanding of zebrafish heart development on a cellular level has been built up without the benefit of direct video time-lapse imaging; we will reveal how studies enabled by our new adaptive prospective optical gating are already yielding evidence that reconciles and extends recent biological literature on cardiac development.

Results

Adaptive prospective optical gating for longitudinal imaging. No existing synchronisation algorithms can maintain day-long time-lapse imaging. Existing prospective synchronisation algorithms fail completely within approximately 1 h due to the changing appearance of the heart (Fig. 1d–f; Supplementary Video 2) and long-term sample drift. As we show later, post-acquisition strategies are not suitable due to their phototoxic and photobleaching effects, and furthermore published postacquisition algorithms cannot even be applied across these timescales without the new developments we report here. We therefore developed a new adaptive prospective optical gating algorithm suitable for automated day-long time-lapse imaging.

Our algorithm is based around a new multi-pass sequence alignment algorithm, to enable us to maintain high-precision beat-to-beat synchronisation in spite of the developmental changes occurring in the organism (Fig. 2a). Prospective gating computationally eliminates intra-beat motion of the cardiac tissue, allowing inter-beat changes (e.g. immune cell migration) to be observed, but phase-lock is lost as the appearance of the heart changes over the course of embryonic development. At regular intervals (typically after each *z* stack) we therefore "refresh" our reference brightfield image sequence (i.e. acquire a new sequence, which is then used for prospective optical gating to assign a cardiac phase to every subsequent image we acquire). To maintain a fixed phase-lock in spite of this refresh we perform a sequence alignment operation (in the terminology of retrospective optical gating algorithms[12]) to identify the location in the new image sequence that matches the target synchronisation phase in the previous reference image sequence (Fig. 1f; Supplementary Video 3). However, we discovered that published retrospective algorithms are unable to work with image sequences of the type required for long-term synchronisation (due to issues associated with phase-wrapping—details in Supplementary Fig. 2), so we developed our multi-pass sequence alignment algorithm to permit robust determination of the absolute shifts between video sequences and maintain phase-lock. To maintain stable phase-lock it is also essential that our algorithm compensates for the natural movement of the heart within the brightfield field of view, due to growth as well as any gradual slight drift of the sample within the mounting apparatus.

To ensure sufficient reliability and robustness for unattended day-long running we also developed an improved strategy for

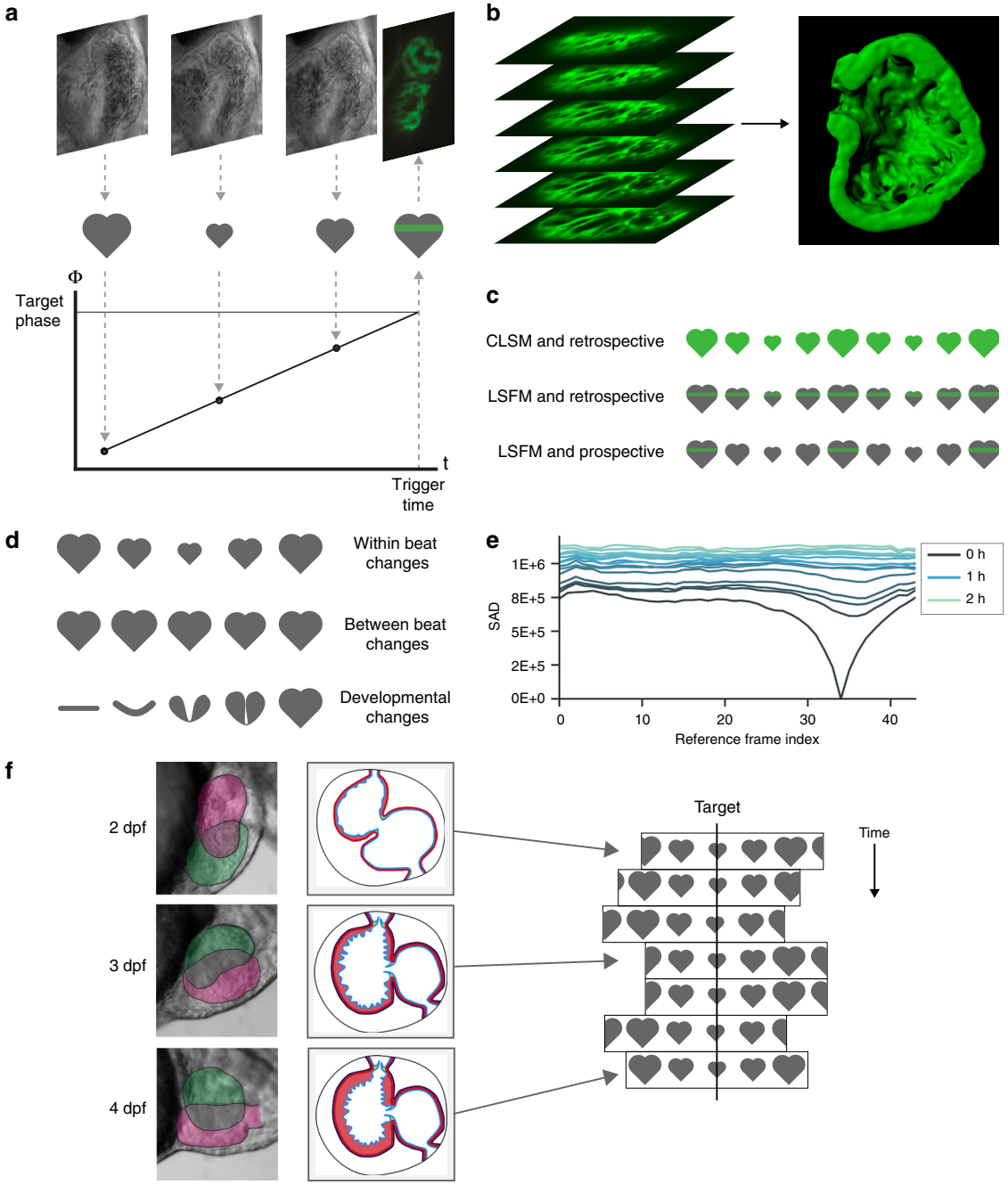

Fig. 1 Developmental changes in cardiac morphology prevent day-long time-lapse imaging with existing algorithms. **a** In prospective optical gating, brightfield images (greyscale) are acquired and analysed in real time to assign a phase (temporal position in the cardiac cycle) to each frame. Forward prediction is then used to accurately trigger acquisition of one synchronised fluorescence image (green) at a user-defined target phase. **b** The sample is scanned through the light sheet to generate a synchronised 3D *z*-stack. **c** The move from confocal laser scanning microscopy (CLSM; upper) to light sheet fluorescence microscopy (LSFM; middle) reduces phototoxic effects by several orders of magnitude by limiting excitation in space. Similarly, the move from retrospective (upper and middle) to prospective gating (lower) reduces phototoxic effects yet further by limiting excitation in time. **d** Prospective optical gating relies on periodic changes within heartbeats (upper) and is able to cope with small changes between heartbeats (middle). However, phase-lock cannot be maintained over developmental time scales, because the heart undergoes drastic morphological changes (lower). **e** These changes mean that image-based similarity metrics are unable to match new brightfield images against the reference heartbeat image sequence recorded at the start of the experiment. **f** A new "smart microscope" is required that can maintain phase-lock in the face of these drastic changes in cardiac morphology over the course of day-long time-lapse imaging

forward prediction in prospective gating, incorporating a biological understanding of heart rhythm variability. Our previously published prospective gating algorithms for acquiring individual *z*-stacks[10] required human fine-tuning of the algorithm parameters for different phases in the cardiac cycle, and different ages of fish. We now incorporate an automated understanding of where in the reference image sequence the refractory period between heartbeats is located. Since this interval varies slightly in duration from one beat to the next, it poses a challenge for forward prediction to anticipate the correct time to

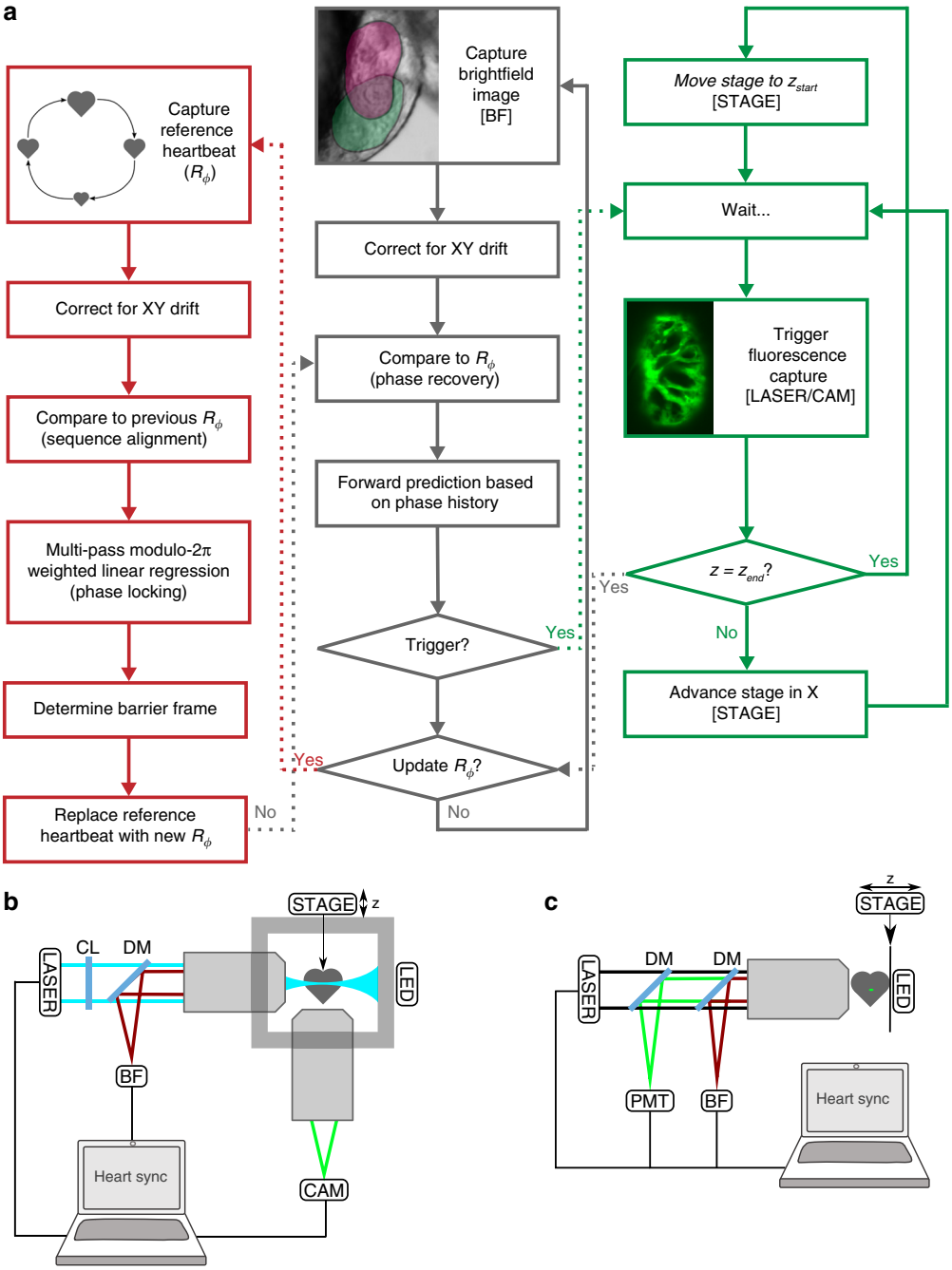

Fig. 2 Adaptive prospective optical gating permits day-long, phase-locked cardiac imaging. **a** Summary flow chart for adaptive prospective optical gating. Each column represents a separate thread running concurrently on the computer. The core prospective optical gating algorithm (centre, grey) identifies the current cardiac phase using the brightfield channel, and computes the correct future trigger time. The day-long phase locking algorithm (left, red) enables the system to cope with developmental-scale changes in cardiac morphology and size. The optical gating algorithms are integrated with fluorescence *z*-stack acquisition and stage movement (right, green). Square brackets refer to hardware components in the schematic diagrams below. **b**, **c** Simplified schematics of the custom light sheet microscope (**b**) and commercial two-photon microscope (**c**) used in this paper, highlighting the key components for adaptive prospective optical gating. Fluorescence (excited by LASER) is imaged onto a triggerable scientific camera (CAM) or photomultiplier (PMT). An infrared light source (LED) provides illumination for a brightfield camera (BF); in **b** this receives light collected through the laser launch objective, for reasons explained in the main text. A full optical diagram for **b** can be found in Supplementary Fig. 1. Other components: STAGE motorised *z*-stage; CL cylindrical lens; DM dichroic mirror to separate different light wavelengths

send an electrical synchronisation trigger. We exploit this knowledge to ensure that our linear fitting for forward prediction does not attempt to fit across this variable interval. Thus we ensure synchronisation can be established reliably by the user at the start of an overnight time-lapse experiment and, most importantly, that performance is maintained throughout the whole experiment in spite of considerable changes in heart rhythm and appearance, for instance due to embryonic development or as a consequence of injury.

Finally, to overcome limitations on available *z* scan range in our previous work, we adopted a different optical strategy for brightfield imaging which enabled us to image both chambers of

the heart in arbitrary orientation, and allowed extra room for growth and movement on developmental timescales, as well as capturing active cells such as immune cells in the external vicinity of the heart. All prior published work has acquired brightfield images through the fluorescence imaging objective. In the present manuscript we instead use side-view brightfield imaging through the laser launch objective in the light sheet microscope (Fig. 2b), which means that during a z scan the brightfield images do not change in focus, and instead the images are simply translated sideways. This alternative strategy was essential to provide the necessary z scan range, as well as being much less cumbersome than our previously published approach involving motor-driven tube lenses[11]. To avoid having to considerably increase the region-of-interest processed by our algorithms (to accommodate this sideways translation) we implemented a real-time-adaptive camera region-of-interest for this brightfield camera (Supplementary Note 1).

Our algorithms ensure that phototoxicity is minimised and dataset sizes are kept manageable, enabling us to perform detailed assessment of structural changes in the developing heart, and visualise cellular and subcellular behaviour, near to continuously, over the course of hours and days.

Capturing developmental changes in the living zebrafish heart. To validate both the technical performance of our method and its biological applicability, we imaged cardiac looping, a stage of cardiac morphogenesis that, although well-characterised, has never before been imaged in its entirety in 3D due to the lack of suitable imaging technology. Cardiac looping commences at approximately 24 h postfertilisation (hpf) when the zebrafish heart tube elongates asymmetrically, and by 36 hpf the future ventricle migrates ventrally in relation to the atrium[19,20]. By 48 hpf, the looped zebrafish heart appears S-shaped and undergoes more subtle changes until both chambers are morphologically distinguishable[19,21]. Using our adaptive prospective optical gating software, we have shown that we can directly witness these changes in 3D time-lapse video (Fig. 3a; Supplementary Videos 4 and 5), acquiring a z-stack every 5 min. We observed the pinching of the atrioventricular canal region, followed by expansion of the outer curvature of the atrium and finally the ventricle. Over the course of this enlargement we measured a 300% increase in endocardial chamber volume between 48 and 72 hpf. To our knowledge, this is the first reported 3D time-lapse movie detailing cardiac morphogenesis of a live beating zebrafish embryonic heart.

Cardiac looping is one of the most challenging scenarios for time-lapse gated imaging, due to the dramatic structural and functional changes involved. To explore the accuracy of our optical gating algorithms we compared our algorithm's phase-lock at a specified phase in the cardiac cycle against a human-based manual annotation over the course of a time-lapse experiment (Fig. 3b), since no previous automated method exists for comparison. For the majority of the experiment there was a strong agreement between the target frame identified by our fully automated software algorithms and that chosen manually by five human experts (who were shown high-quality images of the heart and asked to search for a fixed target phase point in the cardiac cycle—see Online Methods). For the majority of the time-lapse experiment the small variance between our algorithms and the human mean ($\sigma^2 = 0.0035$ radians) was slightly smaller than that between individual experts ($\sigma^2 = 0.0050$ radians), in spite of significant developmental changes in cardiac shape and size. The similar values for variance confirm that the human experts cannot be considered a gold standard: variation between human individuals is on a similar level to any potential difference between algorithm and human assessment. In the first ~3 h of the experiment there was a slight but distinct disagreement between the frames selected by the algorithm and those selected by the humans. This time-frame corresponded to the end of cardiac looping, where the changes in appearance of the heart mean that there is an element of subjective judgement even in determining whether two phase points should be considered equivalent. Nevertheless, even during this time-frame, the stack-to-stack precision of the synchronisation algorithm (the most important quality criterion for applications such as cell tracking) remained within the range of human variance.

Tracking and assessing inflammatory cell behaviour. The ability to track immune cells and image their physical interactions in tissues is essential for understanding any immune response to cardiac injury. However, cardiac motion artefacts dominate completely over immune cell motions, precluding attempts to perform live imaging at a cellular level in the heart. Our ability to computationally freeze the gross motion of the heart over day-long study periods has now made it possible to directly image and study, in 3D, immune cell interactions on, and with, the beating heart.

To demonstrate this novel capability, we subjected 72 hpf zebrafish to a cardiac injury by targeting the ventricular apex with a precise laser pulse[22], and acquired z-stacks of injured hearts at 180 s intervals for approximately 24 h in macrophage and neutrophil fluorescent reporter lines (Fig. 4a, b, respectively). This allowed us to readily observe the morphology, behaviour, and velocity of macrophages and neutrophils accumulating at the injured ventricle (Supplementary videos 6–8). Neutrophils display a rounded morphology and an amoeboid mode of migration to the wound by extending pseudopods[23]. Individual neutrophils and macrophages can be observed interacting with the wounded myocardium, with orthogonal 3D views (Fig. 4c, d) centred on each tracked immune cell confirming that these cells are in direct contact with the myocardium and hence physically interacting with the wound. Tracking of specific individual neutrophils identifies their retention at the wound, distinct from other nearby neutrophils which continue to migrate within surrounding tissue. In contrast, we observe that macrophages display a range of changing morphologies from dendritic-like (Fig. 4e, f) to spherical, and appear to migrate more slowly to and from the wound site, in a mesenchymal mode of migration (Supplementary Video 6).

Exploiting this direct imaging capability, we next assessed whether our optical-gating technique could facilitate quantification of subtle immune cell behaviour at the wound site, as previously studied in non-motile tissues[24,25] but until now impossible in the heart in vivo. Here we challenged ourselves and our imaging modality by focusing on neutrophils (known to be approximately 3× faster than macrophages[26] and therefore more difficult to track precisely in time-lapse). Neutrophils were tracked to determine cell velocity and meandering index (displacement ÷ distance), two parameters commonly used to assess changes in migratory behaviour following injury[25,27]. The meandering index quantifies the tortuosity of a motile cell's track. For example, when neutrophil migration is direct and linear through tissue, the meandering index is high, whereas at a wound site neutrophil migration follows a more zig-zag path and the meandering index is low. Neutrophils observed to scout the wound are distinguishable from other patrolling cells by their low meandering index, thus validating the ability of our imaging approach to extract quantitative data relating to immune cell behaviour.

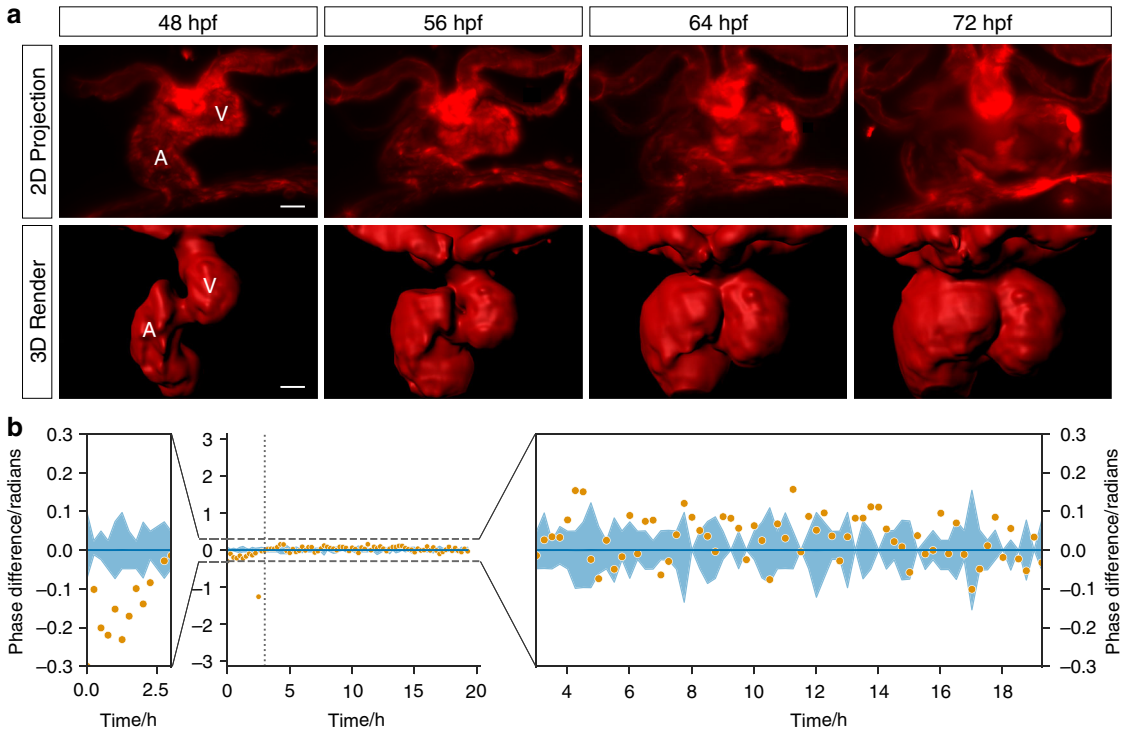

Fig. 3 Phase-locked, day-long cardiac time-lapse imaging of cardiac morphogenesis. **a** The process of cardiac looping, previously observed by histological studies at significantly lower temporal resolution, is now seen in direct 3D video detail (48–72 hpf, at 300 s intervals). The endothelium lining blood vessels and heart chambers is seen during completion of cardiac looping (red—transgene *flk1*:mCherry). Selected timepoints shown as maximum intensity projections (MIPs) of *z*-stacks and 3D render (from Supplementary Videos 4 and 5). V ventricle; A atrium. **b** Adaptive prospective optical gating algorithm (orange) phase-lock performance is compared against human judgements of best-matching frames (blue; line represents mean and shaded area represents the standard deviation). Viewing over the full 2π range (middle) confirms the high precision and accuracy of the gating. Zoomed details (left and right) reveal a minor residual drift in phase during the early time period in which the heart underwent the most dramatic changes in shape and position, but otherwise very high stability

Given the relatively high mean velocity of neutrophils, we demonstrated that the high temporal resolution of our adaptive prospective optical gating was essential for accurate measurement of cell behaviour metrics such as meandering index (Supplementary Fig. 3). Repeating our previous analyses using longer time intervals between *z*-stacks, for example, reveals that intrinsic information on neutrophil migratory behaviour is lost when using longer time intervals. Only with the full range of behavioural information, requiring short-interval 3D acquisition rates, is it possible to make a correct quantitative assessment of the different subpopulations of immune cells migrating in the vicinity of the heart.

Minimal photo-injury and photobleaching. A key advantage of our adaptive prospective optical gating approach is that it minimises the number of fluorescence images acquired, and hence minimises the deleterious effects of laser exposure on the tissue (see refs. [28,29] for recent discussions). Light sheet fluorescence microscopy is well known for its ability to reduce photobleaching and photodamage by limiting fluorescence excitation to only the spatial plane(s) of interest[30]; adaptive prospective optical gating further limits fluorescence excitation to only the times (i.e. cardiac phase) of interest.

To quantify the physiological impact of our own strategy against that of established retrospective gating strategies, we used heart rate as a measure of induced photo-injury (see Online Methods). For fish exposed to 2 h of retrospectively gated imaging at 5 min intervals, we observed an initial increase followed by a significant reduction in heart rate (Fig. 5a). We conjecture that this is due to an initial heating, causing an increase in heart rate, followed by a patho-physiological response, resulting in bradycardia, due to photodamage and phototoxicity to the heart. These effects were accompanied by changes in heart rhythm ($n = 5$ of 6 fish) and reduction in ventricle ejection fraction (Supplementary Video 9), both further signs of physiological impact. In contrast, time-lapse imaging using our method at 5 min intervals caused no significant change in heart rate over a similar time period (Fig. 5a).

The reduced laser dose with our method also has the important effect of reducing the rate of photobleaching. This is particularly important for easily bleached fluorophores and for the low endogenous expression levels obtained using CRISPR-Cas9 technology[31]. We demonstrated this by acquiring 3D time-lapse fluorescence images using two alternative imaging protocols (Fig. 5c, Supplementary Video 10). The first protocol, representing a retrospective optical gating approach, causes rapid and marked bleaching of mKate emission from cardiomyocyte cell membranes and the signal soon becomes indistinguishable from background. In contrast, our imaging protocol causes only mild and gradual photobleaching, and can continue to capture 3D images for over 24 h. Direct reduction in bleaching rate is due to a combination of the stroboscopic nature of imaging[32] and the reduced total laser dose[33]. Additionally, a reduction in photo-injury in the tissue may minimise the oxidative rate of fluorescent molecules, as previously seen in in vitro samples[34], thus indirectly reducing photobleaching still further.

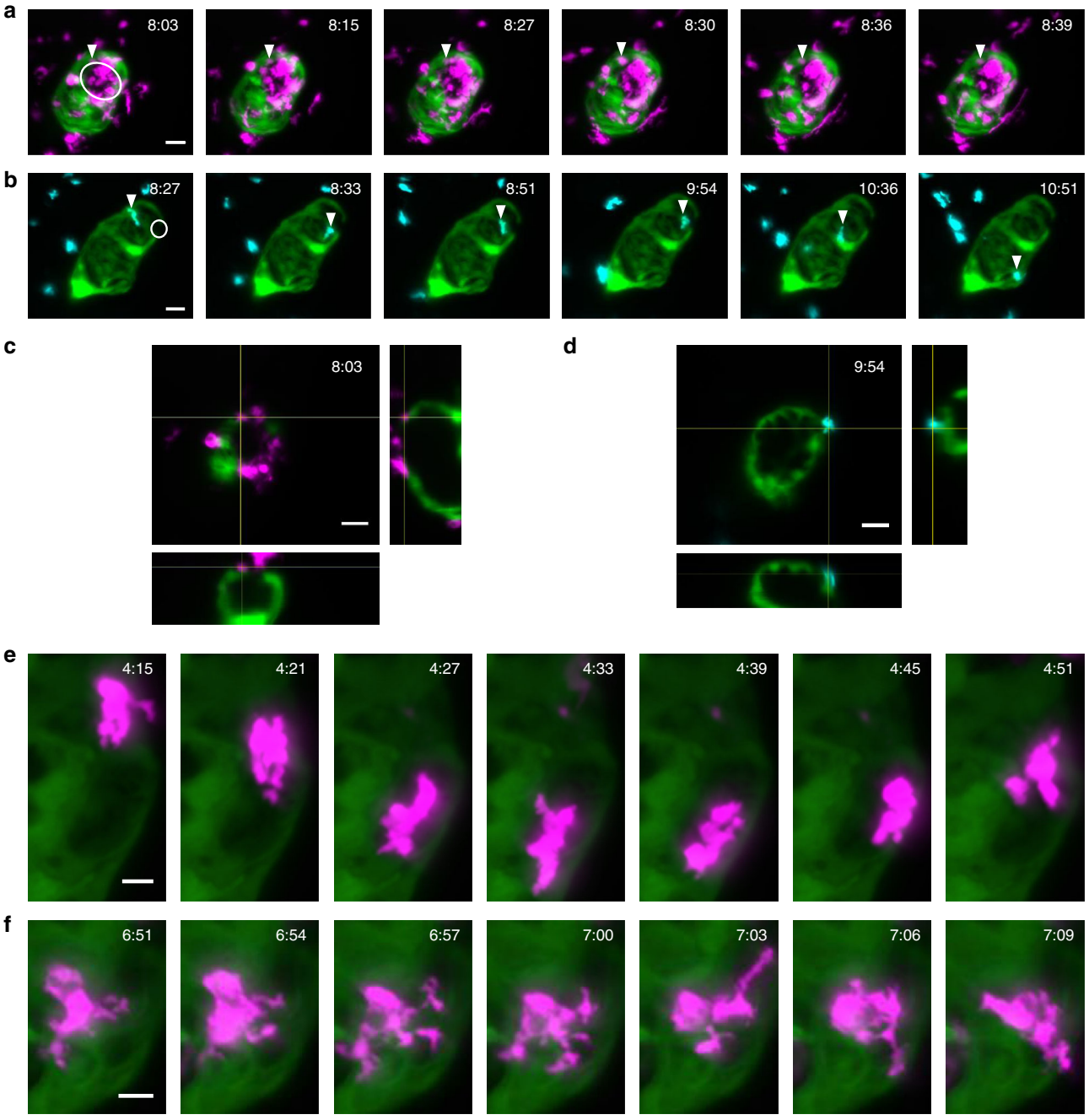

Fig. 4 Sustained beating-heart time-lapse imaging of immune cell responses to cardiac injury. **a**, **b** Sequence of MIPs (from Supplementary Videos 6–8) showing macrophages (**a** magenta *mpeg1*:mCherry) and neutrophils (**b** cyan *mpx*:mCherry) migrating to, and interacting at, the laser wound site (white circle) on the ventricle (*myl7*:GFP, laser injury has bleached myocardial cells at the injury site). Arrowheads mark tracked immune cells interacting with the wound margins, changing shape and reverse migrating from the wound to the pericardium. **c**, **d** Orthogonal plane views co-localising the tracked macrophages (**c**) and neutrophils (**d**) on and within the myocardium at the wound site. **e**, **f** Individual macrophages are seen to undergo complex shape changes during migration. All timestamps show hours post injury (hpi). Scale bars: 30 μm (10 μm for **e**, **f**)

Novel insights into cell proliferation and heart development. Our new platform is allowing us to study complex developmental biological questions. Our ability to capture phase-locked *z*-stacks at time-lapse intervals as close as 3 min apart allowed us to routinely map all cell division events in the beating heart (Fig. 6a, b), capturing the archetypal stages of mitotic cell division at both the subcellular and cellular level (Fig. 6c). In examining such events we observed novel behaviour of dividing cardiomyocytes, involving rapid migration of daughter cells following division. We conjecture that this may be a consequence of the mechanical forces acting on newly formed cardiomyocytes in the beating heart, before they have formed strong cell–cell adhesions. Such events could not have been observed previously where the heart had to be arrested to acquire each *z*-stack. Interestingly, we observed cell division of cardiomyocytes occurring at a rate of roughly 1 per hour between 72 and 96 hpf (Fig. 6b), a higher rate of cell division than reported previously [ref. [6], Fig. 1]. We hypothesise that this is a consequence of the more physiological conditions maintained by using our gating system.

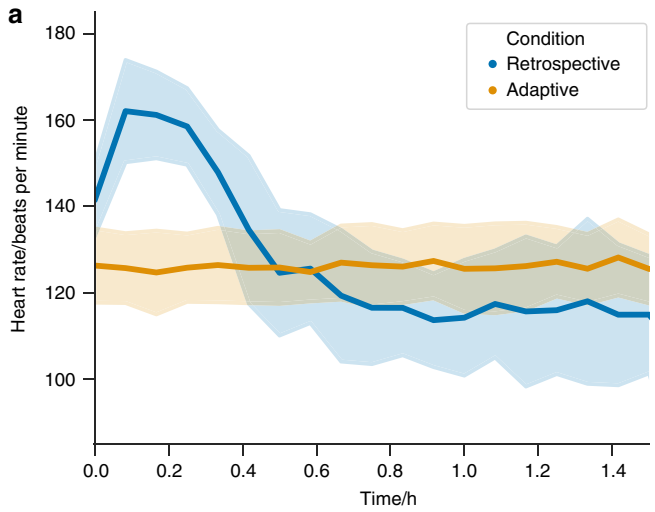

b

	R	AP
Instantaneous Intensity/Wcm^{-2}	118	
Energy per Stack/mJ	280	0.19

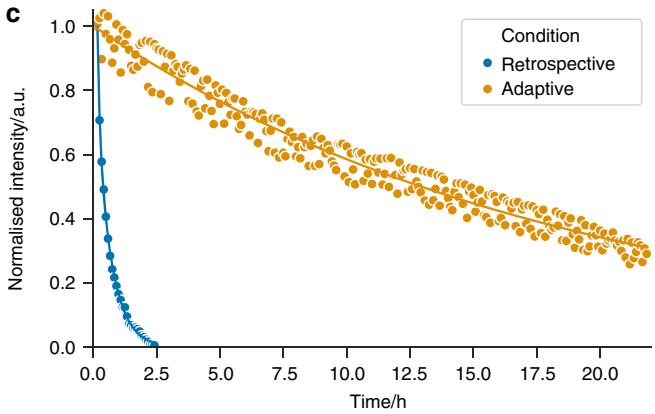

d

	R	AP
Instantaneous Intensity/Wcm^{-2}	113	
Energy per Stack/mJ	290	2.5

Fig. 5 Adaptive prospective optical gating minimises cardiac photo-injury and photobleaching. **a** Acquisition of multiple fluorescent *z*-stacks in a zebrafish heart (transgene *myl7*:GFP; 3 dpf) using a retrospective optical gating protocol (blue; mean (line) with standard deviation (band)) causes an increase, followed by a fall, in heart rate over a 1.6 h imaging period ($n = 6$ fish). Meanwhile 1.6 h of continuous image acquisition using our adaptive prospective optically-gated protocol (orange; mean (line) with standard deviation (band)), with stacks acquired every 5 min, causes no change in heart rate ($n = 5$ fish). Plots for individual fish can be seen in Supplementary Fig. 4. **b**, **d** The high energy per stack required for retrospective gating (R) is significantly reduced with adaptive prospective (AP) gating. **c** When exposed to light levels required for retrospective gating (using typical parameters reported in the literature, and again acquiring *z*-stacks at 5 min intervals), the fluorescence signal from a bleach-susceptible fluorophore (*myl7*:mKate-CAAX) is halved after only 3 *z*-stacks (blue). In contrast, adaptive prospective optical gating achieves 150 *z*-stacks before showing an equivalent fall in fluorescence intensity (orange). Time course shown in Supplementary Video 9. Data show one representative fish for each condition

An important early developmental process where cell division may play a role is trabeculation, whereby multicellular luminal projections of cardiomyocytes are formed as the heart matures (Supplementary Fig. 5a shows trabeculation at the tissue level in the same zebrafish heart during three consecutive days). Two principal mechanisms have been proposed for initiation of trabeculation[35]. The first is referred to as delamination, where cardiomyocytes are physically squeezed-out luminally from the cortical myocardium layer without a cell division event. The second is referred to as orientated cell division where cortical cardiomyocytes divide perpendicular to the ventricular myocardium. Currently, delamination is suggested to be the sole mechanism of trabeculation initiation in zebrafish[35].

Detailed observation of cardiomyocyte cell division and migration enabled us to study cardiac trabeculation initiation (Fig. 6a, b; Supplementary Video 11). Using our imaging system we were able to assess whether orientated cell division could also contribute to trabeculation. We observed cell division events and ventricular cardiomyocyte migration occurring both parallel and perpendicular to the abluminal-lumen axis (Supplementary Fig. 5b). Interestingly, tracking the migration of one such cardiomyocyte in the original plane of acquisition (Fig. 6d) initially indicated that it delaminates from the cortical layer without dividing, and only on closer examination in 3D (re-slicing the full *z*-stack along additional planes) was it revealed that this cardiomyocyte actually undergoes cell division, parallel to the abluminal-lumen axis, while also delaminating perpendicularly to give rise to a trabecular projection into the lumen. These observations appear to suggest what we call a “mixed model" for early trabeculae formation in the ventricle, whereby cardiomyocyte division is immediately followed by luminal migration of a daughter cell (Fig. 6e). It is evident that despite the range of genetic, histological, and imaging techniques available to the community at present, all have failed to capture this biology until now. Combining our high-resolution 4D imaging system with cell signalling reporter lines will permit future investigation of the underlying molecular control of trabeculation; candidates include notch and neuregulin[36,37].

Mitosis of cardiomyocytes has previously been studied in situ using labour-intensive methods that have pushed the limits of what was possible at the time, by imaging after cardiac arrest[5,35] or using high-speed 2D video imaging[6]. However, these

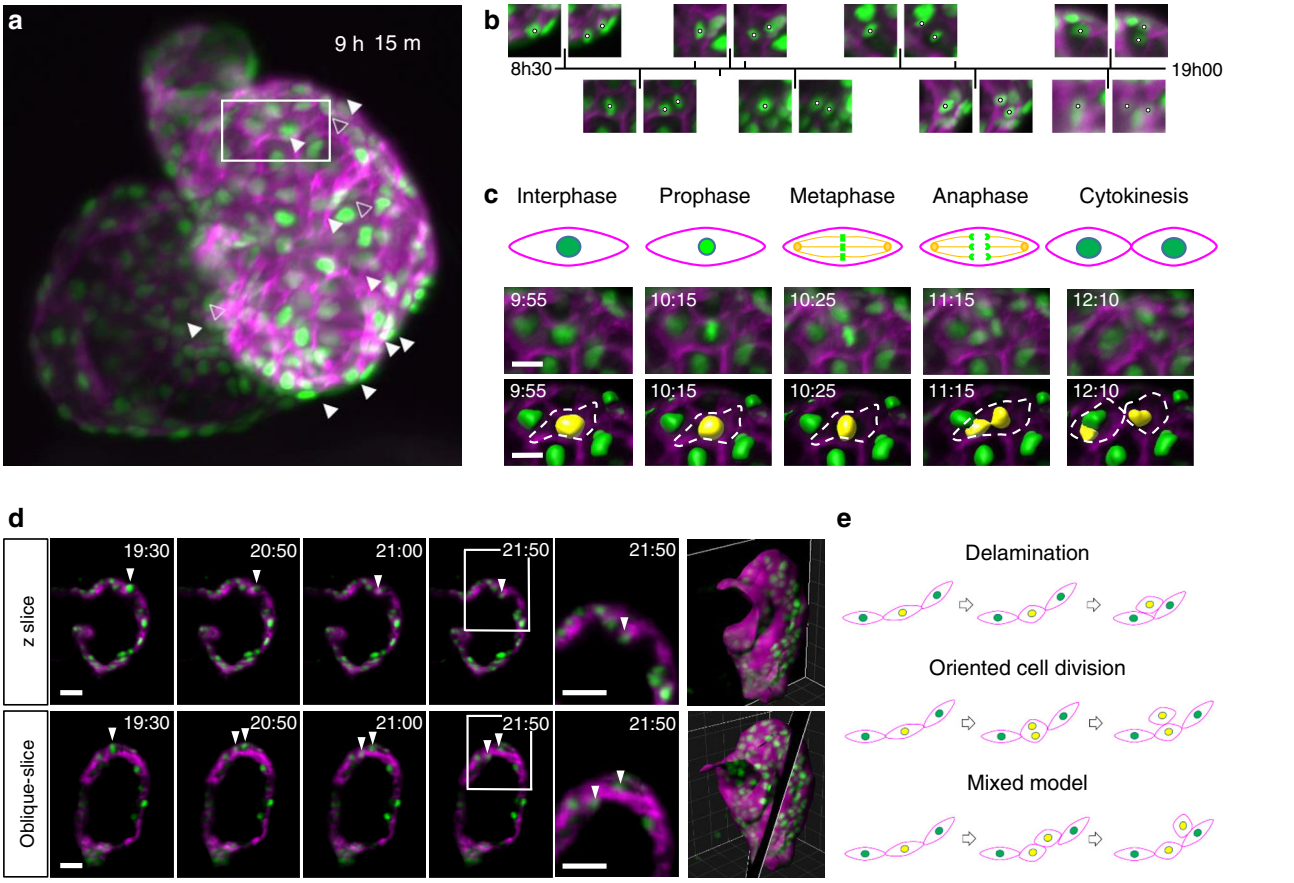

Fig. 6 Mapping cardiomyocyte migration and cell division during myocardial trabeculation. **a** Representative MIP from a 24 h time-lapse of a 72–96 hpf zebrafish (Supplementary Video 10). Image shows cardiomyocyte nuclei (green—transgene *myl7:h2b-gfp*) and cardiomyocyte cell membranes (magenta—transgene *myl7:mKate-CAAX*), with strongest signal expressed in the ventricle. Nuclei of cardiomyocytes which will later divide are indicated by white arrowheads (open-arrowheads for less-obvious divisions near the posterior wall of the heart). Region-of-interest for **c** is indicated with white box. **b** Detail from time-lapse: pairs of images plotted on a timeline, illustrating selected cardiomyocytes shortly before (left) and after (right) cell division; nuclei indicated with white circles. **c** A selected cardiomyocyte division clearly exhibits key stages of mitosis. Mitotic stages (schematic: top row) are visible at selected timepoints from the time-lapse sequence (MIPs: middle row), and the nuclear volume changes and karyokinesis typical of cell division can be seen (dividing nucleus surface-rendered in yellow: bottom row). **d** A dividing cardiomyocyte nucleus is shown in the acquisition plane (*z*-slice, top row) and in the plane of division (oblique slice, bottom row) across two and a half hours of imaging with 5 min time-lapse resolution. White arrowheads highlight the observation of two daughter cardiomyocyte nuclei in the oblique-slice, which would have been missed in the *z*-slice or 2D imaging. The final time point is shown zoomed-in to highlight the migration of the two daughter cells across the time period. Whole rendered heart ventricle (magenta) with rendered nuclei (green) indicate the *z*-slice and oblique-slice views used. **e** Schematic illustrating three models of cardiac trabecular initiation: delamination model (top), cell division model (middle) and mixed model (bottom). Delaminating cardiomyocytes are indicated by a yellow nucleus. Scale bars: 30 μm (10 μm for **c**)

approaches have a number of critical limitations. Firstly, repeated pharmacological arrest and restarting of the heart is liable to impact cellular events, and excessive phototoxic laser exposure will do the same[28]. Secondly, when imaging during cardiac arrest, the heart is not subject to its usual mechanical forces, thus potentially missing key observations linked to stress and strain within the myocardium. Our approach eliminates all these issues. The rapid rate with which daughter cells separate in three dimensions means that our use of short-interval 3D time-lapse imaging was essential to capture cell division and cytokinesis events, interpret them correctly (Supplementary Fig. 5c), and reach the conclusions that we have drawn.

Discussion

Time-lapse imaging cannot offer biological insights if the imaging procedure itself causes severe disruption to the physiology of the organism. Our method and results demonstrate for the first time how to avoid this in the heart, and indeed how to make day-long time-lapse imaging survivable at all at a biologically relevant, rapid acquisition rate. Light sheet microscopy reduces the damaging laser exposure by orders of magnitude compared to confocal imaging, but this benefit is lost when using previous methods for time-lapse beating-heart imaging in which hundreds of fluorescence images must be acquired in each plane prior to retrospective synchronisation[13]. Alternatively, repeated pharmacological arrest of the heart using high-dose anaesthetic permits artefact-free imaging, but at the cost of accumulating exposure of the heart and the whole organism to anaesthetic agent. With our new algorithms we have eliminated both these obstacles to survivable and physiologically realistic long-term imaging. Our quantitative measurements of heart rate as a measure of phototoxic effects are, to our knowledge, the first reported longitudinal quantifications of the patho-physiological impact of fluorescence imaging in vivo in a vertebrate. This is an increasingly important consideration in the context of ethical approval for studies in

older (and legally protected) specimens. We anticipate that our results will not only spark further studies quantifying the impact of imaging, but also inspire further development and validation of suitable in vivo phototoxicity assays.

For the developmental and cell migration studies presented here, only images at a single heart phase need be acquired, minimising phototoxic laser exposure. Conversely, retrospective gating strategies do offer the freedom to make post hoc decisions to reconstruct images from any or all phases of the cardiac cycle, which is advantageous for studies of cardiac dynamics[38]. We note that if additional phases in the cardiac cycle are required, for example for ejection fraction measurement, blood flow mapping[39], or studies of heart wall dynamics, then our approach can be readily adapted to trigger images at multiple precise phases throughout the cardiac cycle (or indeed to assign phases in real time to a continuously acquired stream of fluorescence images[39]). Our multi-modality approach, using brightfield images to trigger synchronised acquisition of the fluorescence image, separates the conflicting requirements for fluorescence imaging (tissue-specific labelling, which may be highly sparse; z-scanning; z-sectioning while minimising photodamage) and heart-synchronisation (phase-diverse periodic signal; invariance during z-scan), offering additional flexibility to optimise future microscope designs for cardiac imaging. Recent advances in fast volume imaging using custom-built adaptations of light sheet microscopes[40–42] may soon permit direct, synchronisation-free snapshot 3D imaging of the heart. Even as these techniques mature, for time-lapse imaging our real-time triggering capability will still remain essential for maintaining phase-lock throughout repeated time-lapse 3D image acquisitions. Using a brightfield synchronisation source also has other potential uses such as fusing and phase-registering multiple fluorescence channels with sparsely labelled (and less clearly periodic) structures[39], or acquiring synchronised images in multi-acquisition modalities such as structured illumination microscopy.

Our method brings two important practical advantages for an experimental campaign: (i) it allows unsupervised day-long imaging, without the need for human intervention at every imaging timepoint; (ii) it substantially reduces data file sizes, eliminating the considerable challenges of storing and processing multi-TB datasets. For example, if a retrospective gating approach had been used for the experiments in Fig. 3, the raw data for one time-lapse would have occupied at least 16 TB (assuming 200 video frames per slice[13]), and would have required days of postprocessing time. In contrast, our datasets occupy only 80 GB of storage space. These relatively modestly sized datasets can also be accessed and reviewed by the user through the course of the experiment, paving the way for future developments such as user-initiated or automated responses to unexpected or atypical biological observations during imaging experiments.

We have demonstrated that our optical gating system can be used to clarify complex biological patterning such as the cellular processes underlying myocardial trabeculation. Previous studies have used genetic tools to stochastically label cardiomyocytes with different fluorophores prior to trabeculation[35,43]. These studies reported that adjacent cortical-trabecular cardiomyocytes rarely share the same fluorophore, implying that orientated cell division does not contribute to trabeculation. However, these studies relied on analysis of single optical and histological slices of the heart and so may have missed daughter cells that have migrated away from each other out of plane. Our own observations have shown that in a number of instances cardiomyocyte cell division was followed by immediate perpendicular migration of a daughter cardiomyocyte. Coupling delamination to proliferation is a plausible strategy for trabeculation: not only would this maintain cortical cardiomyocyte number, but the disassembly of sarcomeres (known to occur prior to proliferation) may also liberate the cell for delamination. We have demonstrated that such events can be missed in studies where time-lapse imaging was acquired only in a single plane, potentially underestimating the contribution of dividing cortical cardiomyocytes to pioneer trabecular cardiomyocytes[5,6,35,43]. Our insight was only possible due to the high spatio-temporal resolution of our optically-gated imaging system.

Our observations of inflammatory cell interactions following heart laser injury also highlight the value of our method for 3D time-lapse imaging. The ability to track individual, rapidly moving inflammatory cells on the injured heart provided novel insights into neutrophil migratory behaviour on the beating heart. There is a clear potential to study pharmacological and genetic manipulation of these aspects of neutrophil migratory behaviour at the cardiac injury site. Similarly, changes in macrophage cell morphology were observed using our system, highlighting the potential to study morphological changes in heart-associated macrophages in vivo. Linking these shape changes with specific molecular phenotypes could provide new insights into distinct macrophage subpopulations in the injured heart.

Our method is equally applicable to embryos of other species such as fly, chick or mouse. It can also be applied to other microscope modalities, such as two-photon or confocal, simply requiring access to a brightfield image channel and the ability to trigger image acquisition. Our synchronisation software can run independently of the existing microscope control software, avoiding any need for complex integration at software level. We have successfully integrated our system with a commercial two-photon microscope (Fig. 2c; Supplementary Fig. 6) with a small degree of cooperation from the manufacturers over hardware integration, and in future our system could also be integrated with commercial light sheet microscopes, as well as other groups' custom-built microscope platforms, to equip them with real-time synchronisation capabilities.

In conclusion, we have shown that our adaptive prospective optically gated imaging system can provide high spatial and temporal resolution time-lapse 3D images of the beating heart, as demonstrated here for zebrafish. The minimal phototoxicity of our method ensures that high-quality 3D images can be reliably acquired throughout 24 h time-lapse studies, allowing us to observe cardiac morphogenesis, inflammatory cell migration and cardiomyocyte cell proliferation. This approach has the potential to provide further novel insights into morphological, cellular and subcellular processes in the beating embryonic heart in the zebrafish and other species. Over the past decade, the transition from confocal microscope to the low-photodamage regime of light sheet microscopy has opened up a whole new landscape of in vivo biological studies involving direct and routine observation of development, cell–cell interactions and whole-embryo cell fates. We anticipate that our now-routine capability to conduct day-long time-lapse beating-heart imaging experiments represents the equivalent tipping point in cardiac biology.

Methods

Fish husbandry and preparation for imaging. Zebrafish husbandry, embryo collection and maintenance were performed according to accepted standard operating procedures[44] and in accordance with the Animals (Scientific Procedures) Act 1986 in a UK Home Office-approved establishment. All experiments were performed on animals aged less than 120 h postfertilisation. Project licence approval for the maintenance of genetically modified lines was given by the UK Home Office and The University of Edinburgh Animal Welfare and Ethical Review Board.

Transgenic zebrafish lines used for imaging are as follows; Tg(*myl7:eGFP*^{twu26})[45], Tg(*kdrl:mCherry*^{ci5})[46], Tg(*mpx:mCherry*^{uwm7})[47], Tg(*mpeg1:mCherry*)[48], Tg(*myl7:h2b-GFP*^{zf52})[13], Tg(*myl7:mKate-CAAX*^{sd11})[49]. Adults were day-crossed as appropriate to yield desired combinations of transgenes in embryos. Embryos were treated with phenylthiourea (Fisher Scientific) at 7 hpf to inhibit pigment

formation and enhance image clarity. Zebrafish were embedded in 0.5% low-melting-point agarose inside FEP tubes (Adtech Polymer Engineering), which was essential to minimise drift whilst still allowing growth during long-term imaging. Fish were used only once for a time-lapse imaging experiment, and any repeats shown come from distinct individuals. All experimental procedures were performed at room temperature (23 °C).

Light sheet microscope set-up. Our custom-built selective plane illumination microscope (SPIM) is optimised for simultaneous multi-channel light sheet fluorescence imaging of zebrafish (Supplementary Fig. 1). The detection arm is based around a Nikon Plan Fluorite ×16/0.8 NA objective lens with ultra-flat dichroic mirrors (Chroma T495lpxr-UF2, T550lpxr-UF2, T700spxr-UF2) separating red/green/blue fluorescence channels, and a near-IR, non-visible brightfield channel (which is not routinely used—see below). Fluorescence images are acquired using QIClick CCD cameras (QImaging) and fluorescence emission filters (Thorlabs MF479-40, MF525-39, MF630-69). Rather than acquiring our brightfield images through the 0.8 NA imaging objective, as might be expected, we acquire these by imaging through the light sheet launch objective (for reasons explained in Supplementary Note 1). A 650 nm shortpass dichroic mirror (Edmund Optics) serves to pick off the collected brightfield light, which is imaged onto a Prosilica GS650 CCD camera (Allied Vision).

Laser excitation is at 488 and 561 nm, using a Versalase laser system (Vortran) with single-mode fibre delivery. Brightfield illumination is via a light emitting diode at 750 nm (near infrared, non-visible). The light sheet (measured full-width-at-half-maximum 2.4 µm) is formed using a cylindrical lens and a ×10/0.3NA objective lens (Nikon). Shadow effects are minimised using an mSPIM configuration[50] using a 4 kHz resonant scan mirror (SC-30, Electro-optical Products Corporation) to modulate the in-plane propagation angle of the light sheet, over the course of each individual image exposure. Laser pulsing and camera triggering is coordinated using a custom-built electronic system based around a StartKit microcontroller board (XMOS; software and hardware details in Supplementary Note 2) which also serves to define a universal timebase for our synchronisation analysis. The sample is positioned and scanned using a combination of manual micrometre stages and motor-driven stages (M-111.1DG, Physik Instrumente).

Image acquisition parameters used for all experiments can be found in Supplementary Table 3.

Real-time, prospective optical gating. Real-time, prospective optical gating[10,11] is used to trigger capture of fluorescence images at a user-selected target phase in the heart's natural cycle. This approach allows us to computationally freeze the heart without any invasive approaches such as pharmaceuticals or pacing. Real-time, prospective optical gating relies on information captured in the brightfield channel (for which even continuous illumination is not sufficiently intense to cause harm to the specimen). First, a reference sequence of brightfield images is collected, lasting precisely one natural heart cycle. Subsequent brightfield images are correlated against this to assign them a phase. A target phase in the heartbeat is selected by the user, and all subsequent fluorescence images will be triggered at this target phase in the heartbeat.

To generate a trigger requires forward prediction of when the heart will next be at the correct point in its cardiac cycle, and for this prediction we assume that the phase evolution of the heart is locally linear. For the most part we find this to be a reasonable first approximation even in the presence of heart rate variability, but the exception is the refractory period between heartbeats, whose duration may vary from one beat to the next, especially in injured or diseased hearts. Our previous approach, in which forward prediction was achieved by a linear fit in the phase domain over a fixed time interval, required manual tuning of parameters by the user, which would depend not only on the characteristics of the individual sample but also on the chosen target phase. To sustain reliable, unsupervised performance over day-long time-lapse experiments it was therefore necessary for us to incorporate into our algorithms a knowledge of where the inter-beat refractory period occurs. We achieved this via an additional algorithm parameter, the "barrier frame" (see below), which enables us to ensure that a linear fit in the phase domain is not performed across this part of the cardiac cycle.

For each brightfield image I_t (composed of pixels $I_t(x,y)$) received at the current time t, the following steps are taken to phase-match the heart images and forward-predict the next fluorescence trigger time:

1. The new brightfield image is windowed to correct for any in-plane (xy) sample motion $\Delta x, \Delta y$, as calculated from the previous-received frame (see step 6).
2. The windowed brightfield image is compared against the one-heartbeat reference image sequence R_ϕ to identify the current phase ϕ_t of the heart using a sum-of-absolute-differences metric (this metric was chosen to maximise real-time processing speed):

$$\mathbf{s} = \sum_{xy} \left| I_t(x,y) - R_\phi(x+\Delta x, y+\Delta y) \right| \quad (1)$$

$$\phi_t = \arg\min_\phi \mathbf{s}. \quad (2)$$

3. The phase ϕ_t is refined to sub-frame precision ϕ_t' by fitting a 'V' function ($s = |\phi - \phi_t'| + s_{\min}$) to the three elements of $\mathbf{s}$ in the immediate vicinity of its minimum element ϕ_t[10]:

$$\phi_t' = \frac{s_{\phi_t - 1} - s_{\phi_t + 1}}{2(\max(s_{\phi_t - 1}, s_{\phi_t + 1}) - s_{\phi_t})}. \quad (3)$$

4. To accommodate unavoidable latencies in the system, linear forward prediction of the phase evolution (details below) is used to calculate the required triggering time for the next acquisition, i.e. the precise time at which the heart will next be at the desired target phase of its heartbeat.
5. A decision is made whether to commit to the calculated trigger time or to await a refined prediction from the next incoming brightfield image. This decision is made based upon the known processing latency (~12 ms from brightfield image exposure to programming of a trigger).
6. The measure of uniform drift $\Delta x, \Delta y$ in the xy plane of the brightfield images (as used in step 1) is updated using a local search to minimise s_{ϕ_t} as a function of Δx and Δy[11]. The new values of $\Delta x, \Delta y$ will be applied when processing the next incoming brightfield image.

If the system decides to send a trigger, the target trigger time is transmitted to the timing controller over a USB/serial link. Once the timing controller has been informed of the required trigger time, it will electrically trigger the next (synchronised) fluorescence image. Following this, the sample is moved to the next z-position in preparation for the next synchronised acquisition.

When assigning a phase to the current brightfield image, by comparing it to the reference sequence, nonperiodic variations (such as the locations of blood cells) may result in a situation where the best match is with the very first (or last) frame in the reference sequence. This may lead to erroneous phase values being computed. We mitigate against this by padding our reference sequence with two extra frames at either end; these extra frames are not used for the initial minimum-finding, but are available in the case where the initial minimum lies at an extremum of the reference sequence.

Forward prediction is achieved by forward-extrapolating a linear fit of the recent measured phase history as a function of time. The linear fit is performed only over the phase values for frames received since the barrier frame was last passed, to ensure the linear fit is restricted to a regime where it represents a good approximation for the temporal evolution of the cardiac phase. (The fit is however always performed over a minimum of three datapoints.) The use of the barrier frame is particularly important in the case of hearts whose rhythm has been affected by injury or disease. The barrier frame is identified automatically at the start of an experiment, and while in principle the user is free to modify its value, we have found the following automated, empirical strategy for barrier frame estimation to be reliable across a range of heart orientations, ages, and states of health. Within the reference sequence, we compute the sum-of-absolute-differences between adjacent frames (yielding a simple metric v_ϕ for the level of motion present in each frame). We first identify the frame with minimal motion ($\arg\max v_\phi$), which is associated with the refractory period between beats. Following the refractory period the heart contracts rapidly, so we search forward in time for the first frame in which the motion metric rises to $(\max v_\phi + \min v_\phi)/2$ and identify this as our barrier frame (located at the end of the refractory period).

Adaptive prospective optical gating. Our adaptive prospective optical gating strategy requires us to be able to refresh our reference sequence, formed from video images of exactly one heartbeat, while still maintaining phase-lock at the same point in the cardiac cycle. In the terminology of the retrospective gating literature, this task is equivalent to computing the absolute alignment between all reference sequences over the course of a time-lapse experiment. However, we found that existing algorithms were not suitable for our purposes, and we had to develop a new multi-pass algorithm for absolute alignment of our reference heartbeat sequences.

Relative alignment between individual pairs of single-heartbeat reference sequences can be computed through pixel-wise temporal cross-correlation of two single-period brightfield video sequences that have been resampled to equal lengths (similar to the method used for postacquisition, retrospective optical gating[12]), as described in more detail below. However we found that use of nearest-neighbour relative alignments alone soon leads to unacceptable accumulation of errors over time, leading to loss of consistent phase-lock at a fixed point in the cardiac cycle. Previous authors have solved this problem by also considering relative alignments between sequences separated by larger time intervals, and solving the resultant over-determined system of equations to recover an improved estimate of the absolute global alignment of all sequences. However, the fact that relative alignments must be computed modulo-2π will inevitably lead to inconsistencies in this system of equations, given that our input sequences can have arbitrary relative alignments (Supplementary Fig. 2). This led us to develop a new multi-pass algorithm[51] to overcome this mathematical obstacle and solve for correct global sequence alignments without accumulating errors.

The algorithm proceeds as follows. First, a new brightfield reference image sequence is acquired, using image self-similarity to identify a video sequence exactly one heartbeat period long[10]. We then determine the equivalent target frame

in this new reference heartbeat that matches the original, user-defined, target heart phase. This is done by cross-correlating between the original and new reference sequences as follows:

1. Each reference heartbeat ($R_{u,\phi}(x,y)$ for timepoint u) is resampled ($\tilde{R}_{u,\phi}(x,y)$) to contain a fixed, integer number of frames.
2. The relative phase shift $\Delta\phi_{ab}$ is computed between this new reference heartbeat, acquired at time b, and each of several (typically three) recent past reference heartbeats, acquired at times a. This shift is computed by minimising a least-squares criterion representing the similarity between relatively shifted image sequences:

$$\Delta\phi_{ab} = \arg\min_{\Delta\phi} \sum_{xy} \left| \tilde{R}_{a,\phi}(x,y) - \tilde{R}_{b,\phi+\Delta\phi}(x+\Delta x_{ab}, y+\Delta y_{ab}) \right|^2, \quad (4)$$

where Δx_{ab} and Δy_{ab} represent any translation that has occurred in the image during the time elapsed between when sequences a and b were acquired. Δx_{ab} and Δy_{ab} are already known since they are tracked in real time by our prospective gating algorithms (see above).

In fact, the above expression can be shown to be equivalent to the following criterion, based on cross-correlation along the phase axis, which we compute in Fourier space for speed:

$$\Delta\phi_{ab} = \arg\max_{\phi} \sum_{xy} \tilde{R}_{a,\phi}(x,y) * \tilde{R}_{b,\phi}(x+\Delta x_{ab}, y+\Delta y_{ab}). \quad (5)$$

3. Each $\Delta\phi_{ab}$ is refined to sub-frame precision by 'V' fitting (Eq. 3). To maintain acceptable precision, while ensuring a runtime compatible with real-time operation, it is essential that we do this rather than oversampling in step 1.
4. All the computed $\Delta\phi_{ab}$, including the relative phase shifts computed during previous reference frame refreshes, are combined into a weighted, linear least-squares regression to determine an absolute phase shift. The matrix equation to be solved has the form $\mathbf{Ax} = \mathbf{r}$, where x_a represents the absolute phase shift for sequence a, r_i represents each computed relative phase shift $\Delta\phi_{ab}$, and $A_{a,i} = -1, A_{b,i} = 1$ (other elements of A are zero).

However, as noted above, the equation to be solved will not yield a correct global solution using least-squares matrix solver algorithms (which are not compatible with modular arithmetic). To overcome this problem, in each iteration of our multi-pass algorithm we only consider relative shifts between sequences such that $b - a \leq \Delta t_{\max}$, where $\Delta t_{\max}$ represents an upper limit on the temporal distance $b - a$ being considered in that iteration. Each iteration of our new algorithm proceeds as follows:

1. Form A' by eliminating all rows from A for which $b - a > \Delta t_{\max}$ (and form r' equivalently by discarding elements from r), to form a reduced equation $\mathbf{A'x'} = \mathbf{r'}$
2. Solve for $\mathbf{x'}$
3. Add or subtract multiples of 2π from each element of $\mathbf{r}$ to minimise $r - (x_b' - x_a')$.

In the first pass of the algorithm, we only consider $\Delta t_{\max} = 1$, i.e. temporally adjacent sequences. The effect of this is to precondition our full vector $\mathbf{r}$ of computed relative shifts, adding or subtracting multiples of 2π in such as way that a self-consistent solution for $\mathbf{x}$ is possible in conventional non-modular arithmetic. In practice, since for the present work we have found good synchronisation performance from only computing relative shifts with $\Delta t_{\max} \leq 3$, we then just performed just one subsequent pass, considering all $\mathbf{r}$. However, in cases where larger temporal distances are considered or there are high uncertainties in the individual computed relative shifts, it is preferable to perform additional passes with gradually increasing values of $\Delta t_{\max}$, to improve tolerance to errors.

We note that the problem we have solved with our new algorithm can also arise when using conducting postacquisition synchronisation using previously published algorithms (and hence our algorithm offers increased robustness for postacquisition as well). In practice, we presume that in previously published postacquisition experiments the problem with modular arithmetic has been largely avoided by considering only adjacent sequences, or by ensuring that adjacent sequences are separated by only a small, consistent time gap. There is absolutely no such guarantee in our more general problem of aligning time-lapse (brightfield) sequences, and it was essential that we develop this multi-pass approach in order to make our synchronisation possible at all.

Gating on a commercial two-photon microscope. As a case study for integration with commercial microscope hardware, we applied our optical gating system to a Scientifica two-photon microscope. This required a small modification to the imaging hardware to permit simultaneous acquisition of brightfield and two-photon images, and triggering of each image acquisition using our synchronisation software and timing electronics.

The microscope has the capability for both two-photon imaging and brightfield trans-illumination in the near infrared (the latter using the same beam path as epifluorescence, which we did not use in this experiment). In a standard system the user would switch between two-photon and brightfield using a flip mirror. With the assistance of the manufacturer we replaced the flip mirror with a 800 nm shortpass dichroic mirror (Supplementary Fig. 6) such that the two-photon excitation laser is reflected at the same time as the 780 nm brightfield illumination is transmitted by the mirror. This ensures that our brightfield imaging camera, attached to the imaging port of the microscope, can be used to acquire images for input into our synchronisation algorithms, but the optical path still supports the standard two-photon image acquisition modality of the microscope. The manufacturer's acquisition software includes a scripting capability which enabled us to sequence a z scan in which the microscope waited for an external electronic trigger before acquiring the next image and advancing to the next z plane. The synchronisation trigger output from our own timing controller provided this trigger input to the microscope.

When two-photon image acquisition is actively in progress, some back-reflected two-photon excitation light leaks through the shortpass dichroic mirror and momentarily saturates the brightfield camera images, but this does not cause problems for the prospective gating algorithms since it comes a considerable time before the next time we will be attempting to predict and schedule the next trigger signal. In fact, this leakage proved helpful during development since it enabled our software to identify automatically when a two-photon image acquisition had been triggered.

In this experiment we did not have control over the microscope hardware design, so it was not convenient to implement the side view or focus-correction strategies described in Supplementary Note 1. As a consequence, the focal plane of the brightfield images varied along with the focal plane of the two-photon imaging. It was therefore necessary for us to repurpose our reference sequence refresh algorithm (see previous section) to address this issue during the two-photon z scan: whereas for day-long time-lapse imaging on our light sheet microscope we applied the sequence refresh algorithm between each full z stack (i.e. at 3–5 min intervals), for this two-photon imaging we applied exactly the same algorithm every 3 µm within each z scan. This ensured that high-quality synchronisation could be maintained even though the brightfield image appearance was changing as its focal plane changed.

Quantitative evaluation of long-term phase-locking. To verify that our method maintains a consistent phase-lock throughout long-term time-lapse imaging, we asked experts in zebrafish heart imaging ($n = 5$) to manually identify the same phase in a heartbeat (ventricular end-diastole) across a subset of the reference heartbeats used to capture the heart looping dataset in Fig. 3. Stacks were captured every 150 s using the real-time, prospective optical gating technique described above; automated long-term updating of the reference heartbeat, also described above, was carried out after every stack. Automated analysis used the (low-resolution) side-view brightfield images as usual, while human experts were shown simultaneously acquired higher-quality brightfield images acquired through the imaging objective at 0.8 NA. Without these high-quality images, it was almost impossible for the human experts to make any accurate judgement at all.

The human experts were provided with reference image sequences in a random order. These human-identified target frames were then compared to the fully automated, adaptive prospective optical gating results. In Fig. 3, neither the human nor the automated updates should be considered as the gold standard, but the close agreement between the two is further evidence that a consistent phase-lock has been maintained throughout the experiment. In the absence of a true gold standard, the human mean was treated as the zero point for each timepoint.

Assessment of photo-injury during imaging. To assess the effect of retrospective optical gating and adaptive prospective optical gating on the physiology of the fish we compared the heart rate of fish in two different scenarios:

1. For fish undergoing 2 h of fully automated, adaptive prospective optically gated time-lapse acquisition (gated stacks acquired every 5 min).
2. For fish undergoing 2 h of retrospective optically gated time-lapse acquisition, acquired in a similar manner to that described in ref. [13]. We used our existing light sheet set-up, but with the laser turned on continuously, to provide illumination equivalent to the acquisition of 600 video frames (each 2.5 ms exposure) per z plane (full details in Supplementary Table 1).

Heart rate was calculated every 5 min using the period-determination codes described in ref. [11]. Any heart rate determined that varied by more than ±25% from the previous heart rate value was discounted and a new period determined, which always varied by less than this amount. Such events occurred infrequently and were due to changes in heart rhythm causing erroneous period determination; eight of these events occurred, all during the retrospective optical gating protocol.

For each protocol (adaptive prospective optical gating and retrospective optical gating) fish were randomly selected from a full clutch of eggs. All fish were given 30 min to acclimatise, from which a resting heart rate was determined. Fish were then imaged for 2 h and the heart rate measured at the start of each new stack.

For the adaptive prospective optical gating protocol, fish were mounted in the microscope and, after acclimatisation, were exposed to pulsed laser illumination to accompany triggered (synchronised) fluorescence image acquisition. For retrospective gating experiments, fish were mounted in the microscope and, after acclimatisation, were exposed to constant laser illumination as required for retrospective optical gating (see above). In all cases the fish were also exposed to the

infrared illumination needed for brightfield imaging (required for heart rate determination as well as for synchronisation analysis).

We note that control fish exposed to no laser light at all show no change in heart rate, similar to the results seen in Fig. 5a for adaptive prospective optical gating experiments. We observed no developmental abnormalities in samples imaged using our method, and fish appear to undergo normal development with no obvious delay for fish developing at 23 °C.

Assessment of photobleaching during imaging. For retrospective gating, the same method was followed as above. For convenience and consistency, rather than performing an actual retrospective gating analysis on a high-speed recording of fluorescence images, we in fact used our own algorithms to trigger synchronised acquisition of the images that were subsequently analysed and compared against results from adaptive prospective optical gating, but throughout the z scan the laser was left on continuously to provide exactly the same illumination conditions as would be required for retrospective gating acquisition.

To quantify the fluorescence signal level in the z stack, an estimate of the global background signal level was made and subtracted from all pixels. The values of all voxels $v(x, y, t)$ within a volume-of-interest around the heart was summed for each timepoint t:

$$I(t) = \sum_{xy} v(x, y, t). \quad (6)$$

The resultant time-sequence was fitted with a double-exponential $I(t) = a + b\exp(-ct) + d\exp(-et)$. The constant term a compensates primarily for faint autofluorescence of red blood cells within the heart: due to the constant turnover of blood cells within the light sheet, this signal is not significantly bleached even at extremely high laser doses. We found that the double-exponential provided a good description of the complex dynamics involved in photobleaching, for the time-sequence from the retrospective gating protocol. A single-exponential was fitted in the case of the adaptive prospective gating protocol, since we found that the time constant of any second exponential term was too long to be reliably determined.

Cardiac laser injury. A Zeiss Photo Activated Laser Microdissection microscope system was used to induce a localised laser injury to the ventricular apex of anaesthetised 72 hpf zebrafish. These were laterally mounted on a glass slide in 20 µl of conditioned water and the laser was fired through a ×20 objective. Individuals were deemed injured when ventricular contractility considerably decreased and the ventricular apex reduced in size without rupturing the myocardial wall. Uninjured (control) fish were treated in the same manner up to the point of laser injury, when they were separated and maintained in the same conditions as injured fish.

Neutrophil tracking in time-lapse experiments. Neutrophil tracking was performed using the automated algorithms available in FIJI[52] via the TrackMate plug-in[53]. Detection parameters were: expected diameter 12 µm and quality threshold 20.0. Approximately the same number of neutrophils per frame were detected for all time intervals (Supplementary Fig. 3g). Tracks were then recovered with the Simple Linear Assignment Problem algorithms. At 3 min time-lapse intervals, a maximum linking distance of 30 µm was used, and a gap-closing maximum distance of 60 µm and 2 frames was used. These settings accommodate a maximum neutrophil velocity of 10 µm/min. Detections for all time intervals (see below) and tracks at 3 min intervals were manually inspected to check there were no obvious errors.

To demonstrate the need for time-lapse intervals as short as 3 min, we examined how track features change with increasing time-lapse intervals. First we created two track sets, which we refer to as "subsampled" and "decimated":

1. Subsampled virtual experiments were performed by starting with 3 min time-lapse dataset but retaining only every second stack for a 6 min interval, every third stack for a 9 min interval, etc. Tracks were recovered for these subsampled experiments as above, except the linking maximum distance and gap-closing maximum distance were scaled to allow the same maximum neutrophil velocity to be captured (Supplementary Fig. 3c shows an example at 30 min intervals). This track set represents our own best attempt at recovering tracks from data taken at longer time intervals, using off-the-shelf analysis tools.
2. Starting from tracks recovered from the 3 min time-lapse dataset, decimated tracks were created by only keeping track points associated with even-numbered stacks for a 6 min interval, and so on. Note that these decimated tracks are the closest to a "ground truth" dataset that can be recovered; it is intuitively apparent that the tracks captured at 3 min will have the fewest accidental track breakages or incorrect linkages (see Supplementary Fig. 3d for an example at 30 min intervals). This track set therefore represents a theoretical upper bound on possible performance (which would likely be impossible to attain in practice), in which the track analysis was actually performed with additional information (3 min interval image stacks) available to ensure correct track linking—that information would not in reality be available in an experiment using longer time-lapse intervals.

From these two track sets we measured the number of neutrophils per frame as a control (Supplementary Fig. 3g), the number of tracks, and the number of tracks that pass through the wound area (Supplementary Fig. 3e, f). We also measured the average absolute velocity and the meandering index[27] for each individual track (Supplementary Fig. 3h, i).

Image acquisition, processing and analysis. Volume datasets are presented as maximum intensity projections (MIPs) unless otherwise stated. A trivial linear colour mapping, starting at zero, was used in all cases. For the local detail presented in Figs. 4 and 6, MIPs were computed over a cropped z range to exclude background clutter.

For time series visualisations (apart from Supplementary Video 10), a small exponential correction was applied as a function of time, to compensate for gradual photobleaching. The intensity of all pixels in frame n was multiplied by $\exp(n/\tau)$. τ was just approximated empirically: for Fig. 6 we used $\tau = 250$ for the red (mKate) channel and $\tau = 330$ for the green (GFP) channel, for Fig. 3 we used $\tau = 500$, and no correction was used in other movies.

Surface rendering was performed using the Imaris software (Bitplane AG). Percentage increase in endothelial chamber volume was calculated by manually cropping the rendered atrium and ventricle and exporting the volume at 48 and 72 hpf.

Image acquisition parameters used for all experiments can be found in Supplementary Table 3.

Software and data handling. The computer code for real-time synchronisation, adaptive prospective optical gating, and image acquisition is implemented on a Unix-like platform (iMac 2015, Apple Inc.) to ensure consistent real-time performance and to benefit from high-quality performance diagnostic tools. The real-time computational demands of the analysis allow it to be run on a standard desktop computer, and we have even achieved good results using low-end portable computers (iBook 2008, Apple Inc.). The computer code implements the algorithms described above, and presents a graphical user interface for imaging, microscope control and initial post-experiment visualisation and processing (Supplementary Fig. 7). In future we intend to migrate our now-mature synchronisation system to a cross-platform framework such as Micromanager.

Data are streamed to the computer's hard disk in real-time. The storage requirements are comparatively modest (approx 100 MB/channel/3D timepoint uncompressed) since the only fluorescence images acquired and stored are from the desired phase in the heartbeat. This contrasts with alternative postacquisition approaches[12,13] that typically require several hundred times this number of images to be recorded for subsequent postprocessing. Maximum intensity projection images of the z-stacks are available for monitoring during acquisition, and on experiment completion data are prepared in a format suitable for importing into visualisation software such as Imaris (Bitplane AG).

Reporting summary. Further information on research design is available in the Nature Research Reporting Summary linked to this article.

Data availability

The data used to produce all results in this paper have been deposited in the University of Glasgow data repository at https://doi.org/10.5525/gla.researchdata.729. This repository contains maximum intensity projections of the fluorescence data shown in: Figs. 3–6; Supplementary Figs. 3 and 5; and Supplementary Videos 4–8 and 10 and 11. Brightfield reference heartbeats used in Figs. 3 and 5, and Supplementary Videos 2 and 9, are also available in this repository. Raw datasets for the experiments in this paper are very large, even using our method, and so most of these are not included in the repository but are available on reasonable request from the corresponding author. However, the full raw data for a small illustrative time range of Fig. 6 have been included in this repository. The repository also includes some processed data for the Jupyter Notebooks provided; this has been described in these Notebooks.

Code availability

The graphical user interface and all codes required to run adaptive prospective optical gating live have been deposited in the University of Glasgow data repository at https://doi.org/10.5525/gla.researchdata.729. This includes codes for prospective optical gating, updating reference frames and the codes needed for hardware interactions. Also available are Python/Jupyter notebooks for recreating the plots in Figs. 3–5 and Supplementary Figs. 3 and 4, and also for generating Supplementary Video 2.

Received: 29 August 2019; Accepted: 15 October 2019;
Published online: 15 November 2019

References

1. Scherz, P. J., Huisken, J., Sahai-Hernandez, P. & Stainier, D. Y. R. High-speed imaging of developing heart valves reveals interplay of morphogenesis and function. *Development* **135**, 1179–1187 (2008).
2. Keller, P. J. et al. Fast, high-contrast imaging of animal development with scanned light sheet-based structured-illumination microscopy. *Nat. Methods* **7**, 637–642 (2010).
3. Olivier, N. et al. Cell lineage reconstruction of early zebrafish embryos using label-free nonlinear microscopy. *Science* **329**, 967–971 (2010).
4. Swoger, J., Muzzopappa, M., López-Schier, H. & Sharpe, J. 4D retrospective lineage tracing using SPIM for zebrafish organogenesis studies. *J. Biophotonics* **4**, 122–134 (2011).
5. Staudt, D. W. et al. High-resolution imaging of cardiomyocyte behavior reveals two distinct steps in ventricular trabeculation. *Development* **141**, 585–593 (2014).
6. Uribe, V. et al. In vivo analysis of cardiomyocyte proliferation during trabeculation. *Development* **145**, dev164194 (2018).
7. Greger, K., Swoger, J. & Stelzer, E. H. K. Basic building units and properties of a fluorescence single plane illumination microscope. *Rev. Sci. Instrum.* **78**, 023705 (2007).
8. Power, R. M. & Huisken, J. A guide to light-sheet fluorescence microscopy for multiscale imaging. *Nat. Methods* **14**, 360–373 (2017).
9. Liebling, M. et al. Rapid three-dimensional imaging and analysis of the beating embryonic heart reveals functional changes during development. *Dev. Dyn.* **235**, 2940–2948 (2006).
10. Taylor, J. M. et al. Real-time optical gating for three-dimensional beating heart imaging. *J. Biomed. Opt.* **16**, 116021 (2011).
11. Taylor, J. M., Girkin, J. M. & Love, G. D. High-resolution 3D optical microscopy inside the beating zebrafish heart using prospective optical gating. *Biomed. Opt. Express* **3**, 3043–3053 (2012).
12. Liebling, M., Forouhar, A. S., Gharib, M., Fraser, S. E. & Dickinson, M. E. Four-dimensional cardiac imaging in living embryos via postacquisition synchronization of nongated slice sequences. *J. Biomed. Opt.* **10**, 054001 (2005).
13. Mickoleit, M. et al. High-resolution reconstruction of the beating zebrafish heart. *Nat. Methods* **11**, 1–6 (2014).
14. Weber, M. et al. Cell-accurate optical mapping across the entire developing heart. *eLife* **6**, 1–14 (2017).
15. Ohn, J., Tsai, H.-J. & Liebling, M. Joint dynamic imaging of morphogenesis and function in the developing heart. *Organogenesis* **5**, 248–255 (2009).
16. Pestel, J. et al. Real-time 3D visualization of cellular rearrangements during cardiac valve formation. *Development* **143**, 2217–2227 (2016).
17. Denvir, M. A., Tucker, C. S. & Mullins, J. J. Systolic and diastolic ventricular function in zebrafish embryos: influence of norepenephrine, ms-222 and temperature. *BMC Biotechnol.* **8**, 21 (2008).
18. Rombough, P. J. Ontogenetic changes in the toxicity and efficacy of the anaesthetic ms222 (tricaine methanesulfonate) in zebrafish (Danio rerio) larvae. *Comp. Biochem. Physiol. A Mol. Integr. Physiol.* **148**, 463–469 (2007).
19. Stainier, D., Lee, R. K. & Fishman, M. C. Cardiovascular development in the zebrafish. I. myocardial fate map and heart tube formation. *Development* **119**, 31–40 (1993).
20. Rohr, S., Otten, C. & Abdelilah-Seyfried, S. Asymmetric involution of the myocardial field drives heart tube formation in zebrafish. *Circ. Res.* **102**, e12–e19 (2008).
21. Beis, D. et al. Genetic and cellular analyses of zebrafish atrioventricular cushion and valve development. *Development* **132**, 4193–4204 (2005).
22. Matrone, G. et al. Laser-targeted ablation of the zebrafish embryonic ventricle: a novel model of cardiac injury and repair. *Int. J. Cardiol.* **168**, 3913–3919 (2013).
23. Hind, L. E., Vincent, W. J. B. & Huttenlocher, A. Leading from the back: the role of the uropod in neutrophil polarization and migration. *Dev. Cell* **38**, 161–169 (2016).
24. Germain, R. N., Miller, M. J., Dustin, M. L. & Nussenzweig, M. C. Dynamic imaging of the immune system: progress, pitfalls and promise. *Nat. Rev. Immunol.* **6**, 497–507 (2006).
25. Read, M. N., Bailey, J., Timmis, J. & Chtanova, T. Leukocyte motility models assessed through simulation and multi-objective optimization-based model selection. *PloS Comput. Biol.* **21**, e1005082 (2016).
26. Barros-Becker, F., Lam, P.-Y., Fisher, R. & Huttenlocher, A. Live imaging reveals distinct modes of neutrophil and macrophage migration within interstitial tissues. *J. Cell Sci.* **130**, 3801–3808 (2017).
27. Henry, K. M. et al. Phagosight: an open-source MATLAB® package for the analysis of fluorescent neutrophil and macrophage migration in a zebrafish model. *PLoS One* **8**, e72636 (2013).
28. Laissue, P. P., Alghamdi, R. A., Tomancak, P., Reynaud, E. G. & Shroff, H. Assessing phototoxicity in live fluorescence imaging. *Nature Methods* **14**, 657–661 (2017).
29. Icha, J., Weber, M., Waters, J. C. & Norden, C. Phototoxicity in live fluorescence microscopy, and how to avoid it. *Bioessays* **39**, 1700003 (2017).
30. Olarte, O. E., Andilla, J., Gualda, E. J. & Loza-Alvarez, P. Light-sheet microscopy: a tutorial. *Adv. Opt. Photonics* **10**, 111–179 (2018).
31. Dean, K. M. & Palmer, A. E. Advances in fluorescence labeling strategies for dynamic cellular imaging. *Nat. Chem. Biol.* **10**, 512–523 (2014).
32. Song, L., Hennink, E., Young, I. T. & Tanke, H. J. Photobleaching kinetics of fluorescein in quantitative fluorescence microscopy. *Biophys. J.* **68**, 2588–2600 (1995).
33. Cranfill, P. J. et al. Quantitative assessment of fluorescent proteins. *Nat. Methods* **13**, 557 (2016).
34. Bogdanov, A. M. et al. Cell culture medium affects GFP photostability: a solution. *Nat. Methods* **6**, 859 (2009).
35. Liu, J. et al. A dual role for erbb2 signaling in cardiac trabeculation. *Development* **137**, 3867–3875 (2010).
36. High, F. A. & Epstein, J. A. The multifaceted role of Notch in cardiac development and disease. *Nat. Rev. Genet.* **9**, 49–61 (2008).
37. Monte-nieto, G. et al. Control of cardiac jelly dynamics by NOTCH1 and NRG1 defines the building plan for trabeculation. *Nature* **557**, 439–445 (2018).
38. Forouhar, A. S. et al. The embryonic vertebrate heart tube is a dynamic suction pump. *Science* **312**, 751–753 (2006).
39. Zickus, V. & Taylor, J. M. 3D + time blood flow mapping using SPIM-microPIV in the developing zebrafish heart. *Opt. Express* **9**, 2418–2435 (2018).
40. Bouchard, M. B. et al. Swept confocally-aligned planar excitation (SCAPE) microscopy for high-speed volumetric imaging of behaving organisms. *Nat. Photonics* **9**, 113–119 (2015).
41. Olarte, O. E., Andilla, J., Artigas, D. & Loza-Alvarez, P. Decoupled illumination detection in light sheet microscopy for fast volumetric imaging. *Optica* **2**, 702 (2015).
42. Truong, T.V., et al. Selective volume illumination microscopy offers synchronous volumetric imaging with high contrast. *bioRxiv* (2018).
43. Gupta, V. & Poss, K. D. Clonally dominant cardiomyocytes direct heart morphogenesis. *Nature* **484**, 479 (2012).
44. Westerfield, M. *The Zebrafish Book: A Guide for the Laboratory Use of Zebrafish (Danio rerio)* (University of Oregon Press, Eugene, 2000).
45. Burns, C. G. et al. High-throughput assay for small molecules that modulate zebrafish embryonic heart rate. *Nat. Chem. Biol.* **1**, 263 (2005).
46. Proulx, K., Lu, A. & Sumanas, S. Cranial vasculature in zebrafish forms by angioblast cluster-derived angiogenesis. *Dev. Biol.* **348**, 34–46 (2010).
47. Yoo, S. K. et al. Differential regulation of protrusion and polarity by PI(3)K during neutrophil motility in live zebrafish. *Dev. Cell* **18**, 226–236 (2010).
48. Ellett, F., Pase, L., Hayman, J. W., Andrianopoulos, A. & Lieschke, G. J. mpeg1 promoter transgenes direct macrophage-lineage expression in zebrafish. *Blood* **117**, e49–e56 (2011).
49. Lin, Y.-F., Swinburne, I. & Yelon, D. Multiple influences of blood flow on cardiomyocyte hypertrophy in the embryonic zebrafish heart. *Dev. Biol.* **362**, 242–253 (2012).
50. Huisken, J. & Stainier, D. Y. R. Even fluorescence excitation by multidirectional selective plane illumination microscopy (mSPIM). *Opt. Lett.* **32**, 2608–2610 (2007).
51. Nelson, C. J., Buckley, C., Mullins, J. J., Denvir, M. A. & Taylor, J. Imaging the developing heart: synchronized time-lapse microscopy during developmental changes. *Proc. SPIE* **10499**, 104991F (2018).
52. Schindelin, J. et al. Fiji: an open-source platform for biological-image analysis. *Nat. Methods* **9**, 676 (2012).
53. Tinevez, J.-Y. et al. Trackmate: an open and extensible platform for single-particle tracking. *Methods* **115**, 80–90 (2017).

Acknowledgements

This work was funded by the British Heart Foundation (BHF) (NH/14/2/31074), with additional support from the BHF (RE/08/001), EPSRC (EP/M028135/1) and the Royal Society (RG130249). Individual support: F.A.B. and C.B. (BHF CoRE award RE/13/3/30183), A.K.B. (Medical Research Scotland project ID 3376798), C.J.N. (EPSRC Doctoral Prize Research Fellowship EP/N509668/1), A.G.R. (UK MRC Programme Grant MR/K013386/1) and J.M.T. (Royal Society of Edinburgh Sabbatical Research Grant RSE58915). We thank Dr. Thai Truong (University of Southern California) for proposing the side-view geometry used for brightfield imaging.

Author contributions

J.M.T and C.J.N. developed the synchronisation algorithms, software, electronics and optics. C.J.N., F.A.B., A.K.B. and C.B. performed the experiments and quantitative analysis, conceived individual experiments and developed the protocols. J.M.T., M.A.D., J.J.M., A.G.R., C.S.T. conceived the study and supervised the research. The manuscript was written with input from all authors.

Competing interests

The authors declare no competing interests.

Additional information

Supplementary information is available for this paper at https://doi.org/10.1038/s41467-019-13112-6.

Correspondence and requests for materials should be addressed to J.M.T.

Peer review information *Nature Communications* thanks the anonymous reviewer(s) for their contribution to the peer review of this work. Peer reviewer reports are available.

Reprints and permission information is available at http://www.nature.com/reprints

Publisher's note Springer Nature remains neutral with regard to jurisdictional claims in published maps and institutional affiliations.

Open Access This article is licensed under a Creative Commons Attribution 4.0 International License, which permits use, sharing, adaptation, distribution and reproduction in any medium or format, as long as you give appropriate credit to the original author(s) and the source, provide a link to the Creative Commons license, and indicate if changes were made. The images or other third party material in this article are included in the article's Creative Commons license, unless indicated otherwise in a credit line to the material. If material is not included in the article's Creative Commons license and your intended use is not permitted by statutory regulation or exceeds the permitted use, you will need to obtain permission directly from the copyright holder. To view a copy of this license, visit http://creativecommons.org/licenses/by/4.0/.

© The Author(s) 2019